INTEGRATED PHOTONIC DEVICES AND COMPONENTS FOR LINEAR, NONLINEAR AND QUANTUM OPTICAL APPLICATIONS

Raktim Haldar

Raktim Haldar. INTEGRATED PHOTONIC DEVICES AND COMPONENTS FOR LINEAR, NONLINEAR AND QUANTUM OPTICAL APPLICATIONS. Optics / Photonic. PhD, 2019. English. NNT : . tel-02469076

HAL Id: tel-02469076
https://hal.science/tel-02469076

Submitted on 6 Feb 2020

INTEGRATED PHOTONIC DEVICES AND COMPONENTS FOR LINEAR, NONLINEAR AND QUANTUM OPTICAL APPLICATIONS

Raktim Haldar

INTEGRATED PHOTONIC DEVICES AND COMPONENTS FOR LINEAR, NONLINEAR AND QUANTUM OPTICAL APPLICATIONS

Thesis submitted to
Indian Institute of Technology Kharagpur
for the award of the degree

of

Doctor of Philosophy

by

Raktim Haldar

under the guidance of

Dr. Shailendra Kumar Varshney
(Associate Professor)
(Electronics and Electrical Communication Engineering (E & ECE) Department)

DEPARTMENT OF ELECTRONICS AND ELECTRICAL COMMUNICATION ENGINEERING (E & ECE)
INDIAN INSTITUTE OF TECHNOLOGY KHARAGPUR
KHARAGPUR-721302, WEST BENGAL, INDIA
NOVEMBER 2019

- To my parents -

&

-To all those children we failed...to all those blossoms shed untimely-

চিত্ত যেথা ভয়শূন্য

চিত্ত যেথা ভয়শূন্য, উচ্চ যেথা শির,
জ্ঞান যেথা মুক্ত, যেথা গৃহের প্রাচীর
আপন প্রাঙ্গণতলে দিবসশর্বরী
বসুধারে রাখে নাই খণ্ড ক্ষুদ্র করি,
যেথা বাক্য হৃদয়ের উৎসমুখ হতে
উচ্ছ্বসিয়া উঠে, যেথা নির্বারিত স্রোতে
দেশে দেশে দিশে দিশে কর্মধারা ধায়
অজস্র সহস্রবিধ চরিতার্থতায়,
যেথা তুচ্ছ আচারের মরুবালুরাশি
বিচারের স্রোতঃপথ ফেলে নাই গ্রাসি,
পৌরুষেরে করে নি শতধা, নিত্য যেথা
তুমি সর্ব কর্ম চিন্তা আনন্দের নেতা,
নিজ হস্তে নির্দয় আঘাত করি, পিতঃ;
ভারতেরে সেই স্বর্গে করো জাগরিত।

--- **রবীন্দ্রনাথ ঠাকুর** ---

Where the mind is without fear

Where the mind is without fear and the head is held high;
Where knowledge is free;
Where the world has not been broken up into fragments
By narrow domestic walls;
Where words come out from the depth of truth;
Where tireless striving stretches its arms towards perfection;
Where the clear stream of reason has not lost its way;
Into the dreary desert sand of dead habit;
Where the mind is led forward by thee;
Into ever-widening thought and action;
Into that heaven of freedom,
My Father, let my country awake.

--- Rabindranath Tagore ---

CERTIFICATE OF APPROVAL

Certified that the thesis entitled **‘Integrated Photonic Devices and Components for Linear, Nonlinear and Quantum Optical Applications’**, submitted by **Raktim Haldar** to the Indian Institute of Technology Kharagpur, for the award of the degree of Doctor of Philosophy has been accepted by the external examiners and that the student has successfully defended the thesis in the viva-voce examination held today.

Prof. Prabir K. Biswas (Chairman)	Prof. Shailendra K. Varshney (Supervisor)
Prof. Akhilesh Mohan (Member of the DSC)	Prof. Prasanta K. Guha (Member of the DSC)
Prof. Sonjoy Majumder (Member of the DSC)	Prof. (External Examiner)

Department of Electronics and Electrical Communication
Engineering (E & ECE)
Indian Institute of Technology Kharagpur
Kharagpur, India-721302

Certificate

This is to certify that this thesis entitled **'Integrated Photonic Devices and Components for Linear, Nonlinear and Quantum Optical Applications'** submitted by **Raktim Haldar**, to the Indian Institute of Technology Kharagpur, is a record of bona fide research work carried out under our supervision and is worthy of consideration for award of Ph.D of the Institute.

Prof. Shailendra K. Varshney
E & ECE Department
Indian Institute of Technology Kharagpur
West Bengal,
India - 721302.

I.I.T. Kharagpur
November 2019

Declaration

I certify that

a. the work contained in the thesis is original and has been done by me under the guidance of my supervisor;

b. the work has not been submitted to any other institute for any other degree or diploma;

c. I have followed the guidelines provided by the Institute in preparing the thesis;

d. I have conformed to ethical norms and guidelines while writing the thesis;

e. whenever I have used materials (data, models, figures and text) from other sources, I have given due credit to them by citing them in the text of the thesis, and giving their details in the references, and taken permission from the copyright owners of the sources, whenever necessary.

Raktim Haldar

Acknowledgment

This dissertation would not have been complete without expressing my sincere gratitude to a large number of supervisors, mentors, peers, colleagues, friends, and family members.

First of all, I'm grateful to my Ph.D. supervisor Prof. Shailendra K. Varshney (E & ECE, IIT Kharagpur) whose constant support played a pivotal role in the completion of this thesis work. This work would not have been a reality without his valuable guidance, constant inspiration, and technical support. He has always been amicable to the students and encouraged their inquisitiveness. He continuously stimulated the group members for thought-provoking discussion, and provided us enough freedom to explore various topics from silicon photonics to quantum-biology, undauntedly. I also thank him for giving me ample opportunities to grow as an academician, sending me to the conferences, giving me responsibilities with equipment purchases, teaching assistantship, and mentoring new students. My supervisor's invaluable suggestions and immense moral support, which came on the back of his own struggles and experiences, helped shape my life to a great extent. Apart from the technical help, his positive attitude towards life, vibrant nature, impeccable work-habits, meticulous paper-works, punctuality, prudence, and efforts to strike work-life balance are exemplary to all of us. I'm also thankful to Prof. Nadia Belabas Plougonven (CNRS, University Paris-Saclay) for hosting and supervising me during the five-month period I spent in France as a part of Raman-Charpak Fellowship to perform experiments on quantum guidonics. She has provided me the necessary access to her experimental facilities, and I have really enjoyed learning several tips and tricks from her to make an experiment work!

I would be forever indebted to Prof. Sonjoy Majumder (Phys., IIT Kharagpur), one of my DSC members and the mentor of the subject 'quantum mechanics and quantum computation'. When I had joined the Ph.D. program, I did not have much knowledge of quantum mechanics, and my background was mostly on

RF & microwave engineering. He never became annoyed even while answering my silliest questions. Without his patience, guidance, and the utmost care, I would have been deprived of perceiving the essence of the magical world of quantum mechanics! Prof. Sayan Kar (Phys.) and Prof. Goutam Biswas (CSE) grew my interest in quantum mechanics and quantum computation in my early Ph.D. days. I'm equally thankful to Prof. Samudra Roy (Phys.) who has an inherent lucid style to explain the most difficult concepts of nonlinear optics. Prof. Prasanta K. Guha (E&ECE, DSC member), Prof. Bijoy K. Das (EE, IITM), and Prof. Selvaraja (IISC) helped me clarifying the fabrication aspects of our proposed devices. Prof. Akhilesh Mohan (E&ECE, IITKGP), a microwave expert and the member of my DSC committee has given me numerous suggestions regarding our proposed resonator design. Apart from that, the constant feedback from Prof. Basudev Lahiri, and Kapil Debnath (E&ECE), Shivakiran Bhaktha (Phys.), Yanne Chembo (Femto-st), Christian Koos (KIT), Wolfgang Freude (KIT), Kamel Bencheikh (CNRS), and Prof. Ariel Levenson (CNRS, University Paris-Saclay) helped me in shaping my thesis. Special thanks to Prof. Prabir K. Biswas (HOD, E&ECE, IIT Kharagpur) and Prof. Prasanta K. Das (Dean, PGS&R) for always being there.

This 'acknowledgment' remains incomplete without mentioning the story of the confused kid, Mr. Arkadev Roy. I can clearly remember that on a sudden morning Mr. Roy, a bachelor student from E&ECE department has appeared to me with a head full of cluttered, however, ingenious ideas, seeking for a proper research-direction. I have seen my childhood dreams in his eyes. With his tremendous fervor, unrequited love, insatiable curiosity, and a keen interest in gaining scientific knowledge, he gradually mastered the nonlinear, and quantum optics. Despite having a significant age-gap, soon we developed a unique camaraderie; however, he did not take it longer to reverse his role and started mentoring me! We published a couple of papers together. I always like his veracious, often harsh, however, constructive criticisms to my technical writings, research works, and important decisions related to my career. Eventually, he made it to his dream-place 'Caltech' as a graduate student last year (2018), the place where Mr. Feynman! had spent the final years of his life.

I'm fortunate to get the technical assistance from some of the extremely talented researchers such as Dr. Jae K. Jang (Columbia), Dr. David Barral (CNRS), Dr. Avik Dutt (Stanford), Mr. Sandeep Ummethala (KIT, Germany), Dr. Lorenzo M. Procopio (CNRS), Dr. Susobhan Das (Aalto), Dr. G. Thavasi Raja (NIT Trichy), Dr. Satya P. Singh (CSIR), whenever required. I am highly thankful to Mr. Utpal Patra, the former lab in-charge of Fiber Optic System Laboratory (FOSLAB), whose caring and avuncular nature was an invaluable treasure to me. I have spent sleepless nights discussing a variety of topics from the origin of the Universe to the role of Mahatma Gandhi and Netaji in Indian politics with my colleagues Dr. Nitin Bhatia (now a faculty member at IIT Jodhpur), Dr. Vishwatosh Mishra, and Mr. (soon a Dr.) Partha Mondal over countless coffee-cups. I would like to thank my other colleagues Mr. Abhik D. Banik (NTT Com), Ms. Maitrayee Saha, Mr. Sawaan K. Bag, Mr. Saroj Mohapatra, Ms. Shubhanshi Sharma, Ms. Ipsita Chakraborty, Mr. Rajat K. Sinha, the new additions to the FOSLAB, Mrs. Anjali Yadav, Ms. Rashmi Kumari and Mr. Sauradeep kar, and all the members of the Research Scholar Lab for their continuous support. Mr. Samrat Mukhopadhyay (E & ECE) frequently helped me to add the mathematical rigor in my works, whereas, without the presence of Sandip (E & ECE), Sovan-da (Rubber Tech.), Niladri (EE-SMST), Ambaresh (Phys.), Debajyoti (Phys.), Sourav (Metallurgy), Sudipan (Trento) it was never easy to handle the huge pressure of my pedagogical tenure. Colleagues from other departments such as ATDC (Dr. Swagata and Dr. Meher Wan), and Nanoscience (Dr. Ravindra Jha, Ms. Priyanka) helped me gaining experimental knowledge. The painstaking grammatical corrections made by a few of my friends are also to be mentioned.

I'm thankful to the hallowed funding agencies: Department of Science and Technology (DST), Ministry of Human Research and Development (MHRD), CEFIPRA, NNetra project initiatives from DST, MEITY, India, INQCA (France), Optical Society of America (OSA) for being equally supportive. I would also like to thank the software developers of Microsoft office, Grammarly, Turnitin, LaTeX(Overleaf), Matlab, Mathematica, Lumerical, Comsol, Optiwave, Origin Pro, Zotero, JMP, Autocad, Adobe Reader, Adobe Photoshop, Adobe Illustrator, Nitro Pro for providing me the essential platform to decorate the thesis. The huge library of IITKGP, numerous books and tea-shops are to be acknowledged as well. I particularly like to mention the well-organized gymnasium and TATA sports complex, IITKGP that helped me to control the adrenaline in my bloodstream and supplied fresh oxygen into my neurons!

Similar to every profession, some people ceaselessly tried to thwart the progress of my career; I'm thankful to them too for being a perennial source of challenge and inspiration.

The 'thrust' to research on 'Photonics' actually came long back during my school-days from Prof. Swagatam Das (ETCE, Jadavpur/ISI) who was then my Physics-teacher. His mellifluous teaching style, eloquent lectures, magical presentations, profound wisdom and intelligence made those complex and dull equations imprinted on the pages, lively. I still remember how his reverberant voice and recitation of the poems written by Rabindranath Tagore played with every string of my brain. I heard about the potency of 'Photonics' for the first-time from him during his introduction to modern electronics. Henceforth, he changed the course of my life and created a lasting impression on my career. Indeed, I'm blessed with many highly motivated teachers (Gurus) who helped me incessantly to navigate through the ebbs and flows of life, and made me reach at the stage to defend my thesis.

Life is incomplete without friends and family. I got my friends, brothers and sisters always with me, especially during those difficult hours when my father's sudden illness turned my life topsy-turvy. Just a few pages are not sufficient to describe their unconditional love and affection for me.

As a child, I was brimmed with curiosity, eager to unravel the mysteries of the world, where I had just arrived. As I grew up, my parents, especially my father, did not let that 'child' in me, die. I remember their patience in answering all my questions; I remember those sleepless nights we spent together on the roof-top to observe constellations and meteor showers in the dark and frigid mid-night cold. My father too is a science-graduate and undoubtedly is the best teacher I have ever seen. However, he was not prejudiced towards science and allowed my thought to hover on literature, history and other subjects with equal attention. They made me familiar with the struggles of the Indian freedom fighters, painters, scientists and so on. Within a few years I developed a penchant towards science and technology, which eventually led me to take up the Ph.D. program.

Finally, I owe much to the Almighty for granting me the required zeal and opportunity to push the cognizance of Mankind even being an insignificant creature from a tiny 'pale blue dot' in the Universe.

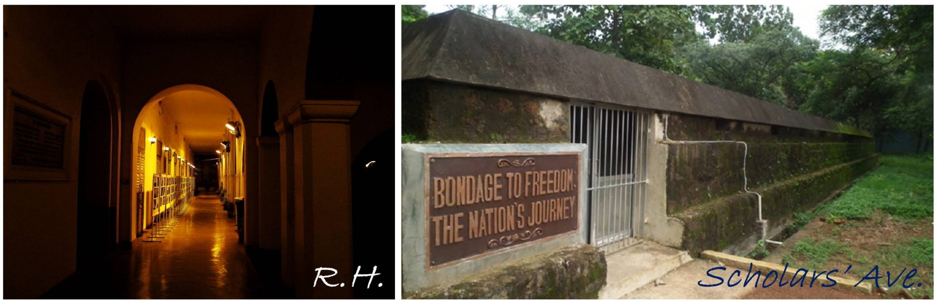

In memory of the martyrs
at Hijli detention camp, IIT Kharagpur

Abstract

Photonic technologies hold the potential to replace electronic technologies in near-future by solving most of the drawbacks of the electronic circuits. Generation and manipulation of photons in an integrated waveguide-based platform are preferred over bulk-optical components, mainly due to their compactness, stability, scalability, connectivity, reproducibility, and low power consumptions. Sophisticated fabrication techniques have enabled to design low-loss intricate planar and non-planar architectures consisting of several twists and turns. Optical directional couplers (DCs), polarization beam splitters (PBSs), microring resonators (MRRs), etc. are some of the indispensable components of the photonic circuits having a plethora of applications in the linear, nonlinear, and quantum optical applications. Silicon (Si) has been the preferred material to design the photonic components due to the high refractive-index, low-loss, low-cost, and high nonlinearity.

A corpus of works has been done to shrink the overall device footprint during the last few decades. At the beginning of the dissertation, a novel scheme to miniaturize the existing designs of optical DCs and PBSs based on off-centered, asymmetric, and hybrid dielectric slot waveguides is discussed. Slot dimensions and positions are optimized to achieve maximum coupling coefficient ($> 88\%$ enhancement) between two adjacent silicon wire-waveguides. The scheme leads to the device-length of $0.9\,\mu$m, and $1.1\,\mu$m, for the DC and the PBS, respectively, which is a significant improvement over their contemporary counterparts. To obtain ripple-free broadband band-pass or band-rejection filters, serially coupled MRRs have been utilized which occupy large space on a chip. To overcome this issue, non-concentric (off-axis) nested MRR has been proposed in this thesis work that reduces the filter-size without compromising its performance, thereby enabling high-density photonic integration on-chip. High thermo-optic coefficient of Si is the Achilles heel of the silicon-on-insulator MRR based electro-optic modulators (EOMs). Off-axis MRR also helps to mitigate the thermal red-shift in the spectral response of an MRR which facilitates its applicability to achieve athermal EOM. By further improvement in non-concentric nested MRRs, it is possible to attain and maintain high quality-factor and high extinction-ratio with a fabrication tolerance of 10–20%. Initial experiments on nested MRRs confirm the theoretical predictions. Such nested configurations will be highly efficient in bio-sensing and quantum applications for a broad ambient temperature range.

The Kerr nonlinearity of the microresonators has been exploited through a narrow line-width continuous-wave laser source for the generation of equispaced coherent frequency lines known as the optical frequency comb (FC). Most of the nonlinear materials used to generate FC, including Si, exhibit nonlinear losses and free-carrier effects in the telecom wavelength range. In the next part of the thesis, an analytical model of FC in the presence of nonlinear losses, free-carrier absorption, and dispersion effects has been developed, which capacitates us to explain several experimental results previously obtained. Further, numerical simulations explore that, using dual-pump, it is possible to generate tunable FC and synchronous all-optical buffers, which are robust to the writing-jitters, 3rd-order dispersion, and Raman effect. Apart from linear and nonlinear applications, integrated optical devices provide an efficient testbed for the realization of the invincible quantum technologies. In the final portion of the dissertation, efficient pumping schemes have been discussed to generate continuous variable bipartite and multipartite entanglement in different waveguide-pairs, simultaneously, using an integrated 5×5 periodically poled lithium niobate waveguide array through spontaneous parametric down conversion.

Keywords: Integrated photonics, nonlinear and quantum optics, optical coupler, polarization beam-splitter, Kerr microring resonator, optical frequency comb.

Contents

List of Abbreviations

A

a-Si	Amorphous silicon
AOM	Acousto-optic modulator
ARROW	Anti-resonant reflective optical waveguide

B

BOX	Buried oxide layer

C

CF	Crystalline fluoride
CMOS	Complementary metal-oxide-semiconductor
CMT	Coupled mode theory
COF	Capillary optical fiber
CPD	Carrier plasma dispersion
CS	Cavity soliton
CV	Continuous variable
CW(B)	Continuous-wave (background)

D

(D)WDM	(Dense) Wavelength division multiplexing
D-FWM	Degenerate four-wave mixing
dc	Direct current
DC	Directional coupler
DUT	Device under test
DV	Discrete variable

E

EBL	e-beam lithography
EDFA	Erbium doped fiber amplifier
EIM	Effective index method
EL	Excess loss
EM	Electromagnetic
EOM	Electro-optic modulator
ER	Extinction ratio

F

FC	Frequency comb
FCA	Free carrier absorption
FCD	Free carrier dispersion
FCE	Free-carrier effects
FDTD	Finite-difference time-domain
FEM	Finite element method
FPC	Fiber polarization controller
FSR	Free-spectral range
FWHM	Full width at half maximum

G

GVD	Group velocity dispersion

H

HSS	Homogeneous steady-state

I

IL	Insertion loss
IR	Infra-red

K

KLM	Knill Laflamme Milburn

L

LLE	Lugiato-Lefever equation

LPCVD	Low-pressure chemical vapor deposition

M

MCF	Multi-clad fiber
MI	Modulation instability
MR	Microresonator
MRR	Microring resonator

N

ND-FWM	Non-degenerate four-wave mixing
NRZ	Non-return-to-zero

O

OB	Optical buffer
OIM	Overlap integral method
OPO	Optical parametric oscillator

P

PBS	Polarization beam splitters
PCF	Photonic crystal fiber
PECVD	Plasma enhanced chemical vapor deposition
PPLN	Periodically poled lithium niobate
PPT	Positive partial transpose

Q

QC	Quantum computing
QCr	Quantum cryptography
QIP	Quantum information processing
QKD	Quantum key distribution
QPM	Quasi-phase matching

R

RI	Refractive index
RIE	Reactive-ion etching

S

SCS	Super cavity soliton
SD	Standard deviation
SFG	Sum frequency generation
SFWM	Spontaneous four-wave mixing
SHG	Second harmonic generation
SMF	Single mode fiber
SNR	Signal-to-noise ratio
SOI	Silicon-on-insulator
SPDC	Spontaneous parametric down conversion
SPS	Single-photon source
SSFM	Split-step Fourier method

T

TE	Transverse electric
THG	Third harmonic generation
TIR	Total internal reflection
TM	Transverse magnetic
TMM	Transfer matrix method
TOC	Thermo-optic coefficient
TOD	Third order dispersion

V

VLF	Van-Loock-Furusawa

W

WDM	Wavelength-division multiplexing
WGM	Whispering gallery mode

List of Figures

List of Tables

CHAPTER 1

Introduction

Optical technologies are ubiquitous, spanning from the detection of the delicate gravitational waves emitted billion years ago by the gargantuan black-holes to the accurate measurements on the minuscule subatomic particles and their sub-picosecond oscillations! Our daily lives are persistently benefited from the subtle omnipresence of the photonic technologies with the high-speed fiber-optic network, medical instruments, LED lamps, LASIK technology, or the mundane compact disks those are scattered carelessly at the corners of our tables. In fact, within a decade, photonic technologies are expected to invade if not topple the electronic technologies that we use in our mobile or personal computers. In this dissertation, several nanophotonic devices such as optical directional couplers (DCs), polarization beam splitters (PBS), microring resonators (MRRs) etc., which can be integrated with the existing electronic components as a part of optical interconnects, are explored. Furthermore, the thesis work is involved in modeling and designing integrated photonic components for nonlinear and quantum optical applications. In this chapter, an overview of photonic devices which are used in different linear, nonlinear and quantum optical applications is provided.

1.1 Photonics over Electronics: On-chip Linear Optical Devices

Electronic technologies, albeit revolutionized the 20th century, have many deficiencies. The reduction in feature size due to advancement in the semiconductor industry and integration of millions of transistors within the same chip, as prognosticated by Moore's law, have steered on-chip communication to the paradigm of multi-core processors which are fast enough to execute huge computations within a billionth of a second. However, the drift velocity of electrons and the parasitic capacitance between two electronic components limit the speed of electronic circuits. The delay at metallic interconnects leads to a bottleneck forcing asynchronous data transfer between the processor and the other parts of a computational system [1,2]. In addition to this, the demand for higher bandwidth of a system is one of the challenging issues. At the beginning of the 21st century, the problem aggravates as electronic chips started defying Moore's law, Koomey's law, and Dennard scaling (dark silicon effect), which finally inspires us to develop different non-Von Neumann architecture such as Harvard architecture and even neuromorphic computing. However, neuromorphic computers that attempt to mimic our brains are still in the incipient stage [3]. On the other hand, by leveraging the mature complementary metal-oxide-semiconductor (CMOS) technology, photonic components and circuits have the nascent potentiality to overcome almost all the drawbacks and limitations of the present-day electronic circuits and systems, including the Von Neumann bottleneck problem. Low power consumption, low latencies, less interference, ultra-compact size, extremely high data-rate, and wide bandwidth are the key advantages of the optical circuits [1–5]. Also, photonic technology with visible light and infrared is safe for in-situ medical applications. Silicon (Si)-photonics is the most suitable pathway to realize the dream of high-speed photonic computers. Various advantages of using silicon as a photonic platform are mentioned below,

- Silicon is cheap and widely available,
- Broad transparency window ($1.1\,\mu$m–$10\,\mu$m) [5],
- Higher refractive index (RI) (3.477) compared to silica (1.445), and air (1) at $1.55\,\mu$m,

- CMOS compatible,
- Availability of natural oxide,
- Can be purified up to 9N (99.9999999 %) by current technology,
- Higher Raman gain coefficient (dominant peak at 15.6 THz with 105 GHz bandwidth at 1.55 μm, 1 nm wider than that of silica),
- High nonlinear RI ($n_2 = 3 \times 10^{-18}\,\mathrm{m}^2/\mathrm{W}$), almost 100 times higher than that of silica,

The state-of-the-art silicon-on-insulator (SOI) technology has made it possible to fabricate new optical components with the existing microelectronic components. High RI contrast offered by Si in optical waveguides leads to strong optical confinement. The strong optical field inside the waveguide-core allows several low-loss sharp bends and made it possible to realize ultra-compact optical devices, such as, microring resonators (MRRs), which are scalable, robust, and have numerous applications in optical communication, data-routing, spectroscopy, and sensing [6–8]. Tight field confinement in the Si-waveguides also ensures very high optical intensity (equivalently, a small effective area), which facilitates the use of the SOI devices for nonlinear applications such as frequency conversion, supercontinuum generation, frequency-comb generation, and so on. [9–13]. These devices also aid to achieve strong light-matter interaction within nano-scale geometry, which gives rise to many novel optical phenomena [12, 13]. Mastering the control on the nano-world using photonic technologies opens up a new field of study called 'Nanophotonics' which administers us an unprecedented command over the molecular interactions, green-energy harvesting, drug delivery (optical tweezing), bio-sensing, and even genetic engineering. "There's Plenty of Room at the Bottom"—indeed, more than fifty years down the lane and now we realize how accurately Feynman envisaged the future-world! Nevertheless, some of the properties of silicon which are not always propitious to the photonic applications are listed below [5]:

- High positive (+ve) thermo-optic coefficient (TOC),
- High nonlinear losses below the wavelength 2.2 μm,
- Indirect band-gap, lack of efficient light emission,
- High electro-absorption,

- Absence of linear electro-optic (Pockel) effect, absence of second-order non-linearity without stress,
- Low Franz-Keldysh effect,
- Cannot be used to detect a signal at optical C-band.

It is interesting to note, though the high RI contrast offered by SOI waveguides is advantageous to most of the applications, high field-confinement and a relatively small coupling coefficient compel the coupling length of the device to be long. As a result, the overall device footprint of optical couplers, PBS, etc. becomes large. Recently, significant attention has been focused on designing very efficient, low-loss, compact on-chip optical couplers based on slotted Si wires [14] and photonic crystal circuits [15]. Also, several designs of compact PBS have been evolved, including dielectric-plasmonic hybrid structures [16, 17]. Nevertheless, the devices are either lossy [17] or numerically intensive [18] to design. It remains a challenge to achieve an efficient ultra-compact on-chip PBS with high extinction ratio (ER) and full-width at half maximum (FWHM) while maintaining very low insertion loss (IL) simultaneously. In the first part of the dissertation, a novel scheme to reduce the device size based on asymmetric slot waveguides is discussed. The proposed strategy can reduce the size of the DC and PBS at least by 88 %.

Optical bandpass/band-rejection filters [19] have extensive use in wavelength division multiplexing (WDM) communication system. One requires higher-order filters comprised of coupled MRRs to suppress the undesired ripples [20] in the pass or the rejection band. However, serially coupled MRRs used to design broadband bandpass filters, have large footprints. We have come up to an intelligent solution to save the space and thereby, integration of additional components within the same area. We refer this approach to non-concentric (or, off-axis) MRRs. Electro-optic modulators (EOMs) based on MRRs is one of the most important photonic components that drive the photonic interconnects to combat the bottle-neck issue. Performances of the MRR-based EOMs are highly affected by the temperature fluctuations [21]. The proposed athermal solutions are either power-inefficient, affects the message signal, or occupy large space in the chip. It is also established that off-axis MRR based EOM behaves athermally for a broad range of ambient temperature as the off-axis MRR can decouple the message signal and the controlling bias very efficiently. Initial experimental results confirm that non-concentric rings are fabrication tolerant ($> 20\%$) while arranged in a nested fashion, which suggests potential use in sensing, nonlinear, and quantum applications.

It is important to contemplate that the physical mechanism which drives an EOM is generally nonlinear (electro-absorption, Pockel or Kerr effect); however, the transfer characteristics of the operating device follows a linear relationship where the output optical signal requires to replicate the electrical input waveform.

1.2 Nonlinear Optics

A system (be it mechanical, electrical, optical; probabilistic or deterministic) is nonlinear if the governing equation capable to describe the dynamics of the system reasonably well, contains nonlinear terms. Nonlinear systems no longer follow the superposition principle. Nonlinearity often leads to the formation of fractals and chaos. In nonlinear optics, one studies the behavior of light in the medium where the dielectric polarization of the medium depends nonlinearly upon the incident electric field [9–11]. Being bosons, weakly interacting photons bestow us interference-free communication channels, on the other hand, necessitate the use of intense coherent light-sources and tight optical confinement to obtain the nonlinear optical phenomena. The discovery of lasers by T. H. Maiman in the middle of the twentieth century empowered us to demonstrate different nonlinear optical phenomena, thereby opening the Pandora's box to the quantum optics. Nonlinear optical processes include second harmonic generation, Pockel's effect, third harmonic generation, sum, and difference frequency generation, self-phase and cross-phase modulation, four-wave mixing, two-photon absorption, optical phase conjugation, optical parametric amplification and oscillation, Raman and Brillouin scattering, etc. Nonlinear interactions, though detrimental for optical communication systems, pave the way to generate optical sources of any required frequencies which were previously unattainable by natural laser sources. Nonlinear spectroscopy is another important application of nonlinear optics. Also, the generation of supercontinuum, optical solitons, frequency combs (FCs), and other nonlinear optical phenomena have been demonstrated using SOI platforms. The nonlinearity of photonic devices has been exploited for frequency conversions [9] both in linear optical waveguides and resonator systems. Narrow linewidth (kHz), continuous-wave (CW) laser sources have been employed to generate optical FC in microresonators (MRs) utilizing Kerr nonlinearity, which manifests itself as cavity soliton (CS) in time-domain [22, 23]. To model FC dynamics in MRs, damped-driven nonlinear Schrödinger equation with boundary condition, also known as Lugiato-Lefever equation (LLE) has been widely used [23]. Most of the optical materials exhibit losses in the telecom wavelength range that restrict their use in realizing various interesting nonlinear properties. However, in search of simplicity, the majority of such theoretical models have mostly condoned the effects of nonlinear losses and free-carriers in their analysis, except a few [24]. The existing studies are either numerical or experimental and do not provide much insight into the dynamics of the comb-formation [25]. An in-depth theoretical analysis of comb formation including the nonlinear losses, has been discussed through the mathematical model in this thesis work. Bichromatic pumping scheme in MRs provides an additional degree of freedom which results in robust and synchronous all-optical buffer. We also investigate the advantages of dual-pump MRs over the conventional monochromatic MRs in this thesis.

1.3 Integrated Quantum Optics

Quantum Mechanics is defined as a branch of physics capable of describing the esoteric behaviors of the atoms, subatomic, and elementary particles at the smallest scale of the energy levels in nature, where classical mechanics usually fails [26]. Photons are considered as the mediator of electromagnetic energy, and ‘Quantum optics’ is a field of research which deals with the light-matter interaction in microscopic level with the help of quantum mechanics and quantum electrodynamics, considering the flow of light as a stream of photons. In general, for the ease of understanding, classical or semi-classical approaches are being adopted to describe most of the linear and nonlinear optical phenomena. For example, though the photo-electric effect cannot be described using classical physics, it can be satisfactorily explained through the semi-classical approach. In contrary, a few optical phenomena such as Hong-Ou-Mandel effect, photon anti-bunching or the sub-Poissonian distribution of light, squeezing of light, parametric optical processes, etc. cannot be described satisfactorily with any of these approaches [26–30] where quantum optics becomes indispensable. At this tiny scale, wave property of the particle becomes prominent. In recent years, photonic platforms (mostly in silicon, silicon nitride, lithium niobate, etc.) are exploited extensively to realize quantum effects such as the on-chip generation of entangled states, which spawns a new and intriguing branch of optics called 'Integrated quantum optics' [31, 32].

1.4 Quantum Computation and Cryptography

As proposed by Feynman, devising the power of quantum entanglement and the immense parallelism of superposed quantum states, quantum information processing (QIP) techniques offer several benefits with respect to their classical counterparts [33]. Apart from quantum computing (QC), in 1984, Bennett and Brassard have suggested that laws of quantum mechanics can also be used for secure communications [34]. Consequently, 'Quantum cryptography' (QCr) emerges, which is an art of science that exploits the fascinating features of quantum mechanics such as Heisenberg's uncertainty principle, no-cloning theorem, Bell's inequality or the quantum entanglement, i.e. 'spooky action at a distance' to perform cryptographic tasks [29]. As an example, quantum key distribution (QKD) allows two remote parties (viz. Alice and Bob) to distribute secret keys through public channels using quantum cryptographic protocols for quantum communications. In principle, QKD can offer unconditional security guaranteed by the laws of quantum physics even in the presence of an omnipotent eavesdropper (Eve), which is long been considered as 'The Holy Grail' of any communication systems [35, 36]. Quantum properties of light can be exploited in a myriad of applications such as QC, QIP, QCr, quantum simulations, spectroscopy, metrology and sensing [37,38]. As discussed earlier, being bosonic in nature, photons show less interaction with other particles and within themselves, thereby are less susceptible to the quantum noise or decoherence. However, in 2001, Knill, Laflamme, and Milburn (KLM protocol) showed that linear optical components such as optical beam splitters and couplers along with single-photon sources and photon detectors are sufficient for quantum computation [30]. KLM protocol is regarded as one of the milestones in realizing quantum computing devices through the discrete variable (DV) photonic systems as obtaining nonlinearity using a few photons is extremely difficult [39].

Generation and manipulation of photons in an integrated on-chip waveguide-based platform are preferred over the crystal-based bulk-optical components mainly due to their compactness, stability, scalability, connectivity, reproducibility, the potential for lower power consumptions, etc. Recent developments in fabrication technologies make integrated quantum photonic circuits a promising and versatile approach for future QIP technologies. Photonic quantum circuits comprised of on-chip photonic components such as optical couplers, PBS, etc., can easily manipulate the polarization of light and the flow of photons. Continuous-variable (CV) approach for QC conversely utilizes low-cost deterministic laser sources and detectors [39]. In the final part of my thesis, the best pumping scheme to generate bipartite and multipartite CV entangled states in periodically poled lithium niobate waveguide array through spontaneous parametric down conversion has been studied. Before proceeding for the experiments, we calculate the bipartite CV-entanglement between waveguide modes through the Peres-Horodecki criteria/positive partial transpose (PPT), whereas, the generation of multipartite entanglement is investigated through the Van Loock Furusawa criteria (VLF) [40,41]. Such entangled states can be used for quantum computations or in a multi-party quantum cryptographic protocols.

To summarize, in this thesis, I have chosen some of the fascinating applications, which can be divided into three major categories, viz. the design of integrated photonic components for (i) linear (DCs, PBSs, and MRR-filters) (ii) nonlinear (FC generation), and (iii) quantum optical applications (entangled CV states generation).

1.5 Motivation

A broad range of enthralling topics on linear, nonlinear, and quantum optics are covered throughout the thesis-work. A few caveats of the existing photonic technologies, specifically in linear and nonlinear devices are found through an extensive literature survey, which acts as the motivation of this dissertation.

- Tight optical confinement in individual SOI-waveguide entails weak evanescent coupling when two optical waveguides are placed close to each other. Weak coupling compels the SOI-based optical couplers and PBS to be longer to attain the desirable performances [4, 5].
- A single MRR has a spectral response equivalent to the notch filter. However, to achieve a bandpass or band-rejection filter, a few of such MRRs are coupled serially, which in turn increases the device footprint. To achieve a ripple-free broadband filter response within a compact size remains a challenge [7, 8].
- Silicon has a high thermo-optic coefficient (TOC $\sim 1.86\times10^{-4}$ /K). Therefore, a small change in temperature or the existence of local hot-spot is reflected by a dramatic change in the transmission characteristics and thereby deforms the output waveform of a high-Q MRR based EOM. The current technologies to mitigate the undesirable thermal effects are either power inefficient, large in size, or CMOS incompatible, and costly.
- MRRs are mostly designed to operate in the critical coupling regime. Some applications also demand the MRR to work either in the slightly over-coupling, or marginally under-coupling condition [6]. The coupling condition of an MRR is very sensitive to the fabrication errors and the ambient temperature.
- Owing to the band-gap energies most of the materials used to build the nonlinear photonic platforms including silicon, possess nonlinear losses such as multi-photon absorptions, free-carrier absorption (FCA), and free-carrier dispersion (FCD) in telecom wavelength range covering the C-band. Existing theoretical models of FC still lack a general mathematical framework that includes the effects of the nonlinear losses [22, 23].

- Monochromatic Kerr MR based all-optical buffers employ the cavity solitons (CSs) as optical-bits. They are asynchronous in nature, and the performance of these CS-based buffers is severely affected by the writing jitters, third-order dispersion, and the Raman Effect.
- Integrated photonic waveguide based continuous variable (CV) bipartite and multipartite entangled sources are highly coveted for the implementation of quantum computing devices on a single chip. Nonetheless, nonlinear losses such as two-photon absorption (2PA) make it difficult to realize squeezed state and entangled photon pairs in telecom C-band within silicon waveguides.

1.6 Research Objectives

Based on the motivation, the following objectives are set for the thesis work:

- To investigate the existing schemes for the miniaturization of optical components; To study the slot-waveguide based DCs and PBSs using overlap-integral method (OIM), super-mode analysis, and 3D finite-difference time-domain (FDTD) method.
- To maximize the coupling between two adjacent slotted silicon wire waveguides by optimizing the slot size and position.
- To develop a theoretical model based on the transfer matrix method (TMM), and FDTD for the study of non-concentric microring resonators. Implementation of the non-concentric MRR to design the compact bandpass/band-rejection filter and compact athermal EOM.
- To model the Kerr frequency-comb based on modified LLE in the presence of multiphoton absorptions and free-carrier effects, which might help to study the steady-state, self-pulsation, and modulation instability in the presence of various nonlinear losses.
- To investigate the advantages of bichromatic pumping over monochromatic Kerr MRs and to exploit the dual-pump Kerr MR configurations as an all-optical buffer.

- To determine the best pumping scheme of a PPLN waveguide array that generates a large number of bipartite and multipartite quantum entanglement in multiple waveguide pairs efficiently, which can be used in quantum computation and cryptographic applications.

1.7 Thesis Organization

Chapter 1 serves as an introduction and literature survey on various linear, nonlinear, and quantum photonic devices and their applications. We briefly explain each category with the relevant state-of-the-art optical devices, their pros, and cons, along with the further scope of work, which motivate the thesis-work. Based on the motivation, research objectives are proposed.

In **chapter 2**, we introduce a novel scheme to design ultra-compact photonic devices maneuvering the asymmetric slot-waveguide.

The first part of **chapter 3** presents non-concentric (or, off-axis) MRRs that has the potential to offer wideband band-pass or band-rejection filter with a reduced device-size, whereas, the next part of chapter 3 describes an athermal EOM based on off-axis MRR, and fabrication-tolerant nonconcentric nested (NN) MRR. Chapter 3 finally ushers the way towards a possible solution to the performance degradation caused by the alteration of coupling conditions.

Chapter 4 of the thesis is devoted in developing a complete mathematical model of the Kerr FC in the presence of all nonlinear losses.

Chapter 5 discusses the potential of dual-pump Kerr MR based optical buffers as a remedy of the problems experienced by the monochromatic Kerr FC.

In **chapter 6** of the thesis, we employ PPLN waveguide arrays for the generation of multipartite entanglement.

In a nut-shell, second and third chapters contain the designs of linear optical devices whereas, chapter 4, chapter 5 and chapter 6 target the various aspects of FC generation in nonlinear optical platforms including quantum optical devices.

Chapter 7 summarizes and concludes the dissertation discussing possible future research directions.

References

[1] L. C. Kimerling, "Photons to the rescue: Microelectronics becomes microphotonics." *Electronic Device Failure Analysis*, vol. 4, no. 3, pp. 15–20, 2002.

[2] A. Alduino and M. Paniccia, "Interconnects: Wiring electronics with light," *Nature Photonics*, vol. 1, no. 3, pp. 153–155, 2007.

[3] P. R. Prucnal and B. J. Shastri, *Neuromorphic photonics.* CRC Press, 2017.

[4] R. Won and M. Paniccia, "Integrating silicon photonics," *Nature Photonics*, vol. 4, pp. 498–499, 2010.

[5] G. T. Reed and A. P. Knights, *Silicon Photonics: An Introduction.* John Wiley & Sons, 2004.

[6] I. Chremmos, O. Schwelb, and N. Uzunoglu, *Photonic microresonator research and applications.* Springer, 2010, vol. 156.

[7] M. Lipson, "Guiding, modulating, and emitting light on silicon-challenges and opportunities," *Journal of Lightwave Technology*, vol. 23, no. 12, pp. 4222–4238, 2005.

[8] M. Lipson, "Compact electro-optic modulators on a silicon chip," *IEEE Journal of Selected Topics in Quantum Electronics*, vol. 12, no. 6, pp. 1520–1526, 2006.

[9] J. Leuthold, C. Koos, and W. Freude, "Nonlinear silicon photonics," *Nature Photonics*, vol. 4, no. 8, pp. 535–544, 2010.

[10] Q. Lin, O. J. Painter, and G. P. Agrawal, "Nonlinear optical phenomena in silicon waveguides: modeling and applications," *Optics Express*, vol. 15, no. 25, pp. 16 604–16 644, 2007.

[11] P. Grelu, *Nonlinear optical cavity dynamics: from microresonators to fiber lasers.* John Wiley & Sons, 2015.

[12] L. Novotny and B. Hecht, *Principles of Nano-Optics.* Cambridge university press, 2012.

[13] Y. S. Yi, *Integrated Nanophotonic Resonators: Fundamentals, Devices, and Applications.* CRC Press, 2015.

[14] H. M. K. Wong, C. Lin, M. A. Swillam, and A. S. Helmy, "Broadband compact Si wire to slot waveguide couplers," in *CLEO: Science and Innovations.* Optical Society of America, 2013, pp. CTu3F–6.

[15] M. J. Zablocki, A. Sharkawy, O. Ebil, S. Shi, and D. Prather, "Electro-optically switched compact coupled photonic crystal waveguide directional coupler," *Applied Physics Letters*, vol. 96, no. 8, p. 081110, 2010.

[16] A. Hosseini, S. Rahimi, X. Xu, D. Kwong, J. Covey, and R. T. Chen, "Ultracompact and fabrication-tolerant integrated polarization splitter," *Optics Letters*, vol. 36, no. 20, pp. 4047–4049, 2011.

[17] Q. Tan, X. Huang, W. Zhou, and K. Yang, "A plasmonic based ultracompact polarization beam splitter on silicon-on-insulator waveguides," *Scientific reports*, vol. 3, p. 2206, 2013.

[18] B. Shen, P. Wang, R. Polson, and R. Menon, "An integrated-nanophotonics polarization beamsplitter with $2.4\times2.4\,\mu\text{m}^2$ footprint," *Nature Photonics*, vol. 9, no. 6, pp. 378–382, 2015.

[19] B. E. Little, S. T. Chu, H. A. Haus, J. Foresi, and J.-P. Laine, "Microring resonator channel dropping filters," *Journal of Lightwave Technology*, vol. 15, no. 6, pp. 998–1005, 1997.

[20] S. Xiao, M. H. Khan, H. Shen, and M. Qi, "A highly compact third-order silicon microring add-drop filter with a very large free spectral range, a flat passband and a low delay dispersion," *Optics Express*, vol. 15, no. 22, pp. 14 765–14 771, 2007.

[21] K. Padmaraju and K. Bergman, "Resolving the thermal challenges for silicon microring resonator devices," *Nanophotonics*, vol. 3, no. 4-5, pp. 269–281, 2014.

[22] T. Herr, V. Brasch, J. D. Jost, C. Y. Wang, N. M. Kondratiev, M. L. Gorodetsky, and T. J. Kippenberg, "Temporal solitons in optical microresonators," *Nature Photonics*, vol. 8, no. 2, pp. 145–152, 2014.

[23] S. Coen, H. G. Randle, T. Sylvestre, and M. Erkintalo, "Modeling of octave-spanning kerr frequency combs using a generalized mean-field lugiato–lefever model," *Optics Letters*, vol. 38, no. 1, pp. 37–39, 2013.

[24] R. K. Lau, M. R. Lamont, Y. Okawachi, and A. L. Gaeta, "Effects of multiphoton absorption on parametric comb generation in silicon microresonators," *Optics Letters*, vol. 40, no. 12, pp. 2778–2781, 2015.

[25] A. G. Griffith, R. K. Lau, J. Cardenas, Y. Okawachi, A. Mohanty, R. Fain, Y. H. D. Lee, M. Yu, C. T. Phare, C. B. Poitras *et al.*, "Silicon-chip mid-infrared frequency comb generation," *Nature Communications*, vol. 6, p. 6299, 2015.

[26] M. Fox, *Quantum optics: an introduction.* Oxford University Press (OUP), 2006, vol. 15.

[27] S. Tanzilli, A. Martin, F. Kaiser, M. P. De Micheli, O. Alibart, and D. B. Ostrowsky, "On the genesis and evolution of integrated quantum optics," *Laser & Photonics Reviews*, vol. 6, no. 1, pp. 115–143, 2012.

[28] M. A. Nielsen and I. Chuang, *Quantum computation and quantum information.* Cambridge University Press (CUP), 2002.

[29] C. H. Bennett and G. Brassard, "Quantum cryptography: public key distribution and coin tossing." *Theor. Comput. Sci.*, vol. 560, no. 12, pp. 7–11, 2014.

[30] E. Knill, R. Laflamme, and G. J. Milburn, "A scheme for efficient quantum computation with linear optics," *Nature*, vol. 409, no. 6816, pp. 46–52, 2001.

[31] J. L. O'brien, A. Furusawa, and J. Vučković, "Photonic quantum technologies," *Nature Photonics*, vol. 3, no. 12, pp. 687–695, 2009.

[32] A. Politi, M. J. Cryan, J. G. Rarity, S. Yu, and J. L. O'brien, "Silica-on-silicon waveguide quantum circuits," *Science*, vol. 320, no. 5876, pp. 646–649, 2008.

[33] R. P. Feynman, "Simulating physics with computers," *International Journal of Theoretical Physics*, vol. 21, no. 6, pp. 467–488, 1982.

[34] C. H. Bennett, G. Brassard, and N. D. Mermin, "Quantum cryptography without bells theorem," *Physical Review Letters*, vol. 68, no. 5, pp. 557–559, 1992.

[35] A. K. Ekert, "Quantum cryptography based on Bell's theorem," *Physical Review Letters*, vol. 67, no. 6, pp. 661–663, 1991.

[36] E. Diamanti, H.-K. Lo, B. Qi, and Z. Yuan, “Practical challenges in quantum key distribution,” *npj Quantum Information*, vol. 2, p. 16025, 2016.

[37] M. Epping, H. Kampermann, D. Bruß *et al.*, “Multi-partite entanglement can speed up quantum key distribution in networks,” *New Journal of Physics*, vol. 19, no. 9, p. 093012, 2017.

[38] X. Su, X. Jia, C. Xie, and K. Peng, “Preparation of multipartite entangled states used for quantum information networks,” *Science China Physics, Mechanics & Astronomy*, vol. 57, no. 7, pp. 1210–1217, 2014.

[39] S. L. Braunstein and P. Van Loock, “Quantum information with continuous variables,” *Reviews of Modern Physics*, vol. 77, no. 2, pp. 513–577, 2005.

[40] R. Simon, “Peres-Horodecki separability criterion for continuous variable systems,” *Physical Review Letters*, vol. 84, no. 12, pp. 2726–2729, 2000.

[41] P. van Loock and A. Furusawa, “Detecting genuine multipartite continuous-variable entanglement,” *Physical Review A*, vol. 67, no. 5, p. 052315, 2003.

CHAPTER 2

Ultra-compact Optical Couplers and Polarization Beam-splitters using Asymmetric Slots

In this chapter, at first, we briefly discuss the basics of various optical waveguides and optical couplers. Subsequently, we introduce the concept of slot waveguides, their fabrication processes, coupling mechanisms, various advantages over the conventional waveguide structures and applications. In the next section, we present novel schemes to design on-chip ultra-compact optical directional couplers (DCs) and broadband polarization beam splitters (PBS) based on off-centered and asymmetric dielectric slot waveguides, respectively. Slot dimensions and positions are optimized to achieve maximum coupling coefficients between two symmetric and non-symmetric slotted silicon wire waveguides through overlap integral method (OIM). We observe $> 88\%$ enhancement in the coupling coefficients when the size-optimized slots are placed in optimal positions, with respect to the same waveguides having no slot. When the waveguides are parallel, in that case, a coupling length as short as $1.73\,\mu$m is accomplished for transverse-magnetic (TM) mode with the off-centered and optimized slots. This scheme enables us to design optical directional couplers with a very small footprint, $L_c \sim 0.9\,\mu$m in presence of S-bends. We also report a compact ($L_\mathrm{c} \sim 1.1\,\mu$m) on-chip broadband PBS with hybrid slots. Extinction ratios of 13 dB and 22.3 dB are realized with very low insertion loss (0.055 dB and 0.008 dB) for TM and transverse-electric (TE) modes at 1.55 μm, respectively. The designed PBS exhibits a bandwidth of 78 nm for the TM mode (C-and partial L-bands) and > 100 nm for the TE mode (S+C+L wavelength bands). Such on-chip devices can be used to design compact photonic interconnects and quantum information processing (QIP) units efficiently. At the final section of this chapter, we have investigated the fabrication tolerances of the proposed devices and described the fabrication steps to realize such hybrid devices. Our results are in good agreement with 3D finite-difference time-domain (FDTD) simulations. [1]

2.1 Introduction

Photonic circuits have the potential to overcome most of the drawbacks and limitations of present-day electronic circuits and systems including the bottleneck issues between processors and interconnects [1, 2]. On-chip optical switches, couplers, modulators, and PBS are essential components of photonic circuits [3]. With recent developments in photonic circuits, analogously, we are approaching an era of QIP that offers several benefits with respect to classical alternatives for several applications [4]. In 2001, Knill, Laflamme, and Milburn showed that linear optical components such as optical beam splitters and couplers along with single-photon sources and photon detectors are sufficient for quantum computation [5, 6] which is known as ‘KLM protocol’. Photonic quantum circuits comprised of on-chip Si-based photonic components such as optical couplers, PBS, etc., can easily manipulate the polarization of light and the flow of photons [7,8]. Entangled quantum state generation and GHz-clocked quantum key distribution systems using photonic circuits have been demonstrated in [8–10].

Due to the high refractive index (RI) contrast between silicon, silica, and air, silicon-on-insulator (SOI) wire waveguides exhibit excellent light-guiding property and has the potential for compact on-chip circuits as they allow small bends with

---

[1] Publications related to this chapter are [46], [47].

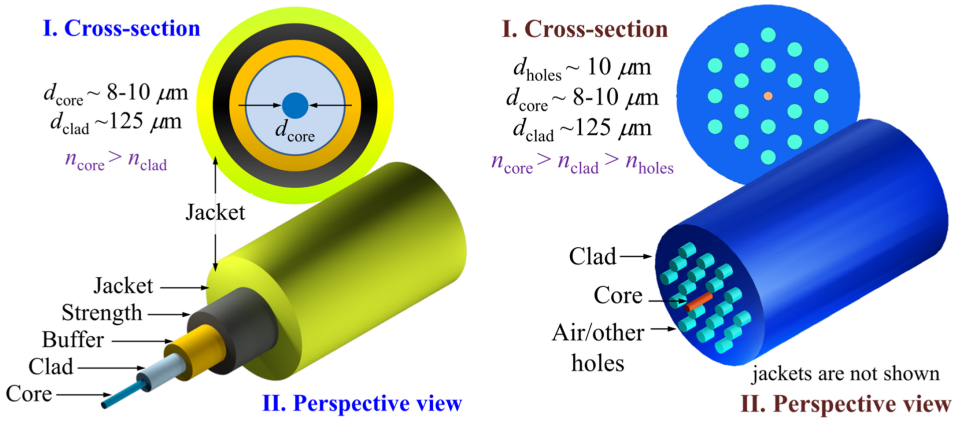

(a) Single-mode fiber (SMF) (b) Photonic crystal fiber (PCF)

Cylindrical optical waveguides

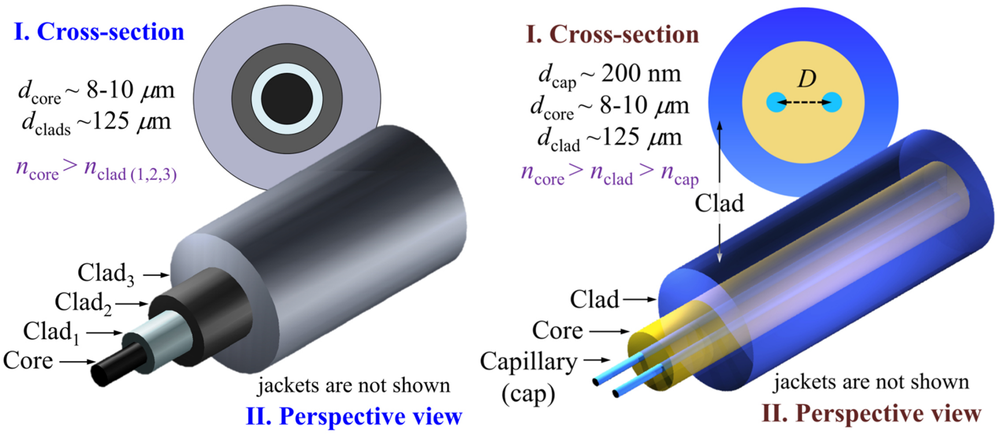

(c) Multi-clad fiber (MCF) (d) Capillary optical fiber (COF)

Figure 2.1: Cross-sectional (I) and perspective view (II) of (a) Conventional SMF, (b) PCF with a core, (c) Fiber with multiple cladding regions, (d) capillary optical fibers. Protective layers, buffers, jackets, etc. are not shown in Figs. (b), (c), and (d) for simplicity and clarity. Note that, the capillary optical fibers are equivalent to the slot waveguides.

negligible losses. Current advancements in complementary metal-oxide semiconductor (CMOS) fabrication technology make it possible to fabricate highly dense nano-scale devices [11, 12]. However, high field confinement and relatively small coupling coefficient compel the coupling length of the device to be large, and as a result, the overall device footprint of optical couplers, PBS etc. is increased. It has been observed that narrow slot/slots in the waveguides further enhance the confinement of particular optical modes in the core region and reduce the

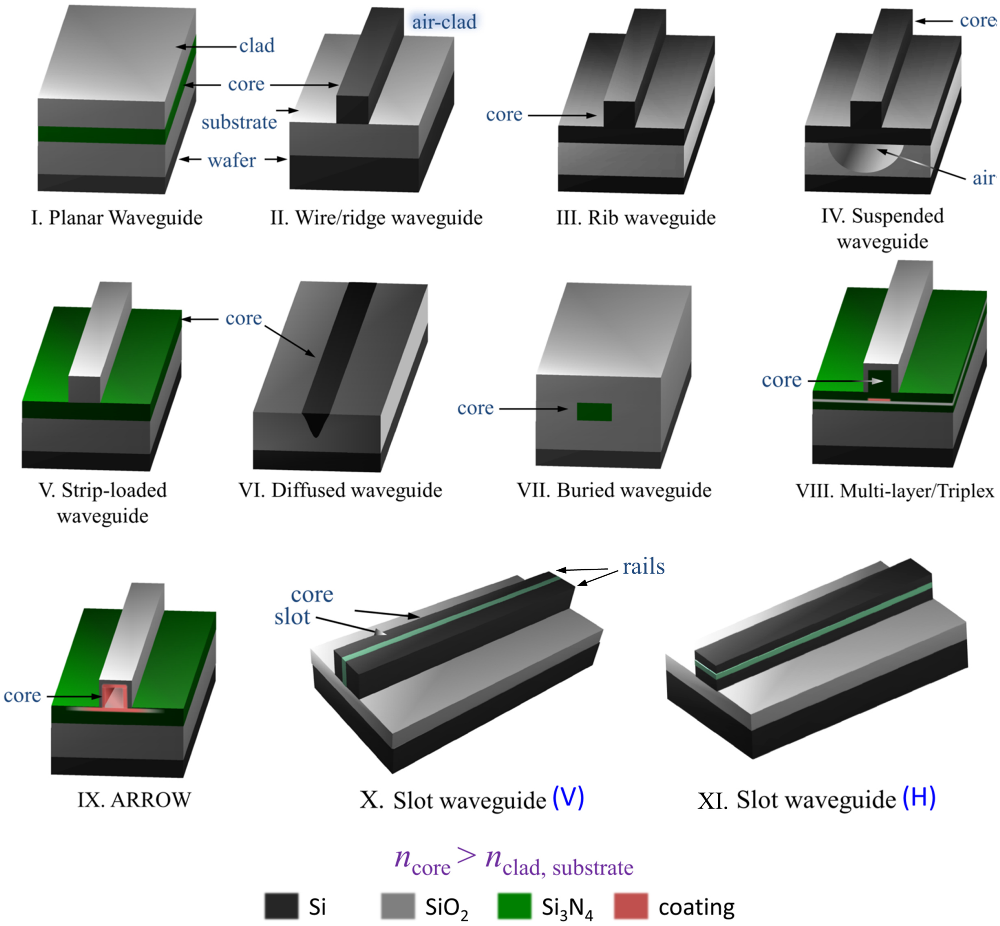

Figure 2.2: 3D perspective view of SOI—(I) planar/slab, (II) wire/ridge waveguide, (III) rib waveguide, (IV) suspended, (V) strip-loaded, (VI) diffused, (VII) buried, (VIII) multi-layered or triplex waveguides, (IX) anti-resonant reflective optical waveguide (ARROW), waveguides with a single—(X) vertical (V) slot, and (XI) horizontal (H) slot.

bending loss of the waveguide [13]. Straight and bent waveguides with slotted cross-sectional regions can be combined to build microring resonators which have wide range of applications in integrated optics [14]. Slotted waveguides are particularly interesting in nonlinear optics due to their very small effective mode area and flat dispersion profiles [15, 16]. Recently, significant attention has been focused on designing very efficient, low-loss, compact on-chip optical couplers based on slotted Si wires [17] and photonic crystal circuits [18].

Over the last few years, several designs of compact PBS have been evolved such as multimode interference splitters [19, 20], DC [21, 22] and adiabatic mode evolution [23, 24]. However, it is challenging to achieve an efficient ultra-compact on-chip PBS with high extinction ratio (ER) and full-width at half maximum (FWHM) while maintaining very low insertion loss (IL) simultaneously. To achieve an ultra-short PBS, often high structural asymmetry or large birefringence is necessary [25]. Plasmonic and hybrid plasmonic waveguides can provide the required birefringence and can reduce the device size considerably [25–29]. Three-core plasmonic PBS designs have also been reported in [30–33]. Plasmonic PBSs are promising; nonetheless, plasmonic devices mostly suffer from very high propagation loss. It is also difficult to fabricate narrow metallic nano-ribbons, required by several plasmonic structures in a SOI platform. Recently, a PBS with foot-print as small as $2.4 \times 2.4\,\mu\text{m}^2$ has been reported [34] making the use of inverse design algorithm [35]. But the design mentioned above [34] has moderately high IL, less ER ($\sim 10\,\text{dB}$), low FWHM ($\sim 32\,\text{nm}$), and most importantly, it takes large time to realize numerically. A few exotic approaches to design a PBS have also been attempted based on photonic crystal circuits [36], grating couplers [37], and periodic dielectric waveguides [38]. Such designs are novel, albeit, impractical to be included for on-chip photonic circuits.

Similar to plasmonic waveguides, slots in the waveguide can also provide extraordinary structural birefringence which can facilitate an efficient design of a PBS. The general convention is to place narrow slots in the middle of the waveguide and enhance the coupling for a particular mode to achieve a compact design. Designs of PBS based on vertical [39, 40] and horizontal [41, 42] slotted Si-wire waveguides have already been reported. The effects and advantages of multiple vertical [43] and horizontal [44] slots are also discussed in the literature. The modal properties of single core optical waveguide with asymmetric slots in different positions are discussed in [45]. While strong confinement of a particular mode is possible within a slot, evanescent coupling for the other modes which are not confined in the slot will be greater. Therefore, introducing slots provides us a route to achieve very compact optical couplers and PBS. The aforementioned designs are mostly based on either super-mode analysis of two symmetric (geometrically identical) couplers or propagation characteristics of two adjacent asymmetric (non-identical) couplers. FDTD and super-mode analysis [39, 40] have been used extensively to analyze such structures; however, the OIM has rarely been used to investigate such devices. In the next subsection, we concisely discuss the basic concepts of the slot-waveguides and their utilities as it is quintessential to proceed further in this chapter.

At the beginning of this chapter, we have tersely discussed the OIM. Then, the optimum slot-size and slot-position are numerically predicted for a particular mode to achieve the highest coupling (κ) between two Si-waveguides using OIM. Thereafter, we propose an on-chip compact broadband two-core PBS consisting of a hybrid slot waveguide coupler (both vertical and horizontal slots) [46, 47]. The Semi-analytical technique, for instance, the variational principle, can be used to optimize such device geometries in achieving the highest coupling coefficients [48]. Incorporating the optimally placed off-centered slots reduces the coupling length L_c and the device size by enhancing the coupling coefficient (κ). Not only does our optimized design have a much smaller footprint compared to the designs reported in [17, 18], but also, we believe, this general scheme enables us to achieve the smallest footprint of an optical coupler reported till date with a very low IL. The practical design of our optical coupler, which contains four S-bends has a sub-micron coupling length of $\sim 0.9\,\mu$m with an excess loss (EL) $\sim 0.12\,$dB for the TM-mode. In the subsequent section, we elaborate the above-mentioned strategy [46, 47] to arrive a novel design of a compact ($L_c = 1.1\,\mu$m in the presence of S-bend) PBS which provides an ER>22.3 dB (TE-mode) at $\lambda = 1.55\,\mu$m and this design is also smaller than that reported in [25–34, 39–44]. Parameters (IL, EL, and ER) essential for performance analysis of the coupler and PBS are defined and explained in the next sub-section. Finally, we conclude our work discussing the future scope of fabricating such devices and using them for various applications. We have used a finite element method (FEM) based full-vectorial mode solver COMSOL Multiphysics and MATLAB to implement the OIM and verified our results with the commercially available package, Lumerical FDTD [49].

2.1.1 Performance Indices for the Proposed Devices

We have studied the performance of the coupler and PBS numerically. For a 2×2 optical coupler, if the input power at port 1 is P_1 and the output power at the coupled (cross) port is P_2, then the IL at the cross port can be defined as [22],

$$\text{IL} = 10\log_{10}\left(\frac{P_1}{P_2}\right) \tag{2.1}$$

If the output power at the second (bar) output port or the transmission port is P_3 and at the isolated port is P_4, then the EL can be defined as,

$$\text{EL} = 10\log_{10}\left(\frac{P_1}{P_2 + P_3}\right) \tag{2.2}$$

On the other hand, for PBS, the ratio of the output power for TM mode at the coupled (cross) port and at the through/transmission (bar) port is defined as the ER for TM mode [29].

2.1.2 Slot Waveguide

Optical waveguides are physical structures which are capable of guiding electromagnetic (EM) waves in the optical spectrum (ultra-violet, visible, infra-red) with a myriad of applications from optical communication, networking, sensing, spectroscopy, nonlinear optics to quantum optics [50–54]. Transmission lines and metallic waveguides become too lossy to guide microwave (0.3 GHz to 300 GHz) and THz optical signals, respectively. Optical waveguides can be dielectric (glass, semiconductor, polymer) or plasmonic (dielectric and metal). These waveguides can broadly be classified into two different categories on the basis of geometrical structures, e.g. (i) cylindrical waveguides or optical fibers (non-planar), (ii) integrated waveguides with rectangular cross-sections (also known as planar/slab or rectangular waveguides). There exist other classifications as well, depending upon the mode propagation such as (i) single-mode, (ii) few-mode, (iii) multi-mode optical waveguides. These waveguides can also be divided into two different categories viz. (i) Graded-index, and (ii) step-index, based on the RI distribution from the core to cladding region. Apart from this, most of the optical waveguides guide light either by following the principle of total internal reflection (TIR) or by creating photonic bandgap structures [50, 54] Fig. 2.1 shows various types of cylindrical optical waveguides. Conventional single mode fibers (SMF) which are broadly

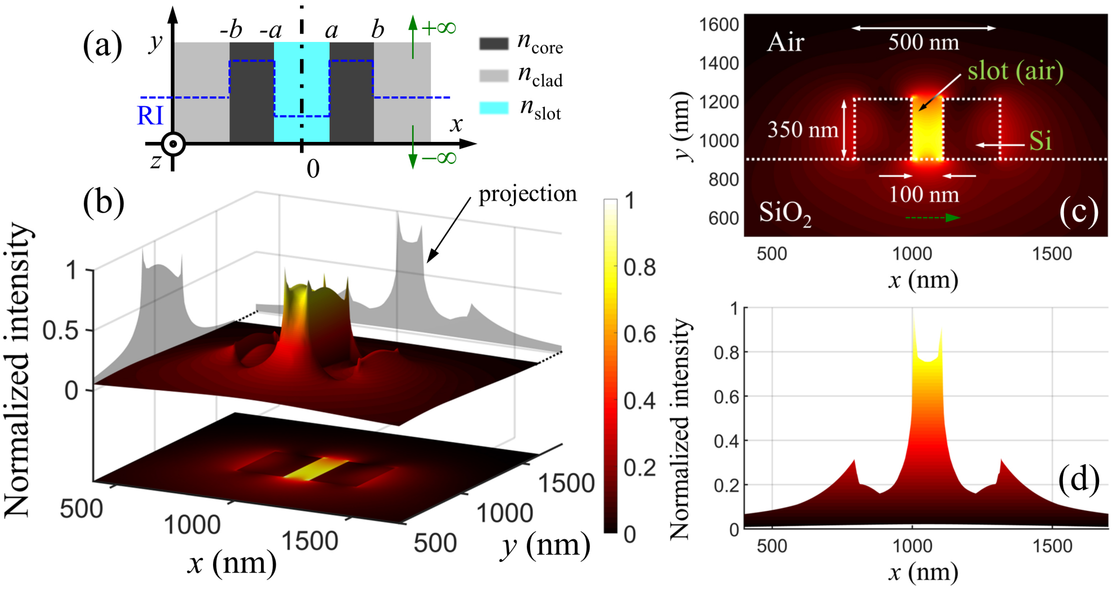

Figure 2.3: (a) Schematic of a slab waveguide with a slot (cyan region). The quantitive RI-distribution (not in scale) of the core, clad and the slot is indicated by a dashed blue curve, overlayed on the waveguide geometry. Modal (quasi-TE) characterization of a 3D rectangular waveguide with a vertical slot in the middle of the waveguide—(b) 3D plot of normalized intensity, (c) cross-sectional view of the waveguide and the modal intensity. The direction of the dominant E-field component is shown by a dotted green arrow, (d) normalized intensity distribution along with the x-axis.

used in optical communication is shown in Fig. 2.1 (a). Fig 2.1 (b) depicts the photonic crystal fibers (PCFs) which are widely used in communication as large mode-area fiber [55], dispersion engineering, frequency conversions [50, 54], etc. Perspective view and the cross-sectional view of the multi-clad optical fiber [56], and the capillary optical fiber [57, 58] are shown in Fig. 2.1 (c) and Fig 2.1 (d), respectively. On the other hand, silicon-on-insulator (SOI) technologies made it possible to fabricate thousands of tiny optical waveguides with rectangular cross-sections (as small as a few hundred nanometers squared), on-chip in a compact fashion. Not only they are vastly used as optical interconnects [3], but also they are used as highly efficient nonlinear platforms due to their small effective modal area and modal volume. Different optical waveguides with planar geometry or rectangular cross-section are shown in Fig. 2.2. Usually, the RI of the core (n_{core}) is higher than both the substrate (n_{sub}) and cladding (n_{clad}) regions and guide light through TIR. However, for ARROW, plasmonic, multi-layer, augmented, and slot waveguides, light can be confined and guided through the lower RI medium. In ARROW, there is an anti-reflecting coating as shown in Fig. 2.2 (IX) to form an optical bandgap that effectively guides light, minimizing the loss. On the other hand, slot-waveguides those work on the principle of TIR were discovered serendipitously by Almeida *et al.* [13] in 2003 and proved themselves as the watershed in optical technologies. In general, the core region of a slot-waveguide is made of materials with high RI such as Si, Si_3N_4, Ge, etc. whereas, the slot is filled in with any of the materials (e.g. air, SiO_2, etc.) having relatively lower RI than that of the core and sometimes even lesser than the core, clad, and the substrate. The speciality of the slot-waveguide is that the optical field confinement factor (Γ) can be enhanced significantly similar to the plasmonic (also known as dielectric-metal hybrid) waveguides, however, with comparatively much lesser propagation loss, just by using a vertical or horizontal slot inside the waveguide core even though the RI of the slot is lower than the core. In this chapter, we restrict ourselves mostly within the discussions on rectangular slot waveguides. Fig. 2.3 (a) shows the schematic of a slab-waveguide with infinite height. A slot of width $2a$ is placed at the center of it. Width of each core region or an individual rail is $(b - a)$. The RI of the core, cladding, and the slot are n_{core}, n_{clad}, and n_{slot}, respectively, such that, $n_{\text{core}} > n_{\text{clad}} \geq n_{\text{slot}}$. In the next paragraph, we derive the expression of the E-field distribution for the slotted optical planar waveguide structure as given in Fig. 2.3 (a).

A. Analytical Expression for the Mode Profile

In the case of Fig. 2.3 (a), the RI of the slotted planar waveguide varies along the x-direction. Therefore, the direction of the electric field should be parallel to the x-axis. The transverse E_x-component of the fundamental TM-mode can be found by solving the Helmholtz equation or the time-independent wave equation for each layer of the slot-waveguide and can be given by,

$$\frac{d^2E_x}{dx^2} + \left(k_0^2 n^2(x) - \beta^2\right) E_x = 0 \tag{2.3}$$

The RI distribution $n(x)$ along with the x-axis is,

$$n(x) = \begin{cases} n_{\text{slot}}, \text{ for } |x| < a \\ n_{\text{core}}, \text{ for } a < |x| < b \\ n_{\text{clad}}, \text{ for } |x| > b \end{cases} \tag{2.4}$$

where, $\beta = k_0 n_{\text{eff}}$; β, k_0 and n_{eff} denote the mode propagation constant, free-space wave-vector, and the effective RI, respectively. One can rewrite Eq. 2.3 as,

$$\begin{cases} \dfrac{d^2E_x}{dx^2} - {\gamma^2}_{\text{slot}} E_x = 0, \text{ if } |x| < a \\ \dfrac{d^2E_x}{dx^2} + {\gamma^2}_{\text{core}} E_x = 0, \text{ if } a\,|x| < b \\ \dfrac{d^2E_x}{dx^2} - {\gamma^2}_{\text{clad}} E_x = 0, \text{ if } |x| > b \end{cases} \tag{2.5}$$

where

$$\begin{aligned} \gamma_{\text{slot}}^2 &= \beta^2 - k_0^2 n_{\text{slot}}^2 \\ \gamma_{\text{core}}^2 &= k_0^2 n_{\text{core}}^2 - \beta^2 \\ \gamma_{\text{clad}}^2 &= \beta^2 - k_0^2 n_{\text{clad}}^2 \end{aligned} \tag{2.6}$$

Eigensolution of the Helmholtz equation yields the effective RI (n_{eff}). E_x for the fundamental TM mode is given by,

$$E_x(x) = \begin{cases} A_1 \cosh\left(\gamma_{\text{slot}} x\right), \text{ for } |x| < a \\ A_2 \cos\left(\gamma_{\text{core}} |x|\right) + B_2 \sin\left(\gamma_{\text{core}} |x|\right), \text{ for } a < |x| < b \\ A_3 e^{-(\gamma_{\text{clad}}|x|)} \text{ for } |x| > b \end{cases} \tag{2.7}$$

where, A_1, A_2, A_3, and B_2 are arbitrary constants and can be determined from the boundary conditions. For TM-mode, the normal component of the electric displacement vectors should be continuous at the boundaries which demarcate the clad and the core regions ($x = \pm b$) i.e. $n_{\text{clad}}^2 E_{x,\text{clad}} = n_{\text{core}}^2 E_{x,\text{core}}$ as well as the core and the slot regions ($x = \pm a$) i.e. $n_{\text{slot}}^2 E_{x,\text{slot}} = n_{\text{core}}^2 E_{x,\text{core}}$. As the $n_{\text{slot}} < n_{\text{core}}$, we witness a field enhancement in the slot region. In addition, dE_x/dx is also continuous at the boundaries. These boundary conditions are used to find out the propagation constant β from the transcendental eigenvalue equation given by Eq. 2.8 which can be solved numerically or graphically.

$$\tan^{-1}\left(\frac{n_{\text{core}}^2\gamma_{\text{clad}}}{n_{\text{clad}}^2\gamma_{\text{core}}}\right)+\tan^{-1}\left(\frac{n_{\text{core}}^2\gamma_{\text{slot}}}{n_{\text{slot}}^2\gamma_{\text{core}}}\tanh\left(\gamma_{\text{slot}}a\right)\right)+m\pi=\gamma_{\text{core}}\left(b-a\right) \tag{2.8}$$

where m is an integer. The analytical expression of the fundamental mode profile can be found as,

$$E_x(x)=\begin{cases}\dfrac{1}{n_{\text{slot}}^2}\cosh\left(\gamma_{\text{slot}}x\right), \text{ for } |x|<a \\ \dfrac{1}{n_{\text{core}}^2}\cosh\left(\gamma_{\text{slot}}a\right)\cos\left(\gamma_{\text{core}}\left(|x|-a\right)\right) \\ +\dfrac{1}{n_{\text{slot}}^2}\dfrac{\gamma_{\text{slot}}}{\gamma_{\text{core}}}\sinh\left(\gamma_{\text{slot}}a\right)\sin\left(\gamma_{\text{core}}\left(|x|-a\right)\right), \text{ for } a<|x|<b \\ \dfrac{1}{n_{\text{clad}}^2}\Bigg(\cosh\left(\gamma_{\text{slot}}a\right)\cos\left(\gamma_{\text{core}}\left(b-a\right)\right) \\ +\dfrac{n_{\text{core}}^2}{n_{\text{slot}}^2}\dfrac{\gamma_{\text{slot}}}{\gamma_{\text{core}}}\sinh\left(\gamma_{\text{slot}}a\right)\sin\left(\gamma_{\text{core}}\left(b-a\right)\right)\Bigg)e^{-\gamma_{\text{clad}}(|x|-b)}, \\ \text{for } |x|>b\end{cases} \tag{2.9}$$

Here, A is an arbitrary constant. The E-field enhancement in the slot region can be explained intuitively by the interaction between the two fundamental eigenmodes of the individual waveguide cores. The E-field remains intense, smooth and maintains its sharp peak throughout the slot if the slot width ($2a$) is much smaller than the characteristics decay length ($1/\gamma_{\text{s}}$) of the EM-field inside the slot ($2a \ll 1/\gamma_{\text{slot}}$) [13].

Modal characteristics of a 3D waveguide with finite thickness, a rectangular cross-section (500 nm×350 nm), and a vertical slot (100 nm×350 nm) at its center are plotted in Fig. 2.3 (b)–2.3 (d). We use COMSOL Multiphysics to find out the modes at an operating wavelength, $\lambda = 1.55\,\mu$m. Note that, the formulations derived in the previous section are equally compatible for the 3D waveguide structures except one requires to transform the original RI of the materials to the corresponding 2D-projected RI values through the effective index method (EIM) [51] before using the same formulations. Also notice that for 3D waveguide structure, pure transverse modes do not exist. Vertical slots can confine the quasi-TE mode (dominant E_x component), whereas, horizontal slots can support the quasi-TM mode (dominant E_y component), respectively [13].

B. Applications of slot waveguide

Slot waveguides are extensively used in sensing and nonlinear frequency conversion due to exceptionally high field confinement factor [16]. Flat dispersion over a broad wavelength range can be achieved using waveguides with multiple slots filled in by novel materials [59]. Therefore, such waveguides are advantageous for supercontinuum generation and frequency-comb generation [59]. Slots, when filled in by nonlinear organic electro-optic polymers [60, 61] or covered with graphene layers [62] can be used to build ring modulators with very high tunability [61], and optical photo-detectors with high sensitivity [63]. On the other hand, the fiber analogue of the slot waveguides, i.e. capillary optical fibers as shown in Fig. 2.1 (d) also find several interesting applications [57, 58].

C. Fabrication and coupling mechanisms

Later in this chapter, we propose a fabrication process-flow of PBS based on hybrid slot waveguides which consist of a vertical slot in one of the wires, whereas, a horizontal slot in the other. Henceforth, it is essential to discuss the conventional procedure to fabricate a single wire waveguide either having a vertical slot or horizontal slot, so that we can better appreciate the design of the hybrid slot waveguides [64, 65]. Fig. 2.4 (a) depicts the necessary process flow to fabricate a void (air) vertical slot while Fig. 2.4 (b) portrays the various steps to fabricate a horizontal slot filled in by silica. To fabricate a wire waveguide with a single vertical slot, at first, (i) a silicon wafer is taken and oxidized at 1000–1200^{0}C temperature in O_2 environment to grow the buried oxide layer (BOX) of thickness $\sim 3\,\mu$m for guiding light and electrical isolation. Thereafter, amorphous silicon (a-Si) is grown to achieve the required waveguide height by plasma enhanced chemical vapor deposition (PECVD) method. One can also use the commercially available SOI wafer directly if the waveguide height is standard (i.e. 220 nm or 250 nm) for single-mode operation at $1.55\,\mu$m. (ii) After Piranha cleaning, a negative e-beam

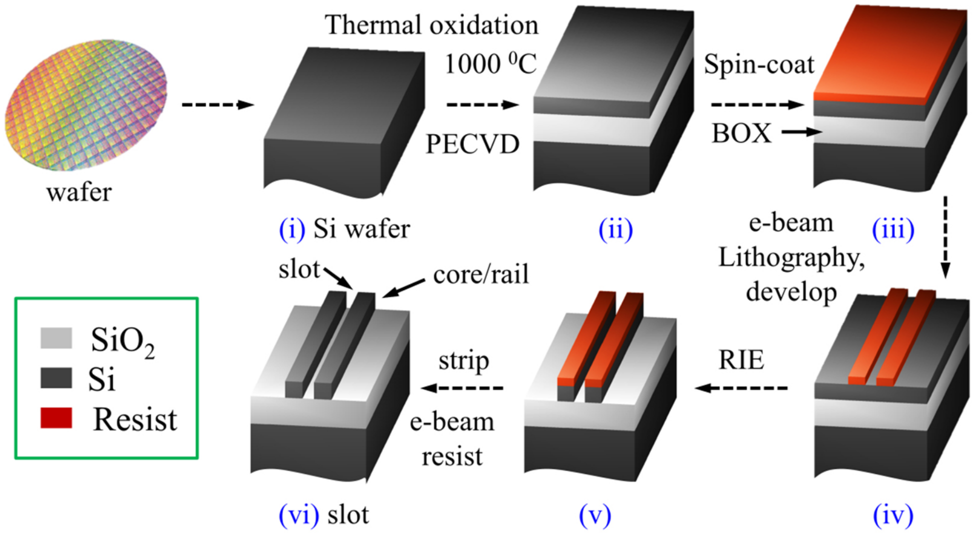

(a) Fabrication of SOI wire-waveguide with vertical slot

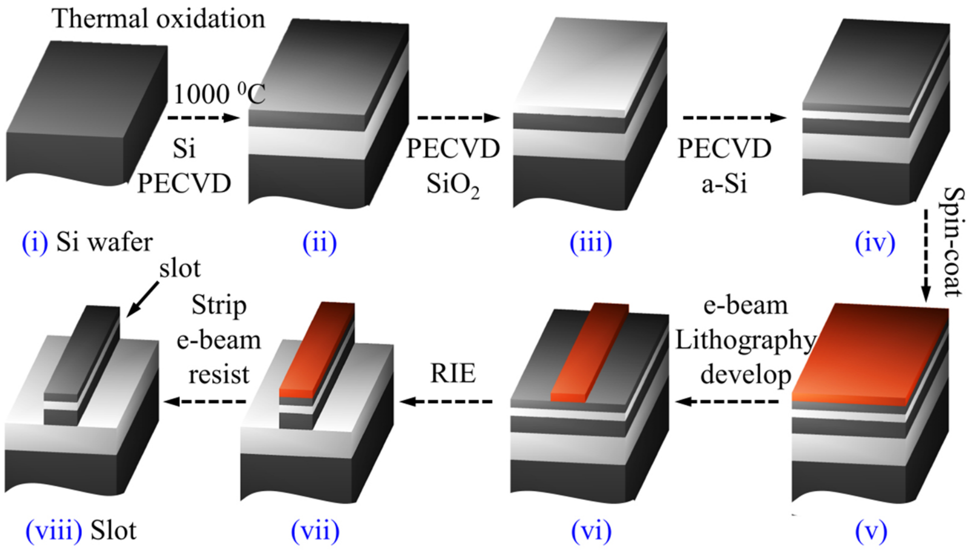

(b) Fabrication of SOI wire-waveguide with horizontal slot

Figure 2.4: Standard CMOS fabrication process of wire-waveguide with (a) a single vertical air-slot, and (b) a single horizontal silica slot.

resist (e.g. ma-N 2400) is spin-coated on the prepared sample. (iii) e-beam lithography is performed to pattern the resist; the sample is developed (HF/CHF_3-O_2), and reactive-ion etching (RIE) is performed to extricate the waveguide pattern as shown in step (v) of Fig. 2.4 (a). Finally, the negative e-beam resist is stripped off to obtain the vertically slotted wire-waveguide. Protective cladding layer (PMMA glass or silica) can be formed on top of the waveguide following the standard process [65]. To fabricate the horizontal silica slot, we need to grow an extra PECVD layer of silica as per the required height of the slot. For Si_3N_4 slot, low-pressure chemical vapor deposition (LPCVD) can also be used [65, 66]. Rest of the fabrication steps are mostly similar to that of the vertical slot. Note that, in general, the loss of the PECVD a-Si layer is higher (6-7 dB/cm) than the crystalline Si (2-3 dB/cm). Normally, obtaining a broadband coupling mechanism from strip to slot-waveguide or from fiber to slot with negligible loss is not straightforward and requires tremendous efforts [67, 68]. Note that, slot can be adiabatically tapered out from a strip waveguide at the inputs and outputs to achieve coupling losses comparable to that of the strip waveguide as demonstrated in the reference [67]. Coupling efficiency as high as 97% and overall coupling loss as low as 0.15 dB are achieved till date by embedding symmetrically tapered nano-wires, and asymmetric rails, respectively [69, 70] within an effective strip-to-slot conversion length of only 10 μm.

2.1.3 Optical Couplers: Theory and Computations

Two dielectric optical waveguides start exchanging energy when they are brought close to each other, as shown in Fig. 2.5 (a). Such coupled system can be treated mathematically through coupled mode equations [51, 71]. Let us consider, β_1 (κ_{11}), and β_2 (κ_{22}) are the propagation constants (self-coupling coefficients) of waveguide-I (W-I), and waveguide-II (W-II), respectively, while κ_{12} and κ_{21} are the mutual coupling coefficients from W-II to W-I, and vice versa. The general expressions for two weakly coupled modes having mode-amplitudes a and b with implicit time-dependence (exp $(i\omega t)$) can be written as [51, 71],

$$\begin{aligned} \frac{da}{dz} &= -i\left(\beta_1 + \kappa_{11}\right)a - i\kappa_{12}b \\ \frac{db}{dz} &= -i\kappa_{21}a - i\left(\beta_2 + \kappa_{22}\right)b \end{aligned} \tag{2.10}$$

When two guides are identical as shown in Fig. 2.5 (a), the coupling coefficients, κ_{12} and κ_{21} will be the same, i.e. $|\kappa_{12}| = |\kappa_{21}| = |\kappa|$. κ can be obtained directly

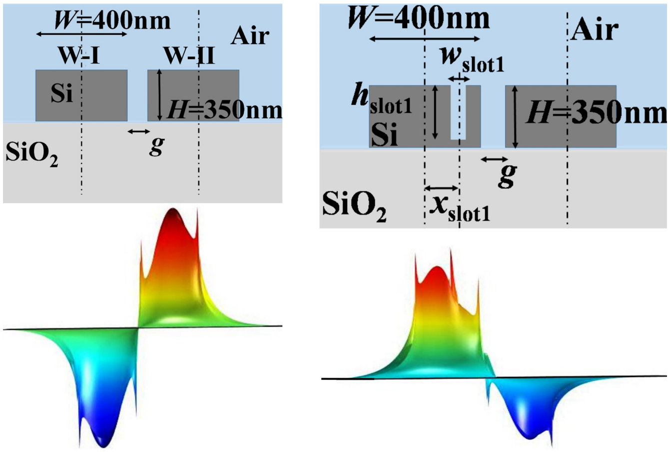

(a) (b)

Figure 2.5: Cross-sectional geometry and corresponding E-field distributions for TM odd-supermode in (a) two identical waveguides, (b) two non-identical waveguides. For non-identical waveguides the two lobes of the odd-supermode are asymmetric (case-(b)).

from the supermode analysis (even: $a = b$, odd: $a = -b$) by,

$$\kappa = \frac{\beta_\mathrm{e} - \beta_\mathrm{o}}{2} \tag{2.11}$$

The method to calculate the propagation constants of even (β_e) and odd (β_o) supermodes from any commercially available software is straightforward. However, when adjacent waveguides are not geometrically identical, then the symmetry between the waveguides breaks down. Due to the asymmetry, coupling coefficients, $\kappa_{12} \neq \kappa_{21}$; rather, κ_{12} and κ_{21} may differ considerably [72]. Electric field distributions of the fundamental TM obtained from FEM are displayed in both the cases—Figs. 2.5 (a) conventional coupler, (b) non-identical waveguide coupler. The vertical slot in the W-I, as seen in Fig. 2.5 (b), breaks the structural symmetry. Though for non-identical coupler the coupling coefficient κ can be found from Eq. 2.11, it is also important to find out individual coupling coefficients, κ_{12} and κ_{21} to understand and describe the complete behavior of the coupler. For couplers consisting of non-identical waveguides, where the individual coupling coefficients κ_{12} and κ_{21} are different, the coupling coefficient κ is defined as [51],

$$\kappa = \sqrt{\kappa_{12}.\kappa_{21}} \tag{2.12}$$

The self ($p = q$) and mutual ($p \neq q$) coupling coefficients, κ_{pq} can be approximated by coupled mode theory and can be given as Eq. 2.13.

$$\kappa_{\mathrm{pq}} = \frac{\omega\varepsilon_0 \int\limits_{-\infty}^{\infty}\int\limits_{-\infty}^{\infty} (N^2 - N_{\mathrm{q}}^2)E_{\mathrm{p}}^{*}E_{\mathrm{q}}dxdy}{\int\limits_{-\infty}^{\infty}\int\limits_{-\infty}^{\infty} u_{\mathrm{z}}.(E_{\mathrm{p}}^{*} \times H_{\mathrm{p}} + E_{\mathrm{p}} \times H_{\mathrm{p}}^{*})dxdy} \tag{2.13}$$

Subscript p and q can either be 1 or 2. N denotes the overall combined RI distribution when both the wires are present. u_{z} is the unit vector along the propagation direction (z-axis). To obtain κ_{12} and κ_{21} for any geometrically non-identical coupled structures, we have used FEM mode solver to implement OIM. Rectangular waveguides support quasi-TE and quasi-TM modes. In quasi-TE and TM modes, the E_{z} and H_{z} field components are nonzero and significant. From the FEM solver, we extract the field components E_{x}, E_{y}, E_{z}, and the propagation constant for a particular mode of each waveguide individually. Thenceforth, we evaluate the overlap integral of Eq. 2.13 by employing 2D Simpson's $1/3^{\mathrm{rd}}$ rule in MATLAB to compute the κ_{12} and κ_{21}. The advantage of using OIM is that the OIM yields the values of κ_{12} and κ_{21} directly, which in turn renders κ and the coupling length, L_{c}. The coupled power in the second waveguide, P_{II} at a distant z from the input can be calculated with the help of analytical relation 2.14 derived by solving the coupled amplitude equations.

$$P_{\mathrm{II}} = F\sin^2(qz);\ \text{where, } F = \left(\frac{\kappa}{q}\right)^2 = \left[1 + \left(\frac{\delta}{\kappa}\right)^2\right]^{-1} \tag{2.14}$$

P_{II} depends upon the power coupling efficiency F and the effective coupling coefficient q; F and q account for mutual coupling coefficient (κ) and the phase propagation mismatch (δ) between the two waveguides [51]. For coupler consisting of non-identical waveguides, the δ will no longer be zero.

To validate the OIM in such strongly coupled systems, we have exploited supermode analysis and Lumerical 3D-FDTD and compared our results with the OIM. These methods are applied to three different coupler configurations consisting of (i) two identical waveguides, (ii) one rectangular waveguide and one circular

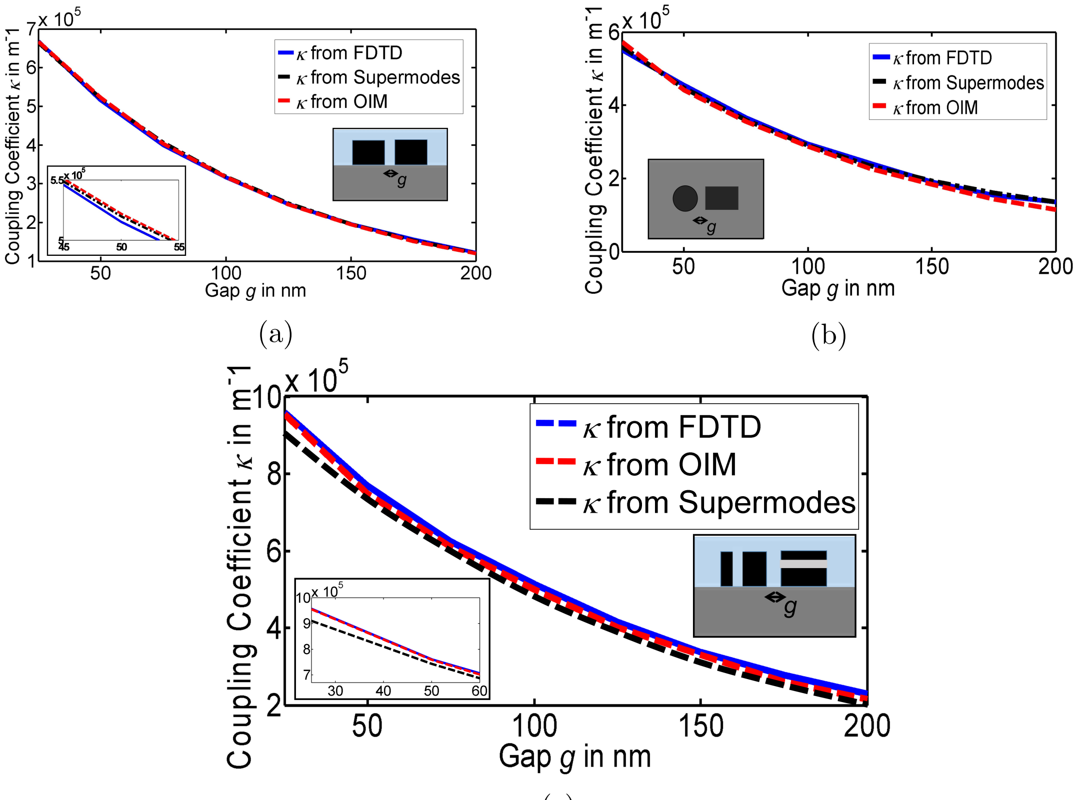

(a)

(b)

(c)

Figure 2.6: Comparison of the coupling coefficients, κ (between parallel wires) with different gap lengths for (a) two identical rectangular waveguides, (b) one circular and a rectangular waveguide, (c) a hybrid-slot waveguide coupler configuration. Three different methods (Supermode, FDTD and OIM) to calculate κ have been used.

waveguide and (iii) two non-identical waveguides, possessing vertical and horizontal slots, as depicted in the insets of Figs. 2.6 (a), 2.6 (b) and 2.6 (c), respectively. For all three cases, the waveguides are parallel, and the core is made of Si. Fused silica and air are used as substrate and cladding, respectively. Simulations for all the results shown in Fig. 2.6, are carried out at wavelength $\lambda = 1.55\,\mu$m and the RIs of Si, silica and air are taken as 3.477, 1.445 and 1, respectively. The dimension of the rectangular waveguide is chosen as 400 nm×350 nm. For configuration (ii), the diameter of the circular waveguide is 350 nm. The coupling coefficients as a function of gap separation (g) for the TM-mode of three different configurations are plotted in Figs. 2.6 (a), 2.6 (b) and 2.6 (c). For configuration (iii), the vertical air-slot as shown in Fig. 2.6 (c) is 50 nm wide and 50 nm shifted to the left (i.e. away from W-II), whereas the horizontal slot (25 nm thick) in the W-II is comprised of silica, and is placed 75.5 nm below from the top. For the first two cases, OIM finds very good agreement with supermode analysis and 3D FDTD method. For the third case, it can be seen from the inset that, when the gap between the adjacent waveguide is <50 nm (for $\kappa > 7.6 \times 10^5\,\mathrm{m}^{-1}$, $L_\mathrm{c} < 2\,\mu$m comparable to operating wavelength, $\lambda = 1.55\,\mu$m), the interaction between the modes becomes extremely strong; consequently, the results obtained from the OIM and supermode analysis start to mismatch. For example, if $g = 25$ nm (inset), $\kappa_{(\mathrm{Supermode})} \sim 9 \times 10^5\,\mathrm{m}^{-1}$ ($L_\mathrm{c} \sim 1.726\,\mu$m) and $\kappa_{(\mathrm{OIM})} \sim 9.6 \times 10^5\,\mathrm{m}^{-1}$ ($L_\mathrm{c} \sim 1.636\,\mu$m) and they differ to each other significantly (5.5%). Still, in our case, OIM is applicable as we have used OIM only to optimize the slot and predict the approximate device size. Once we obtain the necessary parameters from OIM, we run 3D FDTD for further optimization of device size including the S-bends, which saves a lot of time. Hence, our semi-analytic approach is not only much faster than the 3D FDTD method but also fairly accurate to adopt and can be implemented to design the ultra-compact couplers and polarization beam splitters.

2.2 Design of Ultra-compact Directional Couplers

To design the ultra-compact DC numerically, we begin with the DC consisting of parallel silicon wires. Each wire is comprised of an off-centric groove or slot. The schematic cross-section and the perspective view of this initial DC are sketched in Figs. 2.7 (a) and 2.7 (b), respectively. The dimension of each Si-wire is chosen arbitrarily as 400 nm×350 nm. The cladding is air and silica is used as a substrate. The slot width and height of the first waveguide are denoted by w_slot1 and h_slot1, respectively, while, w_slot2 and h_slot2 are the slot width and height of the second waveguide. The symbols **O** and **O'** represent the center of the waveguides W-I and W-II, respectively, whereas, **A** and **B** indicate the location of the slot or groove, respectively, as shown in Fig. 2.7. Lateral shift (O-A) of the vertical slot in W-I is denoted by x_slot1, whereas, the lateral shift (O'-B) in the second waveguide, W-II is denoted by x_slot2.

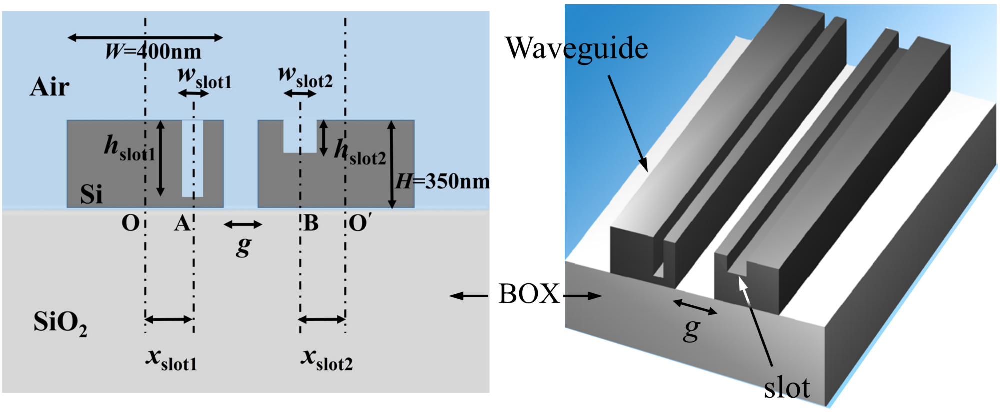

(a) (b)

Figure 2.7: (a) Schematic cross-section of two non-identical Si-wire waveguides with grooves in it, (b) 3-D perspective view.

2.2.1 Design Recipe: Optimization of the Coupling Coefficient

It is known that the quasi-TE mode is well confined within a vertical slot [13] of a Si-wire waveguide, while the quasi-TM mode shows greater evanescent extent into the cladding which would facilitate greater coupling. This suggests that Si-wires with vertical slots can be used to design ultra-compact switches or couplers when operating in the TM-mode. Note that, the low-index air-slot in the wire waveguide reduces the effective index n_{eff} of the TM-mode, affecting the guiding property of the waveguide for TM-mode which deteriorates as the slot-size increases. The aim is to increase the evanescent coupling using suitable slots placed at proper positions while keeping the guiding property of the waveguide nearly unaffected. We select the slot-size and position to ensure that $n_{\text{eff}} > 2$ for the TM-mode that permits to neglect the propagation losses at bends. We discard the other possibilities even if the coupling coefficients for those cases are larger. This scheme should be valid for waveguides with any cross-section. Moreover, decreasing the width of the waveguide increases the coupling coefficient. In optimizing the groove/slot size and position at operating wavelength $\lambda = 1.55\,\mu$m, at first a 25 nm $\times 25\,$nm groove/slot is placed at the center of the W-I, while the W-II has no slot in it. Note that, the wire width is fixed to 400 nm as a trade-off between propagation losses and evanescent coupling. The coupling coefficients κ_{12} and κ_{21} for quasi-TM mode

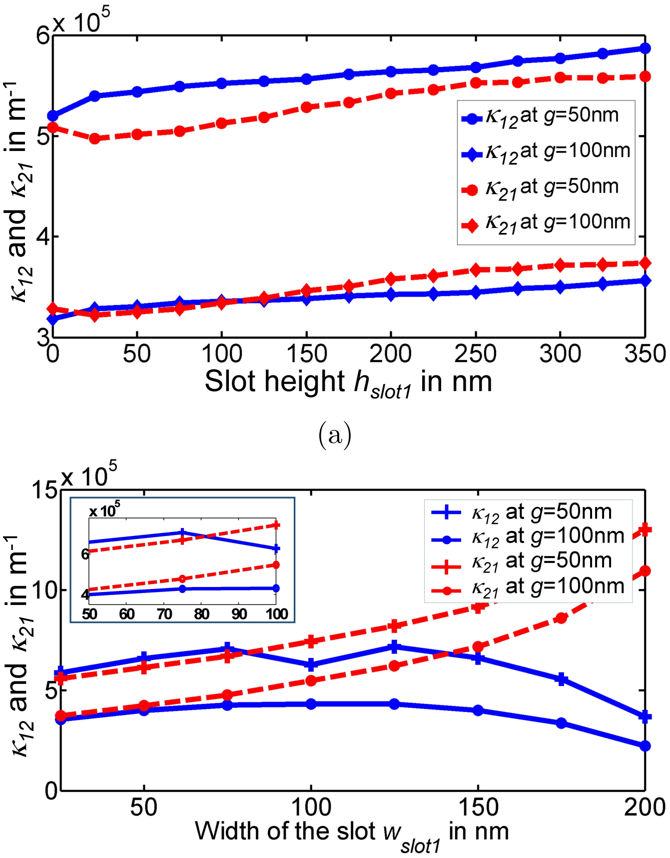

(a)

(b)

Figure 2.8: Variations of κ_{12} and κ_{21} as a function of (a) h_{slot1}, and (b) w_{slot1} for non-identical Si-waveguide couplers as shown in figure 2.7.

are plotted by varying the height of the slot, h_{slot1} from 25 nm to 350 nm, as shown in Fig. 2.8 (a) for two different waveguide separations, $g = 50$ nm and 100 nm. It is evident that the maximum coupling (κ_{12} and κ_{21}) can be attained when the slot height is equal to the wire height, i.e. 350 nm. This numerical process sets the slot height to 350 nm for the rest of the calculations. The slot width is increased from 25 nm to 200 nm, i.e. half of the width of the waveguide at two different gap values. It is observed from Fig. 2.8 (b) that the coupling coefficients are largest for w_{slot1} ranging in between 50 nm to 100 nm. However, for $w_{\text{slot1}} > 50$ nm, the effective index n_{eff1} becomes smaller than 2.0 and the loss becomes high. In order to maintain moderate confinement and large coupling coefficient values, we fix the slot width at 50 nm.

Instead of varying a single parameter, either h_{slot1} or w_{slot1} while keeping the other parameter constant, we have also varied both h_{slot1} and w_{slot1} simultaneously, and obtain the coupling coefficients κ_{12} and κ_{21}. This design parameter space is shown in Figs. 2.9 (a) and 2.9 (b) where color bar shows the magnitude of κ_{12} and κ_{21}, divided by a factor 10^5. The dashed curve indicates the values of h_{slot1} and w_{slot1} for which $n_{\mathrm{eff1}} = 2$ and divides the map into two regions; $n_{\mathrm{eff1}} < 2$ (upper region) and $n_{\mathrm{eff1}} > 2$ (lower region). Again, one has to choose h_{slot1} and w_{slot1} simultaneously within the red-shaded area under the blue dashed curve in such a way that κ_{12} will be the largest while the effective index of the mode in the first waveguide; $n_{\mathrm{eff1}} > 2$ in order to have a balance between greater coupling and admissible propagation loss. Based on this analysis, we choose $h_{\mathrm{slot1}} = 350\,\mathrm{nm}$ and $w_{\mathrm{slot1}} = 50\,\mathrm{nm}$. Next, we optimize the slot-position by shifting the slot gradually from, $x_{\mathrm{slot1}} = -150\,\mathrm{nm}$ to $x_{\mathrm{slot1}} = +150\,\mathrm{nm}$, with respect to the center. Figure 2.10 (a) shows the variation of coupling coefficients for a quasi-TM mode with respect to the lateral shift in the slot-position of W-I. When the slot is moved to the left in W-I ($x_{\mathrm{slot1}} = -50\,\mathrm{nm}$), the electric field is pushed towards W-II, enhancing the evanescent coupling. We have corroborated the same findings by adopting a multivariate approach where we observe κ_{12} by changing three parameters h_{slot1}, w_{slot1}, and x_{slot1}, simultaneously. The scatter plot for κ_{12}, is shown in Fig. 2.10 (b), which confirms that when x_{slot1} is $-50\,\mathrm{nm}$, the coupling coefficient is the highest. The scatter plot as displayed in Fig. 2.10 (c) for n_{eff1} helps to determine the allowed values of h_{slot1}, w_{slot1} and x_{slot1} for which $n_{\mathrm{eff1}} > 2$.

In Fig. 2.11, we show the mechanical analogue that leads intuitively to the final design of our ultra-compact directional coupler. If two balloons kept side-by-side are pressed away from their corresponding centers, as shown in Fig. 2.11, they inflate towards each other. This surprisingly simple and candid example can be correlated easily to our design recipe. For $g = 50\,\mathrm{nm}$, a coupling coefficient of $\kappa_{12} = 7.22 \times 10^5\,\mathrm{m}^{-1}$ is obtained when the slot is placed at an optimal position, whereas, κ_{12} is only $5.22 \times 10^5\,\mathrm{m}^{-1}$ without any slot. This situation is depicted in Fig. 2.12 (a). Although this scheme will enhance the coupling coefficient to its optimum value, but according to Eq. 2.14 the power coupling efficiency will be less due to strong phase mismatch between the two waveguides. Therefore, to enhance the power coupling efficiency, we make similar changes in W-II, as shown

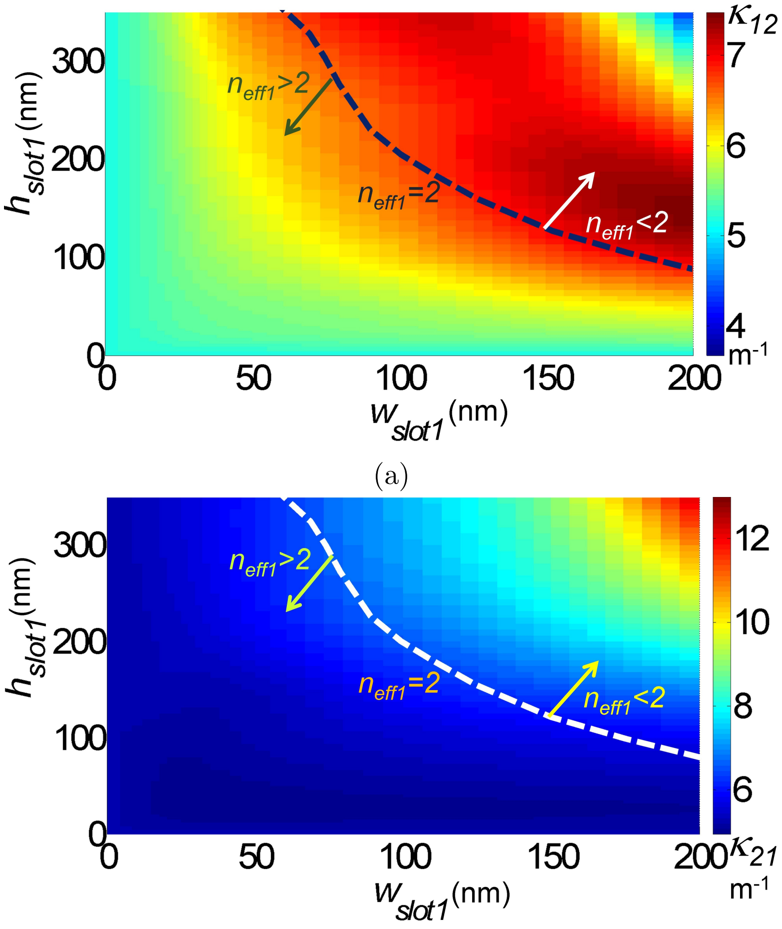

(a)

(b)

Figure 2.9: Two dimensional design parameter space of a slot based coupler for a quasi-TM mode, (a) $\kappa_{12}(\times 10^{-5})$ and (b) $\kappa_{21}(\times 10^{-5})$. The dashed curve ($n_{\mathrm{eff1}} = 2$) indicates the values of w_{slot1} and h_{slot1} for which $n_{\mathrm{eff1}} = 2$. It is preferred to opt parameters from region where $n_{\mathrm{eff1}} \geq 2$ to have balance between the greater coupling and low propagation loss.

in Fig. 2.12 (b). Previously, W-II has no slot in it. Presence of a similar slot in W-II nullifies the phase mismatch and further enhances the $\kappa_{12}(= 9.1 \times 10^5\,\mathrm{m}^{-1})$ because the modal field of the second waveguide is also pushed towards the W-I due to the off-centered slot in the second waveguide. These can be seen from Figs. 2.12 (c)−2.12 (f). Slots in the middle force the electric field to disperse in both the directions while optimized slots push the mode field only towards the opposite waveguide. This is indicated by the arrows in Figs. 2.12 (e) and 2.12 (f).

Finally, the optimized parameters to realize ultra-compact DC are: $h_{\mathrm{slot1}} =$

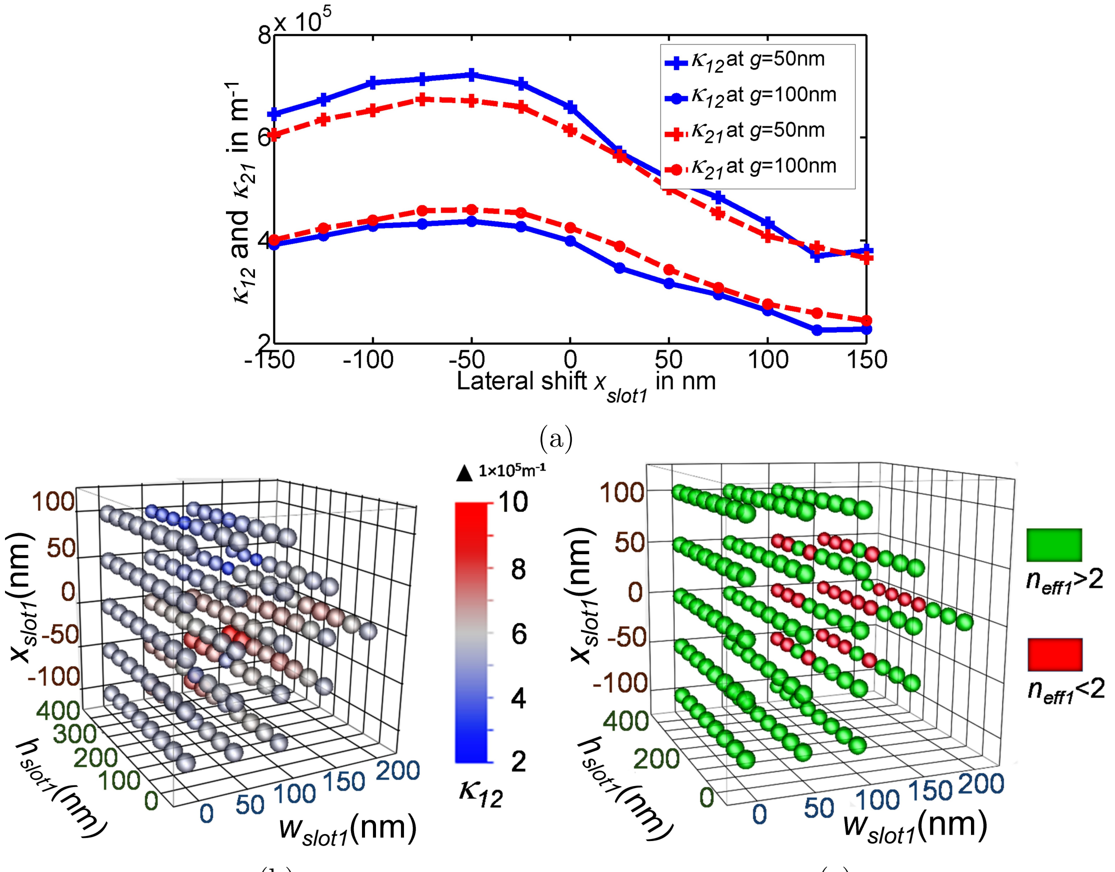

(a)

(b)

(c)

Figure 2.10: (a) Variation of coupling coefficients (κ_{12} and κ_{21}) as a function of lateral shift (x_{slot1}) for two different gaps (g-s), and scatter plot for (b) κ_{12} and (b) n_{eff1} with respect to the simultaneous variation in h_{slot1}, w_{slot1}, and x_{slot1}.

Table 2.1: Enhancement of coupling coefficients with slot positions

Gap (nm)	κ (m^{-1}) **with no slot**	κ (m^{-1}) **with slots in the middle** (%)	κ (m^{-1}) **with optimized slots** (%)
50	5.22×10^5	7.63692×10^5 (46.3%)	9.15×10^5 (75.28%)
100	3.1827×10^5	5.0368×10^5 (58.23%)	5.997×10^5 (88.42%)
200	1.2078×10^5	2.221×10^5 (83%)	2.6037×10^5 (115.57%)
300	0.4656×10^5	0.992×105 (113.04%)	1.138×10^5 (144.4%)
400	0.182×10^5	0.45×10^5 (147.2%)	0.5056×10^5 (177.76%)

$h_{\text{slot2}} = 350\,\text{nm}$, $w_{\text{slot1}} = w_{\text{slot2}} = 50\,\text{nm}$ and $x_{\text{slot2}} = (-x_{\text{slot1}}) = 50\,\text{nm}$ (shifted away from each other). This coupler structure (Fig. 2.12 (b)), where slot waveg-

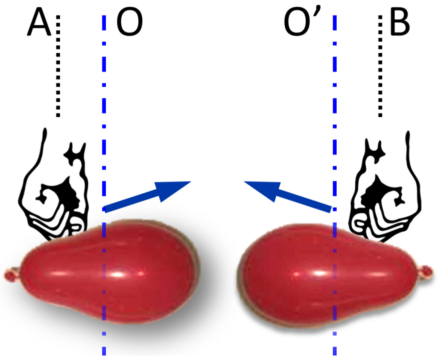

Figure 2.11: Mechanical analogue of the off-shifted slot waveguides which enhances the coupling coefficient. Two adjacent balloons inflate towards each other when mechanical pressure is induced to the balloons at points A and B which are away from each other with respect to the corresponding balloon-centers O and O', respectively.

uides are separated with a gap of 100 nm, can enhance the coupling coefficient by 88%, as demonstrated in Fig. 2.13 (a) in comparison to the coupling without any slot in the waveguides. Following similar design procedure, it might be possible to realize even smaller coupling length ($L_c < 1.73\,\mu$m) by reducing the wire width below 400 nm. However, we restrict the design to the wire width $\geq$ 400 nm as smaller widths may lead to higher propagation losses for quasi-TM mode. The schematic 3D perspective-view of the final design is shown in Fig. 2.13 (b). The results obtained from OIM are verified by 3D-FDTD method and are shown in Figs. 2.13 (c) and (d). The κ-values for different scenarios (i.e., no slot, centrally placed slots with an appropriate size, and optimized slots), are computed and tabulated in Table 2.1. For, g = 100 nm, slots with optimum size can enhance the coupling by 58% but a slot with both optimal size and position can further increase the coupling up to 88%. It is noticed that with the increase in gap, the enhancement in κ with optimized slot increases. This analysis proves that shifting the slots from the center of the waveguide leads to a significant advancement for realizing ultra-compact devices such as optical couplers and PBS.

To summarize, we have achieved coupling lengths as small as 1.73 μm, 2.61 μm and 13.8 μm when the gaps between two waveguides are 50 nm, 100 nm and 300 nm, respectively, using Si-wire waveguides with a moderately large core (400 nm×350 nm). This design scheme can be used to realize fabrication tolerant devices. As an example, similar κ ($5.22\times10^5\,\mathrm{m}^{-1}$) can be achieved for a larger gap of $\sim$ 120 nm

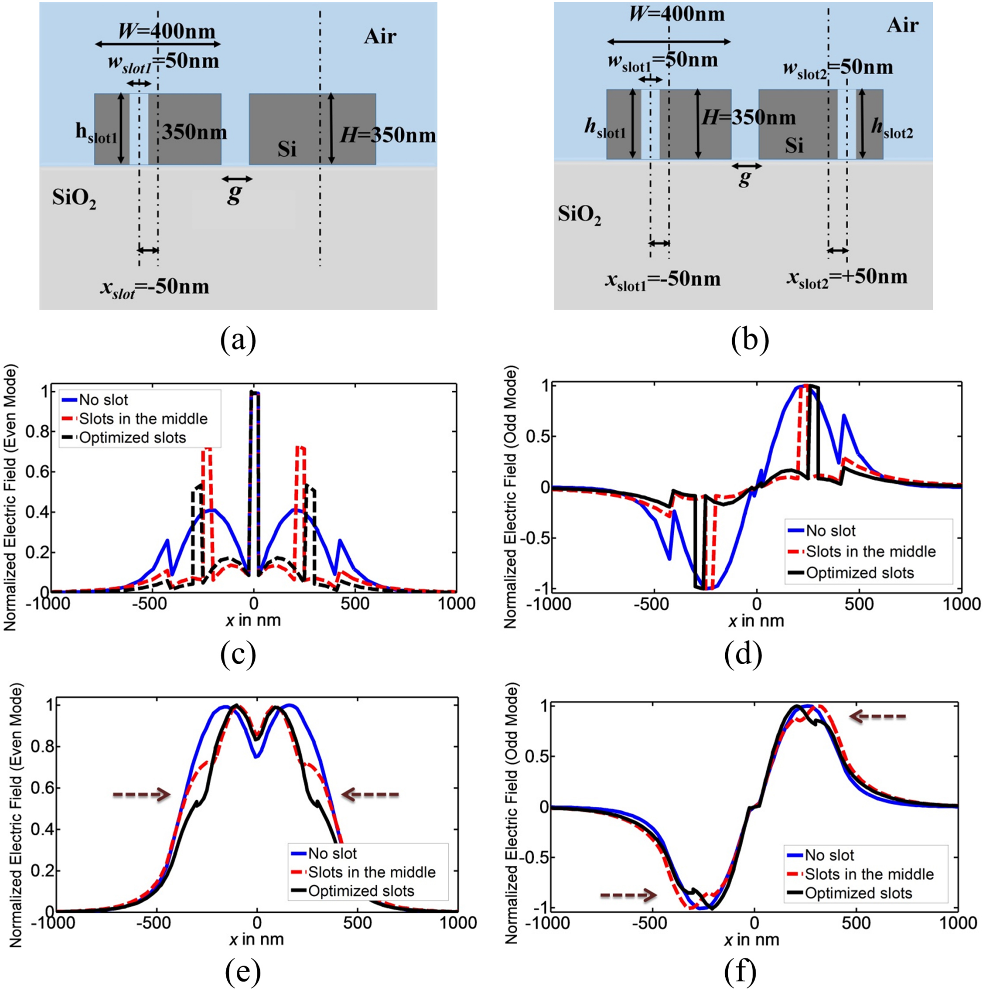

(a) (b) (c) (d) (e) (f)

Figure 2.12: (a) Non-identical waveguide structures for optimized coupling, (b) symmetric cross-section for optimized coupling as well as maximum power coupling efficiency, Normalized electric field profile for the coupler for (c) TE even supermode, (d) TE odd supermode, (e) TM even supermode, (f) TM odd supermode.

when the slots are in optimized positions in comparison to the coupler structure where the gap is 50 nm. This relaxes the stringent requirement on the gap width and provides relative fabrication ease.

2.2.2 Practical Design Considerations

Most of the CMOS compatible wire waveguides have typical cross-sections of (500 nm×500 nm), (500 nm×250 nm) or (500 nm×220 nm). Waveguide with cross-

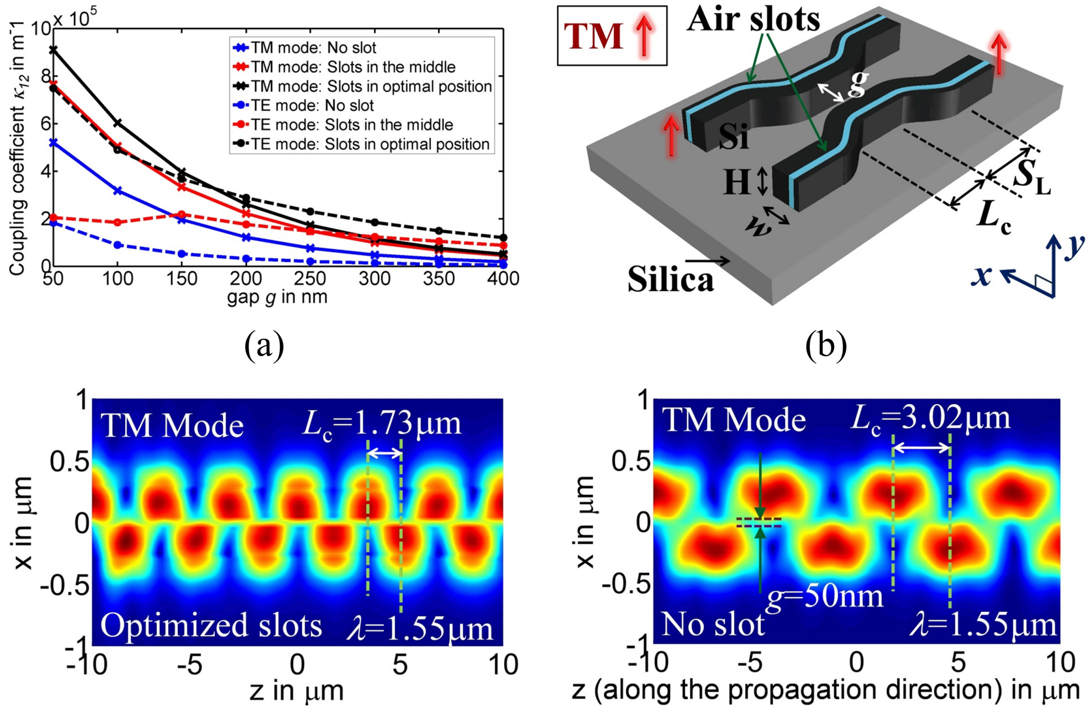

(a) (b)

(c) (d)

Figure 2.13: (a) κ_{12} for TE and TM modes when there is no slot, single slot in each waveguide at the center and single slot in each waveguide at the optimized position, (b) schematic (perspective-view) of the proposed ultra-compact optical coupler with S-bends. The FDTD generated electric field snapshots for parallel waveguides with (c) optimized slots, and (d) with no slot.

section 500 nm×500 nm has well-defined quasi-TE and TM modes, whereas, if the waveguide height is less, between 200 nm–250 nm, the quasi-TM mode becomes less confined with a mode-field discontinuity at the vertical side-walls [73]. Moreover, while fabricating, it is difficult to obtain perfect vertical side-walls as shown in Fig. 2.14 (a). Generally, in practice, side-walls become slanted with an angle θ with vertical axes where θ lies typically between 0-10^0 [74] mainly depending upon the resist used and the etching recipe. In Figs. 2.14 (a) and 2.14 (b), waveguide cross-sections with vertical and slanted waveguide side-walls are shown. We have taken $\theta = 5^0$ in our simulations to emulate the practical situations.

For $H = 500\,\text{nm}$, the maximum coupling can be obtained, keeping the loss within the desired limit (with S-bend $< 0.2\,\text{dB}$) with $h_{\text{slot}} = 500\,\text{nm}$, $w_{\text{slot}} = 130\,\text{nm}$, and $x_{\text{slot}} = 85\,\text{nm}$. For $w_{\text{slot}} > 130\,\text{nm}$, coupling coefficient is improved

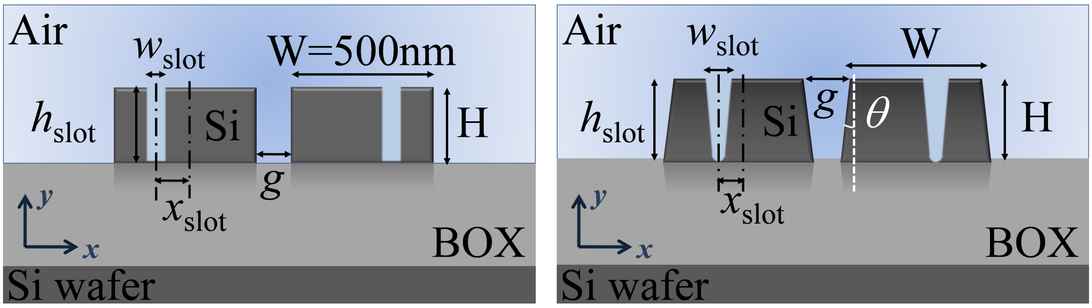

(a) (b)

Figure 2.14: (a) Waveguide cross-section with vertical side-walls. Waveguide height (H) can typically be 500 nm, 250 nm, and 220 nm. (b) Waveguide cross-section with slanted wall.

further; however, the propagation loss increases considerably. For $H = 500\,\text{nm}$ the coupling coefficients between two parallel wires (in the absence of S-bend) without slot, slot in the middle of the wire and optimized slot are listed for 50 nm gap in Table 2.2. Interestingly, when the wall is slanted, the effective gap between the two wires reduces, which further increases the coupling coefficient. The same design parameters are also valid ($h_{\text{slot}} = H$, $w_{\text{slot}} = 130\,\text{nm}$, $x_{\text{slot}} = 85\,\text{nm}$) for the waveguide with $H = 250\,\text{nm}$ or 220 nm; nevertheless, the propagation losses for TM mode will be much higher in those cases. Similarly, off-centered horizontal slots can be used to make compact couplers which will operate in the TE-mode. Horizontal slots can be fabricated using PECVD process as discussed later in this chapter.

Table 2.2: n_{eff}, κ, L_c and % enhancement of κ for practical designs

Slot position (waveguide-wall)	n_{eff}	κ (m^{-1})	L_c (μm)	**Percentage (%) enhancement of κ**
No slot (vertical)	2.90529	2.45×10^5	6.42	100%
Middle (vertical)	2.37974	6.295×10^5	2.495	156.94%
Optimized (vertical)	2.57078	8.12×10^5	1.93	231.43%
Optimized (slanted)	2.70096	8.283×10^5	1.896	238.08%

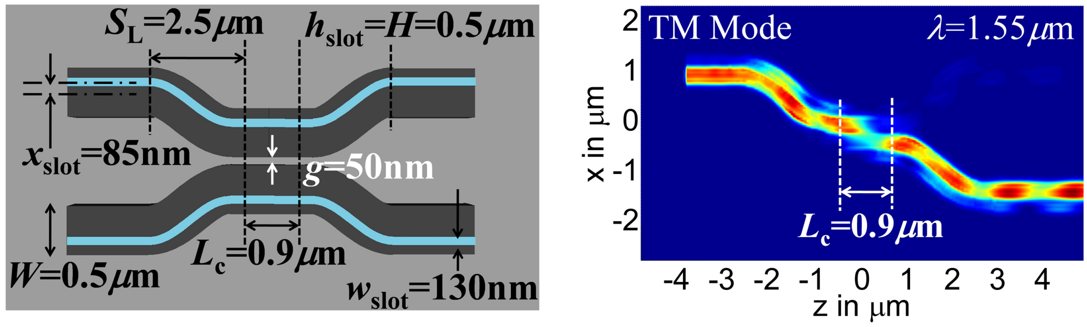

(a) (b)

Figure 2.15: (a) Dimension of each section (coupling region and S-bend) of the proposed optical coupler (top-view), (b) Power distribution in the coupler for TM-mode obtained from 3-D FDTD simulation.

2.2.3 Effect of S-bends

In practice, to decouple the input and output from each other, transition regions called S-bends are essential. S-bends increase the EL of the structure through the bends. However, it reduces the effective coupling length, L_c of the coupler as the optical power not only couples to the other waveguide through the parallel portion of the coupler, but also couples through the S-bends at the portions where the gap between the coupling arms is relatively smaller. Finally, we obtain L_c as small as $0.9\,\mu$m with an overall EL$\sim$0.12 dB and rejection ratio of 18 dB for the TM mode through 3D-FDTD simulations with a cross-section of $500\,\text{nm}\times 500\,\text{nm}$. Figure 2.15 (a) shows the optimized dimensions and positions of coupling region, S-bends, and the air-slots. The power distribution throughout the coupler for TM mode is plotted in Fig. 2.15 (b). Note that, in the previous section for two parallel wires we have considered only the predicted (by OIM) values of w_{slot}, h_{slot} and x_{slot} when $n_{\text{eff}} \geq 2$. For practical design, we start with the predicted values of w_{slot}, h_{slot} and x_{slot} obtained from OIM and further optimize those parameters through FDTD in presence of S-bends and input/output arms. Ultimately, the parameters for which the excess loss is the minimum will be finalized.

2.3 Design of Ultra-Compact Broadband PBS

In this section, we describe the design recipe of an ultra-compact and broadband on-chip PBS, operating at communication wavelength, $\lambda = 1.55\,\mu\text{m}$. The aforementioned ultra-compact DC with 50 nm gap cannot be used as an efficient PBS. Due to existence of symmetry in the structure of the parallel wires (of cross-section 400 nm×350 nm), the κ_{12} for quasi-TM mode is $9.1\times10^5\,\text{m}^{-1}$ and κ_{12} for TE-like mode is $7.4815\times10^5\,\text{m}^{-1}$ a ratio $(\kappa_{12-\text{TM}}/\kappa_{12-\text{TE}})$ of only ~ 1.216. The effective indices of the first and second waveguides (n_{eff1} and n_{eff2}) are also the same for both quasi-TE and quasi-TM modes. For quasi-TM mode $n_{\text{eff1}} = n_{\text{eff2}} = 2.1282$ whereas for quasi-TE mode, n_{eff1} and n_{eff2} are 1.5388. A similar effective index of the guided modes limit us to obtain an ER of ~0.5 dB with a device size of $L_\text{c}(= 1.73\,\mu\text{m})$. This suggests the exploration of a suitable longer device to achieve a greater ER and affects the device's ultimate effective fingerprint when used as a PBS instead of an optical coupler.

To overcome these difficulties, we propose a novel design of an on-chip compact PBS. The cross-sectional view of the proposed PBS is shown in Fig. 2.16 (a). A horizontal silica slot of thickness 25 nm is placed in the W-II. The structure of W-I having optimized vertical slot ($w_{\text{slot1}} = 50\,\text{nm}$, $h_{\text{slot1}} = 350\,\text{nm}$, $x_{\text{slot1}} = -50\,\text{nm}$) is kept unaltered. Location of the horizontal slot, y_{slot2} in the W-II is to be selected in such a way that it can reduce the phase mismatch by making n_{eff2} equal to $n_{\text{eff1}}(= 2.1282)$ for TM mode at $\lambda = 1.55\,\mu\text{m}$. For TE mode, n_{eff} of W-I and W-II should be different. Figure 2.16 (b) plots the variation of effective RI of the guided modes (both TE and TM). It is found that for two distinct values of $y_{\text{slot2}} = 75.5\,\text{nm}$ and $289.5\,\text{nm}$, it is possible to realize the desired condition, $n_{\text{eff2}} = n_{\text{eff1}}$. Hence, for this particular design ($w_{\text{slot1}} = 50\,\text{nm}$, $h_{\text{slot1}} = 350\,\text{nm}$, $x_{\text{slot1}} = -50\,\text{nm}$; $w_{\text{slot2}} = 400\,\text{nm}$, $h_{\text{slot2}} = 25\,\text{nm}$, $y_{\text{slot2}} = 75.5\,\text{nm}$), $n_{\text{eff1}-\text{TM}} = n_{\text{eff2}-\text{TM}} = 2.128197$, $n_{\text{eff1}-\text{TE}} = 2.383632$ and $n_{\text{eff2}-\text{TE}} = 1.538781$. From OIM, it is found that for $g = 50\,\text{nm}$, the κ_{12} for quasi-TM and TE modes at $\lambda = 1.55\,\mu\text{m}$, is $7.845\times10^5\ \text{m}^{-1}$ and $5.3538\times10^4\,\text{m}^{-1}$, respectively, with a coupling ratio $(\kappa_{12-\text{TM}}/\kappa_{12-\text{TE}})$ of ~14.69. Note that, $n_{\text{eff1}} = n_{\text{eff2}}$ for TM-mode, but for the TE-mode, $n_{\text{eff1}}(1.5388) < n_{\text{eff2}}(2.383632)$, which gives rise to a large phase mismatch for the TE-mode.

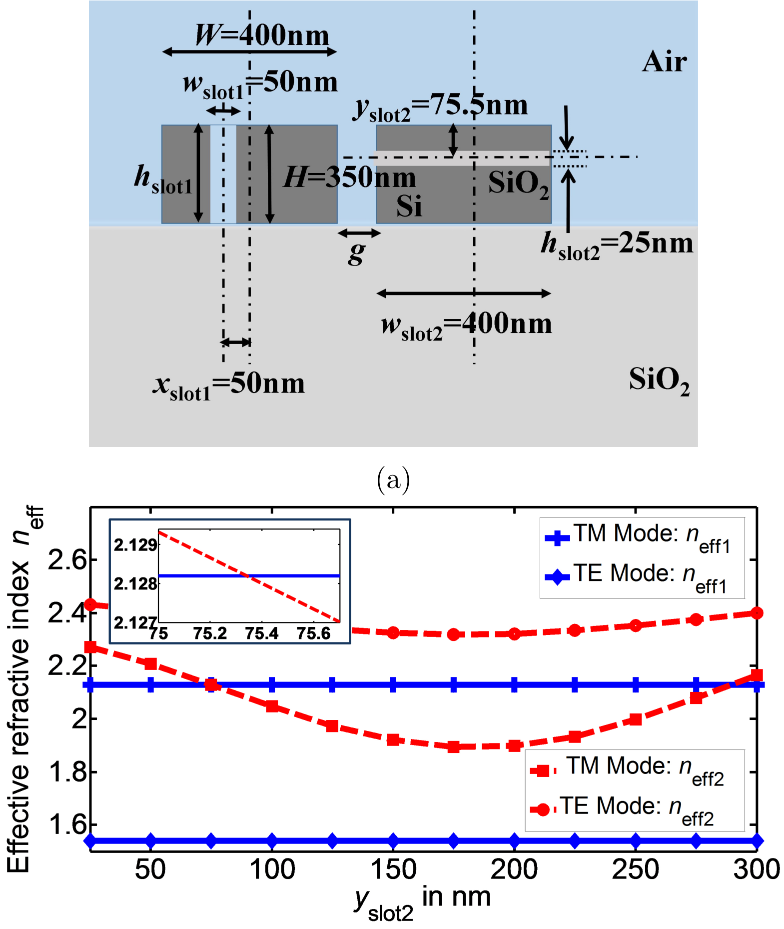

(a)

(b)

Figure 2.16: (a) Schematic cross-section of the proposed PBS, (b) phase matching diagram and the choice of y_{slot2}.

2.3.1 Input Criteria

As discussed above, the optical input must be fed to the second waveguide of the proposed PBS for the device to function efficiently, this is due to the structural asymmetry between two adjacent waveguides. The computed coupling coefficients, $\kappa_{12-\mathrm{TM}}$, $\kappa_{21-\mathrm{TM}}$, $\kappa_{12-\mathrm{TE}}$ and $\kappa_{21-\mathrm{TE}}$ are $\sim 7.845\times10^{5}\,\mathrm{m}^{-1}$, $7.21\times10^{5}\,\mathrm{m}^{-1}$, $5.354\times10^{4}\,\mathrm{m}^{-1}$ and $7.8543\times10^{5}\,\mathrm{m}^{-1}$, respectively. In such case, the coupling ratio $\kappa_{12-\mathrm{TM}}/\kappa_{12-\mathrm{TE}}(=14.69)$ and $\kappa_{21-\mathrm{TM}}/\kappa_{21-\mathrm{TE}}(=0.9178)$ differs from each other considerably. These calculations suggest that the input must be fed into W-II to achieve the desired performances. Note that, we have carried out FDTD simula-

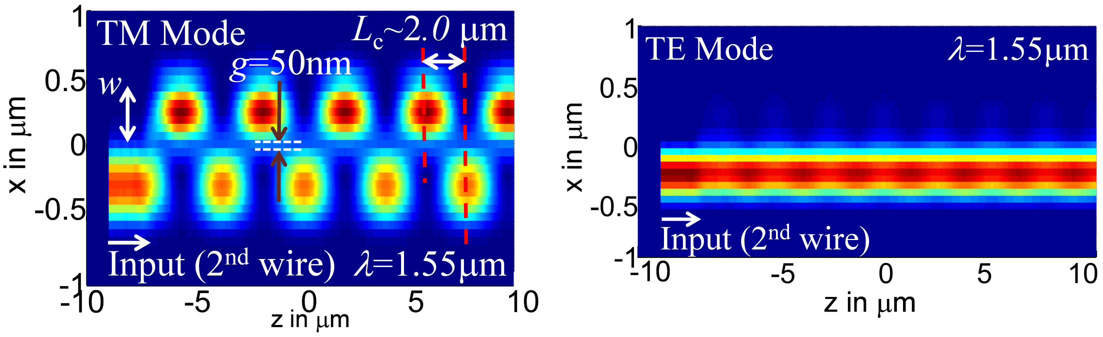

(a) (b)

Figure 2.17: Polarization splitting behavior is demonstrated by the snapshots of electric field distributions in two parallel waveguides with hybrid slots at an operating wavelength of 1550 nm. Electric field distribution when (a) TM input is applied at the second waveguide (W-II) and (b) TE-mode is applied at the second waveguide, W-II.

tions and FDTD results (Figs. 2.17 (a) and 2.17 (b)) are in good agreement with our calculated values of L_c for two parallel waveguides from OIM. The aforementioned input criteria based on OIM are also confirmed through 3D-FDTD. From Figs. 2.17 (a) and 2.17 (b), it is observed that, for parallel wires, when an optical input is given to W-II (with the horizontal slot), the TM-mode couples to the W-I with a coupling length $L_c \sim 2\,\mu$m, whereas for the TE-mode a weak coupling takes place from W-II to W-I that leads to a much larger L_c.

2.3.2 Practical Design Considerations: Effects of S-bends

The practical design of a PBS must contain transition regions (S-bends) along with its parallel coupling region. The proposed waveguide configuration is displayed in Fig. 2.18 (a). FDTD simulations (Figs. 2.18 (b) and 2.18 (c)) suggest that the S-bends further reduce the effective coupling length from $2\,\mu$m to $\sim 1.1\,\mu$m due to the partial coupling through the transition region. The length of the S-bend, S_L is taken as $2.5\,\mu$m. Keeping the cross-section intact as in previous section, with this structure, it is possible to achieve an ER>22.3 dB for TE-mode and ∼13 dB for TM-mode within a very compact device size when the input is applied to the W-II. The insertion losses for the TE mode and TM mode are respectively, 0.008 dB and 0.055 dB, negligibly small values at the coupler section. The EL is always below 0.2 dB. Since the waveguide structure is not symmetric, ER for TE and TM

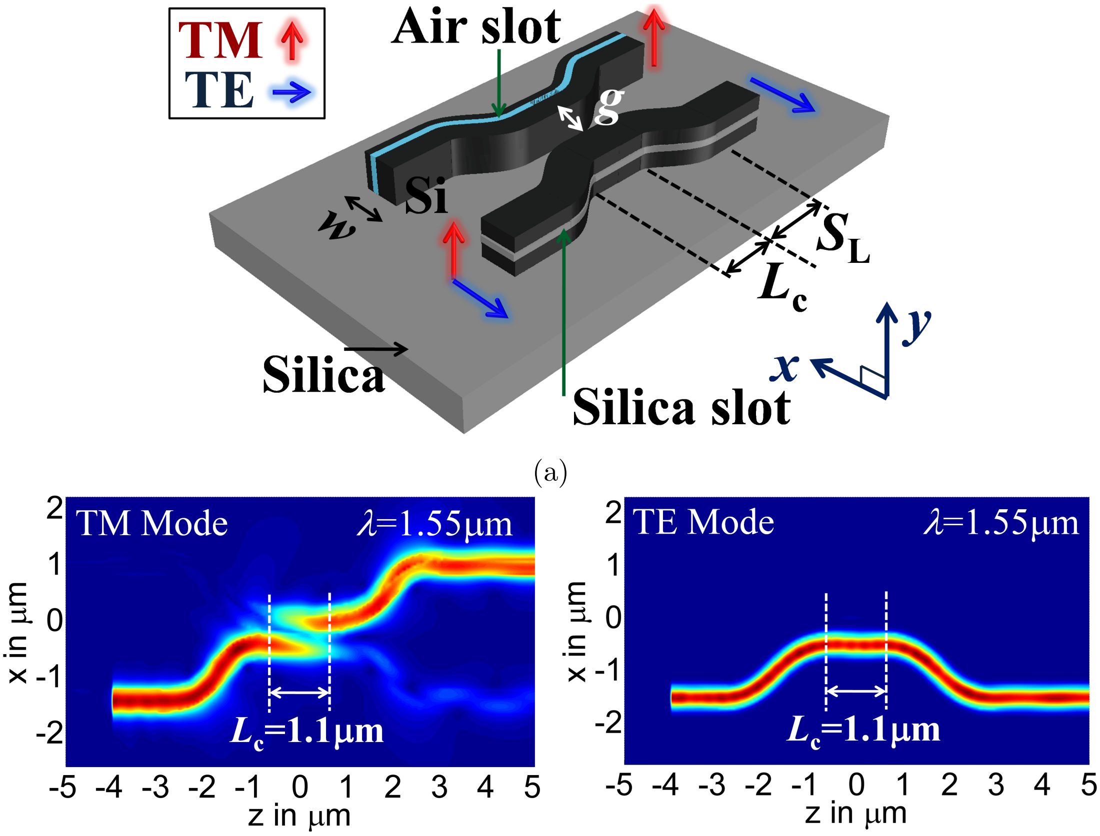

(a)

(b)

(c)

Figure 2.18: (a) Perspective view of the proposed PBS with hybrid slots and S-bends. Snapshots of the electric field distribution through the PBS for (b) TM mode, (c) TE Mode, when both the inputs are applied to the W-II.

modes differ considerably. The spectral variation of ER and IL for TE and TM modes is depicted in Figs. 2.19 (a) and 2.19 (b). The FWHM for the TE-mode is greater than 100 nm which covers the entire C band as well as some portions of the S and L bands. The 3-dB bandwidth for the TM-mode is 78 nm and covers the entire C-band and a part of the L band. We have also optimized the PBS for the wire cross-section, 500 nm×500 nm. For this cross-section the optimized parameters are: $w_{\mathrm{slot1}} = 130\,\mathrm{nm}$, $h_{\mathrm{slot1}} = 500\,\mathrm{nm}$, $x_{\mathrm{slot1}} = 85\,\mathrm{nm}$, $w_{\mathrm{slot2}} = 500\,\mathrm{nm}$, $h_{\mathrm{slot2}} = 50\,\mathrm{nm}$ and $y_{\mathrm{slot2}} = 139.5\,\mathrm{nm}$ from the top. The effective coupling length, L_{c} in presence of S-bends is $1.7\,\mu\mathrm{m}$ for the best performance.

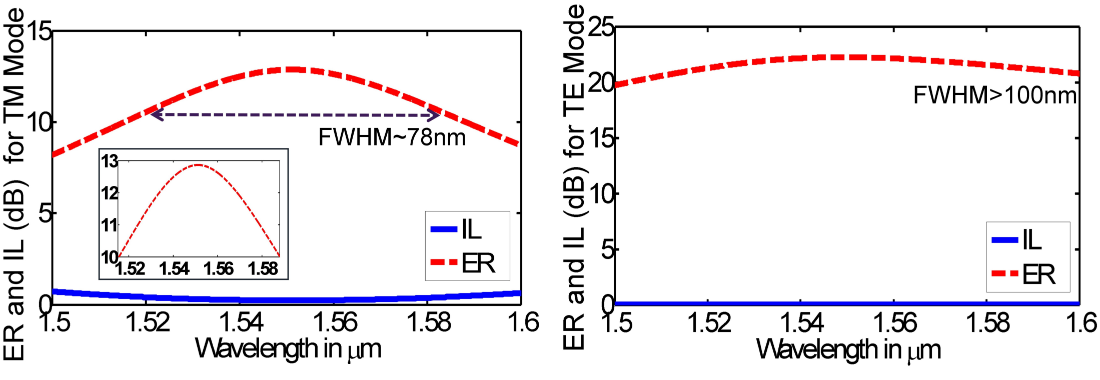

(a) (b)

Figure 2.19: IL and ER for fundamental quasi- (a) TM mode, (b) TE modes. FWHM>100 nm for TE mode, whereas, FWHM is 78 nm for quasi-TM mode.

2.3.3 Proposed Fabrication Scheme and Fabrication Tolerance

Recent advancements in SOI technology enable the fabrication of nanophotonic structures with very narrow slots in Si-waveguides. A vertical air-slot with a width of only 30 nm [75] and a horizontal silica slot with a height as small as 17 nm [76] have already been realized with current state-of-the-art fabrication techniques. Fabrication of cross-slot waveguides with narrow vertical slot and sub-wavelength horizontal slot has been demonstrated in [77]. We propose a scheme to fabricate a vertical air-slot in one waveguide along with a horizontal silica slot in the adjacent waveguide simultaneously as shown in Fig. 2.18 (a). The recipe to create a vertical slot in one waveguide in addition to a horizontal slot in the other waveguide might not seem straightforward at a first glance. Hence, we briefly discuss on a possible process flow to make such a device in a CMOS compatible fashion. A schematic, including the step by step procedure of the proposed fabrication flow, is given in Fig. 2.20 for clarity.

Initially, a bare Si wafer is thermally oxidized to grow a few-micron-thick layer of buried oxide. A 262 nm thick layer of amorphous Si (a-Si) is deposited on the oxidized wafer by PECVD. Note that, a-Si has recently been shown to have relatively low linear and nonlinear loss in the 1.55 μm wavelength [78, 79]. Next, a SiO_2 layer is deposited through PECVD on the top of a-Si. This silica layer will

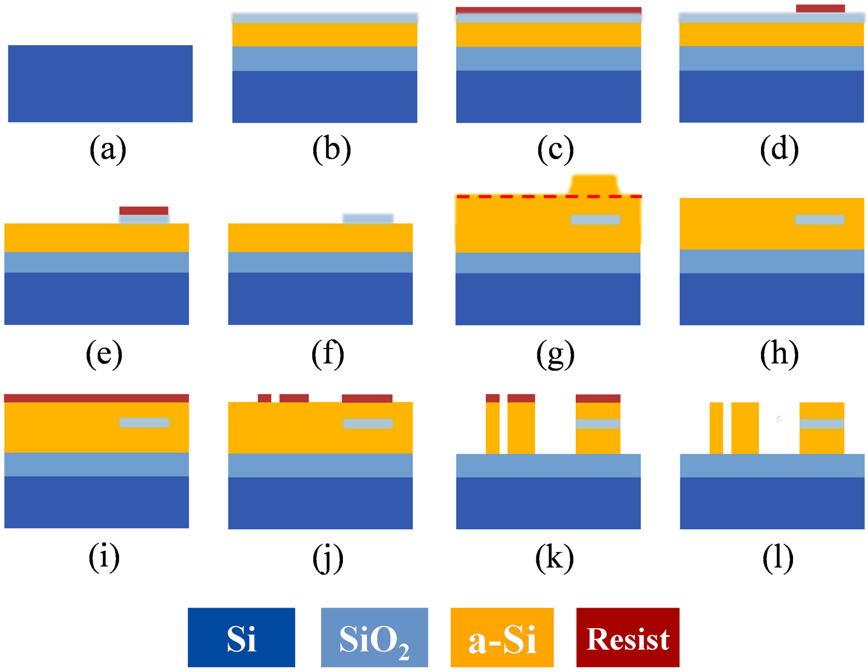

Figure 2.20: Lithography process flow. (a) Begin with Si wafer. (b) Thermally grow oxide, deposit $\sim$ 262 nm thick PECVD amorphous Si layer (a-Si), deposit $\sim$25 nm thick PECVD SiO$_2$ layer (c) Spin-coat resist, (d) Pattern the resist by EBL, (e) RIE etch oxide, (f) Strip resist, (g) Deposit a-Si layer of desired thickness ($>$ 75 nm) by PECVD all over the whole platform (h) CMP is used to flatten the top of the a-Si, (i) Spin-coat resist (j) Create pattern by EBL, (k) Etch Si (l) Strip resist.

act as the horizontal slot. Resist is grown on the silica layer by spin-coating. The resist is patterned with EBL to define the W-II. After spin coating and patterning the resist by EBL, the oxide layer is RIE-etched as shown in Fig. 2.20 (e). Then we strip off the resist. Again, a-Si of desired thickness (more than 75 nm in this case) is deposited through PECVD all over the platform as shown in the Fig. 2.20 (g). However, the final heights of the W-I and W-II are required to be the same. Hence, chemical-mechanical planarization (CMP) is being used to flatten the top of the a-Si as shown in Fig. 2.20 (h). Instead of CMP one may also use shadow-mask or ashable hard mask to deposit PECVD a-Si, selectively until the height of the a-Si becomes the same everywhere. After flattening the top, the vertical slot is defined by patterning the spin-coated resist through EBL. The two EBL steps need to be aligned fairly accurately, making the process slightly challenging, but still within the reach of current technology. Finally, the a-Si is plasma etched and the resist is removed. In the previous section we have discussed an ultra-short coupler. For the coupler consisting of two adjacent vertically slotted waveguides, as shown in Figs. 2.12 (b) and 2.12 (d), the process flow will be relatively easier. As we do not need to fabricate the horizontal slot, we can start with a standard SOI wafer and the two waveguides with asymmetric vertical slots can be patterned using EBL.

We finally carry out the fabrication tolerance analysis of our PBS design, operating at $1.55\,\mu$m, by analyzing the effect of variation in horizontal slot height and position. We have noted the changes in ER and IL of both the modes TE and TM for the PBS structure ($w_{\text{slot1}} = 50\,\text{nm}$, $w_{\text{slot2}} = 400\,\text{nm}$, $h_{\text{slot1}} = 350\,\text{nm}$, $h_{\text{slot2}} = 25\,\text{nm}$, $x_{\text{slot1}} = -50\,\text{nm}$ and $y_{\text{slot2}} = 75.5\,\text{nm}$), when either of the parameters h_{slot2} or y_{slot2} is varied within ±20%. Figure 2.21 demonstrates how the IL and ER of TM and TE modes deviate with ±20% alteration in slot-height and slot-position. The solid curves in Fig. 2.21 (a) depict the impact of slot-position, whereas the dashed curves correspond to slot-height. It is evident that a variation in slot height and slot position in W-II does not affect TE mode characteristics, however for TM mode the IL slightly increases and remains $< 0.1\,\text{dB}$ for shift in h_{slot2} and $> 0.5\,\text{dB}$ when the y_{slot2} is decreased significantly.

On the other hand, the ER for the TM mode, as shown in Fig. 2.19 (b), is not affected by the change in h_{slot2}, and it decreases by less than 2 dB in magnitude for variation in the slot-position. It is further seen that for the TE mode, the ER remains nearly the same irrespective of the change in slot-height, h_{slot2}, but is degraded by almost 5 dB in magnitude for +20% deviations in slot-position, y_{slot2}. We have further extended the tolerance analysis over 100 nm wavelength band (1500 nm–1600 nm). Numerical simulations reveal that ±20% variation in the h_{slot2} and y_{slot2} for TE mode propagation in the designed PBS does not experience any change in the IL over 100 nm wavelength band, however for the TM mode, the IL increases slightly but remains well below 0.5 dB for the entire wavelength range considered. We have noticed that the ER for TM and TE modes changes moderately for deviation in h_{slot2} whereas it decreases by almost 5 dB at shorter wavelengths ($< 1.55\,\mu$m) for deviations of ±20% within y_{slot2} for both the modes. For wavelengths greater than $1.55\,\mu$m, the ER decreases significantly for the TM mode whereas fewer changes are expected for the TE mode. In order to attain

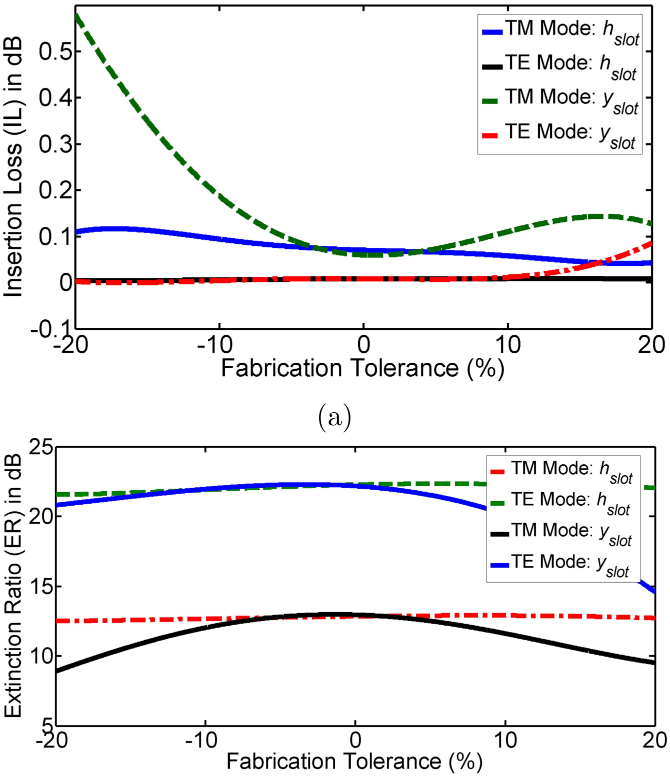

(a)

(b)

Figure 2.21: Fabrication tolerance analysis. Fluctuations in (a) IL and (b) ER with the variation in h_{slot2} and y_{slot2} for the proposed design of PBS operating at $\lambda = 1.55\,\mu$m.

phase matching for the TM mode in both the waveguides (with vertical and horizontal slot), it is recommended to choose h_{slot2} and y_{slot2} appropriately. Note that, n_{eff2} decreases with increasing slot height h_{slot2}. In order to maintain $n_{\text{eff2}} = n_{\text{eff1}}$, one has to select a material of RI higher than silica for the horizontal slot in case a design with $h_{\text{slot2}} > 25\,\text{nm}$ is desired. Initial simulation results suggest that it is possible to choose $h_{\text{slot2}} > 25\,\text{nm}$ (e.g. 40 nm–50 nm) if the horizontal slot is comprised of a different material with RI>silica ($n_{\text{silica}} \sim 1.445$) at $\lambda = 1.55\,\mu$m. An appropriate choice of such a material might be silicon nitride which is CMOS compatible with negligible nonlinear absorption as an added advantage [80]. The higher slot-width in W-II (h_{slot2}) would facilitate the fabrication of the designed PBS. Currently, we are investigating such on-chip PBS designs based on silicon nitride slots.

2.4 Summary and Conclusion

To summarize, we have numerically evaluated the coupling coefficient through OIM after deducing the electric fields from the FEM based mode solver. OIM enables us to find the coupling coefficient between any two arbitrary shaped waveguides comprised of any material. An ultra-compact optical coupler and PBS design have been proposed by optimizing the slot-size and position to maximize the coupling between the waveguides for a particular mode. It is shown that, off-centered slots enhance the coupling coefficient significantly compared to waveguides with no slots in it and waveguides with conventional slots (at center positions). We believe, introducing off-centered slots is an important step towards achieving ultra-compact photonic devices. The designed PBS which has a very low footprint of $L_{\mathrm{c}} \sim 1.1\,\mu$m, exhibits a high ER, a broad 3-dB bandwidth and very low IL at an operating wavelength of $1.55\,\mu$m. It might be possible to fabricate such complex devices with the combination of both the vertical and horizontal slots, and to make a justice, fabrication scheme has been put forward. The tolerance analysis provides us the flexibility in design and indicates the robustness of the device to the fabrication variations. All the results are confirmed by 3D-FDTD simulations.

References

[1] D. A. Miller, "Rationale and challenges for optical interconnects to electronic chips," *Proceedings of the IEEE*, vol. 88, no. 6, pp. 728–749, 2000.

[2] A. Shacham, K. Bergman, and L. P. Carloni, "Photonic networks-on-chip for future generations of chip multiprocessors," *IEEE Transactions on Computers*, vol. 57, no. 9, pp. 1246–1260, 2008.

[3] M. Lipson, "Guiding, modulating, and emitting light on silicon-challenges and opportunities," *Journal of Lightwave Technology*, vol. 23, no. 12, pp. 4222–4238, 2005.

[4] M. A. Nielsen and I. Chuang, *Quantum computation and quantum information.* Cambridge University Press, 2002.

[5] E. Knill, R. Laflamme, and G. J. Milburn, "A scheme for efficient quantum computation with linear optics," *Nature*, vol. 409, no. 6816, pp. 46–52, 2001.

[6] P. Kok, W. J. Munro, K. Nemoto, T. C. Ralph, J. P. Dowling, and G. J. Milburn, "Linear optical quantum computing with photonic qubits," *Reviews of Modern Physics*, vol. 79, no. 1, pp. 135–174, 2007.

[7] J. L. O'Brien, A. Furusawa, and J. Vučković, "Photonic quantum technologies," *Nature Photonics*, vol. 3, no. 12, pp. 687–695, 2009.

[8] A. Politi, M. J. Cryan, J. G. Rarity, S. Yu, and J. L. O'Brien, "Silica-on-silicon waveguide quantum circuits," *Science*, vol. 320, no. 5876, pp. 646–649, 2008.

[9] P. J. Shadbolt, M. R. Verde, A. Peruzzo, A. Politi, A. Laing, M. Lobino, J. C. Matthews, M. G. Thompson, and J. L. O'Brien, "Generating, manipulating and measuring entanglement and mixture with a reconfigurable photonic circuit," *Nature Photonics*, vol. 6, no. 1, pp. 45–49, 2012.

[10] M. Sasaki, M. Fujiwara, R.-B. Jin, M. Takeoka, H. Endo, K.-I. Yoshino, T. Ochi, S. Asami, A. Tajima *et al.*, "Quantum photonic network: concept, basic tools, and future issues," *IEEE Journal of Selected Topics in Quantum Electronics*, vol. 21, no. 3, pp. 49–61, 2014.

[11] W. Bogaerts, R. Baets, P. Dumon, V. Wiaux, S. Beckx, D. Taillaert, B. Luyssaert, J. Van Campenhout, P. Bienstman, and D. Van Thourhout, "Nanophotonic waveguides in silicon-on-insulator fabricated with CMOS technology," *Journal of Lightwave Technology*, vol. 23, no. 1, pp. 401–412, 2005.

[12] B. Jalali and S. Fathpour, "Silicon photonics," *Journal of Lightwave Technology*, vol. 24, no. 12, pp. 4600–4615, 2006.

[13] V. R. Almeida, Q. Xu, C. A. Barrios, and M. Lipson, "Guiding and confining light in void nanostructure," *Optics Letters*, vol. 29, no. 11, pp. 1209–1211, 2004.

[14] K. R. Hiremath, J. Niegemann, and K. Busch, "Analysis of light propagation in slotted resonator based systems via coupled-mode theory," *Optics Express*, vol. 19, no. 9, pp. 8641–8655, 2011.

[15] Q. Lin, O. J. Painter, and G. P. Agrawal, "Nonlinear optical phenomena in silicon waveguides: modeling and applications," *Optics Express*, vol. 15, no. 25, pp. 16 604–16 644, 2007.

[16] P. Muellner, M. Wellenzohn, and R. Hainberger, "Nonlinearity of optimized silicon photonic slot waveguides," *Optics Express*, vol. 17, no. 11, pp. 9282–9287, 2009.

[17] H. M. K. Wong, C. Lin, M. A. Swillam, and A. S. Helmy, "Broadband compact si wire to slot waveguide couplers," in *CLEO: Science and Innovations.* Optical Society of America, 2013, pp. CTu3F–6.

[18] M. J. Zablocki, A. Sharkawy, O. Ebil, S. Shi, and D. Prather, "Electro-optically switched compact coupled photonic crystal waveguide directional coupler," *Applied Physics Letters*, vol. 96, no. 8, p. 081110, 2010.

[19] B.-K. Yang, S.-Y. Shin, and D. Zhang, "Ultrashort polarization splitter using two-mode interference in silicon photonic wires," *IEEE Photonics Technology Letters*, vol. 21, no. 7, pp. 432–434, 2009.

[20] A. Hosseini, S. Rahimi, X. Xu, D. Kwong, J. Covey, and R. Chen, "Ultracompact and fabrication-tolerant integrated polarization splitter," *Optics Letters*, vol. 36, no. 20, pp. 4047–4049, 2011.

[21] I. Kiyat, A. Aydinli, and N. Dagli, "A compact silicon-on-insulator polarization splitter," *IEEE Photonics Technology Letters*, vol. 17, no. 1, pp. 100–102, 2004.

[22] H. Fukuda, K. Yamada, T. Tsuchizawa, T. Watanabe, H. Shinojima, and S.-i. Itabashi, "Ultrasmall polarization splitter based on silicon wire waveguides," *Optics Express*, vol. 14, no. 25, pp. 12 401–12 408, 2006.

[23] M. Watts, H. Haus, and E. Ippen, "Integrated mode-evolution-based polarization splitter," *Optics Letters*, vol. 30, no. 9, pp. 967–969, 2005.

[24] D. Dai and J. E. Bowers, "Novel ultra-short and ultra-broadband polarization beam splitter based on a bent directional coupler," *Optics Express*, vol. 19, no. 19, pp. 18 614–18 620, 2011.

[25] Q. Tan, X. Huang, W. Zhou, and K. Yang, "A plasmonic based ultracompact polarization beam splitter on silicon-on-insulator waveguides," *Scientific Reports*, vol. 3, p. 2206, 2013.

[26] F. Lou, D. Dai, and L. Wosinski, "Ultracompact polarization beam splitter based on a dielectric–hybrid plasmonic–dielectric coupler," *Optics Letters*, vol. 37, no. 16, pp. 3372–3374, 2012.

[27] X. Guan, H. Wu, Y. Shi, and D. Dai, "Extremely small polarization beam splitter based on a multimode interference coupler with a silicon hybrid plasmonic waveguide," *Optics Letters*, vol. 39, no. 2, pp. 259–262, 2014.

[28] X. Guan, H. Wu, Y. Shi, L. Wosinski, and D. Dai, "Ultracompact and broadband polarization beam splitter utilizing the evanescent coupling between a hybrid plasmonic waveguide and a silicon nanowire," *Optics Letters*, vol. 38, no. 16, pp. 3005–3008, 2013.

[29] K.-W. Chang and C.-C. Huang, "Ultrashort broadband polarization beam splitter based on a combined hybrid plasmonic waveguide," *Scientific Reports*, vol. 6, p. 19609, 2016.

[30] J. T. Kim and S. Park, "Vertical polarization beam splitter using a hybrid long-range surface plasmon polariton waveguide," *Journal of Optics*, vol. 16, no. 2, p. 025501, 2014.

[31] Y. Ma, G. Farrell, Y. Semenova, H. P. Chan, H. Zhang, and Q. Wu, "Low loss, high extinction ration and ultra-compact plasmonic polarization beam splitter," *IEEE Photonics Technology Letters*, vol. 26, no. 7, pp. 660–663, 2014.

[32] J. Chee, S. Zhu, and G. Lo, "CMOS compatible polarization splitter using hybrid plasmonic waveguide," *Optics Express*, vol. 20, no. 23, pp. 25 345–25 355, 2012.

[33] Y. Xu, J. Xiao, and X. Sun, "Proposal for compact polarization splitter using asymmetrical three-guide directional coupler," *IEEE Photonics Technology Letters*, vol. 27, no. 6, pp. 654–657, 2015.

[34] B. Shen, P. Wang, R. Polson, and R. Menon, "An integrated-nanophotonics polarization beamsplitter with $2.4{\times}2.4\,\mu\mathrm{m}^2$ footprint," *Nature Photonics*, vol. 9, no. 6, pp. 378–382, 2015.

[35] A. Y. Piggott, J. Lu, K. G. Lagoudakis, J. Petykiewicz, T. M. Babinec, and J. Vučković, "Inverse design and demonstration of a compact and broadband on-chip wavelength demultiplexer," *Nature Photonics*, vol. 9, no. 6, pp. 374–377, 2015.

[36] Y. Shi, D. Dai, and S. He, "Proposal for an ultracompact polarization-beam splitter based on a photonic-crystal-assisted multimode interference coupler," *IEEE Photonics Technology Letters*, vol. 19, no. 11, pp. 825–827, 2007.

[37] J. Feng and Z. Zhou, “Polarization beam splitter using a binary blazed grating coupler,” *Optics Letters*, vol. 32, no. 12, pp. 1662–1664, 2007.

[38] W. Huang, Y. Zhang, and B. Li, “Ultracompact wavelength and polarization splitters in periodic dielectric waveguides,” *Optics Express*, vol. 16, no. 3, pp. 1600–1609, 2008.

[39] Y.-F. Ma, M.-J. Sung, and D.-W. Huang, “Controlling the polarization dependence of dual-channel directional couplers formed by silicon-on-insulator slot waveguides,” *Applied optics*, vol. 49, no. 36, pp. 6979–6985, 2010.

[40] S. Lin, J. Hu, and K. B. Crozier, “Ultracompact, broadband slot waveguide polarization splitter,” *Applied Physics Letters*, vol. 98, no. 15, p. 151101, 2011.

[41] Y. Yue, L. Zhang, R. G. Beausoleil, and A. E. Willner, “Very short polarization splitting/combining using two horizontally-slotted waveguides,” in *Conference on Lasers and Electro-Optics*. Optical Society of America, 2009, p. CTuC4.

[42] H. Zhang, Y. Huang, S. Das, C. Li, M. Yu, P. G.-Q. Lo, M. Hong, and J. Thong, “Polarization splitter using horizontal slot waveguide,” *Optics Express*, vol. 21, no. 3, pp. 3363–3369, 2013.

[43] J. Wang, J. Xiao, and X. Sun, “Design of a compact polarization splitter composed of a multiple-slotted waveguide and a silicon nanowire,” *Journal of Optics*, vol. 15, no. 3, p. 035501, 2013.

[44] J. Xiao, X. Liu, and X. Sun, “Design of a compact polarization splitter in horizontal multiple-slotted waveguide structures,” *Japanese Journal of Applied Physics*, vol. 47, no. 5R, p. 3748, 2008.

[45] R. Ding, T. Baehr-Jones, W.-J. Kim, B. Boyko, R. Bojko, A. Spott, A. Pomerene, C. Hill, W. Reinhardt, and M. Hochberg, “Low-loss asymmetric strip-loaded slot waveguides in silicon-on-insulator,” *Applied Physics Letters*, vol. 98, no. 23, p. 104, 2011.

[46] R. Haldar, V. Mishra, and S. K. Varshney, “Ultra compact optical switches and polarization splitter based on non-symmetric slotted si wire waveguides,” in *Photonic Networks and Devices*. Optical Society of America, 2015, pp. JM3A–24.

[47] R. Haldar, V. Mishra, A. Dutt, and S. K. Varshney, “On-chip broadband ultra-compact optical couplers and polarization splitters based on off-centered and non-symmetric slotted Si-wire waveguides,” *Journal of Optics*, vol. 18, no. 10, p. 105801, 2016.

[48] K. Gehlot and A. Sharma, “Optimization of Si slot waveguide using approximate semi-analytical method,” *Optics Express*, vol. 24, no. 5, pp. 4722–4729, 2016.

[49] Lumerical FDTD Solutions, “FDTD Solutions 8.5,” *http://www. lumerical. com/tcad-products/fdtd.*

[50] A. Ghatak and K. Thyagarajan, *An Introduction to Fiber Optics*. Cambridge university press, 1998.

[51] K. Okamoto, *Fundamentals of Optical Waveguides*. Academic press, 2006.

[52] G. Lifante, *Integrated Photonics: Fundamentals*. John Wiley & Sons, 2003.

[53] L. Jia-ming, *Photonic devices*. Cambridge University Press, 2010.

[54] J. D. Joannopoulos, S. G. Johnson, J. N. Winn, and R. D. Meade, "Molding the flow of light," *Princeton Univ. Press, Princeton, NJ [ua]*, 2008.

[55] G. T. Raja, R. Halder, and S. Varshney, "Numerical analysis of lasing characteristics in highly bend-compensated large-mode-area ytterbium-doped double-clad leakage channel fibers," *Applied optics*, vol. 54, no. 35, pp. 10 314–10 320, 2015.

[56] V. Mishra, R. Haldar, P. Mondal, and S. K. Varshney, "Efficient all-optical transistor action in short-length multimode optical fibers," *Journal of Lightwave Technology*, vol. 36, no. 13, pp. 2582–2588, 2018.

[57] A. Dutt, S. Mahapatra, and S. K. Varshney, "Capillary optical fibers: design and applications for attaining a large effective mode area," *JOSA B*, vol. 28, no. 6, pp. 1431–1438, 2011.

[58] V. Mishra, S. P. Singh, R. Haldar, and S. K. Varshney, "Sub-wavelength dual capillaries-assisted chalcogenide optical fibers: Unusual modal properties in mid-IR (2–5 μm) spectral range," *IEEE Journal of Selected Topics in Quantum Electronics*, vol. 22, no. 2, pp. 208–213, 2015.

[59] L. Zhang, C. Bao, V. Singh, J. Mu, C. Yang, A. M. Agarwal, L. C. Kimerling, and J. Michel, "Generation of two-cycle pulses and octave-spanning frequency combs in a dispersion-flattened micro-resonator," *Optics Letters*, vol. 38, no. 23, pp. 5122–5125, 2013.

[60] C. Koos, P. Vorreau, T. Vallaitis, P. Dumon, W. Bogaerts, R. Baets, B. Esembeson, I. Biaggio, T. Michinobu, F. Diederich *et al.*, "All-optical high-speed signal processing with silicon–organic hybrid slot waveguides," *Nature Photonics*, vol. 3, no. 4, pp. 216–219, 2009.

[61] T. Baehr-Jones, M. Hochberg, G. Wang, R. Lawson, Y. Liao, P. A. Sullivan, L. Dalton, A.-Y. Jen, and A. Scherer, "Optical modulation and detection in slotted silicon waveguides," *Optics Express*, vol. 13, no. 14, pp. 5216–5226, 2005.

[62] F. Sun, L. Xia, C. Nie, C. Qiu, L. Tang, J. Shen, T. Sun, L. Yu, P. Wu, S. Yin *et al.*, "All-optical modulator based on graphene-plasmonic slot waveguide at 1550 nm," *Applied Physics Express*, 2019.

[63] J. Wang, Z. Cheng, Z. Chen, X. Wan, B. Zhu, H. K. Tsang, C. Shu, and J. Xu, "High-responsivity graphene-on-silicon slot waveguide photodetectors," *Nanoscale*, vol. 8, no. 27, pp. 13 206–13 211, 2016.

[64] Q. Xu, V. R. Almeida, R. R. Panepucci, and M. Lipson, "Experimental demonstration of guiding and confining light in nanometer-size low-refractive-index material," *Optics Letters*, vol. 29, no. 14, pp. 1626–1628, 2004.

[65] C. A. Barrios, B. Sánchez, K. B. Gylfason, A. Griol, H. Sohlström, M. Holgado, and R. Casquel, "Demonstration of slot-waveguide structures on silicon nitride/silicon oxide platform," *Optics Express*, vol. 15, no. 11, pp. 6846–6856, 2007.

[66] K. Luke, "Parametric frequency comb generation in visible and mid-infrared wavelengths with integrated silicon nitride ring resonators," Ph.D. dissertation, Cornell University, 2016.

[67] R. Palmer, L. Alloatti, D. Korn, W. Heni, P. Schindler, J. Bolten, M. Karl, M. Waldow, T. Wahlbrink, W. Freude *et al.*, “Low-loss silicon strip-to-slot mode converters,” *IEEE Photonics Journal*, vol. 5, no. 1, pp. 2 200 409–2 200 409, 2013.

[68] I. S. Maksymov and Y. S. Kivshar, “Broadband light coupling to dielectric slot waveguides with tapered plasmonic nanoantennas,” *Optics Letters*, vol. 38, no. 22, pp. 4853–4856, 2013.

[69] Z. Wang, N. Zhu, Y. Tang, L. Wosinski, D. Dai, and S. He, “Ultracompact low-loss coupler between strip and slot waveguides,” *Optics Letters*, vol. 34, no. 10, pp. 1498–1500, 2009.

[70] A. Säynätjoki, L. Karvonen, T. Alasaarela, X. Tu, T. Liow, M. Hiltunen, A. Tervonen, G. Lo, and S. Honkanen, “Low-loss silicon slot waveguides and couplers fabricated with optical lithography and atomic layer deposition,” *Optics Express*, vol. 19, no. 27, pp. 26 275–26 282, 2011.

[71] W.-P. Huang, “Coupled-mode theory for optical waveguides: an overview,” *JOSA A*, vol. 11, no. 3, pp. 963–983, 1994.

[72] S. Ghadirli, K. Thyagarajan, and A. Kumar, “Band stop filter characteristics of non identical waveguides directional couplers; a comparison of three methods,” *Optics Communications*, vol. 84, no. 3-4, pp. 144–148, 1991.

[73] W. Bogaerts, P. De Heyn, T. Van Vaerenbergh, K. De Vos, S. Kumar Selvaraja, T. Claes, P. Dumon, P. Bienstman, D. Van Thourhout, and R. Baets, “Silicon microring resonators,” *Laser & Photonics Reviews*, vol. 6, no. 1, pp. 47–73, 2012.

[74] V. Passaro and M. La Notte, “Optimizing SOI slot waveguide fabrication tolerances and strip-slot coupling for very efficient optical sensing,” *Sensors*, vol. 12, no. 3, pp. 2436–2455, 2012.

[75] M. Häyrinen, M. Roussey, A. Säynätjoki, M. Kuittinen, and S. Honkanen, “Titanium dioxide slot waveguides for visible wavelengths,” *Applied Optics*, vol. 54, no. 10, pp. 2653–2657, 2015.

[76] R. Sun, P. Dong, N.-n. Feng, C.-y. Hong, J. Michel, M. Lipson, and L. Kimerling, “Horizontal single and multiple slot waveguides: optical transmission at λ=1550 nm,” *Optics Express*, vol. 15, no. 26, pp. 17 967–17 972, 2007.

[77] A. Khanna, A. Säynätjoki, A. Tervonen, and S. Honkanen, “Control of optical mode properties in cross-slot waveguides,” *Applied Optics*, vol. 48, no. 34, pp. 6547–6552, 2009.

[78] S. Zhu, G. Lo, and D. Kwong, “Low-loss amorphous silicon wire waveguide for integrated photonics: effect of fabrication process and the thermal stability,” *Optics Express*, vol. 18, no. 24, pp. 25 283–25 291, 2010.

[79] J. Matres, G. Ballesteros, P. Gautier, J. Fédéli, J. Martí, and C. Oton, “High nonlinear figure-of-merit amorphous silicon waveguides,” *Optics Express*, vol. 21, no. 4, pp. 3932–3940, 2013.

[80] D. J. Moss, R. Morandotti, A. L. Gaeta, and M. Lipson, “New CMOS-compatible platforms based on silicon nitride and Hydex for nonlinear optics,” *Nature Photonics*, vol. 7, no. 8, pp. 597–607, 2013.

CHAPTER 3

Non-concentric Microring Resonators

This chapter focuses on the linear characteristics of another important integrated photonic component, microring resonator (MRR). We have developed the theory of a non-concentric/off-axis MRR with single and multiple off-axis rings. The off-axis inner ring introduces high-quality (Q) tunable extra notches with many striking features in the transmission spectrum which facilitates its use as efficient modulators and sensors. A few such notches when closely packed have been used to design a compact band rejection filter with improved bandwidth ($> 10\,\mathrm{nm}$). In the next portion, we demonstrate the performance of silicon-on-insulator (SOI) off-axis MRR as electro-optic modulator (EOM). Adding an extra off-axis inner-ring to the conventional microring structure provides control to compensate thermal effects on EOM. It is shown that dynamically controlled bias-voltage applied to the outer ring has the potency to quell the thermal effects over a wide range of temperature. In the final section, we propose a non-concentric nested (NN) MRR configuration that relaxes the stringent requirement of the critical coupling condition by 20%. Numerical simulations reveal that unlike conventional MRRs, NN-MRRs maintain a high Q-factor ($> 10^5$) and a large transmission notch-depth $> 10\,\mathrm{dB}$, irrespective of rings' coupling conditions. We also corroborate our numerical findings, exper-

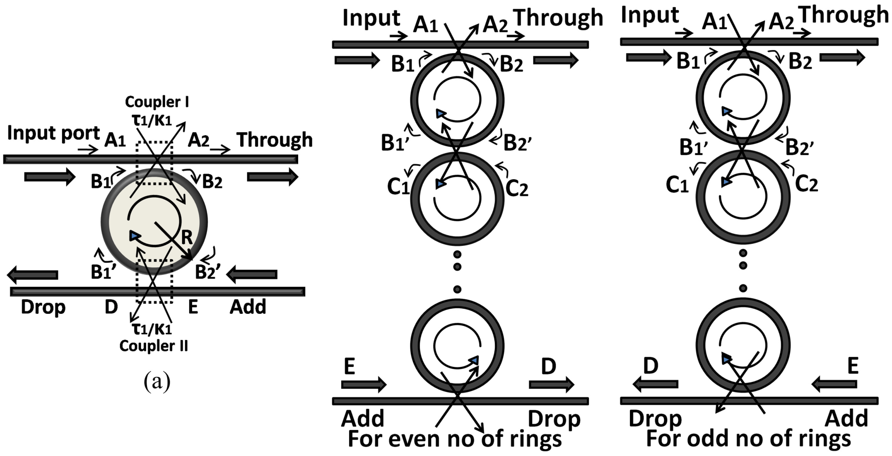

(a) (b) (c)

Figure 3.1: (a) Schematic of a conventional MRR with two linear waveguides. Basic topology of serially coupled MRRs with (b) odd, and (c) even number of rings with two parallel buses.

imentally. The biggest appealing feature of the proposed non-concentric MRR structure is the compactness. We believe that the off-axis/NN-MRR arrangement will be highly efficient for bio-sensing, nonlinear and quantum applications within a broad ambient temperature range. [1]

3.1 Off-axis MRR: Theory and Applications

Microring resonator, a simple albeit essential integrated photonic component, finds potpourri of applications from optical switching, signal processing, data routing, optical communication, amplification, sensing, nonlinear frequency conversions to quantum optics [1–17]. If multiple frequencies are sent into an MRR, it resonates only with the waves of particular frequencies, satisfying the phase matching condition, i.e. the ring perimeter becomes exactly equal to the integral multiple of the effective optical wavelengths. The MRR passes other frequencies which are not resonant via 'through' port. Such characteristic can be used to build add-drop filter using MRRs [3, 5]. A single MRR has spectral response similar to an optical notch filter. Systematic theory to understand the working principle of an MRR has already been established by several researchers [1–3], which has been

---

[1] Publications related to this chapter are [18], [49], [50].

further extended to cascaded MRRs either in serial or parallel configurations. The cascaded MRR have been employed to construct band-pass or band-rejection filters. However, such configurations show several drawbacks such as, large device size, high sensitivity to the fabrication errors, presence of several ripples either in pass band or in rejection band, signal degradation, slow response, and dispersion. To overcome most of the drawbacks of the conventional MRR, off-axis MRR configuration has been proposed. In support of the proposal, we derive a complete theory to characterize MRRs with a single and multiple off-axis inner rings. The off-axis MRR generates extra resonant notches in the transmission spectrum which are attributed due to an extra phase matching between outer ring and the inner off-axis ring. This feature has been utilized to build compact band pass or band rejection filters with improved bandwidth and faster response. Transfer matrix method (TMM) is used to analyze the off-axis MRR. We have also used the finite-difference time-domain (FDTD) method to validate our simulation results. A close agreement is observed between these two.

3.1.1 Transfer Matrix Method

In this section, TMM is discussed to analyze the transmission characteristics of a conventional MRR of radius R with two linear waveguides as depicted in Fig. 3.1 (a). Direction of the light-propagation is also shown by the arrows. The light wave is launched from the input-port through the linear waveguide. The evanescent field of the input wave couples to the ring through coupler-I, as shown by the dotted box in Fig. 3.1 (a). The evanescent optical field excites the whispering gallery mode in the microring. To drop a signal from the ring, another linear waveguide is placed in parallel to the input bus. Light can couple to the second linear bus and exit through the drop port. A_1 and B_1 are the amplitudes of input waves at input port and in the ring at coupler-I, whereas A_2 and B_2 are the amplitudes of the output waves at through port and in the ring, respectively. An evanescent wave, which is coupled to the ring, propagates in clockwise direction as displayed in Fig. 3.1 (a). The input wave amplitudes to the coupler-II are ${B_2}'$ and E (add-port), whereas the output wave amplitudes are ${B_1}'$ and D at drop port. The light wave with amplitude A_2 and D appear at through and drop ports, respectively with corresponding phase delays. Using TMM [18], one can write,

$$\begin{bmatrix} A_2 \\ B_2 \end{bmatrix} = \begin{bmatrix} \tau_1 & i\kappa_1 \\ i\kappa_1 & \tau_1 \end{bmatrix} \begin{bmatrix} A_1 \\ B_1 \end{bmatrix} \tag{3.1}$$

where the coupling and transmission coefficients of the coupler-I are κ_1 and τ_1, respectively. For lossless couplers, $|\tau_1|^2 + |\kappa_1|^2 = 1$. After rearranging, Eq. 3.1 can conversely be written as,

$$\begin{bmatrix} A_1 \\ A_2 \end{bmatrix} = \frac{1}{i\kappa_1} \begin{bmatrix} -\tau_1 & 1 \\ -1 & \tau_1 \end{bmatrix} \begin{bmatrix} B_1 \\ B_2 \end{bmatrix} = L \begin{bmatrix} B_1 \\ B_2 \end{bmatrix} \tag{3.2}$$

If the dimensionless round-trip loss factor that includes the coupling, bending, radiation and all the other types of losses is α_1, then

$$\begin{bmatrix} {B_1}' \\ {B_2}' \end{bmatrix} = \begin{bmatrix} \frac{1}{\sqrt{\alpha_1}} e^{i\phi_1} & 0 \\ 0 & \sqrt{\alpha_1} e^{-i\phi_1} \end{bmatrix} \begin{bmatrix} B_1 \\ B_2 \end{bmatrix} = P \begin{bmatrix} B_1 \\ B_2 \end{bmatrix} \tag{3.3}$$

P is the propagation matrix. ϕ_1 is the phase difference due to the path difference $l\,(= \pi R)$ between output of coupler-I and the input of the coupler-II and also is equivalent to the half round-trip phase in the MRR. If β is the propagation constant and n_{eff1} is the effective refractive index (RI) of the guided mode, the phase delay is given by,

$$\phi_1 = \beta l = \frac{2\pi^2 n_{\text{eff1}} R f}{c} = \frac{2\pi^2 n_{\text{eff1}} R}{\lambda} \tag{3.4}$$

Similarly,

$$\begin{bmatrix} D \\ E \end{bmatrix} = \frac{1}{i\kappa_1} \begin{bmatrix} \tau_1 & -1 \\ 1 & -\tau_1 \end{bmatrix} \begin{bmatrix} {B_1}' \\ {B_2}' \end{bmatrix} = L' \begin{bmatrix} {B_1}' \\ {B_2}' \end{bmatrix} \tag{3.5}$$

Using Eqs. 3.2, 3.3 and 3.5, we can relate the amplitudes at input port (A_1), through port (A_2), drop port (D) and add port (E) via coupling and propagation matrices as expressed in Eq. 3.6,

$$\begin{bmatrix} A_1 \\ A_2 \end{bmatrix} = LP^{-1}L'^{-1} \begin{bmatrix} D \\ E \end{bmatrix} = M \begin{bmatrix} D \\ E \end{bmatrix} = \begin{bmatrix} M_{11} & M_{12} \\ M_{21} & M_{22} \end{bmatrix} \begin{bmatrix} D \\ E \end{bmatrix} \tag{3.6}$$

In absence of any signal at the add port ($E = 0$), the normalized transmission at through port can be calculated in dB from $20\log_{10}(|\sigma_{\mathrm{th}}|)$, where,

$$\sigma_{\mathrm{th}} = A_2/A_1 = \left.\frac{M_{21}}{M_{11}}\right|_{E=0} \tag{3.7}$$

Higher-order filter response with improved pass-band characteristics and rejection ratio can be achieved by cascading the MRRs [5]. Series and parallel combinations of rings yield deeper notches with higher rejection ratio, wider rejection band and ultra-high Q-factor, compared to the single MRR. Coupled mode theory (CMT) in time domain is another powerful analytic tool to design a serially coupled band pass filter [1, 5, 17, 19]. In Fig. 3.1 (b) and 3.1 (c), basic configurations of serially coupled MRRs with odd and even number of rings are illustrated with two parallel bus lines. If the total number of rings in the structure is odd, then output signal is dropped from the same side of the input, while the output is measured from the opposite side for even number of rings as indicated by the arrows in Fig. 3.1 (b), and (c). Note that, serially coupled MRRs would possess larger device size to achieve desired spectral response and filter performance. If N numbers of rings are serially coupled then for odd value of i.e., $N = N_{\mathrm{odd}}$, general expression for transmission characteristics can be written as:

$$\begin{bmatrix} A_1 \\ A_2 \end{bmatrix} = L(\psi_1\psi_2)^{\frac{N_{\mathrm{odd}}-1}{2}}\psi_1 \begin{bmatrix} D \\ E \end{bmatrix} = M_{\mathrm{odd}} \begin{bmatrix} D \\ E \end{bmatrix} \tag{3.8}$$

and instead, if N is even, i.e. $N = N_{\mathrm{even}}$, then the expression is given by,

$$\begin{bmatrix} A_1 \\ A_2 \end{bmatrix} = L(\psi_1\psi_2)^{\frac{N_{\mathrm{even}}}{2}} \begin{bmatrix} E \\ D \end{bmatrix} = M_{\mathrm{even}} \begin{bmatrix} E \\ D \end{bmatrix} \tag{3.9}$$

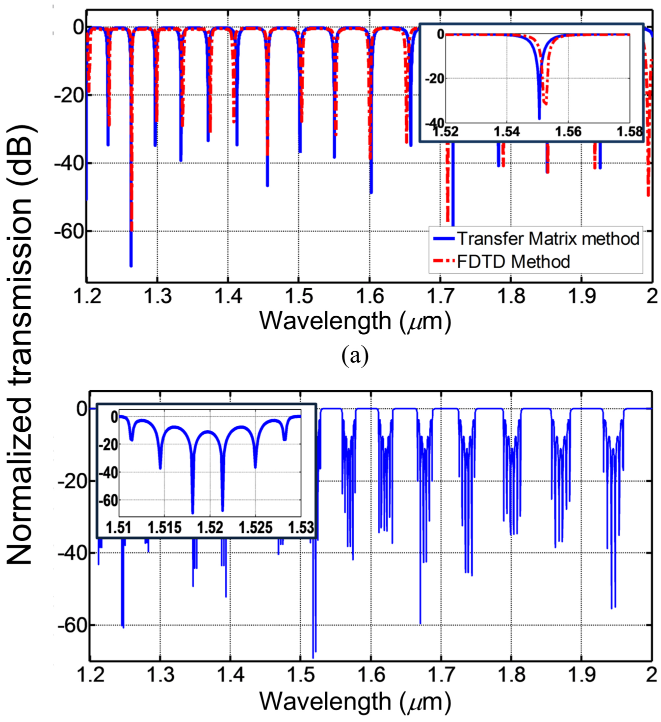

(a)

(b)

Figure 3.2: Transmission characteristics of (a) single MRR (TMM and FDTD), (b) six identical serially coupled rings with $R = 3\,\mu$m. All gaps (ring-ring/bus) are set to 100 nm.

where the ψ_1 and ψ_2 are as follow,

$$\begin{aligned} \psi_1 &= P^{-1}L'^{-1} \\ \psi_2 &= PL^{-1} \end{aligned} \tag{3.10}$$

The transmission characteristics is found from the Eq. 3.7. We have simulated a single MRR (both TMM and FDTD) and a serially coupled microring (TMM) structure with six identical rings of radius $R = 3\,\mu$m each, as shown in Fig 3.1. Each waveguide dimension is 400 nm×350 nm. The gap between the waveguide and the ring or in between two adjacent rings is 100 nm. Silicon and silica are chosen as key materials for guiding and substrate, respectively. The transmission characteristics for single MRR and serially coupled MRRs are shown in Fig. 3.2 (a), and Fig. 3.2 (b), respectively. It is evident that five $(N-1)$ resonant dips/notches are created by six (N) microrings in series connection.

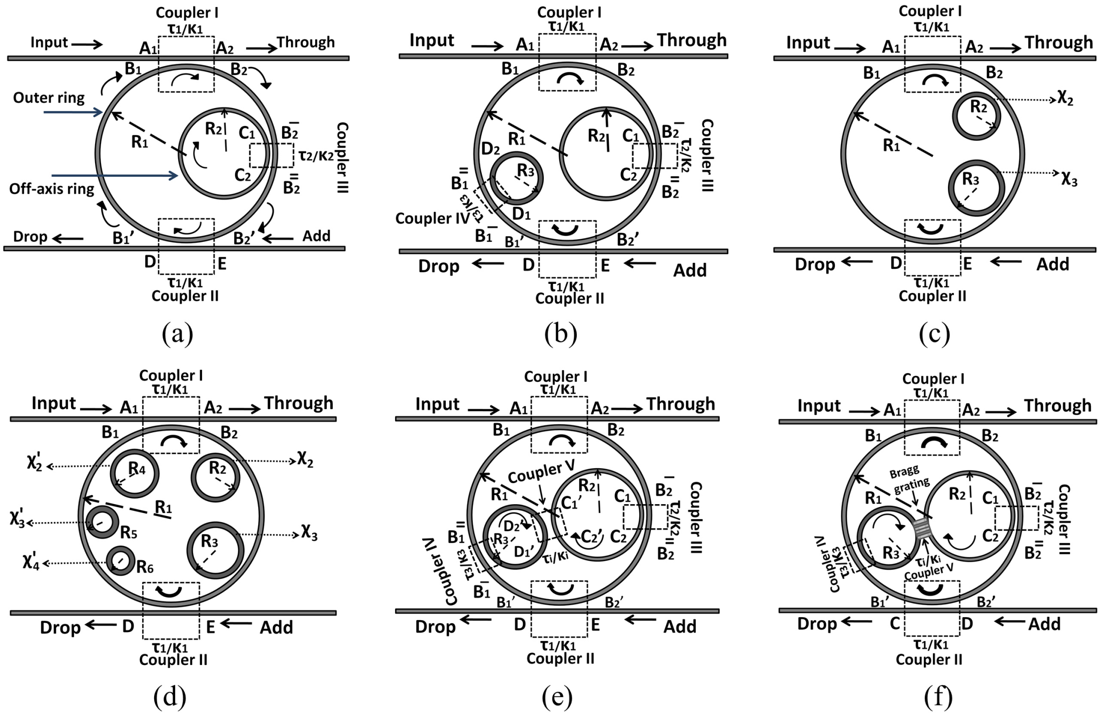

Figure 3.3: (a) Schematic of an off-axis MRR with parallel bus lines. The coupling regions are shown by the dotted boxes. Off-axis MRR with (b)–(f) various configurations.

3.1.2 Theory of Off-axis MRR

A concrete theory to describe MRR with single and multiple off-axis inner rings have been developed in this section. The structure is simulated by TMM and compared to the results obtained from FDTD method. Inner rings can be either concentric or off-axis. Concentric MRR configuration has been proposed (analyzed through CMT in time) and demonstrated (in SOI platform) by Zhang *et al.* in 2008 [20]. The primary difference between a concentric inner ring and an off-axis inner ring is the geometry. The center of off-axis circular ring does not overlap with the center of the outer ring as seen in the schematic of an off-axis MRR (Fig. 3.3 (a)), where R_1 and R_2 ($\ni R_1 > R_2$) are the radii of the outer and the inner rings, respectively. Variety of other MRR configurations with single and multiple non-concentric inner rings are also shown in Fig. 3.3 (b)–(f). From the geometry of off-axis MRR (Fig. 3.3 (a)), it can be seen that there are three coupling regions through which light can couple. τ_2 and κ_2 are the transmission and the coupling coefficients of the additional coupler (coupler-III) appears in Fig. 3.3 (a), respectively. In our calculations, we assume that the incoming wave amplitudes are A_1, B_1 at coupler-I, ${B_2}'$, E at coupler-II and C_1, ${B_2}^-$ at coupler III and the outgoing wave amplitudes are A_2, B_2 at coupler I, D, ${B_1}'$ at coupler-II, C_2, ${B_2}^=$ at coupler-III, and it is assumed that coupler-I and II are identical. Therefore, from TMM we obtain [18],

$$\begin{bmatrix} A_2 \\ B_2 \end{bmatrix} = \begin{bmatrix} \tau_1 & i\kappa_1 \\ i\kappa_1 & \tau_1 \end{bmatrix} \begin{bmatrix} A_1 \\ B_1 \end{bmatrix} \tag{3.11a}$$

$$\begin{bmatrix} D \\ {B_1}' \end{bmatrix} = \begin{bmatrix} \tau_1 & i\kappa_1 \\ i\kappa_1 & \tau_1 \end{bmatrix} \begin{bmatrix} E \\ {B_2}' \end{bmatrix} \tag{3.11b}$$

$$\begin{bmatrix} B_2^= \\ C_2 \end{bmatrix} = \begin{bmatrix} \tau_2 & i\kappa_2 \\ i\kappa_2 & \tau_2 \end{bmatrix} \begin{bmatrix} B_2^- \\ C_1 \end{bmatrix} \tag{3.11c}$$

If α_1 and α_2 denote the round-trip dimensionless loss-factors of the outer and the inner rings, respectively, then the modified propagation matrix P' can be given by,

$$P' = \begin{bmatrix} \frac{1}{\sqrt{\alpha_1}} e^{i\phi_1} & 0 \\ 0 & \sqrt{\alpha_1} e^{-i\phi_1} \chi_2 \end{bmatrix} \tag{3.12}$$

where, the term χ_2 includes the effect of the inner off-axis (2nd ring) microring,

$$\chi_2 = \frac{B_2^=}{B_2^-} = \left[\tau_2 + \alpha_2 (i\kappa_2)^2 \left(e^{i\phi_2} - \alpha_2 \tau_2 \right)^{-1} \right] \tag{3.13}$$

Here, the ϕ_1 is the half round-trip phase evolution of the outer-ring with radius R_1 and is given by Eq. 3.4. The symbol R is replaced by R_1. ϕ_2 denotes the round-trip phase evolution in the inner ring of radius R_2, and is given by,

$$\phi_2 = \beta_2 l_2 = \frac{4\pi^2 n_{\text{eff2}} R_2 f}{c} = \frac{4\pi^2 n_{\text{eff2}} R_2}{\lambda} \tag{3.14}$$

where, n_{eff2} is the effective RI of the propagating mode in the inner ring. Rest of the Eqs. are similar to those of the single MRR case and the transmission char-

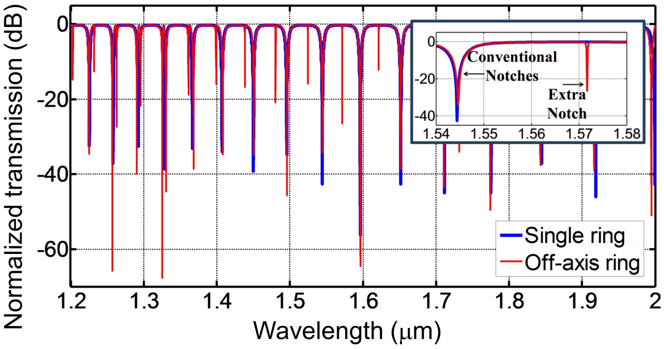

Figure 3.4: Comparison of transmission characteristics of a conventional MRR and an off-axis MRR. Simulation parameters: $n_{\mathrm{eff1}} = 1.8$, $n_{\mathrm{eff2}} = 2.4$, $R_1 = 3\,\mu\mathrm{m}$, $R_2 = 2\,\mu\mathrm{m}$, $W = 400\,\mathrm{nm}$, $H = 350\,\mathrm{nm}$, $\tau_1 = 0.8$, $\tau_2 = 0.9$. In practice, if both the MRR configurations are made of the same materials, then, $n_{\mathrm{eff1}} \lesssim n_{\mathrm{eff2}}$, and $\alpha_2 \lesssim \alpha_1 \approx 1$, due to the bending.

acteristics found from Eq. 3.7 is plotted in Fig. 3.4 (red curve) and is compared with the transmission spectra of a conventional MRR (blue curve). Off-axis MRRs are able to create extra resonant notches. These extra notches appear in between the existing notches of conventional MRR, which is a distinctive feature of the off-axis MRR. It is observed that the extra resonant dips appearing in the transmission generally possess a larger Q-factor in comparison with the conventional notches. Such resonances can be compared to the 'Fano resonances' those appear in mutually coupled asymmetric resonating systems [21].

3.1.2.1 MRR with Multiple Inner Rings

Multiple off-axis rings can be accommodated in the outer ring if the outer ring has large radius. In Fig. 3.3 (b)–3.3 (f), we show a few such examples. The inner rings can be placed either in diagonal positions (Fig. 3.3 (b)) or can be aligned to be on the same side (Fig. 3.3 (c)). More generic cases with closely-packed multiple inner rings are sketched in Fig. 3.3 (d). In case the radii of the inner rings are small enough, one can neglect the mutual coupling between them. Moreover, coupling due to counter propagating optical waves can be neglected unless there exists, for instance, a Bragg grating in the coupling regime between two closely spaced inner rings. This special case is shown in Fig. 3.3 (f). If there are M and N number of inner rings at the left and right-hand sides of the outermost ring, respectively, we

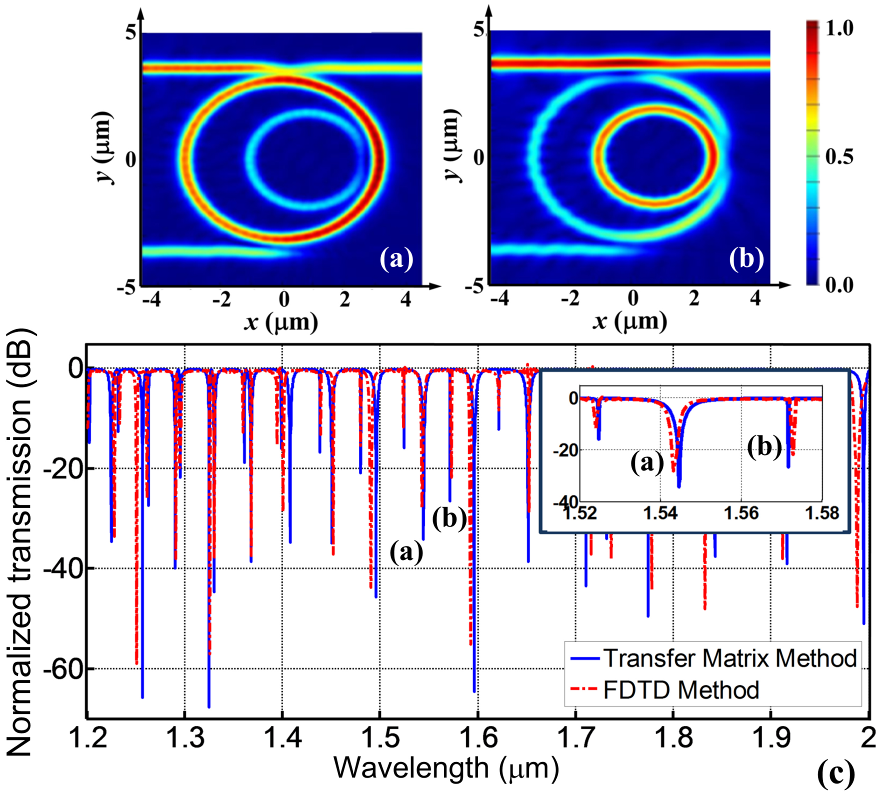

Figure 3.5: Snapshots of the normalized E-field distribution when resonance occurs in (a) the outer ring, and (b) the inner off-axis ring. (c) Normalized transmission (in dB) obtained from TMM and FDTD simulations where the resonant notches corresponding to the particular resonant modes are also indicated.

can write a general expression for the propagation matrix (P'') as:

$$P'' = \begin{bmatrix} \frac{1}{\sqrt{\alpha_1}} e^{i\phi_1} {\chi_2'}^{-1} {\chi_3'}^{-1} \cdots {\chi_{\mathrm{M+1}}'}^{-1} & 0 \\ 0 & \sqrt{\alpha_1} e^{-i\phi_1} \chi_2 \chi_3 \cdots \chi_{\mathrm{N+1}} \end{bmatrix} \tag{3.15}$$

where, χ_{i}, and χ_{i}' represent the contributions of the $(i-1)$-th inner rings located at the right-hand side and the left-hand side of the outer ring, respectively.

$$\chi_{\mathrm{i}},\, \chi_{\mathrm{i}}' = \left[\tau_{\mathrm{i}} + \alpha_{\mathrm{i}} (i\kappa_{\mathrm{i}})^2 (e^{i\phi_{\mathrm{i}}} - \alpha_{\mathrm{i}}\tau_{\mathrm{i}})^{-1}\right] \tag{3.16}$$

Special case where there is a Bragg grating in between two inner coupled rings is also examined in detail [18].

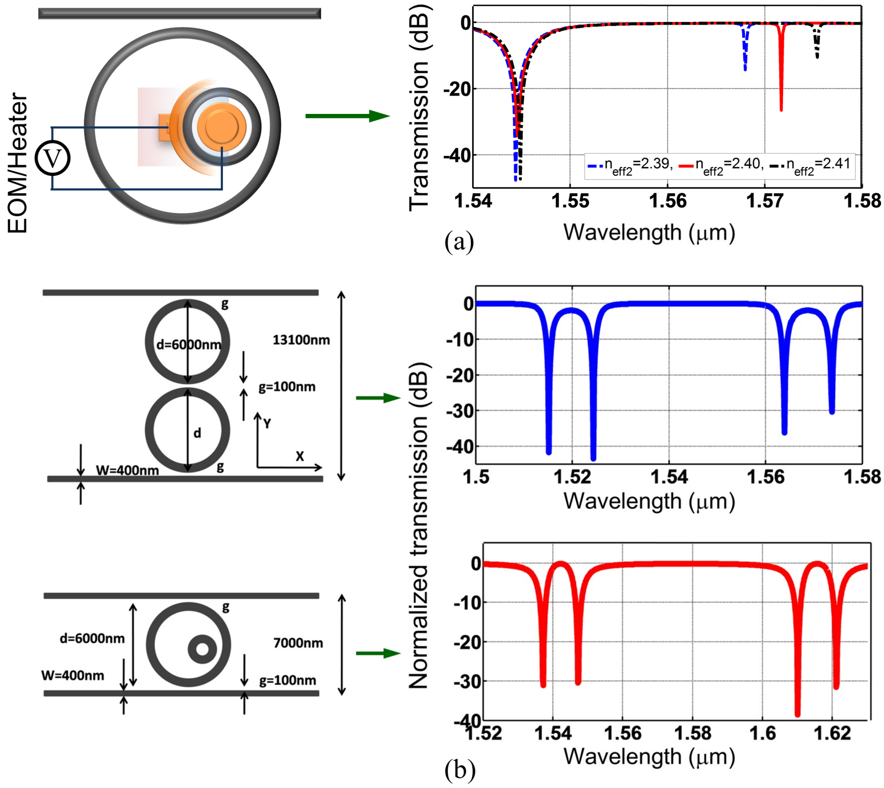

Figure 3.6: (a) Tunability of the off-axis MRR, (b) Design of compact devices through off-axis MRR.

3.1.2.2 Tunability and Compactness

The extra notches engendered due to the presence of the inner rings can be tuned thermo/electro-optically to reject arbitrarily chosen single or multiple wavelength-division multiplexing (WDM) channels [18] (Fig. 3.6 (a)). We observe that a small change in n_{eff2} reflects in a considerably large deviation ($d\lambda/dn_{\text{eff2}} \sim 0.37\,\mu$m) of the high-$Q$ extra notches those have been instigated by the inner off-axis ring. Nevertheless, the shift in conventional notch is negligible ($d\lambda/dn_{\text{eff2}} \sim 0.025\,\mu$m). This property can be used to design efficient bio-chemical/temperature sensors. In the next section, the tunability feature of non-concentric MRR is being exploited to design thermally insensitive EOM.

Wide-band compact photonic band-rejection filter can be achieved using serially coupled MRRs with very small ring radii. The free-spectral range (FSR) can be enhanced by the Vernier effect [2]. However, fabrication complexity, dispersion

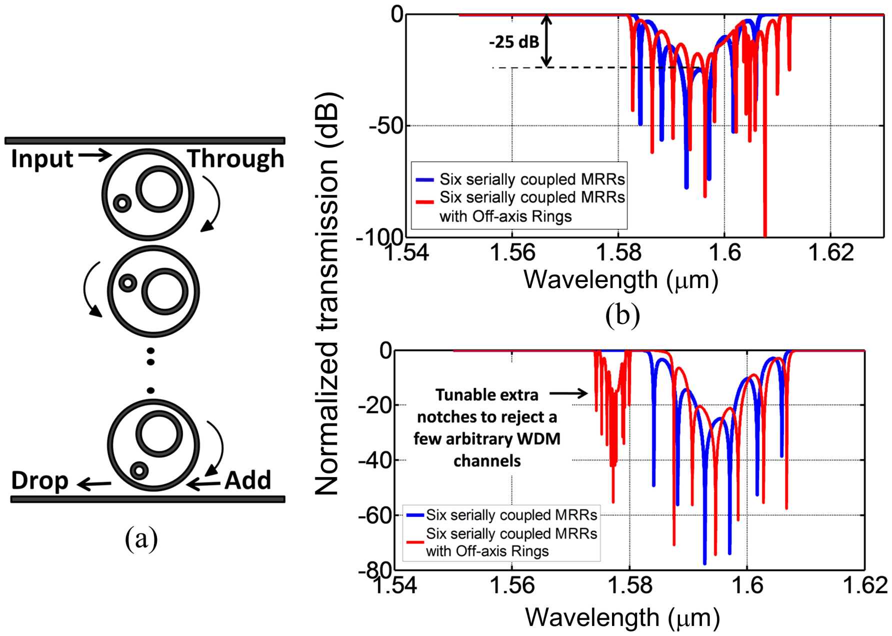

(a)

(b)

(c)

Figure 3.7: (a) Proposed serially coupled off-axis MRRs with two inner rings in each outer ring. (b) Normalized transmission of the proposed structure with optimized coupling efficiencies between bus to ring and ring to ring to enhance the notch depth. (c) Closely packed extra resonant notches are tunable and are able to reject arbitrarily chosen WDM channels.

effect and the bending loss increase with smaller bending radius of ring structure. The issues associated with very small serially coupled rings to attain band-pass or band-rejection filter can be overcome by utilizing non-concentric MRRs. we propose a new design based on off-axis ring that would enhance the rejection band, and at the same time it will occupy less space than the conventional one. Tunable extra-notches of the off-axis MRRs can be employed to build a band-rejection filter with improved bandwidth. Fig. 3.6 (b) presents a comparative study between the transmission characteristics of two serially-coupled concentional MRRs and a single off-axis MRR. It is shown that a similar spectral response compared to the conventional MRR can be achieved by using the off-axis MRR, however, the device footprint shrinks to 7 μm from 13 μm i.e., almost half of the conventional (serial) architecture, which definitely is a significant reduction in device-size. Therefore, serially coupled off-axis MRRs as shown in Fig. 3.7 is expected to yield a broadband band-rejection filter within a very small device extent. We adopt the strategy and optimize six serially coupled MRRs each having two non-concentric inner rings in it and finally, able to enhance the bandwidth of the band-rejection filter by >10–12 nm. The extra-notches are easily tunable and therefore, can flexibly eliminate unwanted noise or undesired channels as per the requirement of a WDM-link (Fig. 3.7). We believe the proposed structure is highly beneficial for integrated on-chip optical communication networks.

3.2 Athermal Electro-optic Modulators

It is well-known that, parasitic capacitance between the electronic components and the drift velocity of electron limits the speed of electronic circuits. The delay at the metallic interconnects forces asynchronous data transfer between the processor and the other parts of a computational system and consequently creates an important bottleneck problem [22–24]. Photonic interconnects have the ability to address this issue [25, 26]. Low power consumption, low latencies, less interference, ultra compact size and wide bandwidth are the key advantages of optical circuits [27]. Such key benefits have engendered interest among scientists to find out an efficient design of EOM, which is an indispensable active optical component of photonic circuits [7]. Recent advancements in SOI technology [28, 29] has opened up a new window for the fabrication of micro optical devices with microelectronics on chip [8]. Nonetheless, to design a compact, high-speed EOM is still a big challenge due to the absence of Pockel's effect, very low Franz-Keldysh and moderate Kerr effect of pure crystalline Si [7]. Carrier plasma dispersion (CPD) effect of Si is the only effective way to achieve a considerable amount of RI variation by applying moderate external electromagnetic field avoiding the breakdown of Si-device. Soref *et al.* have predicted the change in RI (Δn) and absorption coefficient ($\Delta\alpha$) of Si due to the CPD effect [30]. Carrier dispersion and absorption [7] at $\lambda = 1.55\,\mu$m are approximated by Eqs. 3.17 (a) and 3.17 (b),

$$\Delta n = \Delta n_{\mathrm{e}} + \Delta n_{\mathrm{h}} = -\left[8.8 \times 10^{-22}\Delta N + 8.5 \times 10^{-18}\,(\Delta P)^{0.8}\right] \tag{3.17a}$$

$$\Delta\alpha = \Delta\alpha_{\mathrm{e}} + \Delta\alpha_{\mathrm{h}} = \left[8.5 \times 10^{-18}\Delta N + 6 \times 10^{-18}\Delta P\right] \tag{3.17b}$$

Δn_{e} and $\Delta\alpha_{\mathrm{e}}$ (cm^{-1}) are the changes in RI and absorption coefficient variation due to the electron concentration change ΔN (cm^{-3}), Δn_{h} and $\Delta\alpha_{\mathrm{h}}$ (cm^{-1}) are the RI change and absorption coefficient variation due to the change in hole concentration ΔP (cm^{-3}), respectively. According to the previous results [7], a carrier depletion/injection of $\sim 10^{18}\,\mathrm{cm}^{-3}$ can yield a RI change $\Delta n \sim 2 \times 10^{-3}$. A modulating device typically of the order of few millimetres is capable to provide a high modulation with extinction ratio (ER) as high as 20 dB with sufficient variation of RI [7] until the development of resonator based SOI-EOM. Microring confines light within the ring cavity and can provide relatively longer path length without increasing the device size. A small change in RI can detune an MRR and yields a very high modulation-depth [7]. One of the critical issues of network-on-chip is to keep power budgets manageable while increasing performance. Dense WDM (DWDM) is one such solution which offers massive parallelism and is considered very important in order to realize high performance optical interconnects which can be achieved through MRRs. However, Si has high thermo-optic coefficient [31] (TOC $= \Delta n/\Delta T$), $\sim 1.86 \times 10^{-4}/\,\mathrm{K}$. Small amount of change in RI results drastic variation in transmission characteristics of SOI based MRR due to its large Q-factor and narrow bandwidth [32]. MRRs are highly susceptible to the thermal fluctuations. Heat generated from the surroundings, off-chip continuous-wave laser sources, local hot-spots etc. can cause shift in resonance wavelength, as shown in Fig. 3.8. Without the thermal effect, EOM can produce exact sinusoidal replica of the input, whereas, thermal instability can deform the output signal or disturb precise channel allocations for DWDM systems (Fig. 3.8). The shift in resonant wavelength can be represented as [32],

$$\frac{d\lambda}{dT} = \left(n_{\mathrm{eff}}\alpha_{\mathrm{clad}} + n_{\mathrm{eff}}\alpha_{\mathrm{sub}} + \frac{\partial n_{\mathrm{eff}}}{\partial T}\right)\frac{\lambda_0}{n_{\mathrm{g}}} \approx \frac{\partial n_{\mathrm{eff}}}{\partial T}\frac{\lambda_0}{n_{\mathrm{g}}} \tag{3.18a}$$

$$\frac{\partial n_{\mathrm{eff}}}{\partial T} = \Gamma_{\mathrm{core}}\frac{\partial n_{\mathrm{core}}}{\partial T} + \Gamma_{\mathrm{clad}}\frac{\partial n_{\mathrm{clad}}}{\partial T} + \Gamma_{\mathrm{sub}}\frac{\partial n_{\mathrm{sub}}}{\partial T} \tag{3.18b}$$

where λ_o is the resonant wavelength at the room temperature. n_{eff} denotes the effective RI and n_{g} is the group index. The cladding and substrate expansion coefficients are α_{clad} and α_{sub}, respectively. Both the α_{clad} and α_{sub} can be neglected in Eq. 3.18 (a) for air-clad and $\mathrm{SiO_2}$-substrate [32]. The change of effective RI

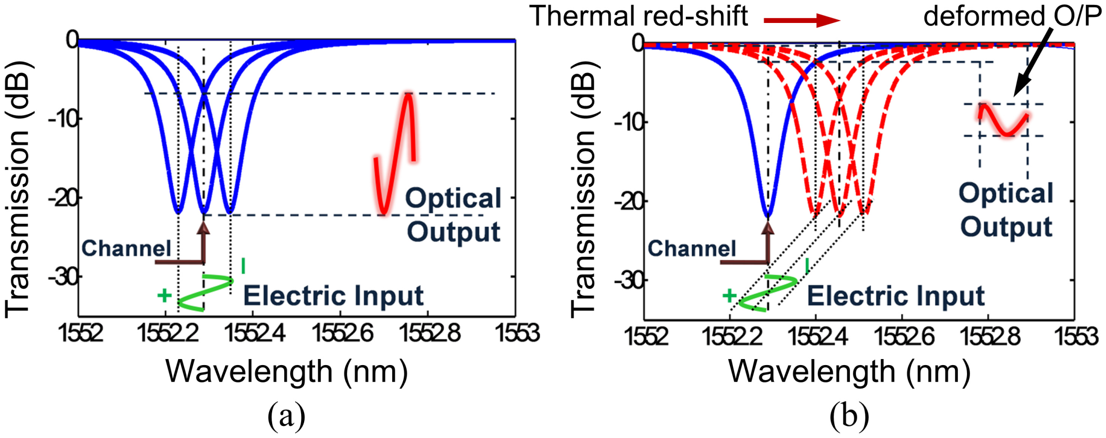

Figure 3.8: Working principle of EOM, (a) EOM without thermal effect, (b) deformed sinusoidal output in presence of thermal effect.

with the temperature is given by Eq. 3.18 (b) where Γ is the modal confinement factor. In recent years, a few attempts were made to build athermal EOMs. A detailed comparative study on these approaches has been discussed in [32]. Methods to compensate the thermal effects can be broadly classified in two major categories—(i) athermal, and (ii) control-based solutions. One of the most well-known control-based solution procedures to combat thermal degradation is the use of heat sink and integrated heater simultaneously [33–35] which later on has been proved highly power-inefficient [36]. Padmaraju *et al.* proposed an adaptive, innovative and dynamic athermal design exploiting the heating effect of current [36], which is more effective to deliver/extract heat using an external bias, albeit, this bias voltage can affect the message signal. This approach also fails to compensate wide range of temperature change. Moreover, it is not suitable for high data-rate due to its large response delay and inability to use pre-emphasized [37] input signal. Parallel efforts (athermal solution) to neutralize the thermal effect using negative temperature coefficient materials e.g. polymers [38–40] as the key component of the device cladding also exist. To overcome the thermal effects, one must produce a zero effective TOC. Since the TOC of Si is very high, according to Eq. 3.18 (b) either we need a polymer with very high negative TOC or the mode confinement factor of the core must be deliberately reduced. Mode confinement can be reduced using narrow-ridged or slotted waveguides but these structures associate with high losses, greater radiation, lower Q-factor, small and corrupted FSR. The weak confinement of the mode also leads to higher device footprint. Furthermore, this method is not a successful commercial solution till date because of the CMOS-incompatibility of these polymers. CMOS compatible titanium oxide (TiO_2) with negative TOC [41] may be a possible future solution which allows moderate optical confinement in Si-core. Still the performance of these devices is not satisfactory due to low Q-factor and low FSR. Temperature independent operation over a small range has been shown employing MZI-coupled MRRs [42] and multiple cavity coupled devices [43]. However, relatively large footprints make them ineffectual for high-density on-chip applications. Adiabatic microdisk/microring modulators and cascaded MRRs [44, 45] are capable of operating at as high data rate as 40 Gbps and provide uncorrupted FSR but these devices are also very susceptible to the change in ambient temperature. Recently, resonant mode-splitting method to negate the temperature effect has been reported [46]. Though, this method has potential to eliminate most of the previously mentioned drawbacks, it possesses a few serious disadvantages. Negative TOC CMOS incompatible polymers have been used to achieve satisfactory performance. Device size is large and it is impossible to implement this device in DWDM system due to its inability of using broad range of adjacent channels during the operation. It is also cumbersome to define and retain the material properties intact throughout the entire operational range. The inefficacy of all the aforementioned mechanisms motivate us to propose a novel design of EOM using off-axis MRR.

Previous section has revealed many striking features of MRR with inner off-axis ring [18]. The tunability aspects of conventional and extra resonant notches usher us the way to obtain a highly efficient and compact EOM. Two rings within the same structure provide us an extra degree of freedom of designing; we use one ring to deliver message and another to minimize the thermal effects. According to [32], our method falls in control-based solutions to avoid thermal degradation. Thus, besides the appositely biased conventional microring, off-axis inner microring with pre-emphasized electrical input message signal enables our proposed structure suitable for high data-rate DWDM scheme of optical communication systems within a very compact device size. In this work, device parameters are extracted from commercial TCAD electro-optic device simulator based on FDTD-

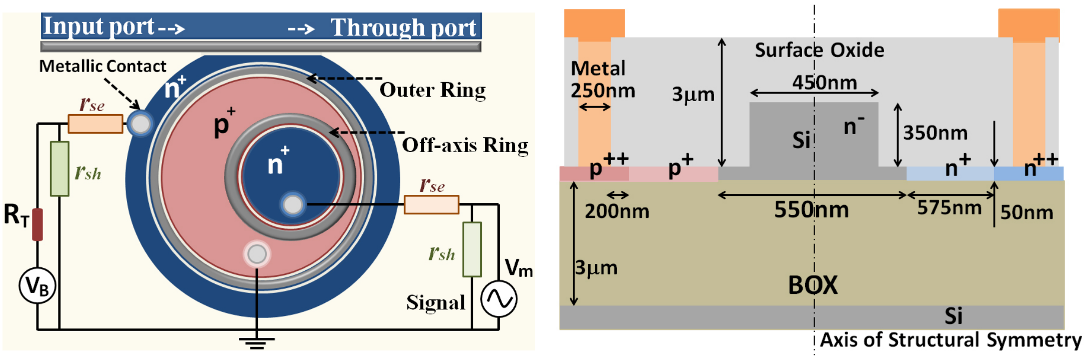

(a)

(b)

Figure 3.9: (a) Schematic of MRR with off-axis inner ring structure used as a modulator; r_{sh}, r_{se} and R_{T} represent the shunt, series and temperature dependent equivalent resistances of the device, V_{m} and V_{B} are voltage sources. (b) Cross-section of $\mathrm{p^+n^-n^+}$ SOI waveguide structure.

Gummel solver. RI variations due to carrier injection or depletion are calculated from mode solver. Other necessary design parameters are calculated from TMM and verified by FDTD method.

3.2.1 Design of Off-axis MRR as an EOM

In Fig. 3.9 (a), it is depicted how an MRR with off-axis inner ring can be used as an EOM. One can apply a modulating signal, V_{m} as an input to the off-axis ring and another voltage source V_{B} to the outer MRR to nullify the thermal effect. Note that, V_{m} and V_{B} are interchangeable. Cross-sectional view of the waveguide is shown in Fig. 3.9 (b). A rib structure has been grown on buried oxide (BOX) layer. Waveguide with dimension of $450\,\mathrm{nm}\times350\,\mathrm{nm}$ is placed ontop a $50\,\mathrm{nm}$ thick plateau which provides electrical connections to the optical device. The junction volume is $3.48\times10^{-12}\,\mathrm{cm}^3$. We have created a $\mathrm{p^+n^-n^+}$ type structure. As the conductivity of pure Si is very low, $\mathrm{n^-}$ epitaxial layer with nominal carrier concentration $\sim10^{15}\,\mathrm{cm}^{-3}$ has been sandwiched between $\mathrm{p^+}$ and $\mathrm{n^+}$ regions to keep the carrier flow uninterrupted. Moreover, this denuded layer reduces the number of recombination centres which further prevents the alteration of diode current (RG current [47]) with the change in temperature. One must keep in mind that high doping concentration in $\mathrm{n^-}$ region will obtain a better RI sensitivity $(\Delta n/\Delta V)$ for the waveguide with respect to applied bias but it will increase the device loss due to higher absorption coefficient [7]. We optimize our structure to limit the absorption loss due to extra carrier injection within 20 dB/cm. Doping concentration of p^+ and n^+ layers are $\sim 10^{19}\,\mathrm{cm}^{-3}$; metallic contacts are made through n^{++} and p^{++} with doping concentration of $\sim 10^{20}\,\mathrm{cm}^{-3}$. The doping concentration of n^- layer is much lesser than the concentration of n^+ or p^+ layer. Basically, this layer acts as an intrinsic layer.

3.2.2 Theory, Results and Discussions

We have applied an 8-bit, 3 Gbps pre-emphasized non-return-to-zero (NRZ) signal, $V_\mathrm{m} = \pm 1\,\mathrm{V}$ ($V_\mathrm{p-p} = 2\,\mathrm{V}$) to the inner off-axis ring with an off-set dc bias of 1 V. The minority charge carriers diffuse from the junction to the terminal when a voltage is applied to the $p^+n^-n^+$ device (forward biasing). If n_p0 and p_n0 are the minority carrier concentrations at p and n sides at room temperature in thermal equilibrium, we can write the extra charge carrier density as the function of distance x [47, 48] from the depletion layer as,

$$\Delta N(x) = n_\mathrm{p0}\left[\exp\left(\frac{\mathrm{ev}}{\mathrm{kT}}\right) - 1\right]\exp\left(\frac{x_\mathrm{p}+x}{L_\mathrm{p}}\right) \tag{3.19a}$$

$$\Delta P(x) = p_\mathrm{n0}\left[\exp\left(\frac{\mathrm{ev}}{\mathrm{kT}}\right) - 1\right]\exp\left(\frac{x_\mathrm{n}+x}{L_\mathrm{n}}\right) \tag{3.19b}$$

where, x_n and x_p denote the depletion region widths at the n and p sides. L_n and L_p represent the diffusion lengths of electrons and holes, respectively. The L_p ($\sim 22\,\mu$m) and L_n ($\sim 35\,\mu$m) are greater than the depletion layer width (~ 640 nm) which assures moderate current flow through the device. Figure 3.10 (a) shows the schematic cross-section of an off-axis micro ring resonator with three coupling regions dictated by dashed rectangular boxes where R_1 and R_2 are the radii of outer and inner rings, respectively. In order to understand the behavior of the off-axis MRR, we compute the effective index of the guided mode by full-vectorial finite element method (FEM) solver. Effective RI of a particular quasi-TE mode for outer ring ($R_1 = 3\,\mu$m) n_eff1 and off-axis ring ($R_2 = 2\,\mu$m) i.e., n_eff2 have been determined by changing applied bias and are plotted in Fig. 3.10 (b), whereas the spectral variation of the effective RI of the quasi-TE mode for different ring

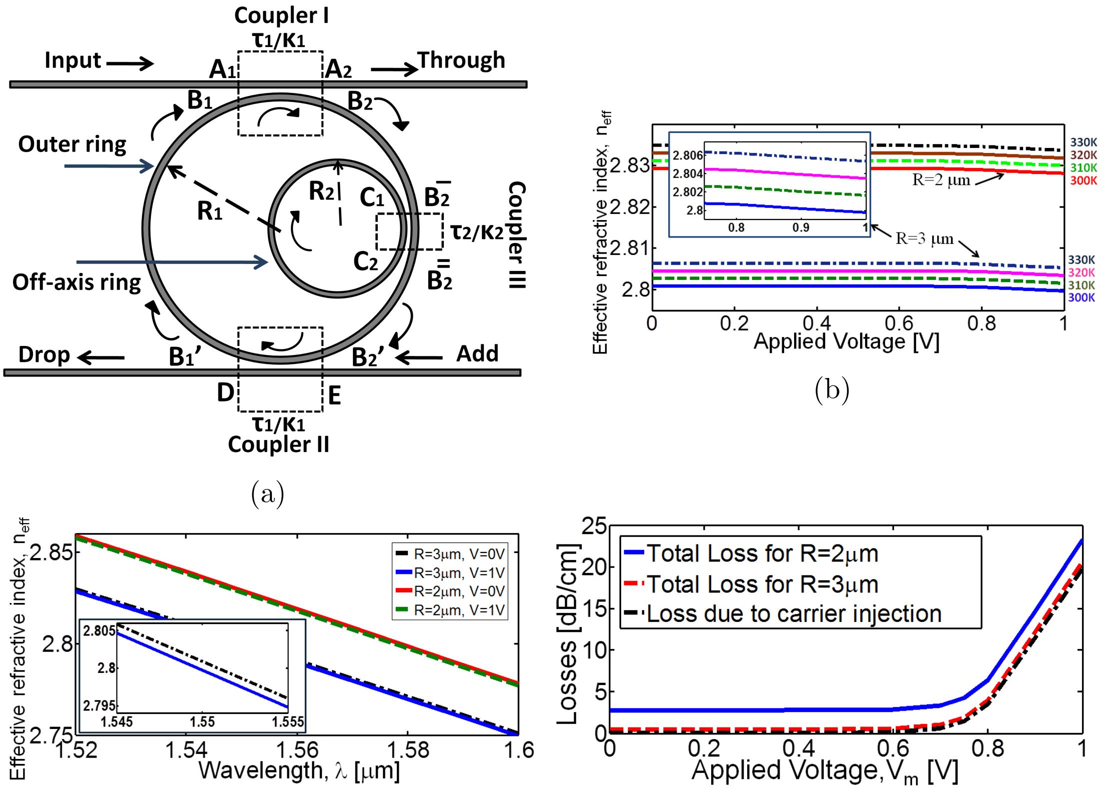

(a)

(b)

(c)

(d)

Figure 3.10: (a) Schematic of an off-axis MRR with necessary design parameters. (b) Effective RI variation of outer and inner rings with respect to bias voltage, V_{B} at 1.55 μm, (c) spectral variation of guided mode index for different ring radii at different biasing voltages, and (d) loss as a function of applied voltage V_{m}, at wavelength 1.55 μm.

radii and different biasing voltages is depicted in Fig. 3.10 (c). At wavelength 1.55 μm, the dispersion coefficient $D\,(=\partial n_{\mathrm{eff}}/\partial\lambda)$ for outer and inner rings are obtained as $-0.98965\,\mu\mathrm{m}^{-1}$ and $-1.0135\,\mu\mathrm{m}^{-1}$, respectively, when no voltage is applied and $-0.9897\,\mu\mathrm{m}^{-1}$ and $-1.01295\,\mu\mathrm{m}^{-1}$, respectively when an external bias of 1 V is applied across the $\mathrm{p}^{+}\mathrm{n}^{-}\mathrm{n}^{+}$ junction of outer and inner rings, respectively. Since we intend to implement the structure for several DWDM channels within a broad operating wavelength range. Dispersion effect is taken into consideration. The bending radius of the inner-ring is smaller than the outer ring, thereupon both the effective RI and the dispersion coefficient of the inner ring is slightly greater than the outer ring. The values of effective RIs and dispersion coefficients depend upon external bias. In Fig. 3.10 (d), we plot the total losses (absorption, bending, radiation etc.) as a function of applied voltage V_m. As discussed earlier, absorption losses have been restricted within 20 dB/cm. It is noticed that both absorption loss and effective RI change rapidly after $V_\mathrm{m} > 0.7\,\mathrm{V}$ (built-in potential of Si p-n junction). In this work, we have achieved $\Delta n = -1.163 \times 10^{-3}$ and $\Delta n = -1.179 \times 10^{-3}$ for outer and inner rings with an external bias voltage of 1 V when applied individually on outer and inner rings, respectively at $\lambda = 1.55\,\mu\mathrm{m}$. Propagation matrix for the non-concentric rings is found from Eq. 3.12. The change in ambient temperature of MRR affects the effective RI (n_eff1 and n_eff2) of outer and inner rings, modifying the transmission characteristics. Voltages applied at the individual rings change the RI of the respective rings only. Propagation matrix P' is a function of both $\phi_1\,(n_\mathrm{eff1})$ and $\phi_2\,(n_\mathrm{eff2})$. A positive voltage to the outer ring modifies the P' and blue shifts the conventional resonant notches as well as extra resonant notches. In this case, the shift in conventional resonant notches is larger in comparison to the extra notches. If we apply a positive voltage at the inner ring, blue-shift in extra notches will be greater than the blue-shift in conventional notches. It has been observed that the shift of extra resonant notches due to the change in n_eff1 is more than the shift of conventional resonant notches due to the change in n_eff2. These facts have been theoretically established and validated by FDTD method [18, 49, 50]. Mathematically, the phase matching conditions for the outer and the inner ring are given by [18], Eqs. 3.20 (a), and 3.20 (b), respectively.

$$\phi_1 = \frac{2\pi^2 n_\mathrm{eff1} R_1}{\lambda} = m\pi \tag{3.20a}$$

$$\phi_1 + \frac{{\kappa_2}^2 \sin(\phi_2)}{\tau_2\,(1+\tau_2) - \cos(\phi_2)\,(1+{\tau_2}^2)} = m\pi \tag{3.20b}$$

where $m = 1,\ 2,\ 3 \ldots$ Both ϕ_1 and ϕ_2 depend on n_eff1 and n_eff2, respectively. From Eq. 3.20 (b) it is viable that change in n_eff1 (due to the voltage applied to outer MRR) is capable for a slight shift in the extra resonant notches. On contrary, from Eq. 3.20 (a), it is conspicuous that change in n_eff2 (due to the voltage applied to the inner MRR) has ideally no effect on the conventional resonant notches. The details are tabulated in Table 3.1. This makes us confident to negate the thermal effects on MRR using an extra biasing voltage V_B at outer ring. The position of V_m and

Table 3.1: Applied voltage at outer and inner MRRs and corresponding resonant notch shifts.

Positive voltage applied to	**RI Change**	**Major blue shift in**	**Minor blue shift in**	**Negligible blue shift in**
Outer ring	n_{eff1}	Conventional notches	Extra notches	Not applicable
Inner off-axis microring	n_{eff2}	Extra notches	Not applicable	Conventional notches

V_{B} can be swapped at the cost of overall performances. For example, if we apply a message signal at the outer ring and an extra bias voltage to the inner ring, it will take higher voltage and consume more power to compensate the thermal effect as the effect of external bias in the inner microring (or, change in n_{eff2}) is negligible on conventional notches. Moreover, due to high Q-factor and narrow bandwidth of the extra resonant notches, only a small message signal applied to inner ring would be sufficient to achieve acceptable ER. Thereof, it is always preferable to apply the message signal at the inner ring. The normalized power transmission of off-axis MRR within optical communication wavelength range is depicted in Fig. 3.11 (a). It is conspicuous from inset of Fig. 3.11 (a) that $V_{\mathrm{m}} = +1\,\mathrm{V}$ results into $\sim 380\,\mathrm{pm}$ blue-shift of extra resonant notches (negligible blue-shift in conventional notches) which is sufficient to achieve almost 100% ($> 20\,\mathrm{dB}$ ER) modulation due to an ultra-high Q-factor of extra resonant notches of off-axis MRR. Figure 3.11 (b) shows the effect of V_{B} on conventional and extra resonant notches. Applying $\sim 1\,\mathrm{V}$ at conventional ring (i.e. outer ring) causes a blue shift of ~250–300 pm in the conventional resonant notches while ~50–100 pm blue shift of extra resonant notches. It is found that per Kelvin temperature rise can incur ~40–50 pm and ~50–70 pm red shifts for conventional and extra notches, respectively. Even 5 K change in temperature may result in 20–30% change in modulation as Q-factor is very high. Temperature effect, a nonlinear phenomenon in silicon waveguides, can be compensated through proper biasing voltage V_{B} at the outer ring. In Fig. 3.11 (c), it is shown that $V_{\mathrm{B}} = 3.4\,\mathrm{V}$ has nullified the effect of 20 K rise in temperature. The solid blue curve shows an extra resonant notch at $T = 300\,\mathrm{K}$ with no voltage bias applied at outer ring. When 1 V modulating signal is applied to the inner ring the notch is blue-shifted towards the left-hand side as shown by

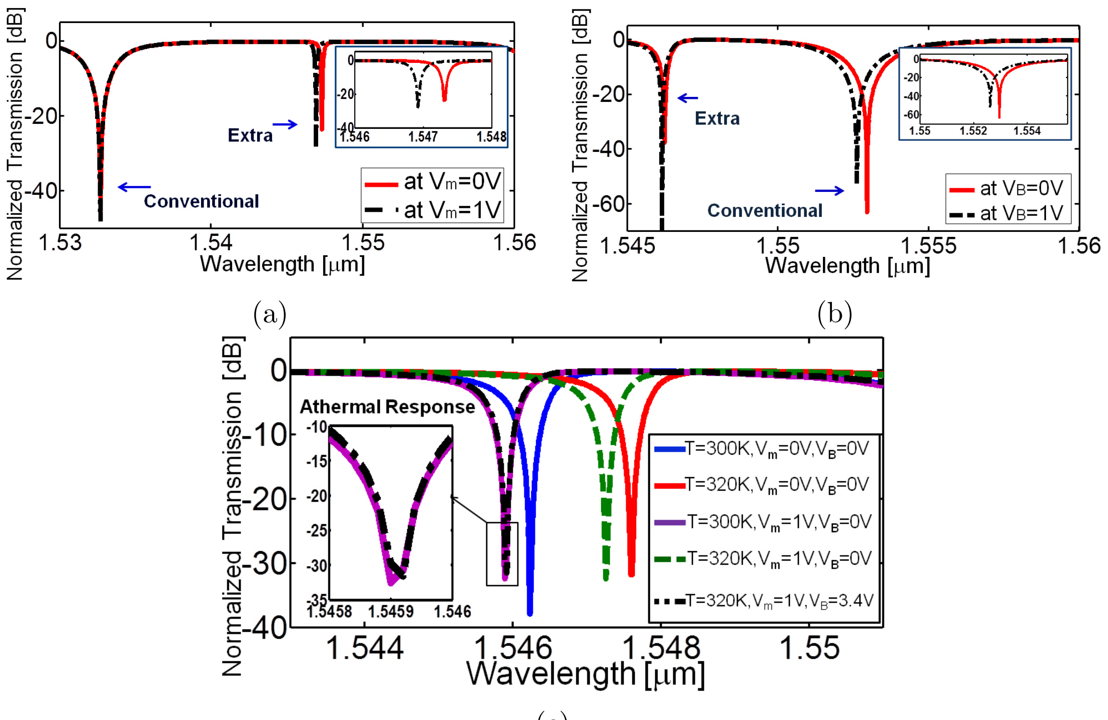

(a) (b)

(c)

Figure 3.11: Normalized transmission (dB) of an non-concentric MRR with change in (a) V_m, (b) V_B, and (c) transmission characteristics of thermally-compensated non-concentric MRR.

the solid violet curve. At 1 V, the off-axis MRR renders an extinction ratio of ~38 dB. The solid red curve shows the transmission of the MRR with 20 K rise in temperature without modulating signal while the solid green curve depicts the transmission of the MRR with 20 K rise in temperature with an applied message signal of 1 V to the inner ring. The solid black curve represents the transmission characteristics of MRR with a temperature compensating extra bias $V_\mathrm{B} = 3.4\,\mathrm{V}$ applied to the outer ring. This bias voltage can counterbalance the thermal effect, which is clearly visible from the inset where the solid black curve overlaps the solid violet curve. Therefore, for the Fig. 3.11 (c) one can write,

$$\Delta\lambda_{V_\mathrm{m}=1\,\mathrm{V}} = \Delta\lambda_{\Delta T=20\,\mathrm{K}} + \Delta\lambda_{V_\mathrm{B}=3.4\,\mathrm{V}} + \Delta\lambda_{V_\mathrm{m}=1\,\mathrm{V}} \tag{3.21}$$

where $\Delta\lambda_{V_\mathrm{m}=1\,\mathrm{V}}$, $\Delta\lambda_{\Delta T=20\,\mathrm{K}}$, $\Delta\lambda_{V_\mathrm{B}=3.4\,\mathrm{V}}$ represent the shift in resonant wavelength due to $V_\mathrm{m} = 1\,\mathrm{V}$, $\Delta T = 20\,\mathrm{K}$ and $V_\mathrm{B} = 3.4\,\mathrm{V}$, respectively.

The athermal behavior has been further validated and corroborated through the eye diagrams. Figure 3.12 (a) shows the waveform of user defined pre-emphasized message signal. NRZ signal is passed through a low noise amplifier-differentiator block and the output is added with the original NRZ signal itself to provide pre-emphasized NRZ signal. Using pre-emphasized input, rise time (t_r) and fall-time (t_f) can be reduced significantly (as small as 100 ps and 40 ps, respectively) [37]. Figure 3.12 (b) shows the eye-diagram for the optical transmission in room temperature. The parameters μ_1 and μ_2 refer to the eye amplitude levels, the standard deviations (SDs) σ_1 and σ_2 measure the noises at the levels μ_1 and μ_2, respectively. The eye-opening is defined as $(\mu_2 - \mu_1)$ which varies from 0 to 1 without thermal effects. The eye signal-to-noise ratio (SNR) can be defined as: $\mathrm{SNR} = (\mu_2 - \mu_1) \,/\, (\sigma_1 + \sigma_2)$. From TMM, it has been found numerically that the modulator amplitude varies from ~ 0.42 to 1 (3.82 dB) at 5 K rise in temperature. Consequently, the eye squints, which is demonstrated in Fig. 3.12 (c). Figure 3.12 (d) establishes that an extra bias of 2.2 V at the outer ring can nullify the thermal effect. It is clearly observed that $(\mu_2 - \mu_1) > (\mu_2^5 - \mu_1^5)$, $\sigma_2^5 > \sigma_2$ and $\sigma_1^5 > \sigma_2$ due to the thermal effects, but at the same time $(\mu_2 - \mu_1) \approx \left(\mu_2^{5'} - \mu_1^{5'}\right)$, where the superscript 5 has been used to explicate the amplitude levels at $\Delta T = 5\,\mathrm{K}$ and a prime is used in superscript to indicate the thermally compensated eye-levels. One should also note carefully that even after the recompense, $\sigma_2^{5'} \approx \sigma_2$, and $\sigma_1^{5'} \approx \sigma_1$ as the thermal noise in Si waveguide remains intact and cannot be eliminated through this procedure. If temperature is raised to 10 K the eye opening further gets reduced and the transmission amplitude varies from 0.65 to 1 (swing 1.86 dB). The closed eye can be reopened by counteracting the thermal effect using a bias voltage V_B of $\sim$2.82 V. These two cases have been delineated in Figs. 3.12 (e) and 3.12 (f). Further, an additional voltage of only 0.58 V can negate the temperature effect of 20 K.

Padamraju *et al.*, has clearly mentioned that thermal compensation with control-based solution consumes more power than athermal based solutions, which is the main disadvantage of the control-based solutions. Our process can be conceived as control-based solution. Besides the fabrication complexity, low fabrication tolerance and the requirement of an extra power source are the challenges in the off-axis MRR. While the thermal noise cannot be eliminated, however this does not affect the performance of the proposed device. Moreover, the RI change with respect to

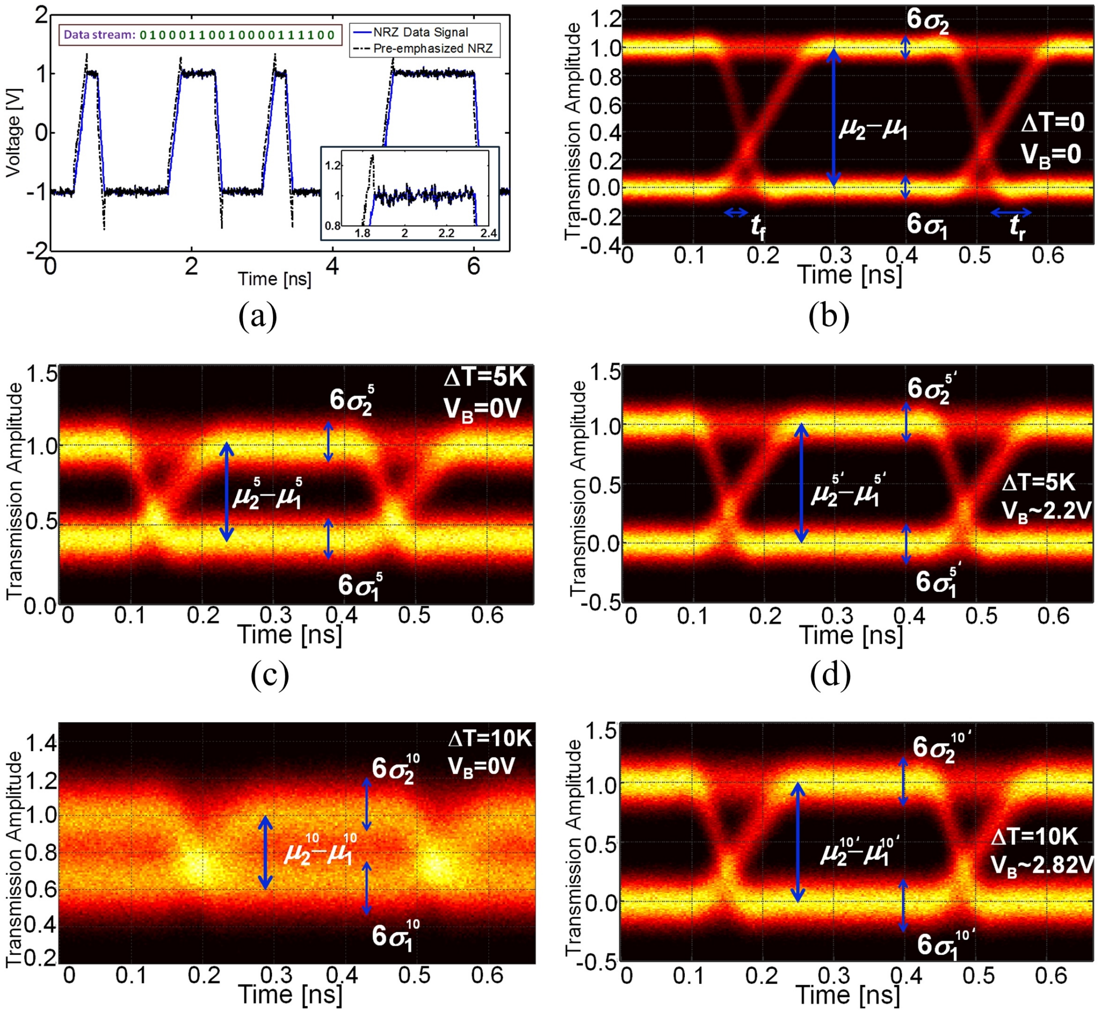

(a) (b)

(c) (d)

(e) (f)

Figure 3.12: (a) Pre-emphasized modulating signal waveform. (b) Eye-diagram of transmission at room temperature (c) Eye-diagram at $\Delta T = 5\,\mathrm{K}$ and $V_\mathrm{B} = 0\,\mathrm{V}$. (d) Voltage compensated eye-diagram of the transmission at $\Delta T = 5\,\mathrm{K}$. (e) Eye-diagram at $\Delta T = 10\,\mathrm{K}$. (f) Voltage compensated eye-diagram at $\Delta T = 10\,\mathrm{K}$.

the bias voltage is nonlinear due to the exponential I-V characteristics [48] of the PIN-diode. Until the device breaks down, this characteristic enables the device worthwhile to control the temperature effects more easily when the bias voltage is already very high. Note that, the extra bias voltage (ΔV_B) applied to the outer ring in order to compensate the thermal effect will be lesser for the same amount of temperature rise (ΔT) while the temperature is already high in comparison to the required feedback voltage for low initial temperature value, for example, if ΔV_{B1} and ΔV_{B2} are the bias voltages to compensate the effect of same amount of temperature rise ΔT at two different room temperatures T_1 and T_2 ($\ni T_1 \leq T_2$), respectively, then within the break-down limit of the SOI-EOM one can assume, $\Delta V_{\mathrm{B1}} > \Delta V_{\mathrm{B2}}$. The power consumption in the proposed device is therefore not high in comparison with the other control-based solutions, which is one of the important features of the proposed device. Apart from previously reported techniques [32, 36], dynamic temperature control can also be achieved using proper thermal coefficient of the resistance R_{T} (i.e., $\Delta R_{\mathrm{T}}/\Delta T$) (Fig. 3.9 (a)) by choosing suitable material and doping concentration. An ultra-sensitive on-chip optical MRR sensor, temperature monitoring integrated photo-detector or fibre Bragg grating sensor can be used to detect the ambient temperature. One can also use pre-calibrated external feedback mechanism to control and maintain the required value of V_{B} dynamically to compensate thermal effect.

3.3 Nested-nonconcentric MRRs

3.3.1 Motivation: Quality-factors and Critical-coupling

Devices such as micro-cavities made of silicon photonic wires (strip waveguides) can exhibit large Q-factor due to strong lateral confinement of the optical modes. Sharp resonant notches in the transmission spectrum make these devices particularly suitable for add-drop filters [3], EOMs [8] and so on. High RI and the large third-order nonlinearity of Si make them attractive for several applications [51,52] where small effective mode volume and high Q-factor are desired. The resonant effect in ultra-compact and high-Q optical micro-cavities can greatly enhance the efficiency of the nonlinear processes to achieve frequency comb [14], four-wave mixing (FWM) [15], and electromagnetic induced transparency once the detrimental two photon absorption effect is overcome. MRRs have also been employed in cavity quantum electrodynamics (QED), on-chip optical squeezing [16] and entangled photon pair generation [53]. The wide versatility of MRRs has made them indispensable for next-generation on-chip optical functionalities. Other than numerous nonlinear applications, MRRs have also been utilized for sensing purposes [54]. In most of the applications based on MRR, high Q-factor and large notch depths are required which is only possible when critical coupling between the straight bus waveguide and the microring is maintained [4]. To harness the utmost advantages of the resonance, the high Q-factor can be attained by reducing the propagation losses and the side-wall roughness, as demonstrated in [55–60]. MRRs comprising rib waveguide exhibit very low losses (0.1 dB/cm), but at the same time their minimum bending radius is limited to hundreds of micrometers [60]. Smaller bend radii (sharper bends) at the cost of larger losses are provided by wire waveguides [61]. The Q-factor of MRRs with Si wire waveguides can further be improved by adopting various novel fabrication techniques [58–60]. Recently, it has been reported [16] that MRR based on Si_3N_4 material exhibits losses < 0.5 dB/cm, but at the cost of a reduced nonlinearity (10% that of Silicon). The Q-factor and the resonant notch depths are very sensitive to the coupling condition (under-coupled, critically coupled or over-coupled) of the microring and its input or output bus waveguides, respectively. MRR with a single input bus, which is referred to as all-pass configuration offers deepest transmission notch in critical coupling [62]. The fabricated MRR parameters in general deviate from the optimized parameters (5%-10%) which result either into over-coupled or under-coupled regimes of MRR departing the MRR from the properties that were designed. Thermal and electro-optic tunability of the MRR resonant notches have also been utilized [63–65] to compensate the fabrication errors. In most of the applications such as bio-sensing and quantum photonic, MRRs are designed to operate in critically coupled condition [4,15]. For on-chip optical squeezing, photon pair generation in MRR etc. the preferred choice is to consider slightly over-coupled regime [16,53]. On the other hand, when an MRR is slightly under-coupled, the loaded Q-factor becomes greater than the Q-factor for critical coupling [60, 62], facilitating its use in the applications where high-Q is more crucial rather than the transmission notch depth. However, with further increase in transmission coefficient (decrease in coupling) due to fabrication errors, notch depth rapidly decreases and eventually becomes negligible. It is well known that Si has high TOC. Therefore, similar to the fabrication errors, the increase in local temperature may also alter the desired coupling condition and can be detrimental for such applications. As a rule of thumb, we can say that the higher the Q-factor of MRR, it would be more susceptible to the fabrication errors. This poses a strong challenge to achieve a perfect critical coupling between the MRR and the input bus. To achieve exact critical coupling, large numbers of devices are fabricated by sweeping the gap separation between the input bus and the microring within a possible range [4, 63]. Once the technological parameters for critical coupling are ensured, that particular MRR is further being used. This is certainly undesirable for the commercialization of on-chip photonic circuits with MRRs as crucial components. In order to relax the critical coupling, while maintaining high Q-factor and large transmission notch depth, in this work, we report a recipe based on coupled resonators which we refer to as nested non-concentric MRR (NN-MRR) and provide an analytical model of internally-coupled, nested MRR through the TMM [18]. In the previous section [18], we demonstrate the usage of two non-concentric MRRs that exhibits extra distinctive sharp transmission notches with high-Q and have been used to attain athermal CMOS compatible EOM [49]. The inclusion of additional ring in dual-ring system fosters large Q-factor ($> 10^5$) and notch depth ($> 10\,\text{dB}$) irrespective of the coupling conditions. Such CMOS compatible compact high-Q coupled MRRs would be fabrication tolerant and highly suitable for sensing, nonlinear and cavity QED applications. Relaxation in critical coupling condition in serially coupled MRRs has been previously reported in [66]. However, the reported design occupies a large space which might not be suitable for high-density all-optical functionalities. Our proposed NN-MRR outperforms the reported one and is very compact and suitable for on-chip integration. The modal properties of the silicon wire waveguides have been calculated through commercially available full-vectorial FEM based solver, COMSOL Multiphysics, where, the bending effects are taken into consideration through conformal mapping. The TMM calculations have been performed in MATLAB.

3.3.2 Theory and Design of NN-MRR

Figure 3.13 (a) depicts the schematic of the proposed all-pass NN-MRR which is comprised of three microrings of radii R_1, R_2 and R_3 ($\ni R_3 < R_2 < R_1$). The outermost microring is side coupled to a bus waveguide. The dashed rectangular boxes in Fig. 3.13 (a) mark the coupling regions (CRs) which are characterized by straight-through (τ) and cross-coupling (κ) coefficients for an optical wave. In-

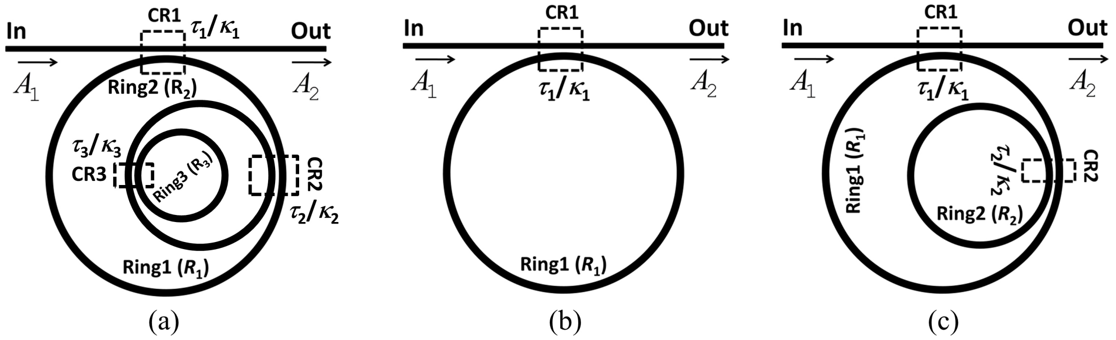

Figure 3.13: Geometrical configurations: (a) proposed all-pass NN-MRR configuration with three coupled rings having radii R_1, R_2, and R_3, depicting different coupling regions (CRs). (b) Conventional MRR, (c) nonconcentric dual-MRR (off-axis MRR).

dividual microrings possess internal loss factors $a_{\mathrm{m}} = \exp(-\alpha_{\mathrm{m}} L_{\mathrm{m}}/2)$, where α_{m} is the linear loss coefficient (per unit length) and $L_{\mathrm{m}} = 2\pi R_{\mathrm{m}}$ is the circumference of the respective ring where $m = 1, 2, 3 \ldots$ corresponding to the microring numbers. The semi-round trip phase change in the largest microring of radius R_1 is ϕ_1, whereas ϕ_2, ϕ_3 are the respective round-trip phase shifts of the inner rings. Input bus waveguide is coupled to the outermost microring through CR1, owning transmission and coupling coefficients τ_1 and κ_1, respectively, as indicated in Fig. 3.13 (a). Inner ring 2 (radius R_2) is coupled with the outer microring of radius R_1 through CR2, possessing transmission and coupling coefficients τ_2 and κ_2, whereas the innermost microring with radius R_3 is coupled with the second microring with radius R_2 through CR3 which has transmission and coupling coefficient τ_3 and κ_3, respectively. A_1 is the complex input wave amplitude and A_2 is the complex output wave amplitude. Let, for a total n-number of serially coupled NN-MRRs with single bus (all-pass configuration), the general expression for the normalized transmission (in dB) be $20\log_{10}|T_{\mathrm{n}}|$, where the T_{n} is given by,

$$T_n = \frac{A_2}{A_1} = \left|\frac{A_2}{A_1}\right| e^{\mathrm{i}\phi_{\mathrm{n_{eff}}}} = \tau_1 + a_1 (i\kappa_1)^2 \left(\mathrm{e}^{\mathrm{i}2\phi_1}\chi_1^{-1} - a_1\tau_1\right)^{-1} \tag{3.22}$$

where, $\phi_{\mathrm{n_{eff}}}$ is the effective phase change/delay of the output wave with respect to the input wave. a_{j}, τ_{j}, and κ_{j} ($j = 1, 2, 3 \ldots$) represent the lumped amplitude loss, straight-through transmission coefficients and cross-coupled transmission coefficients for the j-th ring or the j-th coupler, respectively. χ_2, χ_3, $\chi_{\mathrm{n}-1}$ and χ_{n}

represent the effects of the second, third, $(n-1)$-th and n-th inner non-concentric rings. The theoretical model is valid for n number of total rings, with $(n-1)$ inner rings and $\chi_{\mathrm{n}} = 1$. Therefore,

$$\chi_1 = \tau_2 + a_2(i\kappa_2)^2\left(\mathrm{e}^{\mathrm{i}\phi_{in_1}}\chi_2^{-1} - a_2\tau_2\right)^{-1} \tag{3.23a}$$

$$\chi_{n-1} = \tau_n + a_n(i\kappa_n)^2\left(\mathrm{e}^{\mathrm{i}\phi_{in_{n-1}}}\chi_n^{-1} - a_n\tau_n\right)^{-1} \tag{3.23b}$$

So, for the NN-MRR with 3 rings (2 inner rings), $\chi_3 = 1$. The effective phase evolution ($\phi_{\mathrm{j_{eff}}}$) at the transmission port for n-number of nested-rings is given by,

$$\begin{aligned} \phi_{\mathrm{j_{eff}}} &= \tan^{-1}\left(\frac{a_{\mathrm{j}}\sin{\phi_{\mathrm{j}}}'}{\tau_{\mathrm{j}} - \alpha_{\mathrm{j}}\cos{\varphi'}_{\mathrm{j}}}\right) - \tan^{-1}\left(\frac{a_{\mathrm{j}}\tau_{\mathrm{j}}\sin{\phi_{\mathrm{j}}}'}{1 - \tau_{\mathrm{j}}a_{\mathrm{j}}\cos{\phi_{\mathrm{j}}}'}\right) \\ {\phi_{\mathrm{j}}}' &= \phi_{\mathrm{j+1_{eff}}} + \phi_{\mathrm{j}},\ \phi_{\mathrm{j}} = \frac{4\pi^2 n_{\mathrm{eff_j}} R_{\mathrm{j}}}{\lambda_0},\ \text{for j} = 1,\ 2,\ \ldots\ \text{to}\ \ldots\ n \end{aligned} \tag{3.24}$$

where, ϕ_{j} is the round-trip phase-shift at the j-th ring with radius R_{j} and $\phi_{\mathrm{n+1}} = 0$. We assume each waveguide of the NN-MRR is comprised of a photonic wire waveguide of dimensions of 500 nm×250 nm. In our simulations we have considered the dispersion effect (material and waveguide). The ring radii are, $R_1 = 30\,\mu$m, $R_2 = 20\,\mu$m, $R_3 = 10\,\mu$m. We have considered two different practical situations for our analysis, (A) waveguide with rough side-walls (RSW) and (B) waveguide with smooth side-walls (SSW). In both the scenarios, the losses are different. For the case of RSW (case-A), we assume relatively higher dimensionless loss factors α_1, α_2 and α_3 corresponding to 0.5 dB/cm, 1 dB/cm and 2 dB/cm, for rings 1, 2, and 3, respectively. Similarly for the case of SSW (case-B), the propagation losses are relatively low and α_1, α_2 and α_3 are related to 0.3 dB/cm, 0.5 dB/cm and 1 dB/cm, respectively. The overall loaded Q-factor, Q_{loaded} in terms of intrinsic and coupling Q-factor can be written as, ${Q_{\mathrm{loaded}}}^{-1} = {Q_{\mathrm{intrinsic}}}^{-1} + {Q_{\mathrm{coupling}}}^{-1}$. We assume that it is possible to achieve Q-factor as high as 10^6 when the waveguide has smooth side-walls.

3.3.3 Evolution of NN-MRR: Design Recipe

In the subsequent sections, we describe the methodology to arrive at NN-MRR system, as shown in Fig. 3.13 (a). To produce a design space, we have mainly focused on the achievable high Q-factor and large transmission notch depth when the coupling condition is close and far from the critically coupled condition in both the cases A and B, as explained before.

3.3.3.1 Single Microring

We start our analysis with a single microring (radius R_1) in all-pass configuration (inset of Fig 3.13 (b)). Strip-waveguide is being used having a cross-section of $500\,\mathrm{nm}\times 250\,\mathrm{nm}$. The calculated Q-factor and maximum transmission notch depth, P_{T} for this MRR configuration for different losses and transmission coefficients in two scenarios RSW and SSW, are plotted in Fig. 3.14 (a) and Fig. 3.14 (b), respectively. We consider two different coupling situations (i) large deviation in critical coupling condition, and (ii) less deviation from critical coupling condition. The ratio of transmission coefficient and dimensionless loss factor i.e., (τ_1/a_1) determines the region of operation of the microring. The microring is critically, over or under coupled if the ratio (τ_1/a_1) is 1, < 1 or > 1, respectively. The dashed green curve indicates the maximum possible transmission notch depth (dB), P_{T1} whereas the dashed-dotted red curve tells about intrinsic quality-factor of this particular MRR. Note that, notch depth$< -52\,\mathrm{dB}$ is possible to achieve for case-B. It is also possible to achieve high-$Q(> 10^5)$ even the notch depth is very less. However, it is preferred to use a particular resonant frequency possessing both sharp and deep transmission notches and high-Q in applications such as sensing [54] and modulators [7]. In Fig. 3.14, we plot the quality factor (dashed-dotted red curve) and maximum transmission notch depth (dashed green-curve) for a conventional all-pass MRR. Note that, transmission notches with notch-depth, $|P_{\mathrm{T}}| > 3\,\mathrm{dB}$ have only been included for both the cases. It is known that even if the MRR is slightly under-coupled, a maximum $Q > Q_{\mathrm{critical}}$ can be achieved at the cost of reduced P_{T}. For over-coupled situation, both the Q-factor and notch depth fall rapidly, but with a relatively lower slope in comparison with the under-coupled regime. It is well established that the coupling coefficient κ per unit length depends upon

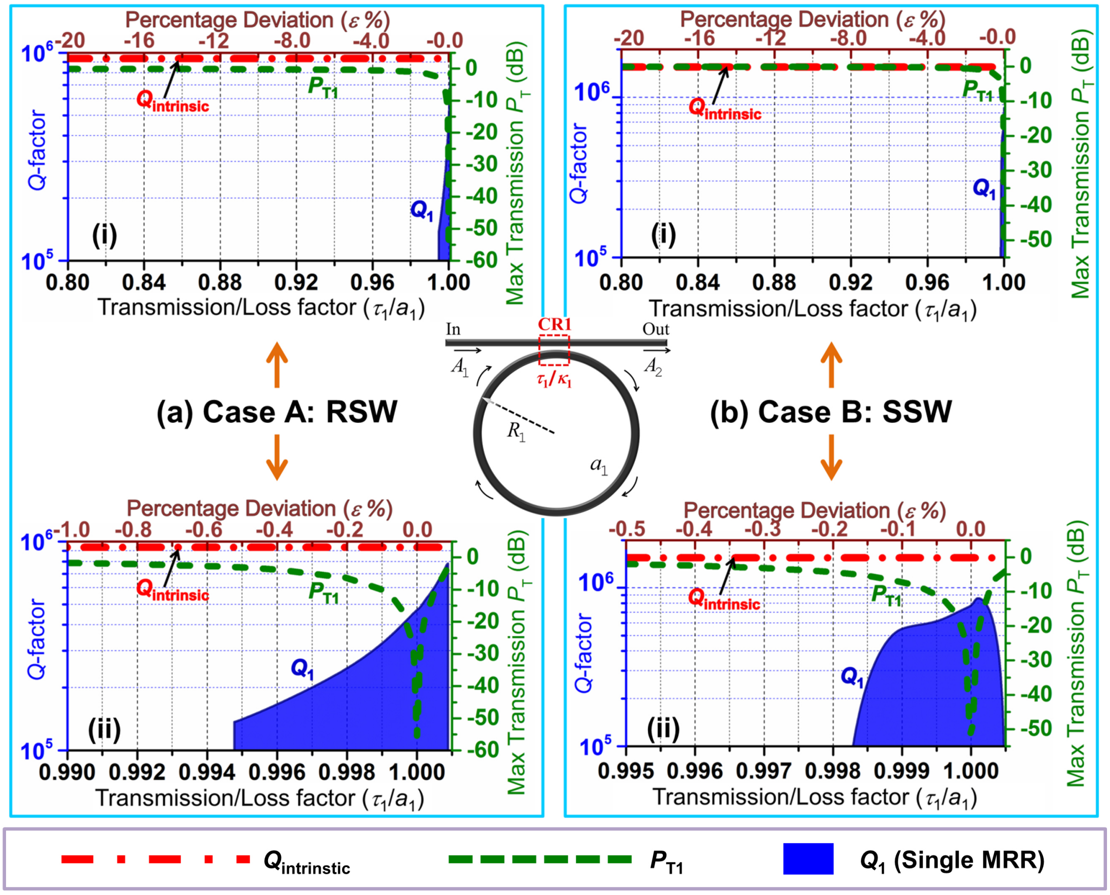

Figure 3.14: Design space parameters and availability of high Q-factor and transmission notch depths in case of all-pass single ring MRR (conventional MRR). The plots govern all possible Q-factors, Q_1, and maximum transmission notch depth P_{T1} for transmission/loss factor (τ_1/a_1), when the fabrication error (ϵ) from the critical coupling is varied for two different loss scenarios: (a) RSW, (b) SSW, where the deviation is assumed (i) far from the critical coupling and (ii) closer to critical coupling condition. For all situations, transmission notches greater than 3 dB in the wavelength range of 1.5 μm-1.6 μm are considered.

the gap between the bus and the ring. A small deviation in fabrication is sufficient to prevent the MRR from being in critically coupled condition. Also, it is evident that MRR with less propagation loss (i.e. with SSW) is more sensitive towards fabrication errors [59]. In Fig. 3.15, we summarize the accessibility of high quality factor and transmission notch depth for different coupling conditions and deviations for a single-ring MRR. We provide a comparative study of Q-factors and maximum notch depths P_T obtained for a MRR in different coupling regimes (2%

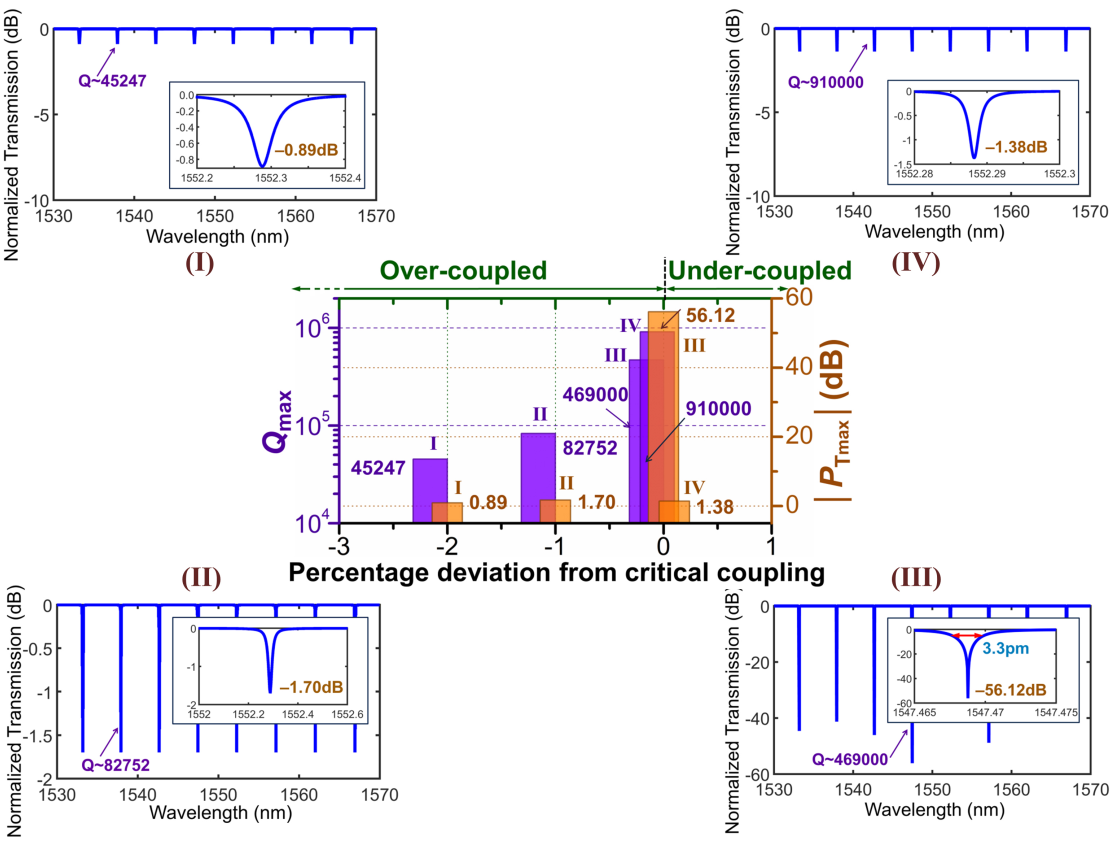

Figure 3.15: Comparison of Q and $|P_T|$ for single MRR in different coupling regimes. Normalized transmission of the single MRR of radius R_1 (case-A) side-coupled to a single input bus with (I) 2% over-coupling, (II) 1% over-coupling, (III) critical coupling, (IV) 0.1% under-coupling.

and 1% over-coupling, critical-coupling and 0.1% under-coupling) after evaluating the normalized transmission, where the waveguide in MRR has rough side walls. In case of critical coupling, maximum notch depth of $-56.12\,\text{dB}$ along with a Q-factor of $\sim 4.7 \times 10^5$ is achievable. The notch depth P_T and the Q-factor drop to $-1.7\,\text{dB}$ and $\sim 8.3 \times 10^4$, respectively even for 1% over-coupling scenario. This establishes that the performance of the MRR is very sensitive to coupling that might result even from a very small fabrication error.

3.3.3.2 Non-concentric Dual-Ring MRR

As an intermediate step to design NN-MRR, we consider a situation where a non-concentric MRR of smaller radius is added in a conventional MRR (referred as non-concentric dual MRR/off-axis ring). We analyze the Q-factor and notch depth of two-ring MRR configuration, as shown in the inset of Fig. 3.16 (or, Fig. 3.13 (c)). The extra microring of smaller radius creates sharp extra notches as predicted recently by authors in previous work [18, 50]. It was shown that MRR with non-concentric inner ring provides greater flexibility in controlling different parameters. For instance, it is not necessary for the non-concentric dual ring MRR to be critically coupled to obtain a large Q and deep transmission notches as depicted through Fig. 3.16. In Figs. 3.16 (a) and 3.16 (b), possible Q-factors and the maximum transmission notch depth corresponding to the outermost (largest) ring (denoted by Q_1 and P_{T1}) and due to the second non-concentric inner microring (represented by Q_2 and P_{T2}) are plotted. The dashed and solid green curves stand for P_{T1} and P_{T2}, respectively. The transparent blue and light purple regions indicate the possible values of the Q-factors for the conventional notches (Q_1) and the extra notches (Q_2). It is observed that even though the outer MRR is over-coupled with the bus waveguide (i.e. $\tau_1 < a_1$) a Q-factor greater than 10^5 can be obtained. We find that up to 12% (case-A: RSW) and 8% (case-B: SSW) deviations from the critical coupling conditions, the Q-factors greater than 10^5 of the resonant modes can be sustained easily with notch depths $|P_{\mathrm{T2}}| > 3\,\mathrm{dB}$ for dual NN-MRR configuration. It is to be noted that the solid green curve has two dips. At critical coupling, the total power supplied to the outer ring from bus is equal to the power dissipated. The second dip appears due to the fact that at over-coupling, the total power dissipation in the coupled ring system is exactly compensated by the power supplied externally.

3.3.3.3 Non-concentric Nested MRR (NN-MRR)

The inclusion of another smaller non-concentric microring into the first inner ring, as shown in Fig. 3.17 (as well Fig. 3.13 (a)), improves the performance in comparison to the dual-ring MRR case discussed in previous sub-section. We refer this three coupled rings configuration as non-concentric nested MRR. This structure mimics the serially coupled microring resonators with different ring sizes. However, the key benefit of the proposed NN-MMR structure is the compactness. Similar performances can be achieved at much smaller device footprint which facilitates

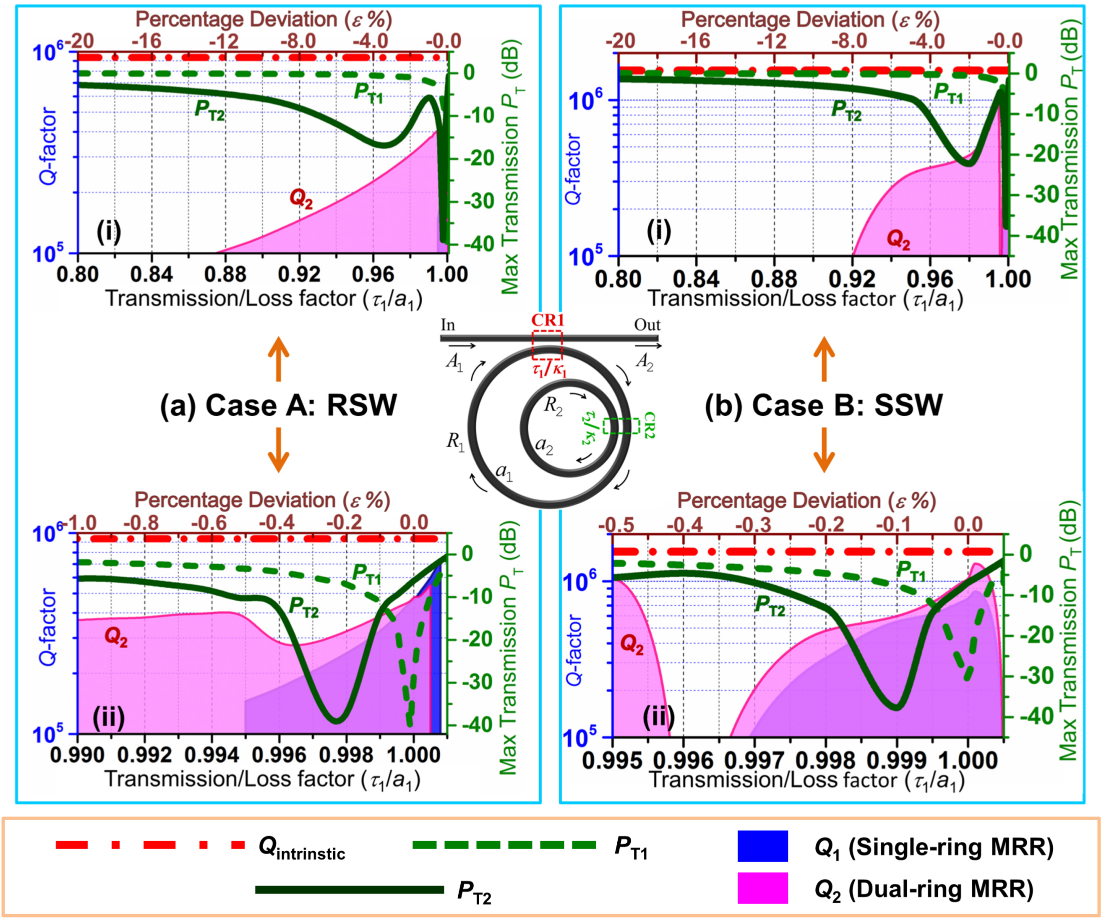

Figure 3.16: Design space parameters and availability of high-Q and transmission notch depths in case of NN dual-MRR. The plots show all possible Q-factors (Q_1, Q_2) and notch depths ($|P_{\mathrm{T1}}|$, $|P_{\mathrm{T2}}|$) when (τ_1/a_1), and ϵ are varied for two different loss scenarios: (a) RSW (b) SSW, where the deviation is assumed to be (i) far from, and (ii) closer to the critical coupling condition.

the integration of more components on the same chip. The smallest microring coupled to the larger inner ring creates a few additional extra resonant notches with very high-Q, even if the outermost MRR is over-coupled to the input bus [50]. Similar to the analysis carried in previous subsections, we analyze the Q-factor and notch depths for two different cases, RSW and SSW when the outermost ring is coupled either far or near from the critically-coupled condition to the input bus waveguide. In Figs. 3.17 (a) and 3.17 (b), possible Q-factors and the maximum transmission notch depth due to only outermost ring (Q_1, P_{T1}), in presence of the non-concentric single inner ring (Q_2, P_{T2}) and due to both non-concentric inner

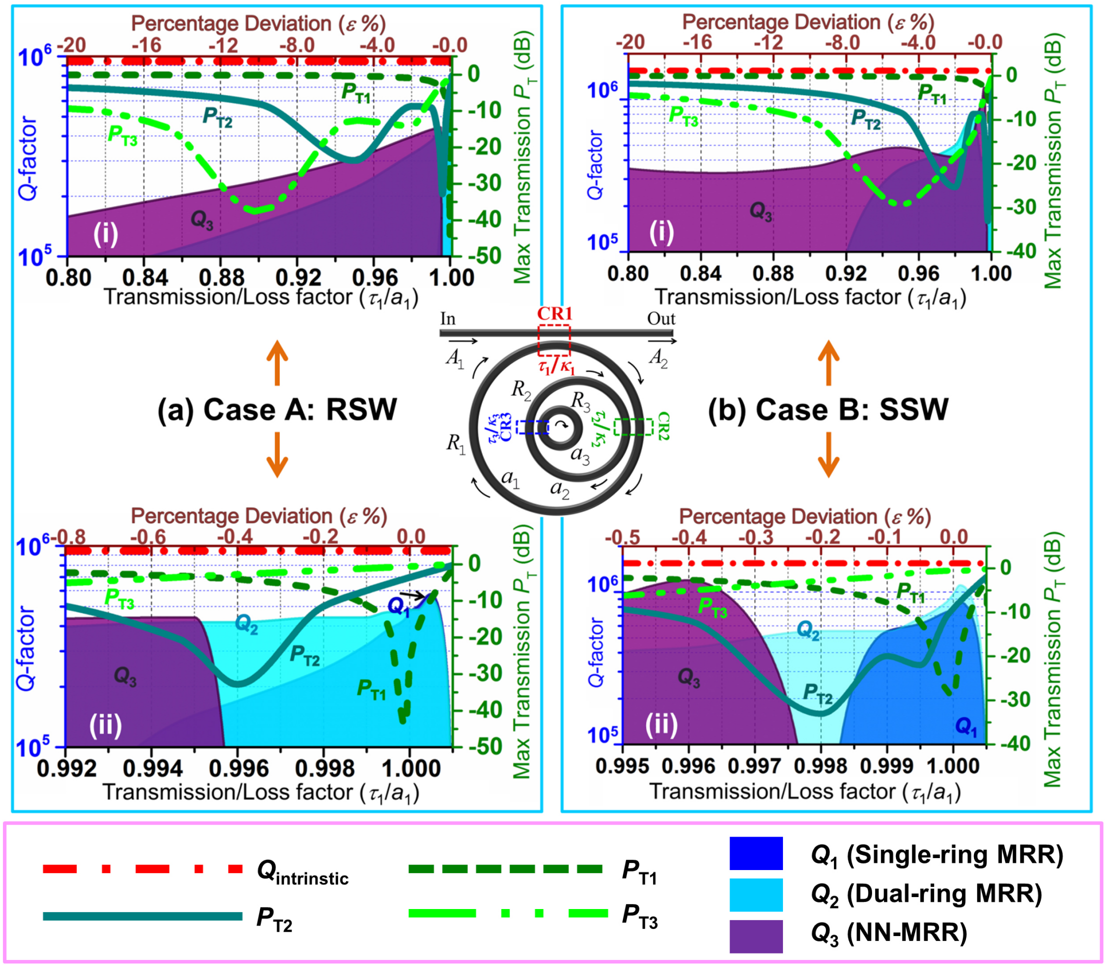

Figure 3.17: Design space parameters and availability of high-Q transmission notches in case of NN-MRR with three rings. The plots govern all possible Q-factors (Q_1, Q_2, Q_3) and maximum transmission notch depths $|P_{T1}|$, $|P_{T2}|$ and $|P_{T3}|$ when (τ_1/a_1), and ϵ are varied for two different loss scenarios: (a) RSW (b) SSW, where the deviation is assumed to be (i) far from, and (ii) closer to the critical coupling condition.

rings (Q_3, P_{T3}) are plotted for wavelength range $1.5\,\mu$m–$1.6\,\mu$m. The transparent blue, cyan and purple regions indicate allowed range of Q_1, Q_2 and Q_3, respectively. A maximum possible Q for the extra notches due to the smallest inner ring viz. $Q_3 > 10^5$ with $|P_{T3}| > 10\,$dB can be attained even at the large deviation of greater than 20% from the critical coupling, whereas the conventional notches (due to outer ring) and the extra notches due to the largest inner ring are already disappeared for a slight variation in the critical coupling condition. An additional dip

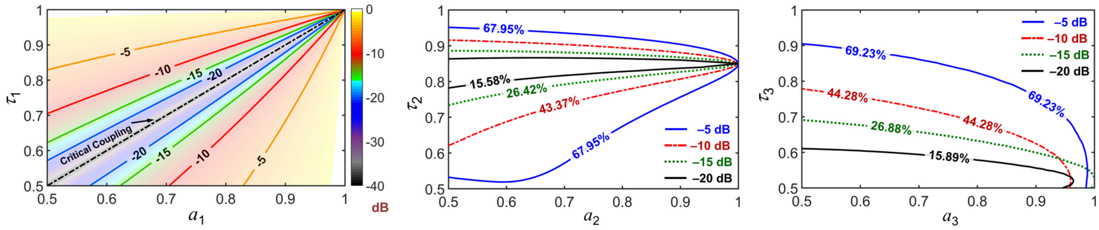

(a) (b) (c)

Figure 3.18: (a) Sets of possible values of a_1 and τ_1 are indicated by the enclosed regions under the orange, red, green, and blue curves for which the transmission notch depth can reach up to 5 dB, 10 dB, 15 dB and 20 dB, respectively for single microring. (b) Introducing another ring in a nested fashion allows 67.95%, 43.37%, 26.42%, and 15.58%, of all the possible sets of values of a_2 and τ_2 (i.e., the choice of a_1, and τ_1) to enhance the area under the orange, red, green and blue curves for which the transmission notch depth at the through-port can reach up to 5 dB, 10 dB, -15 dB, and -20 dB, respectively. This clearly indicates the relaxation for the requirement of the critical coupling. Again, (c) 69.23%, 44.28%, 26.88%, and 15.89% of all possible values of a_3 and τ_3 can further relax the critical coupling condition for the outermost microring to the input bus, respectively while τ_2 is fixed at an optimized value 0.86.

appears in the transmission curve (P_{T3}, the dashed-dotted green curve), similar to what has been observed in case of two rings system. The conclusions remain the same even if all the outer rings are slightly more or less over-coupled to its immediate inner rings. The maximum percentage deviation from the critical-coupling towards the over-coupling regime for which Q-factors of single, dual and nested MRR can be maintained greater than 10^5, are listed in Table 3.2. The innermost ring improves the fabrication tolerance in comparison with single microring and dual-ring MRR.

Table 3.2: Maximum percentage (%) deviation from critical-coupling towards the over-coupling regime.

Device Config.	**Case A: RSW**				**Case B: SSW**			
	$Q > 10^5$	$\lvert P_{\mathrm{T}}\rvert > 3\,\mathrm{dB}$	$\lvert P_{\mathrm{T}}\rvert > 5\,\mathrm{dB}$	$\lvert P_{\mathrm{T}}\rvert > 10\,\mathrm{dB}$	$Q > 10^5$	$\lvert P_{\mathrm{T}}\rvert > 3\,\mathrm{dB}$	$\lvert P_{\mathrm{T}}\rvert > 5\,\mathrm{dB}$	$\lvert P_{\mathrm{T}}\rvert > 10\,\mathrm{dB}$
Single-MRR	~ 0.5	~ 0.5	~ 0.35	~ 0.1	~ 0.2	0.2	0.15	~ 0.05
Dual-MRR	~ 12	~ 16	11	7	8	8	6	4
NN-MRR	> 20	> 20	> 20	~ 18	> 20	> 20	18	10

3.3.3.4 Flexibility of parameters: Fabrication tolerance

In this section, we show how introducing another ring within a single MRR in a nested fashion relaxes the stringent requirement of the critical coupling condition quantitatively. We also observe the transmission notch depth at throughput improves if we introduce a third ring within the second ring from a different perspective. Fig. 3.18 (a) indicates all possible sets of values of τ_1 and a_1 marked by the enclosed regions under the orange, red, green, and blue curves for which the transmission notch depth can reach up to $-5\,\text{dB}$, $-10\,\text{dB}$, $-15\,\text{dB}$ and $-20\,\text{dB}$, respectively for a single microring. We know if the value of a_1 approaches to 1, the propagation loss of the microring becomes negligible, whereas, the black dashed-dotted straight-line given by the equation $\tau_1 = a_1$ dictates the critical coupling condition. Thus, for the single MRR the notch-depth is highest at the critical coupling and a small deviation from the critical coupling decreases the notch-depth. Now, our goal is to enhance the area under the orange, red, green, and blue curves which in turn will relax the coupling condition. We observe, if another smaller ring is introduced inside the outer-ring in a nested fashion, the area under these curves are enhanced. In Fig. 3.18 (b) we illustrate that 67.95%, 43.37%, 26.42%, and 15.58% of all the possible values of the τ_2 and a_2, the area under the blue, red, green, and black curves are increased, respectively. From the same plots we also observe that for the transmission notch depths improve if the second ring is over-coupled to the first microring, i.e. $\tau_2 < a_2$ if the loss of the second ring is very less ($a_2 \approx 1$). This clearly corroborates the fact that the second ring relaxes the requirement of the critical coupling and enhances the fabrication tolerances. Now, the overall propagation loss of the microring depends upon the material loss, bending loss, radiation loss etc. and one cannot choose the exact values of a_1 or a_2. With the advancement of the recent fabrication technologies and the post-processing trimming, one can even achieve the values of a_1 and a_2 as high as > 0.999. Thus from Fig. 3.18 (b) we observe that for values of a_2 that approaches to 1, a prudent choice of τ_2 will be ~ 0.86 for the best performance of the dual configuration. Now, keeping the value of τ_2 fixed at 0.86 we introduce the third ring inside the second ring in a nested fashion. We plot τ_3 with respect to a_3 while the values of a_2 and τ_2 are fixed and calculate the set of values of a_1 and

τ_1 for which the area under the orange, red, green, and blue curves are increased. From Fig. 3.18 (c) we inspect that for 69.23%, 44.28%, 26.88%, and 15.89% of all the possible values of a_3 and τ_3, the area under the brown, yellow, cyan and blue curves are further enhanced. Hence, Fig. 7 (a), (b), and (c) clearly suggest a further relaxation of the requirement of the critical coupling can be achieved using a 3-ring nested configuration. Again for the practical cases a_3 approaches to 1 and the third ring must be over-coupled for the best performances. The over-coupling condition between the microrings can be assured just by keeping the gap length very small. We further investigate the underlying mechanism that gives rise to the relaxation of critical coupling condition. Critical coupling condition occurs while the input energy to the microring through the input bus is exactly equals to the energy consumption or the overall energy decay/loss of the microring resonator, whereas, if the input power is more than the power loss, then the microring is over-coupled to the bus waveguide. However, it is easier to fabricate a microring which is over-coupled to an input bus instead of achieving a perfect critical coupling. If there are internal microrings properly placed in a nested fashion, the extra power that is supplied by the input bus is consumed by the internal microrings and thus one can still achieve deeper resonant notches even if the outermost microring is not over-coupled with the input bus. Hence, To elicit maximum advantages from this newly proposed nested off-axis MRR, our design objective is to make sure that the gaps between ring-to-ring and bus-to-ring are such that all the rings are over-coupled with its next inner ring and the largest ring is also over-coupled to the input bus. It should be noted that even though the outermost microring is large enough to accommodate many nested inner rings, one cannot keep on adding arbitrary number of nested inner rings as with the decreasing ring radius, bending loss would also will increase.

3.3.4 Experimental Results

Our theoretical model has previously been verified through FDTD based numerical simulations [18]. To corroborate the robustness of the performance of the 3-ring NN-MRR, we fabricate the NN-MRR with dual and triple rings through the electron beam lithography facility at KIT Germany. We have used the stan-

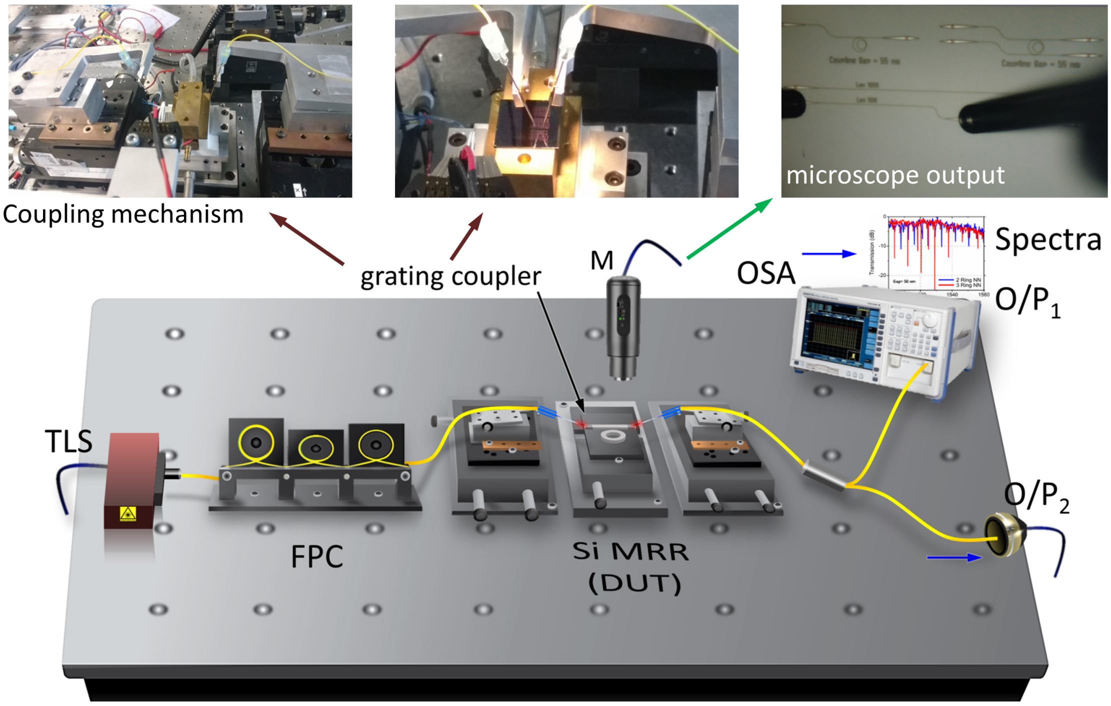

Figure 3.19: Experimental set-up (at Karlsruhe Institute of Technology (KIT), Germany) to characterize the NN-MRR. The magnified views of the coupling region are shown in the insets.

dard SOI wafer with silicon thickness of 220 nm. The designed parameters of the waveguide cross-section are 450 nm×220 nm. The experimental set-up is shown in Fig. 3.19. Light is coupled (collected) from fiber to chip (chip to fiber) using standard grating coupler. Fig. 3.20 (a) depicts the SEM image of a single-bus dual-ring MRR with a gap separation of 50 nm. The radii of two rings are 30 μm and 20 μm. Fig. 3.20 (b) shows the image of a NN-MRR with three rings where the radius of the third microring is 10 μm. The gap is $\sim$ 50 nm which resembles the case of strong over-coupling regime. The chip was coated with PMMA to protect the waveguide surfaces. Note that our theoretical findings hold true irrespective of the waveguide dimension and cladding material. Fig. 3.20 (c) shows the measured transmission spectra for both the dual-ring (solid blue curve) and three-ring (solid red curve) MRRs, respectively. Initial results shown in Fig. 3.20 (c) suggest that if the rings are strongly over-coupled to each other and the bus waveguide having all the gap separations of 50 nm, deeper transmission notches can be obtained for the NN three-ring structure in comparison with the NN two-ring structure.

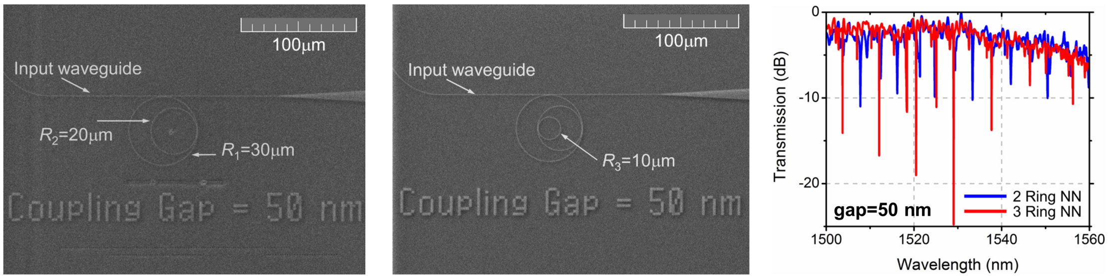

(a) (b) (c)

Figure 3.20: (a) Fabricated NN 2-ring structure, (b) fabricated NN 3-microring structure. Both the cases the coupling gaps are 50 nm. (c) Transmission (dB) from 2 ring NN structure and 3 ring NN structure for wavelength 1500 nm to 1560 nm.

3.4 Further discussions

It is well established that positive TOC of silicon red-shifts the resonant notches in MRR which in other words we can say that the coupling condition between bus and the ring waveguide alters. Temperature effect can be highly detrimental for different applications such as sensing, WDM communications, EOMs, nonlinear and quantum optics, etc [32]. For example, photon pair generation rate is heavily affected even with a small increase in temperature [53]. As temperature rises during the experiment due to the power dissipation in the device, often microrings slightly over-coupled with the input buses are used to achieve the maximum photon pair generation rate [53]. For a fixed gap separation between the microring and the input bus, the coupling coefficient, κ_1 decreases (τ_1 increases). If a MRR is designed to operate in critical coupling condition, the mode of operation may change to under-coupling for a slight variation in temperature. Therefore, for applications such as sensing, nonlinear and quantum optics, where the precise location of the transmission notches are not always that important rather deep and sharp transmission notches are necessary, NN-MRR can be a solution since nested MRR can maintain high-Q and large notch depth at any coupling condition.

3.5 Summary and Conclusions

To conclude this chapter,
In the first part of our work, we have devised a panoptic theoretical model for

off-axis MRR using the well-established TMM. Different designs and all possible combinations of inner rings in multiple off-axis MRRs have been analyzed analytically. Phase matching conditions for off-axis MRR have been developed. The results from more rigorous FDTD method are in good agreement with analytical method. The off-axis MRR shows a distinctive feature of extra resonant dips with very high Q-factor and high sensitivity towards a small change in effective RI and radius of the inner off-axis ring. Moreover, the design of compact band-rejection filter which is capable to reject arbitrarily chosen WDM channelshas been demonstrated using serially coupled off-axis MRRs. The presence of extra notches in the spectrum of off-axis MRR helps to reduce the device size considerably which would offer an extra space to integrate more components on the same photonic chip.

In section 3.2, we establish that off-axis MRR EOM can obviate the thermal effects for wide range of temperatures very effectively through an extra ring within the same MRR structure which not only creates highly sensitive and sharp resonant notches (with high Q-factor) but also offers another degree of freedom of designing. This renders us an opportunity to build up an EOM untarnished by thermal effects within the same compact dimension of a single MRR. The eye diagrams of the proposed off-axis MRR show the potential to overcome the thermal detuning for DWDM applications.

In the final section of this chapter, we demonstrate (both numerically and experimentally) that unlike single MRR (all-pass configuration), the nested NN-MRR creates extra resonant notches which maintains extremely large Q-factor ($> 10^5$) and high notch depth ($> 10\,\mathrm{dB}$) irrespective of its coupling conditions with the input bus. Such high-Q compact resonators would be fabrication tolerant, flexible to design, cost-effective, commercially viable and highly suitable in sensing, nonlinear applications, cavity-QED and other quantum applications for a broad range of ambient temperature.

References

[1] K. Vahala, *Optical Microcavities.* World Scientific, 2004.

[2] I. Chremmos, O. Schwelb, and N. Uzunoglu, *Photonic Microresonator Research and Applications.* Springer, 2010, vol. 156.

[3] W. Bogaerts, P. De Heyn, T. Van Vaerenbergh, K. De Vos, S. Kumar Selvaraja, T. Claes, P. Dumon, P. Bienstman, D. Van Thourhout, and R. Baets, "Silicon microring resonators," *Laser & Photonics Reviews*, vol. 6, no. 1, pp. 47–73, 2012.

[4] A. Yariv, "Universal relations for coupling of optical power between microresonators and dielectric waveguides," *Electronics Letters*, vol. 36, no. 4, pp. 321–322, 2000.

[5] B. E. Little, S. T. Chu, H. A. Haus, J. Foresi, and J.-P. Laine, "Microring resonator channel dropping filters," *Journal of Lightwave Technology*, vol. 15, no. 6, pp. 998–1005, 1997.

[6] V. R. Almeida, C. A. Barrios, R. R. Panepucci, and M. Lipson, "All-optical control of light on a silicon chip," *Nature*, vol. 431, no. 7012, pp. 1081–1084, 2004.

[7] M. Lipson, "Compact electro-optic modulators on a silicon chip," *IEEE Journal of Selected Topics in Quantum Electronics*, vol. 12, no. 6, pp. 1520–1526, 2006.

[8] Q. Xu, B. Schmidt, S. Pradhan, and M. Lipson, "Micrometre-scale silicon electro-optic modulator," *Nature*, vol. 435, no. 7040, pp. 325–327, 2005.

[9] Q. Xu, B. Schmidt, J. Shakya, and M. Lipson, "Cascaded silicon micro-ring modulators for wdm optical interconnection," *Optics Express*, vol. 14, no. 20, pp. 9431–9436, 2006.

[10] Q. Xu and R. Soref, "Reconfigurable optical directed-logic circuits using microresonator-based optical switches," *Optics Express*, vol. 19, no. 6, pp. 5244–5259, 2011.

[11] R. Ji, L. Yang, L. Zhang, Y. Tian, J. Ding, H. Chen, Y. Lu, P. Zhou, and W. Zhu, "Microring-resonator-based four-port optical router for photonic networks-on-chip," *Optics Express*, vol. 19, no. 20, pp. 18 945–18 955, 2011.

[12] O. Schwelb and I. Frigyes, "Series-coupled microring resonator filters with embedded semiconductor optical amplifiers," *Microwave and Optical Technology Letters*, vol. 42, no. 5, pp. 427–432, 2004.

[13] V. Passaro, F. DellOlio, and F. De Leonardis, "Ammonia optical sensing by microring resonators," *Sensors*, vol. 7, no. 11, pp. 2741–2749, 2007.

[14] A. G. Griffith, R. K. Lau, J. Cardenas, Y. Okawachi, A. Mohanty, R. Fain, Y. H. D. Lee, M. Yu, C. T. Phare, C. B. Poitras *et al.*, "Silicon-chip mid-infrared frequency comb generation," *Nature Communications*, vol. 6, p. 6299, 2015.

[15] A. C. Turner, M. A. Foster, A. L. Gaeta, and M. Lipson, "Ultra-low power parametric frequency conversion in a silicon microring resonator," *Optics Express*, vol. 16, no. 7, pp. 4881–4887, 2008.

[16] A. Dutt, K. Luke, S. Manipatruni, A. L. Gaeta, P. Nussenzveig, and M. Lipson, "On-chip optical squeezing," *Physical Review Applied*, vol. 3, no. 4, p. 044005, 2015.

[17] A. Yariv, *Optical Electronics in Modern Communications.* Oxford University Press, 1997.

[18] R. Haldar, S. Das, and S. K. Varshney, "Theory and design of off-axis microring resonators for high-density on-chip photonic applications," *Journal of Lightwave Technology*, vol. 31, no. 24, pp. 3976–3986, 2013.

[19] C. Manolatou, M. Khan, S. Fan, P. R. Villeneuve, H. Haus, and J. Joannopoulos, "Coupling of modes analysis of resonant channel add-drop filters," *IEEE Journal of Quantum Electronics*, vol. 35, no. 9, pp. 1322–1331, 1999.

[20] Z. Zhang, M. Dainese, L. Wosinski, and M. Qiu, "Resonance-splitting and enhanced notch depth in soi ring resonators with mutual mode coupling," *Optics Express*, vol. 16, no. 7, pp. 4621–4630, 2008.

[21] B. Lahiri, A. Z. Khokhar, M. Richard, S. G. McMeekin, and N. P. Johnson, "Asymmetric split ring resonators for optical sensing of organic materials," *Optics Express*, vol. 17, no. 2, pp. 1107–1115, 2009.

[22] L. C. Kimerling, "Photons to the rescue: Microelectronics becomes microphotonics." *Electronic Device Failure Analysis*, vol. 4, no. 3, pp. 15–20, 2002.

[23] D. A. Miller, "Device requirements for optical interconnects to silicon chips," *Proceedings of the IEEE*, vol. 97, no. 7, pp. 1166–1185, 2009.

[24] A. Alduino and M. Paniccia, "Interconnects: Wiring electronics with light," *Nature Photonics*, vol. 1, no. 3, pp. 153–155, 2007.

[25] D. A. Miller, "Rationale and challenges for optical interconnects to electronic chips," *Proceedings of the IEEE*, vol. 88, no. 6, pp. 728–749, 2000.

[26] J. D. Meindl, J. A. Davis, P. Zarkesh-Ha, C. S. Patel, K. P. Martin, and P. A. Kohl, "Interconnect opportunities for gigascale integration," *IBM Journal of Research and Development*, vol. 46, no. 2.3, pp. 245–263, 2002.

[27] A. Shacham, K. Bergman, and L. P. Carloni, "Photonic networks-on-chip for future generations of chip multiprocessors," *IEEE Transactions on Computers*, vol. 57, no. 9, pp. 1246–1260, 2008.

[28] C. Gunn, "CMOS photonics/spl trade/-SOI learns a new trick," in *2005 IEEE International SOI Conference Proceedings.* IEEE, 2005, pp. 7–13.

[29] B. Jalali and S. Fathpour, "Silicon photonics," *Journal of Lightwave Technology*, vol. 24, no. 12, pp. 4600–4615, 2006.

[30] R. A. Soref and B. R. Bennett, "Kramers-Kronig analysis of electro-optical switching in silicon," in *Integrated Optical Circuit Engineering IV*, vol. 704. International Society for Optics and Photonics, 1987, pp. 32–38.

[31] Y. P. Varshni, "Temperature dependence of the energy gap in semiconductors," *Physica*, vol. 34, no. 1, pp. 149–154, 1967.

[32] K. Padmaraju and K. Bergman, "Resolving the thermal challenges for silicon microring resonator devices," *Nanophotonics*, vol. 3, no. 4-5, pp. 269–281, 2014.

[33] K. Padmaraju, D. F. Logan, X. Zhu, J. J. Ackert, A. P. Knights, and K. Bergman, "Integrated thermal stabilization of a microring modulator," *Optics Express*, vol. 21, no. 12, pp. 14 342–14 350, 2013.

[34] C. T. DeRose, M. R. Watts, D. C. Trotter, D. L. Luck, G. N. Nielson, and R. W. Young, "Silicon microring modulator with integrated heater and temperature sensor for thermal

control," in *Conference on Lasers and Electro-optics.* Optical Society of America, 2010, p. CThJ3.

[35] S. Manipatruni, R. K. Dokania, B. Schmidt, N. Sherwood-Droz, C. B. Poitras, A. B. Apsel, and M. Lipson, "Wide temperature range operation of micrometer-scale silicon electro-optic modulators," *Optics Letters*, vol. 33, no. 19, pp. 2185–2187, 2008.

[36] K. Padmaraju, J. Chan, L. Chen, M. Lipson, and K. Bergman, "Thermal stabilization of a microring modulator using feedback control," *Optics Express*, vol. 20, no. 27, pp. 27 999–28 008, 2012.

[37] Q. Xu, S. Manipatruni, B. Schmidt, J. Shakya, and M. Lipson, "12.5 Gbit/s carrier-injection-based silicon micro-ring silicon modulators," *Optics Express*, vol. 15, no. 2, pp. 430–436, 2007.

[38] Y. Kokubun, N. Funato, and M. Takizawa, "Athermal waveguides for temperature-independent lightwave devices," *IEEE Photonics Technology Letters*, vol. 5, no. 11, pp. 1297–1300, 1993.

[39] J. Teng, P. Dumon, W. Bogaerts, H. Zhang, X. Jian, X. Han, M. Zhao, G. Morthier, and R. Baets, "Athermal silicon-on-insulator ring resonators by overlaying a polymer cladding on narrowed waveguides," *Optics Express*, vol. 17, no. 17, pp. 14 627–14 633, 2009.

[40] J.-M. Lee, D.-J. Kim, H. Ahn, S.-H. Park, and G. Kim, "Temperature dependence of silicon nanophotonic ring resonator with a polymeric overlayer," *Journal of Lightwave Technology*, vol. 25, no. 8, pp. 2236–2243, 2007.

[41] B. Guha, J. Cardenas, and M. Lipson, "Athermal silicon microring resonators with titanium oxide cladding," *Optics Express*, vol. 21, no. 22, pp. 26 557–26 563, 2013.

[42] B. Guha, B. B. Kyotoku, and M. Lipson, "CMOS-compatible athermal silicon microring resonators," *Optics Express*, vol. 18, no. 4, pp. 3487–3493, 2010.

[43] Y. Vlasov, W. M. Green, and F. Xia, "High-throughput silicon nanophotonic wavelength-insensitive switch for on-chip optical networks," *Nature Photonics*, vol. 2, no. 4, pp. 242–246, 2008.

[44] A. Biberman, E. Timurdogan, W. A. Zortman, D. C. Trotter, and M. R. Watts, "Adiabatic microring modulators," *Optics Express*, vol. 20, no. 28, pp. 29 223–29 236, 2012.

[45] Y. Hu, X. Xiao, H. Xu, X. Li, K. Xiong, Z. Li, T. Chu, Y. Yu, and J. Yu, "High-speed silicon modulator based on cascaded microring resonators," *Optics Express*, vol. 20, no. 14, pp. 15 079–15 085, 2012.

[46] Q. Deng, X. Li, Z. Zhou, and H. Yi, "Athermal scheme based on resonance splitting for silicon-on-insulator microring resonators," *Photonics Research*, vol. 2, no. 2, pp. 71–74, 2014.

[47] R. F. Pierret, *Semiconductor Device Fundamentals.* Pearson Education India, 1996.

[48] D. A. Neamen, "Semiconductor physics and devices: Basic principles. 2003."

[49] R. Haldar, A. D. Banik, M. Sanathanan, and S. Varshney, “Compact athermal electro-optic modulator design based on soi off-axis microring resonator,” in *CLEO: QELS_Fundamental Science*. Optical Society of America, 2014, pp. JW2A–37.

[50] R. Haldar, A. D. Banik, and S. K. Varshney, “Design of cmos compatible and compact, thermally-compensated electro-optic modulator based on off-axis microring resonator for dense wavelength division multiplexing applications,” *Optics Express*, vol. 22, no. 19, pp. 22 411–22 420, 2014.

[51] Q. Lin, O. J. Painter, and G. P. Agrawal, “Nonlinear optical phenomena in silicon waveguides: modeling and applications,” *Optics Express*, vol. 15, no. 25, pp. 16 604–16 644, 2007.

[52] J. Leuthold, C. Koos, and W. Freude, “Nonlinear silicon photonics,” *Nature Photonics*, vol. 4, no. 8, pp. 535–544, 2010.

[53] M. Savanier, R. Kumar, and S. Mookherjea, “Photon pair generation from compact silicon microring resonators using microwatt-level pump powers,” *Optics Express*, vol. 24, no. 4, pp. 3313–3328, 2016.

[54] V. Passaro, C. Tullio, B. Troia, M. Notte, G. Giannoccaro, and F. Leonardis, “Recent advances in integrated photonic sensors,” *Sensors*, vol. 12, no. 11, pp. 15 558–15 598, 2012.

[55] J. Niehusmann, A. Vörckel, P. H. Bolivar, T. Wahlbrink, W. Henschel, and H. Kurz, “Ultrahigh-quality-factor silicon-on-insulator microring resonator,” *Optics Letters*, vol. 29, no. 24, pp. 2861–2863, 2004.

[56] S. Xiao, M. H. Khan, H. Shen, and M. Qi, “Compact silicon microring resonators with ultra-low propagation loss in the C band,” *Optics Express*, vol. 15, no. 22, pp. 14 467–14 475, 2007.

[57] A. Biberman, M. J. Shaw, E. Timurdogan, J. B. Wright, and M. R. Watts, “Ultralow-loss silicon ring resonators,” *Optics Letters*, vol. 37, no. 20, pp. 4236–4238, 2012.

[58] A. Naiman, B. Desiatov, L. Stern, N. Mazurski, J. Shappir, and U. Levy, “Ultrahigh-Q silicon resonators in a planarized local oxidation of silicon platform,” *Optics Letters*, vol. 40, no. 9, pp. 1892–1895, 2015.

[59] Y. Chen, J. Feng, Z. Zhou, J. Yu, C. J. Summers, and D. S. Citrin, “Fabrication of silicon microring resonator with smooth sidewalls,” *Journal of Micro/Nanolithography, MEMS, and MOEMS*, vol. 8, no. 4, p. 043060, 2009.

[60] L.-W. Luo, G. S. Wiederhecker, J. Cardenas, C. Poitras, and M. Lipson, “High quality factor etchless silicon photonic ring resonators,” *Optics Express*, vol. 19, no. 7, pp. 6284–6289, 2011.

[61] Q. Xu, D. Fattal, and R. G. Beausoleil, “Silicon microring resonators with 1.5-μm radius,” *Optics Express*, vol. 16, no. 6, pp. 4309–4315, 2008.

[62] J. M. Choi, R. K. Lee, and A. Yariv, “Control of critical coupling in a ring resonator–fiber configuration: application to wavelength-selective switching, modulation, amplification, and oscillation,” *Optics Letters*, vol. 26, no. 16, pp. 1236–1238, 2001.

[63] M. J. Strain, C. Lacava, L. Meriggi, I. Cristiani, and M. Sorel, “Tunable Q-factor silicon microring resonators for ultra-low power parametric processes,” *Optics Letters*, vol. 40, no. 7, pp. 1274–1277, 2015.

[64] Y. Long and J. Wang, “Optically-controlled extinction ratio and Q-factor tunable silicon microring resonators based on optical forces,” *Scientific Reports*, vol. 4, p. 5409, 2014.

[65] S. A. Miller, Y. Okawachi, S. Ramelow, K. Luke, A. Dutt, A. Farsi, A. L. Gaeta, and M. Lipson, “Tunable frequency combs based on dual microring resonators,” *Optics Express*, vol. 23, no. 16, pp. 21 527–21 540, 2015.

[66] L. Y. Tobing, S. Darmawan, D. R. Lim, M.-K. Chin, and T. Mei, “Relaxation of critical coupling condition and characterization of coupling-induced frequency shift in two-ring structures,” *IEEE Journal of Selected Topics in Quantum Electronics*, vol. 16, no. 1, pp. 77–84, 2010.

CHAPTER 4

Kerr Frequency-comb with Nonlinear Losses

This chapter describes the nonlinear characteristics of microresonators (MRs), where the primary goal is to model and study the Kerr frequency comb (FC) in the presence of nonlinear losses and free-carrier effects. At first, we discuss the fundamental concepts relevant to the nonlinear MR-based FC and its applications. Subsequently, we elucidate various theoretical modeling, numerical simulations and experimental methods to generate an optical FC in a concise manner. Different material platforms used for frequency conversions within integrated optical cavities, their unique features, advantages, disadvantages, fabrication techniques, etc. are also discussed in details. Finally, we deduce, relate and implement our mathematical model in explaining several numerical and experimental results which are previously reported. This generalized mathematical framework is able to provide a better understanding of the comb dynamics in practical scenarios where different material platforms containing nonlinear losses are being utilized. [1]

---

[1] Publications related to this chapter are [88], [91], [92].

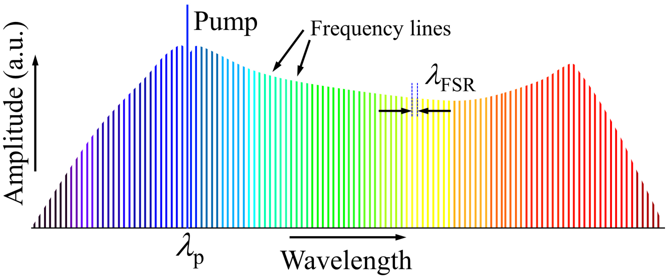

Figure 4.1: Schematic of an optical frequency comb. The pump wavelength is λ_p. Frequency lines are apart from each other by approximately one cavity free spectral range (FSR), i.e. λ_{FSR}.

4.1 Fundamentals and Background

Optical FC, as shown in Fig. 4.1, is a set of equidistant and coherent frequency lines in the ultraviolet, visible, and infrared regions [1], which can be used in precision measurement [2, 3], microwave signal synthesis [4], optical communication [5, 6], sensing, spectroscopy [3, 5], molecular fingerprinting [7, 8], astronomy [9,10], entangled photon pair generation [11,12], or as an optical ruler [1,5,13]. In recent years, FC is even employed in determining the size and shape of the atoms/molecules accurately and has helped in resolving the 'proton-size puzzle' [14, 15]. Mode-locked femtosecond lasers and fiber lasers have extensively been used for the generation of optical FC [2, 16–19] until recently the parametric frequency conversion using continuous-wave (CW) optical pump in optical micro-cavities (Fig. 4.2 (a) microspheres, (b) micro-disks, and (c) microring resonators, (d) fabricated structures) have revolutionized the technology for comb generation [20–23]. Eventually, the device footprint has been reduced to a few hundred micrometers while a repetition rate as high as >10 GHz can easily be achieved [22, 23]. There are several advantages of such on-chip microcavity-based parametric FC which are:

(i) Compact in size (typical diameter$<100\,\mu$m),

(ii) High-Q (typically 10^4–10^9),

(iii) Very small effective modal area (A_{eff}) and modal volume (V_{eff}) that ensure higher effective nonlinear coefficient (γ) compared to the fiber-ring cavities,

(iv) Mode-spacing can be controlled by the perimeter length,

(v) Low/flat and controllable dispersion; octave-spanning FC can be obtained,

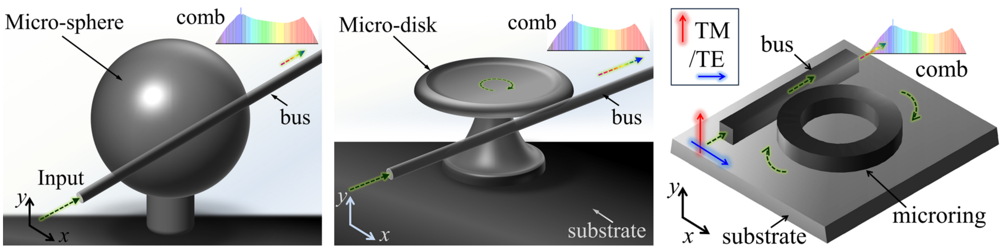

(a) Microsphere (b) Micro-disk (c) Microring (integrated/on-chip)

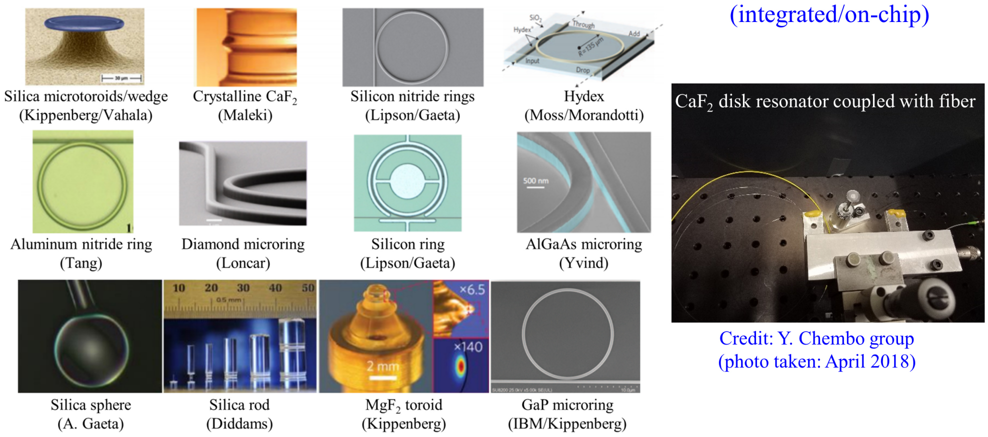

(d) Microresonator platforms with variety of different materials for comb generation

Figure 4.2: Schematic of various optical microcavities which can be used as a platform for FC generation: (a) Whispering gallery mode (WGM) microsphere, (b) WGM microdisk, (c) microring resonators (MRRs), (d) fabricated MR platforms made of various materials for comb generations. (Photo credits: collected from pioneering group websites or personal archive).

(vi) Threshold power ($P_{\rm th}$) is less,

(vii) Advanced fabrication techniques (e.g., CMOS technologies) are available, low-cost integrated chip-scale packaging, easy for mass production,

(viii) Higher repetition rate (typically>10 GHz),

(ix) Saturable absorber which is an indispensable component of the mode-locked laser based FC in not required in this case,

In spite of these advantages, there exist a few drawbacks of using integrated platforms which are:

(i) Although easy to fabricate, most of the coupling mechanisms including fiber or grating based coupling methods are not robust and sophisticated, thereby unstable and lossy,

(ii) Bending radius is small in comparison to the fiber-ring cavities, thus the bending loss is very high.

(iii) Conversion efficiencies are often low.

4.2 Theory and generation of Frequency Comb

There are numerous routes to generate FC as summarized in Fig. 4.3. In the materials platform where $\chi^{(2)}$ nonlinearity is dominant, comb formation occurs through second harmonic generation (SHG), and sum frequency generation (SFG). In third-order (Kerr) nonlinear materials, FC is generated through third harmonic generation (THG), modulation instability (MI), degenerate four-wave mixing (D-FWM), and non-degenerate four-wave mixing (ND-FWM). For both the second and third order nonlinear processes, pump-photon energy is absorbed by the electronic clouds. Secondary radiations from the oscillating electron clouds manifest themselves as frequency comb. Apart from that, FC can also be originated from inelastic Raman scattering and Brillouin scattering where some part of the incident optical energies are dissipated as the optical and acoustic phonons through the molecular and lattice vibrations, respectively. In this chapter, we mainly focus on third-order/Kerr nonlinearity based FC that exploits the hyper (third-order)-parametric frequency conversion in high-Q microcavities [5, 24, 25].

4.2.1 Formation of Kerr Comb: Basic Principle

To obtain a near- or mid-infrared (IR) frequency comb, a narrow linewidth (typically 5–10 kHz) continuous wave (CW) tunable laser source (TLS) is generally employed. The signal of the CW-laser source (CW_1) is amplified by an erbium doped fiber amplifier (EDFA) as shown in Fig. 4.4 to accomplish an input power level more than the Kerr comb threshold [23]. The polarization of the input signal is maintained by the fiber polarization controller (FPC). The light is coupled to a device under test (DUT), e.g. a MR through one of the various coupling methods such as free-space coupling [5], prism coupling [5], butt-coupling [22, 26], grating coupling [27], and most recently using photonic wire-bonds [28], etc. depending upon the DUT. Silicon nitride (Si_3N_4) MRR is a popular choice as a platform for nonlinear frequency conversion due to its low propagation loss and relatively high Kerr nonlinearity [22]. Butt-coupling is being preferred to couple the light from

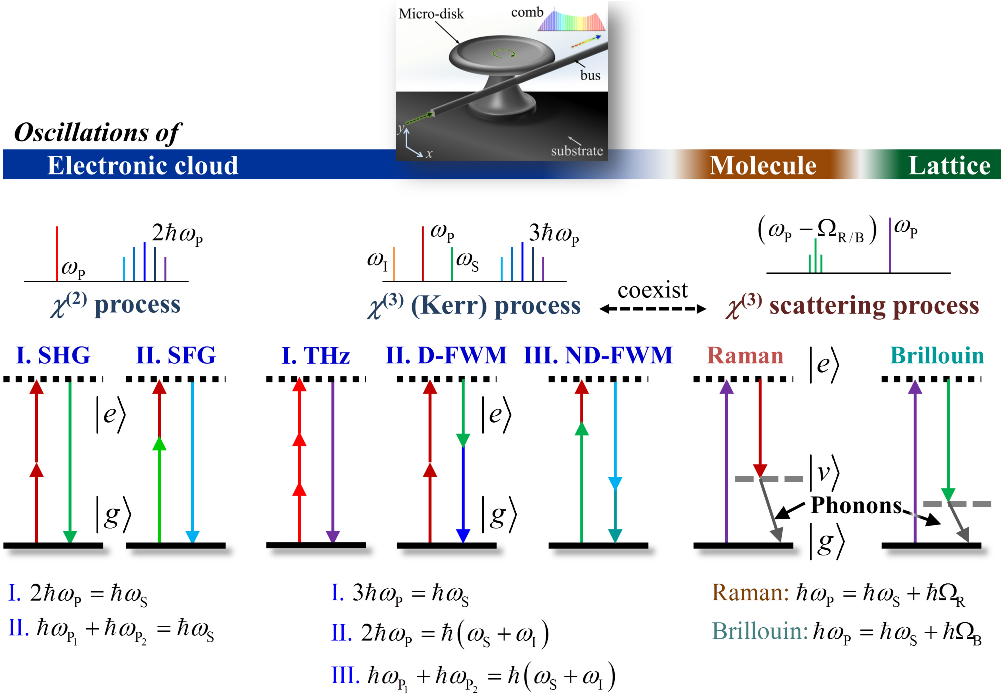

Figure 4.3: Summary of different nonlinear processes to generate optical FC with their energy-level diagrams and initial spectrums. $|g\rangle$, $|v\rangle$, and $|e\rangle$ represent the ground state, virtual state, and the excited states, respectively.

fiber to the Si_3N_4 chip as shown in Fig. 4.4. For efficient butt-coupling often lensed fiber and tapered waveguides are used [21, 26]. However, the grating coupling is the most efficient ($> 70\,\%$ light coupled with an overall insertion loss < 6–$7\,$dB) and well-established method to couple light from an input fiber into a silicon-on-insulator (SOI) chip [27] and recently has also been implemented for silicon-nitride waveguides [29]. If an MR operates in the under-coupled regime, then the comb threshold is minimum, albeit the maximum nonlinear conversion efficiency can be achieved when the resonator is over-coupled with the input waveguide [30]. For butt-coupling, the light from the through port of the DUT is collected by an objective and again coupled to the fiber. The fiber can be connected to an optical coupler. A small amount of light is sufficient to examine the spectral characteristics of the generated FC, whereas, the rest of the output power can be used for other applications.

Theoretical analysis suggests that the comb dynamics depends upon the effec-

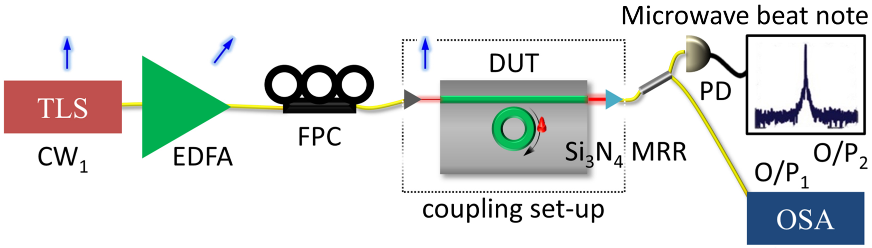

(a) Block diagram

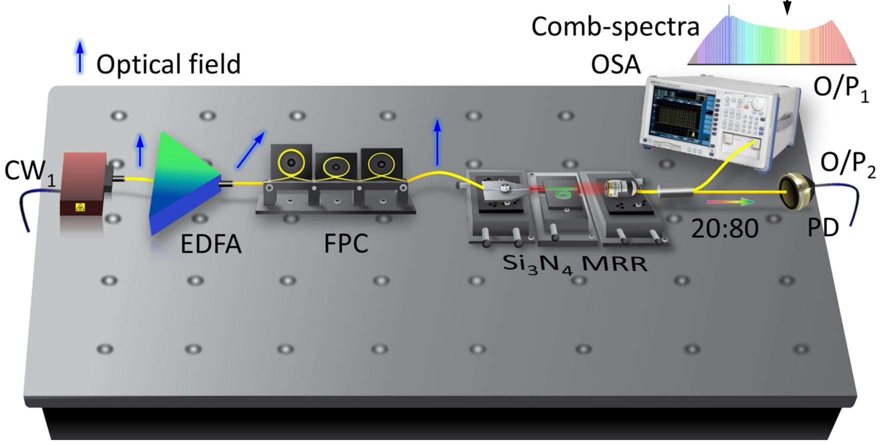

(b) Realistic picture

Figure 4.4: (a) Schematic/block diagram of the experimental set-up to generate an optical frequency comb. (b) A realistic picture of the set-up.

tive frequency detuning between the external pump and microcavity mode along with the input pump power [22]. However, it is important to note that the cold cavity resonance positions are no longer the same as of the new effective resonance positions under the influence of external pump induced Kerr and thermo-optic effects. In general, the locations of the cavity resonances fluctuate dynamically with time and experience an overall shift towards the longer wavelength. Therefore, in practice, it is extremely difficult to determine the effective pump detuning from the nearest cavity-mode. Several well-known techniques are available to stabilize the laser frequency by locking it to a cavity resonance such as Pound-Drever-Hall [30], thermal self-locking [21,31], external thermal detuning [32], and self-injection locking [33], etc. Finally, one has to stabilize the carrier-envelope offset frequency, to generate a self-referenced fully sustained steady FC or equivalently a dissipative CS in time-domain [21, 34, 35]. For silicon MRRs multi-photon absorptions, free-carrier absorption (FCA) and free-carrier dispersion (FCD) play a crucial role in determining the existence and dynamics of FC, which is discussed elaborately later in this chapter. It is noteworthy that mode-locking of the FC in silicon MRRs can also be achieved via controlling the free-carrier lifetime and free-carrier dispersion effect [35].

4.2.2 Analytical Modeling

Dynamics of the FC can be understood analytically by two distinct, however, equivalent approaches, viz. (i) the damped-driven nonlinear Schrödinger equation, which is also known as the mean-field Lugiato Lefever Equation (LLE) [36, 37], and (ii) coupled mode equation (CME) or modal expansion methods [38,39]. Each of these analytical models has its advantages [40]. The salient features of the LLE based approach are:

- LLE is a time-domain approach,
- Resembles the nonlinear Schrödinger equation, thus, familiar; easier to perceive and solve numerically through fast and well-known simulation methods (e.g. split-step Fourier method (SSFM)),
- Helps to connect the experimental findings to the numerical results as one can obtain temporal solitons through the simulation of LLE, directly,
- Easier to include the nonlinear losses such as two-photon absorptions (2PA), three-photon absorption (3PA), four-photon absorption (4PA), FCA, and FCD effects in comparison with the CME approach,
- Easier to add self-steepening effect,
- Easier to incorporate Raman-effect,

Whereas, the important features and the advantages of the CME over the LLE are:

- CME is a frequency domain approach,
- Evolution of each frequency components with the cavity round-trips can be observed, directly,
- Frequency-dependent absorptions can be considered easily,
- Frequency-dependent coupling coefficient can be considered easily,

- If the local dispersion for particular comb lines are severely perturbed and can no longer be interpolated by the Taylor series expansions [40], such rebarbative effects can be studied through CME with relative ease,
- CME approach is more convenient to handle for the modeling of coupled-cavity systems [41] compared to the LLE.

Previously, it was anticipated that CME is inefficient in order to simulate FCs with a large number of comb-lines (e.g. for octave spanned FCs), nonetheless, soon it was discovered by Hansson *et al.* [42] that thousands of CMEs can be efficiently integrated numerically by fast Fourier transform. It is now well-understood that CME description is nothing but the discrete Fourier transform of the LLE approach! Our main work focuses on the influence of nonlinear losses and free-carrier effects on the FC dynamics; therefore, we limit our analytical description only by adopting the LLE based approach.

4.2.2.1 Proof of the Lugiato-Lefever Equation

Let us assume an MR is driven by a CW-pump of wavelength λ_p and an electric-field amplitude E_{in}, as shown in Fig. 4.5 (a). In MR, to obtain a temporal cavity soliton (CS), the group velocity dispersion (GVD) has to be balanced by the Kerr nonlinearity and the overall propagation loss should be compensated by the external pump power. This balance occurs only for a suitable range of the pump power and the cavity detuning which are capable of sustaining [22, 37] the CS. In the frequency/Fourier ($\mathfrak{F}$) domain, the dissipative temporal CS manifests itself as frequency-comb. Note that, FC can also be attained without creating a CS in the temporal domain, however for simplicity, we restrict ourselves only to the FCs arise from the CSs or sech pulse shapes in time [43]. Suppose the intra-cavity field amplitude at the beginning and at the end of m-th round-trips are $E^{(\mathrm{m})}(z = 0, T)$, and $E^{(\mathrm{m})}(z = L = 2\pi R, T)$, respectively where the cavity circumference is L. z, T, and θ measure the propagation distance, propagation time, and the power-coupling strength of the MR, respectively. Therefore, the intra-cavity field-amplitude at the beginning of the $(m + 1)$-th round-trip is,

$$E^{(m+1)}(0,T) = \sqrt{1-\theta}E^{(m)}(L,T)\, e^{i\phi_0} + \sqrt{\theta}E_{\text{in}} \tag{4.1}$$

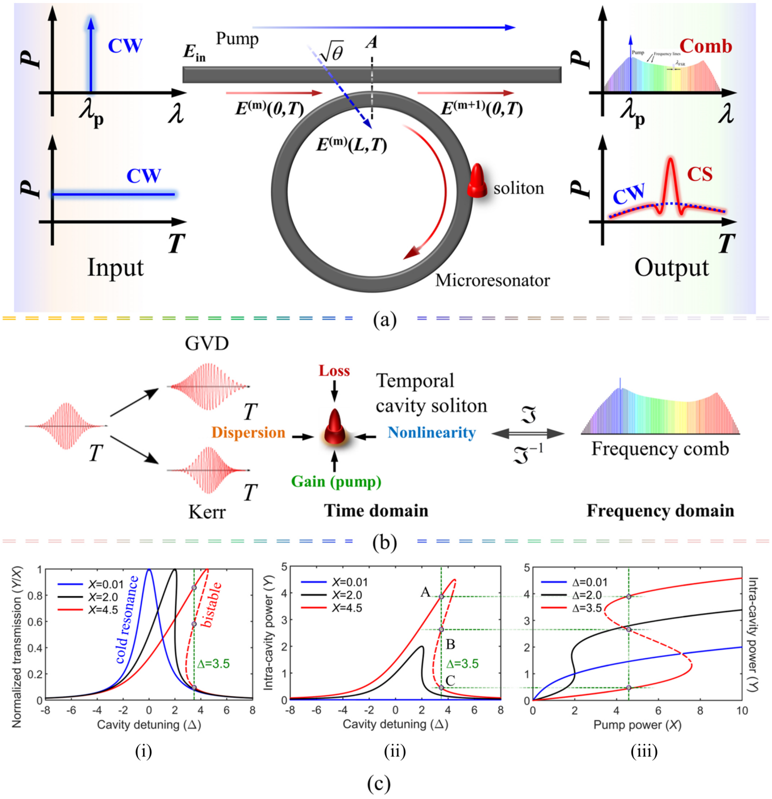

Figure 4.5: (a) Schematic of an MRR with CW input. At the throughport, FC is generated. (b) Underlying physics to generate a temporal CS which is the Fourier-equivalent of the FC. (c) Kerr-tilt and corresponding bistable behavior of the nonlinear cavity under external pump.

where the linear phase accumulation in a single round-trip is denoted by ϕ_0. This equation dictates the boundary condition of the MR. The Kerr nonlinearity is taken into consideration by nonlinear Schrödinger equation,

$$\frac{\partial E\left(z,T\right)}{\partial z}=\left[-\frac{\alpha_{\mathrm{i}}}{2}+i\sum_{k\geq 2}\frac{\beta_k}{k!}\left(i\frac{\partial}{\partial T}\right)^k+i\gamma\left|E\left(z,T\right)\right|^2\right]E\left(z,T\right) \tag{4.2}$$

Equation 4.1 combined with Eq. 4.2 represent the infinite dimensional Ikeda map which is adequate to describe the complete dynamical behavior of the Kerr MR under the slowly varying envelope approximation [44]. Eq. 4.2 is homologous to,

$$\begin{aligned}\frac{E\left(z+\Delta z,T\right)-E\left(z,T\right)}{\Delta z}=&-\frac{\alpha_{\mathrm{i}}}{2}E\left(z,T\right)+i\sum_{k\geq 2}\frac{\beta_k}{k!}\left(i\frac{\partial}{\partial T}\right)^k E\left(z,T\right)\\&+i\gamma\left|E\left(z,T\right)\right|^2E\left(z,T\right)\end{aligned} \tag{4.3}$$

where α_{i} is the round-trip power loss coefficient, β_{k} is the k-th order dispersion coefficient associated with the Taylor series expansion of the propagation constant β. $\gamma\,(= n_2\omega_0/cA_{\mathrm{eff}})$ is the nonlinear coefficient where n_2 is the nonlinear refractive index and A_{eff} represents the effective modal area. If the evolution of the intracavity field is sufficiently slow on the round-trip time scale, one can infer that,

$$\begin{aligned}\frac{E^{(m)}\left(L,T\right)-E^{(m)}\left(0,T\right)}{L} &\approx \frac{\partial E^{(m)}\left(0,T\right)}{\partial z}\\ &\approx \left[-\frac{\alpha_{\mathrm{i}}}{2}+i\sum_{k\geq 2}\frac{\beta_k}{k!}\left(i\frac{\partial}{\partial T}\right)^k+i\gamma\left|E^{(m)}\left(0,T\right)\right|^2\right]E^{(m)}\left(0,T\right)\end{aligned}\tag{4.4}$$

The Eq. 4.4 can be rewritten as,

$$E^{(m)}\left(L,T\right)\approx\left[1-\frac{\alpha_{\mathrm{i}}L}{2}+i\sum_{k\geq 2}\frac{\beta_k L}{k!}\left(i\frac{\partial}{\partial T}\right)^k+i\gamma L\left|E^{(m)}\left(0,T\right)\right|^2\right]E^{(m)}\left(0,T\right)\tag{4.5}$$

Equation 4.5 is obtained by integrating Eq. 4.4 from 0 to L considering an average value of the $E^{(\mathrm{m})}(z,T) = E^{(\mathrm{m})}(0,T)$ throughout the integration and henceforth is known as Mean-field equation. We define the cavity detuning δ_0 equals to $(2l\pi - \phi_0)$ where l corresponds to the nearest cold cavity resonance to the ϕ_0. Thus, the intra-cavity E-field at the beginning of the $(m+1)$-th round-trip is given by,

$$\begin{aligned}E^{(m+1)}\left(0,T\right)=&\sqrt{1-\theta}E^{(m)}\left(L,T\right)e^{i\phi_0}+\sqrt{\theta}E_{\mathrm{in}}\\ \simeq&\left(1-\frac{\theta}{2}-i\delta_0\right)E^{(m)}\left(L,T\right)+\sqrt{\theta}E_{\mathrm{in}}\end{aligned}\tag{4.6}$$

We assume the loss factor ($\theta \to 0$) and the cavity detuning (δ_0) is very small. In deriving LLE one also requires to assume that the Q-factor and the finesse $\mathcal{F} \sim 10^2$–10^5 [36,37] of the cavity is sufficiently high and the dispersion is low over the single round-trip, i.e., $\sum_{k\geq 2}\beta_{\mathrm{k}}L\Delta\omega^k/k! \leq \pi$ where $\Delta\omega$ is the spectral width of the generated comb. Therefore, putting the value of $E^{(m)}\left(L,T\right)$ (from Eq. 4.5) in terms of $E^{(m)}(0,T)$ to Eq. 4.6, we can further obtain,

$$E^{(m+1)}(0,T) - E^{(m)}(0,T) = \Bigg(-\alpha - i\delta_0 + i\sum_{k\geq 2} \frac{\beta_k L}{k!}\left(i\frac{\partial}{\partial T}\right)^k + i\gamma L\left|E^{(m)}(0,T)\right|^2 \Bigg) E^{(m)}(0,T) + \sqrt{\theta}E_{\text{in}} \tag{4.7}$$

We obtain Eq. 4.7 from Eq. 4.6 by linearizing and neglecting the nonlinear multiplicative terms of α_{i}, δ_0, and β_{k}, etc. as they are very very small, assuming, $\alpha = (\alpha_{\text{i}}L + \theta)/2$. Now, one can define a continuous time variable viz. slow time (t) which relates the discrete cavity round-trip number m with the cavity round-trip time t_{R} as $t = mt_{\text{R}}$ such as,

$$E^{(m)}(L=0,T) = E(t = mt_{\text{R}}, T) \tag{4.8}$$

It is crucial to note that this slow-time (t) frame fundamentally differs from the fast-time (T). Slow-time provides the information about how many times the pulse has been revolved (or crossed the point 'A' in Fig. 4.5 (a)) around the resonator whereas, the fast-time frame that moves with the pulse describes the temporal evolution of the pulse. One can also relate the slow-time corresponds to an integer value of m with the distance (z) traversed by the pulse as, $z\ (t = mt_{\text{R}}) = mL$. Hence, the expression of the E-field in the left-hand side of the Eq. 4.7 can be represented in terms of the slow-time (t) as

$$t_{\text{R}}\frac{\partial E(t,T)}{\partial t} = \left(-\alpha - i\delta_0 + i\sum_{k\geq 2}\frac{\beta_k L}{k!}\left(i\frac{\partial}{\partial T}\right)^k + i\gamma L|E(t,T)|^2\right)E(t,T) + \sqrt{\theta}E_{\text{in}} \tag{4.9}$$

The Eq. 4.9 also known as Lugiato-Lefever equation is numerically less intensive, can be solved easily through SSFM and is sufficiently accurate in predicting the pulse behavior influenced by Kerr nonlinearity in an optical microresonator.

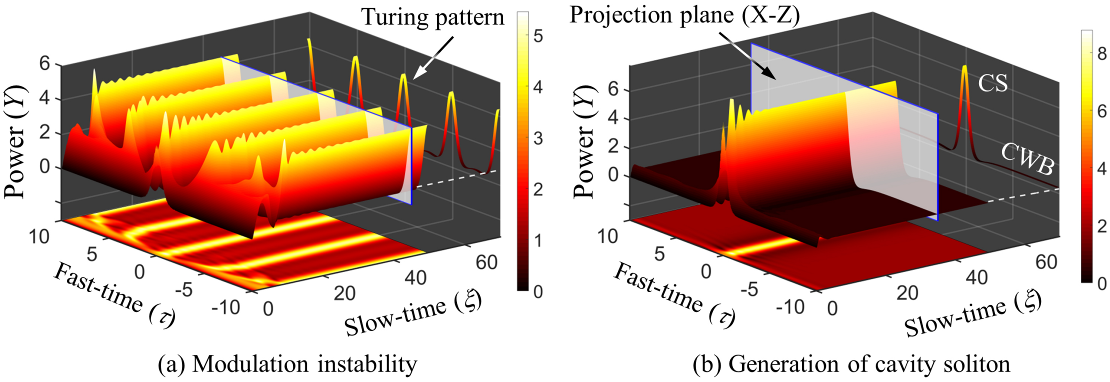

(a) Modulation instability

(b) Generation of cavity soliton

Figure 4.6: (a) Generation of Turing rolls from vacuum fluctuation. The SSFM-simulation parameters are: $\Delta = 1.5$, $X = 2.5$, (b) generation of temporal CS with the simulation parameters: $\Delta = 2.8$, $X = 3$. All the parameters plotted (e.g. fast-time (τ), slow-time (ξ), and intra-cavity power (Y)) are normalized at anomalous dispersion regime.

4.2.2.2 Normalization and Universal Scaling Law

It is more convenient to handle the normalized form of the LLE compared to the form given by Eq. 4.9 [37],

$$\frac{\partial u\left(\xi,\tau\right)}{\partial \xi} = -\left(1 + i\Delta\right)u - i\frac{s}{2}\frac{\partial^2 u}{\partial \tau^2} + \sum_{k\geq 3}\frac{d_k}{k!}\frac{\partial^k u}{\partial \tau^k} + i|u|^2 u + S \tag{4.10}$$

where $u(\xi,\tau)$, ξ, τ, Δ, s, d_k, and S denote the normalized field amplitude, normalized slow-time, normalized fast-time, normalized cavity detuning, normalized second-order dispersion coefficient (e.g. $s = -1$ for anomalous and $s = 1$ for normal dispersion), higher-order dispersion coefficient, and the normalized input pump amplitude, respectively. The normalized factors are as follows: $u = E\sqrt{\left(\frac{\gamma L}{\alpha}\right)}$, $\tau = T/T_0$, $T_0 = \sqrt{\frac{|\beta_2| L}{\alpha}}$, $\xi = t/L_{\mathrm{D}}$, $L_{\mathrm{D}} = t_{\mathrm{R}}/\alpha$, $\Delta = \delta_0/\alpha$, $S = \sqrt{\frac{\theta\gamma L}{\alpha^3}}E_{\mathrm{in}}$.

The steady-state homogeneous solution of Eq. 4.10 is given by,

$$X = \left[\left(1+\Delta^2\right)Y - 2\Delta Y^2 + Y^3\right] \tag{4.11}$$

where $X = |S|^2$ and $Y = |u|^2$ are the normalized input power and the normalized intra-cavity power, respectively. If the normalized detuning $\Delta > \sqrt{3}$, then bistability (BS) response or S-shaped hysteresis curve can be obtained as shown in Fig. 4.5 (c) where the dotted middle portion is unconditionally and homogeneously unstable with respective to the periodic perturbations. The cavity resonance is also tilted (peak at $\Delta = X = Y$) as a consequence of Kerr nonlinearity, whereas, peak occurs at $\Delta = 0$ (known as cold cavity response) in case of linear cavity. Kerr-tilt is shown in Fig. 4.5 (c-i) and for the plotting purpose we choose $X = 0.01 \approx 0$ to display the cold-resonance. Therefore, for a passive cavity, a weak periodic perturbation leads to the MI which in turn is ultimately stabilized by the dissipation of the cavity to spawn a periodic pattern called the Turing rolls, both in anomalous and normal dispersion regime. To obtain MI-gain, both the intra-cavity power and pump power required to be ≥ 1. In anomalous dispersion ($s = -1$), if $\Delta > 2$, minimum Y that initiates the MI has to be greater than $\Delta/2$ implying the entire upper branch of the homogeneous response will be unstable [37].

We validate our model through SSFM [36, 37]; Fig. 4.6 (a) illustrates the formation of turing pattern at $\Delta = 1.5$, and $X = 2.5$, while the Fig. 4.6 (b) delineates the evolution of a CS at $\Delta = 2.8$, and $X = 3$, both in anomalous dispersion regime. Note that, in anomalous regime, MI occurs sub- and super-critically at $\Delta > 41/30$ and $\Delta < 41/30$, respectively (higher-order dispersions are neglected). Stable CS co-exists with the CW-background (CWB) as shown in Fig. 4.6 (b) and becomes stable approximately from $\pi^2 X/8$. The in-depth analysis of the spatio-temporal dynamics of such nonlinear cavity-system is given in [45, 46].

4.3 Effects of Nonlinear Losses on Kerr Comb

As it is discussed earlier in this chapter, CW pumped optical MRs have been vastly exploited to generate FC utilizing the Kerr nonlinearity. Most of the nonlinear materials used to build photonic platforms exhibit nonlinear losses such as multi-photon absorption, FCA, and FCD which can strongly affect their nonlinear performances. In this section, we model the Kerr FC based on modified LLE along with the rate equation and develop analytical formulations to make a quick estimation of the steady-state, BS, self-pulsation (SP), MI gain and bandwidth in presence of nonlinear losses. The analytical model is valid over a broad wavelength range as it includes the effects of all nonlinear losses. Higher order (>3) characteristic polynomial of intra-cavity power describing the steady-state homogeneous solution of the modified LLE are discussed in detail. We derive the generalized analytical expressions for the threshold (normalized) pump detuning that initiates the optical BS when nonlinear losses are present. Free-carrier dispersion-led nonlinear cavity detuning is observed through the reverse Kerr-tilt of the resonant peaks. We further deduce the expressions of the threshold pump intensity and the range of possible cavity detuning for the initiation of the MI considering the presence of nonlinear losses. The proposed model will be helpful in explaining several numerical and experimental results which are previously reported and thereby will be able to provide a better understanding of the comb dynamics.

4.3.1 Motivation: Different Material Platforms

Varieties of materials have been used along with different novel fabrication techniques to design ultra-high quality factor MRs [5, 47, 48] for low threshold, stable FC generation; however, the search for the most suitable material is still on. FC generation in crystalline fluorides [49–53], hydex glass [54], diamond [55], quartz [56], aluminum nitride (AlN) [57, 58], lithium niobate ($LiNbO_3$) [59], aluminium gallium arsenide (AlGaAs) [60], silica (SiO_2) [5, 22], and silicon nitride (SiN/Si_3N_4) [61] have already been demonstrated. Table A.1 contains some of the relevant optical properties of the vastly used potential fluoride glasses which have a broad transparency window. Beryllium fluoride (BeF_2) and radium fluoride (RaF_2) are discarded as BeF_2 is soluble in water and harder to shape or produce MR through the conventional process flow [62] whereas, RaF_2 is radioactive. Most of the fluorides have cubic crystalline (Pearson symbol cF12 and space group $Fm\bar{3}m$, #225) structure except magnesium fluoride (MgF_2), that has rutile/tetragonal crystal structure (tP6, space group $P4_2/mnm$, #136) and shows birefringence which makes the material platform interesting for myriad of nonlinear applications. The resonators made of CFs have typically more than a billion Q-factor, and a threshold power (P_{th}) as low as 0.30 mW. Additionally, they do not exhibit nonlinear losses in telecom wavelength due to their high band-gap energies (E_{g}) as adduced from Table A.1. Nevertheless, they are not CMOS compatible [63].

Silicon-based platforms are often preferred due to several advantages such as tight optical confinement, high Kerr-coefficient, transparency over a broad wavelength range (telecom to mid-IR), low-cost and most importantly its compatibility with the existing microelectronics industry [64]. High refractive index (RI) contrast between silicon and other cladding materials (air, silica) results in strong optical confinement in silicon waveguides which allows sharp waveguide bends that help to reduce the device footprint [65]. Tight confinement also enhances the effective nonlinearity, which facilitates the realization of different nonlinear phenomena with a very low input power [66, 67]. It has been shown that efficient dispersion engineering in slot waveguide has the potential to achieve broadband frequency combs [68]. Silicon, on the other hand, exhibits strong 2PA when operating below $2.2\,\mu$m wavelength [69, 70], which has been exploited to realize all-optical logic operations [71] as well as all-optical signal processing [72]. Note that, nonlinear RI, 2PA, free-carrier absorption, etc. depend upon the material structure, bandgap energy and wavelength of operations. The allotropes of silicon viz. crystalline silicon (c-Si) (face-centered diamond-cubic, Fd-3m, #227), and amorphous silicon (a-Si) having bandgap energies of 1.1 eV and ∼1.6–1.7 eV, respectively, are being used in various optical applications [73] (Table A.2). Although optical waveguides made of c-Si has a very low linear propagation loss (0.2–1 dB/cm) and high $\chi^{(3)}$ nonlinearity, high 2PA reduces the figure of merit (FOM) of c-Si in nonlinear applications [67] thereby restricting the use of c-Si in most of the nonlinear and quantum photonic applications in the telecom and near-IR (NIR) wavelength ranges [74]. a-Si is easier to deposit and therefore, has been used to fabricate slot-waveguides [75]. The waveguides made of a-Si have relatively higher propagation loss (∼6–7 dB/cm) due to high material absorption [75]. If hydrogenated (a-Si:H), the effective bandgap/mobility gap of a-Si can increase up to 1.9 eV [73]. Interestingly, though the effective bandgap energy of a-Si or a-Si:H is much higher than the c-Si, still a-Si and a-Si:H exhibit comparatively larger 2PA in the C-band due to the amorphous nature of the material (i.e., the presence of exponential band tails). However, overall FOM for a-Si:H can be improved by 5-15 times as the nonlinear RI of a-Si:H is an order higher than that of c-Si [73].

Apart from silicon, GaAs, AlGaAs, Ge, etc. have 2PA in C-band owing to their bandgap energies. $\mathrm{Al}_x\mathrm{Ga}_{1-x}\mathrm{As}$ has similar lattice structure (zincblende) as that of GaAs with slightly larger bandgap depending upon 'x', and therefore, exhibits 2PA in relatively shorter wavelength (Table A.3). Nevertheless, AlGaAs is identified as one of the potential nonlinear materials for FC generation due to its very high nonlinear refractive index [60] and popularly known as the 'silicon of nonlinear optics'! SiC, chalcogenide glasses such as As_2S_3, As_2Se_3 possess 3PA, whereas, GaN has 4PA in telecommunication wavelength. Silicon also exhibits 3PA and 4PA losses in mid-IR and far-IR wavelength ranges [76]. Due to its low nonlinear losses, silicon-nitride (SiN) or trisilicon tetranitride (Si_3N_4) is often a preferred choice over silicon for nonlinear applications [77] at an expense of Kerr coefficient (an order lesser than the silicon). Recently, octave-spanning FC has been demonstrated both in Si_3N_4 [78] and Si-MRRs [79, 80]. Note that, comb generation is possible through both the 2nd and 3rd order nonlinear interactions in Pockels/non-centrosymmetric medium, e.g. AlGaAs, AlN, GaP, as well as in Kerr/centrosymmetric materials such as Si_3N_4, Si, etc. either at crystal-surface or in the presence of external stress [81, 82]. Different optical properties of widely used essential nonlinear materials are listed in Table A.3. Other than these, FC is also demonstrated in a few exotic platforms, for instance, organically modified silica micro-cavities by Shen *et al.* in 2017 [83] with a very low threshold power, microring resonator partially molded by graphene layer with wide tunability [84], etc. Thus, a more realistic theoretical study on comb dynamics applicable for a broad wavelength range of operation becomes indispensable where all the nonlinear losses and higher-order dispersion terms are being considered. Nonlinear losses include multi-photon absorptions (2PA, 3PA, 4PA), FCA, and FCD. As discussed earlier, generalized mean-field LLE is used to model the Kerr FC in a high-Q, high-finesse optical micro-cavity where the dispersion, nonlinear phase accumulation over a round-trip and pump detuning is low [36]. It is known that temporal CS generates Cherenkov radiation (dispersive-wave) in the presence of higher-order dispersions, which leads to octave-spanning FC [36]. Recently, numerical studies have shown that FCA-induced FCD causes nonlinear cavity detuning which in turn helps to generate optical FC even in the absence of linear detuning of the CW pump [85]. 2PA in telecom/NIR and 3PA with FCA, FCD in short and mid-IR wavelength range generally inhibit the parametric oscillation in silicon-waveguide [76]. External reverse-biased p-i-n junction, which is fabricated along the cross-section of the Si-waveguide, has been employed to combat the free-carrier induced nonlinear losses [79]. The external bias minimizes the FCA-FCD effects by sweeping the generated free-carriers. This method facilitates broadband (2.1 μm–3.5 μm [79] and 2.4 μm–4.3 μm [35]) FC over the mid-IR wavelengths. Breather solitons have been demonstrated both in Si_3N_4 and Si-waveguides and the effect of 3PA along with the corresponding FCA-FCD is taken into consideration in the theoretical models [35, 86]. Self-pulsating phenomenon in the presence of 2PA is also discussed [87]. However, a detailed theoretical study that includes the effects of all nonlinear losses and free-carriers on the generation of Kerr-comb is still scarce.

In this chapter, we obtain the steady-state homogeneous solutions of free-carrier driven generalized mean-field LLE and report the reverse Kerr-tilt as a consequence of FCA-FCD induced nonlinear cavity detuning [88]. The characteristic polynomials for the steady-state homogeneous solutions of the LLE possessing all the nonlinear losses are derived having an order greater than three instead of the well-known cubic polynomial [37]. In subsequent sections, we discuss the threshold detuning to initiate the BS in the presence of multi-photon absorption and free-carrier effects, which is a necessary condition to obtain FC. Finally, we generalize the existing formulations [37, 89, 90] to study the MI in the presence of higher-order dispersion terms, 2PA, 3PA, 4PA, FCA, and FCD. Most of the parameters used in simulations are taken from [76]. To validate the analytical model, we solve the modified LLE along with the coupled rate equations numerically through the SSFM. Our theoretical study can explain several experimental results [35, 76, 78], and thereby provides an in-depth understanding of the FC dynamics in the most practical scenarios.

4.3.2 Theoretical Model

Micro-resonator based Kerr FC can be modeled by mean-field LLE. Solving the LLE is computationally less intensive than other methods [36, 39], while the numerical results obtained from LLE match with the experiments reasonably well even for octave-spanning FC.

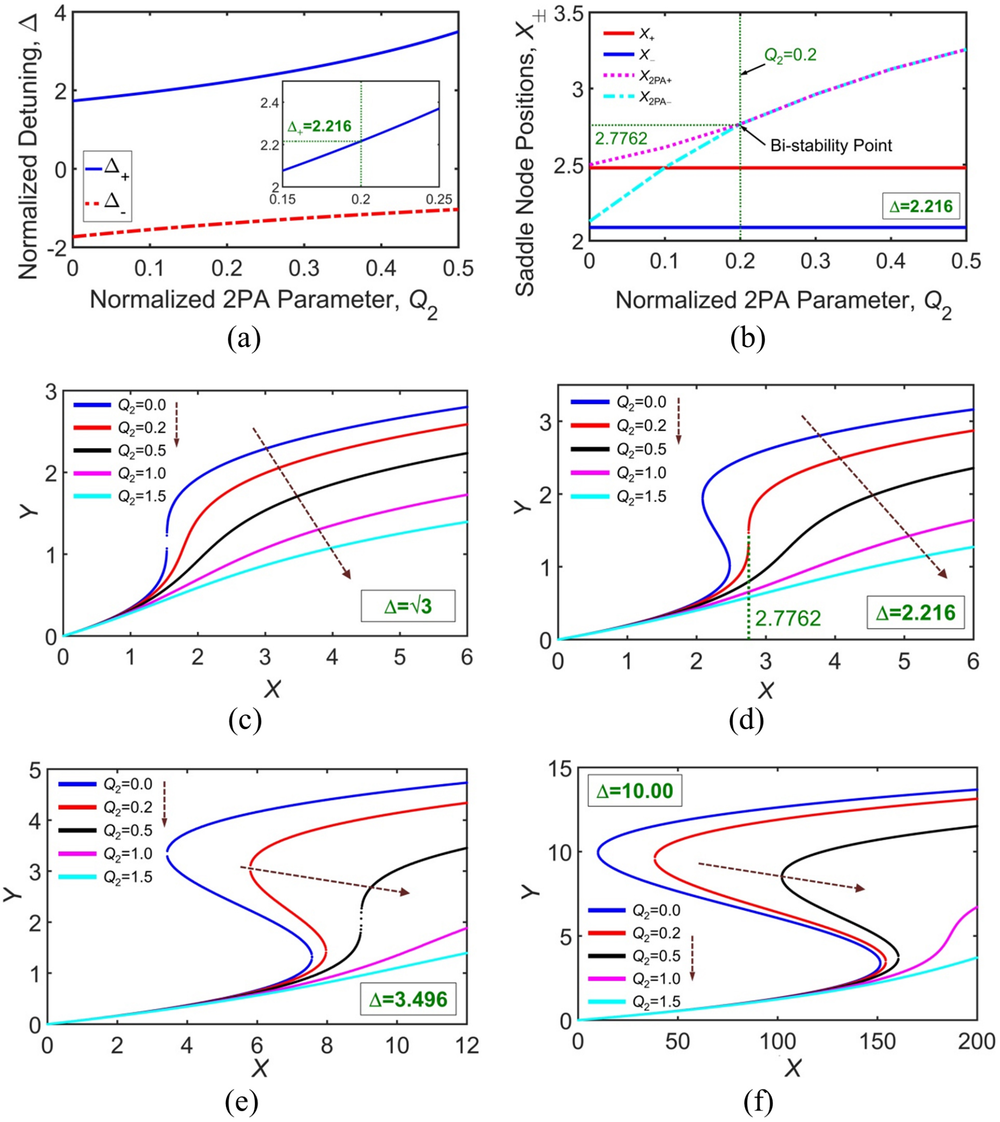

(a) (b)

(c) (d)

(e) (f)

Figure 4.7: Effect of 2PA on optical BS. (a) Normalized detuning Δ vs. normalized 2PA coefficient Q_2, (b) Saddle node positions, $X_\pm$ and $X_{2\mathrm{PA}\pm}$ with Q_2 when Δ is fixed at 2.216. Intra-cavity power Y with the change in input pump power, X for (c) $\Delta = \sqrt{3}$, (d) $\Delta = 2.216$, (e) $\Delta = 3.496$, and (f) $\Delta = 10$, with a set of five different values of Q_2, in each case ($Q_2 = 0, 0.2, 0.5, 1.0$ and 1.5). Bistable behavior initiates at $\Delta = \sqrt{3}$, 2.216, and 3.496 when the Q_2 is 0, 0.2 and 0.5, respectively. For $Q_2 > 2/\sqrt{3}$, bistability does not occur even if Δ is as high as 10.0 (4.7 (a) and 4.7 (f)) with positive and realistic values of X and Y.

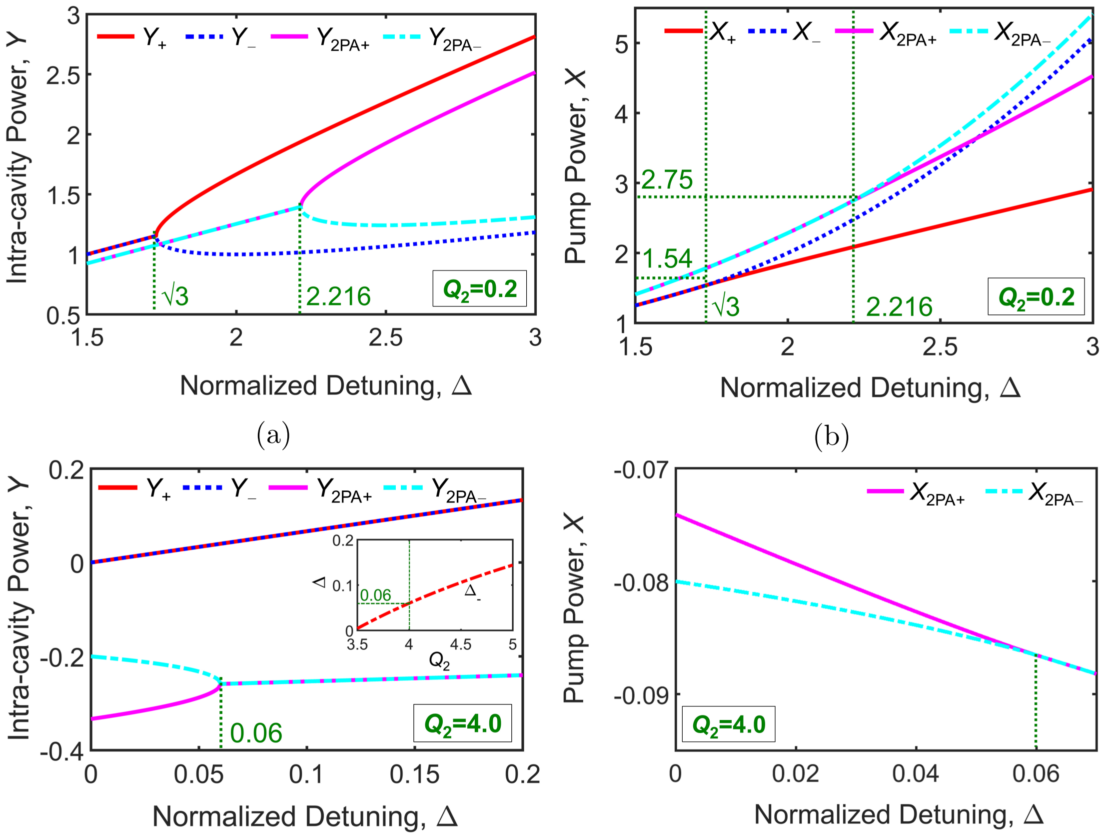

(a) (b) (c) (d)

Figure 4.8: The possible range of 2PA coefficient for which BS can occur. Intra-cavity power Y with respect to normalized detuning Δ at (a) $Q_2 = 0.2$, (c) $Q_2 = 4$. Input pump power X vs. Δ at (b) $Q_2 = 0.2$, (d) $Q_2 = 4.0$. Bistability occurs at a positive value of Y and X if $Q_2 = 0.2 (< 2/\sqrt{3})$, whereas, BS can be obtained for a very small value of Δ, with negative values of X and Y when $\Delta = 4 (> 2\sqrt{3})$.

4.3.2.1 Normalization of LLE

The generalized mean-field Lugiato-Lefever equation including multi-photon absorption, FCA and FCD to model the Kerr-comb along with the rate equation can be written as [76],

$$t_{\mathrm{R}} \frac{\partial E(t,T)}{\partial t} = \Bigg[-(\alpha + i\delta_0) + iL \sum_{k\geq 2} \frac{\beta_{\mathrm{k}}}{k!} \left(i\frac{\partial}{\partial T} \right)^k + \left(1 + \frac{i}{\omega_0} \frac{\partial}{\partial T} \right)$$

$$\left(i\gamma L |E(t,T)|^2 - \frac{\beta_{2\mathrm{PA}} L}{2A_{\mathrm{eff}}} |E(t,T)|^2 - \frac{\beta_{3\mathrm{PA}} L}{3A_{\mathrm{eff}}^2} |E(t,T)|^4 \right.$$

$$-\frac{\beta_{4\mathrm{PA}}L}{4A_{\mathrm{eff}}^{3}}|E\,(t,T)|^{6}\Bigg)-\frac{\sigma L}{2}\,(1+i\mu_{\mathrm{c}})\,N_{\mathrm{c}}\,(t,T)\Bigg]E(t,T)+\sqrt{\theta}E_{\mathrm{in}} \tag{4.12}$$

$$\frac{\partial N_{\mathrm{c}}\,(t,T)}{\partial T}=\frac{\beta_{2\mathrm{PA}}}{2\hbar\omega_0}\frac{|E\,(t,T)|^{4}}{{A_{\mathrm{eff}}}^{2}}+\frac{\beta_{3\mathrm{PA}}}{3\hbar\omega_0}\frac{|E\,(t,T)|^{6}}{{A_{\mathrm{eff}}}^{3}}+\frac{\beta_{4\mathrm{PA}}}{4\hbar\omega_0}\frac{|E\,(t,T)|^{8}}{{A_{\mathrm{eff}}}^{4}}-\frac{N_{\mathrm{c}}\,(t,T)}{\tau_{\mathrm{eff}}} \tag{4.13}$$

Where t, T and $t_{\mathrm{R}}\,(=\mathrm{FSR}^{-1})$ represent the fast-time, slow-time, and the round-trip time, respectively. $E(t,T)$ is the field amplitude, whereas α, δ_0, L, β_k, ω_0, E_{in} denote the dimensionless total round-trip loss coefficient, external pump detuning, cavity perimeter length, k-th order dispersion coefficient, the angular frequency of the CW-pump and input pump amplitude, respectively. $\beta_{\mathrm{nPA}}(n=2,3,4)$, σ, μ_{c}, N_{c}, A_{eff}, t_{eff}, and $\hbar\,(=h/2\pi)$ are the multi-photon absorption coefficient, FCA, FCD, free-carrier density, effective mode area, carrier lifetime and reduced Plancks constant, respectively. At first, we neglect the self-steepening term and normalize [36] the LLE and the rate-equation including multi-photon absorption (nPA), FCA and FCD terms in convenient compact series forms, as given by Eqs. 4.14 and 4.15, respectively where n runs from 2 to 4.

$$\frac{\partial u}{\partial\xi}=-\left(1+i\Delta\right)u-\frac{1}{2}\left(1+iK\right)\phi_{\mathrm{c}}u-i\frac{s}{2}\frac{\partial^2 u}{\partial\tau^2}+\sum_{k\geq 3}\frac{d_{\mathrm{k}}}{k!}\frac{\partial^k u}{\partial\tau^k}$$
$$+\,i|u|^2u-\sum_{n=2}^{4}\frac{Q_{\mathrm{n}}}{n}|u|^{2(n-1)}u+S \tag{4.14}$$

$$\frac{\partial\phi_{\mathrm{c}}}{\partial\tau}=\sum_{n=2}^{4}\theta_{\mathrm{c_n}}|u|^{2n}-\frac{\phi_{\mathrm{c}}}{\tau_{\mathrm{c}}} \tag{4.15}$$

$u(\xi,\tau)$, ξ, τ, Δ, K, ϕ_{c}, s, d_{k}, Q_{n} (n = 2, 3, 4), S , θ_{cn} (n=2, 3, 4) and τ_{c} are the normalized- intra-cavity field amplitude, slow-time, fast-time, pump detuning, FCD coefficient, free-carrier density, second and higher-order dispersion terms, multi-photon absorption coefficients, pump amplitude, FCA coefficients and normalized carrier lifetime, respectively where possible values of the normalization factors are given in Table A.4 [91,92]. One can easily calculate the values of normalized parameters that correspond to the experimentally obtained parameters from table-2 of Ref. [91]. As the carrier life-time (τ_{eff}) is usually greater than round-trip time (t_{R}), one should consider the carrier accumulation over successive round-trips through the boundary condition, $N_{\mathrm{c}}(t, -t_{\mathrm{R}}/2) = N_{\mathrm{c}}(t + \Delta t, +t_{\mathrm{R}}/2)$. Similarly, t_{c} is also greater than normalized cavity round-trip time $t'_{\mathrm{R}}(= t_{\mathrm{R}}/L_{\mathrm{D}})$ and $\phi_{\mathrm{c}}(\xi, -t'_{\mathrm{R}}/2) = \phi_{\mathrm{c}}(\xi + \Delta\xi, +t'_{\mathrm{R}}/2)$. At the steady-state, $\phi_{\mathrm{c}}(\xi, -t'_{\mathrm{R}}/2) = \phi_{\mathrm{c}}(\xi + \Delta\xi, +t'_{\mathrm{R}}/2) = \phi_0$ where ϕ_0 is the steady-state free-carrier concentration. Equations 4.14 and 4.15 can further be simplified by assuming the dominant multi-photon absorption terms only in the operating pump wavelength range. This assumption holds satisfactorily true when the nonlinear losses either inhibit the formation of FC or significantly reduce the span of the frequency comb. Nevertheless, Eqs. 4.14 and 4.15 are more suitable if the FC is octave spanned. Therefore, Eqs. 4.14 and 4.15 that include only the dominant nPA, FCA and FCD, and rate equations can be rewritten as,

$$\begin{aligned}\frac{\partial u}{\partial \xi} =& -(1 + i\Delta)\, u - \frac{1}{2}(1 + iK)\,\phi_{\mathrm{c}} u - i\frac{s}{2}\frac{\partial^2 u}{\partial \tau^2} \\ &+ \sum_{k\geq 3} \frac{d_{\mathrm{k}}}{k!}\frac{\partial^k u}{\partial \tau^k} + i|u|^2 u - \frac{Q_{\mathrm{n}}}{n}|u|^{2(n-1)} u + S \end{aligned} \tag{4.16}$$

$$\frac{\partial \phi_{\mathrm{c}}}{\partial \tau} = \theta_{\mathrm{c_n}}|u|^{2n} - \frac{\phi_{\mathrm{c}}}{\tau_{\mathrm{c}}} \tag{4.17}$$

where n=2 in case of 2PA is dominant, n=3 while 3PA is significant and n=4 while 4PA is the dominant nonlinear loss mechanism. As an example, depending upon the band-gap energy of silicon (i.e. E_{g} ~1.1 eV), only 2PA, 3PA or 4PA is significant at the operating wavelength $\lambda < 2.2\mu$m (telecommunication and near IR wavelength), $\lambda > 2.2\,\mu$m to $\lambda < 3.3\,\mu$m (short wavelength IR) and $\lambda > 3.3\,\mu$m (mid-IR), respectively, for silicon waveguides. Note that the operating wavelength range depends upon the doping concentration of the intrinsic material of the optical waveguide [79]. Free-carriers are generated through multi-photon absorption that induces additional FCA losses to the system. FCA is associated with the FCD as free-carriers are also able to modify the RI of the medium [76,79]. Particularly, if the intensity of the input incident pulse is very high, the effects of FCA and FCD will be crucial. However, in suitable conditions such as low pulse energy or in the presence of external bias that is able to sweep the free-carriers, the effects of FCA-FCD can be neglected [76]. The carrier-evolution given in Eq. 4.15 with respect to the slow-time can be rewritten in the following form after including the boundary condition:

$$\frac{\partial \phi_{\mathrm{c}}}{\partial \xi} = \theta_{\mathrm{c_n}} \left(\frac{1}{t_{\mathrm{R}}} \int_{-\frac{t_{\mathrm{R}}}{2}}^{\frac{t_{\mathrm{R}}}{2}} |u|^{2n} d\tau \right) - \frac{\phi_{\mathrm{c}}}{\tau_{\mathrm{c}}} \approx \theta_{\mathrm{c_n}} |u|^{2n} - \frac{\phi_{\mathrm{c}}}{\tau_{\mathrm{c}}} \tag{4.18}$$

The approximation given in Eq. 4.18 works reasonably well at steady-state or at the onset of both the SP and the MI. Realistic values of different parameters are taken from [76] and normalized [91]. In our simulations, the waveguide area and the effective area (A_{eff}) are equivalents [76, 93].

4.3.2.2 Steady-state Solutions

We find the stationary ($\partial u/\partial \xi = 0$), CW ($\partial u/\partial \tau = 0$) solutions of Eq. 4.16. In steady-state [94], the wave amplitude, u follows the relationship with the pump amplitude, S given by Eq. 4.19.

$$u = \frac{S}{(1+i\Delta) + \frac{1}{2}(1+iK)\sum_{n=2}^{4} C_{\mathrm{n}} |u|^{2\mathrm{n}} - i|u|^2 + \sum_{n=2}^{4} \frac{Q_{\mathrm{n}}}{n} |u|^{2(\mathrm{n}-1)}} \tag{4.19}$$

If the intra-cavity power and input pump power are denoted by $Y(= |u|^2)$ and $X(= |S|^2)$, respectively, the homogeneous, steady-state (HSS) solution of LLE can be expressed by the characteristics polynomial of Y having a degree of (2n+1) and can be written as Eq. 4.20 where n varies from 2 to 4 if 2PA, 3PA, and 4PA all are present. Thus the characteristic polynomial satisfies a nonic polynomial of Y.

$$\begin{aligned} X = {} & \left(1+\Delta^2\right) Y - 2\Delta Y^2 + Y^3 + 2\sum_{n=2}^{4} \frac{Q_{\mathrm{n}}}{n} Y^n \\ & + (1+\Delta K) \sum_{n=2}^{4} C_n Y^{n+1} - K \sum_{n=2}^{4} C_n Y^{n+2} + \sum_{n=2}^{4} \frac{{Q_{\mathrm{n}}}^2}{n^2} Y^{2n-1} \\ & + \frac{1}{4}\left(1+K^2\right) \sum_{n=2}^{4} C_n^2 Y^{2n+1} + \sum_{n=2}^{4}\sum_{q=2}^{4} \frac{C_{\mathrm{n}} Q_{\mathrm{q}}}{q} Y^{\mathrm{n+q}} \end{aligned} \tag{4.20}$$

In case, only one out of 2PA, 3PA and 4PA is dominant along with the FCA and FCD, Eq. 4.20 can be simplified as:

$$\begin{aligned} X = &\left(1+\Delta^2\right)Y - 2\Delta Y^2 + Y^3 + \frac{2}{n}Q_\mathrm{n}Y^n + C_\mathrm{n}\left(1+\Delta K\right)Y^{n+1} \\ &- KC_\mathrm{n}Y^{n+2} + \frac{{Q_\mathrm{n}}^2}{n^2}Y^{2n-1} + \frac{C_\mathrm{n}Q_\mathrm{n}}{n}Y^{2n} + \frac{{C_\mathrm{n}}^2}{4}\left(1+K^2\right)Y^{2n+1} \end{aligned} \tag{4.21}$$

Equation 4.21 can be reduced further into Eq. 4.22 in the presence of only multi-photon absorption whereas, FCA and FCD are negligible.

$$X = \left(1+\Delta^2\right)Y - 2\Delta Y^2 + Y^3 + \frac{2}{n}Q_\mathrm{n}Y^n + \frac{{Q_\mathrm{n}}^2}{n^2}Y^{2n-1} \tag{4.22}$$

Equation 4.23 is the HSS solution of LLE while multi-photon absorption, along with FCA is considered while the effect of FCD can be neglected.

$$\begin{aligned} X = &\left(1+\Delta^2\right)Y - 2\Delta Y^2 + Y^3 + \frac{2}{n}Q_\mathrm{n}Y^n + C_\mathrm{n}Y^{n+1} \\ &+ \frac{{Q_\mathrm{n}}^2}{n^2}Y^{2n-1} + \frac{C_\mathrm{n}Q_\mathrm{n}}{n}Y^{2n} + \frac{{C_\mathrm{n}}^2}{4}Y^{2n+1} \end{aligned} \tag{4.23}$$

It is clearly visible that the Eq. 4.23 becomes quintic, septic and a nonic polynomial of Y in the presence of either 2PA, 3PA or 4PA along with the corresponding FCA-FCD, respectively. Note that, all these Eqs. 4.20–4.23 are reduced to the well-known cubic polynomial of Y if all the nonlinear losses are neglected [37], as given in Eq. 4.11. C_n is defined as the product of θ_cn and the τ_c. Thus, the polynomial of degree (2n+1>3) accounts for the HSS solutions of LLE with all nonlinear losses.

4.3.3 Bistability and Kerr-tilt

Different important features such as the threshold pump power and threshold pump detuning that initiate the Turing pattern and eventually the stable FC can be retrieved from the BS curve and the Kerr-tilt which are obtained from the steady-state behavior of LLE [37, 89, 90]. In addition, the dynamics of FC can partially be understood through Kerr-tilt and the BS curve as the CS solutions of LLE results from the coexistence of patterned and CW solutions [94].

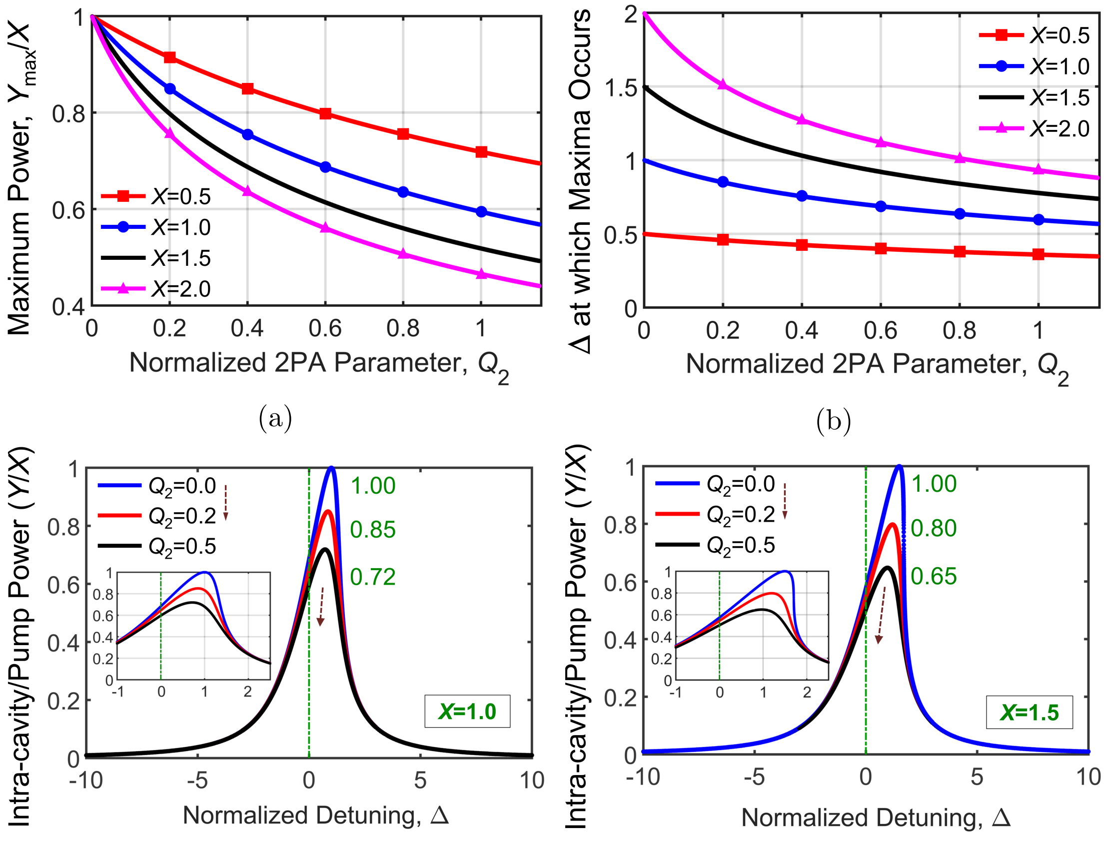

(a) (b) (c) (d)

Figure 4.9: Effect of 2PA on Kerr-tilt. (a) The ratio of maximum normalized intra-cavity power ($Y_{\max}$) and the normalized pump power (X) with 2PA parameters, (b) normalized detuning (Δ) with 2PA coefficient (Q_2) where the maxima occur. Kerr tilts with different 2PA coefficients when normalized input power is (c) $X = 1$, and (d) $X = 1.5$.

4.3.3.1 Threshold Condition to Initiate Optical Bistability

It is known that the minimum value of the normalized cavity detuning that can initiate the optical BS in the absence of all the nonlinear losses is $\sqrt{3}$ [37, 89, 90]. Multi-photon absorption along with FCA-FCD changes the threshold value of the cavity detuning. We show, in presence of 2PA, FCA-FCD, the HSS solution of the LLE satisfies the quintic polynomial of Y. However, if the FCA and FCD are negligible, the polynomial reduces to a cubic polynomial having 2PA coefficient

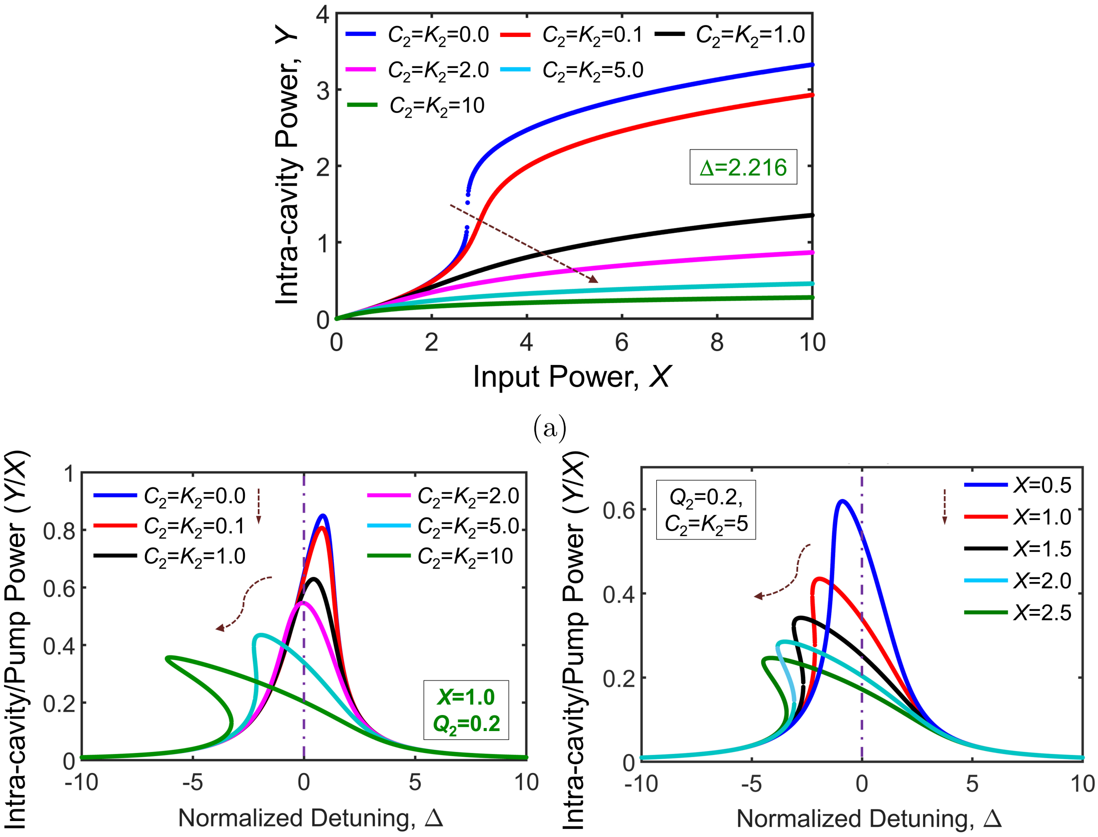

(a)

(b)

(c)

Figure 4.10: (a) Bistability curve at $\Delta = 2.216$, and (b) Kerr-tilt at $X = 1$, for a set of six different values of 2PA induced FCA-FCD (C_2 and K_2, respectively). (c) Dependence of Kerr tilt on input pump power X when $C_2 = K_2 = 5$. For all the cases, the 2PA coefficient, Q_2 is taken as 0.2.

$(Q_2 \neq 0, C_2 = 0, K = 0)$, and is given by:

$$X = \left(1 + \Delta^2\right) Y + \left(Q_2 - 2\Delta\right) Y^2 + \left\{1 + \frac{Q_2^2}{4}\right\} Y^3 \tag{4.24}$$

In this case, as Eq. 4.24 is a cubic polynomial of Y, it is possible to find out an analytical expression of the threshold value of the normalized cavity detuning that initiates the optical bistability. Equating the $dX/dY = 0$, one can obtain the value of detuning beyond which the intra-cavity power will be multi-valued, which is given by Eq. 4.25:

$$\Delta_{\pm} \geq \frac{8Q_2}{4-3Q_2^2} \pm \frac{\sqrt{3}}{4-3Q_2^2}\left(Q_2^2+4\right) \tag{4.25}$$

Negative values of Δ being neglected. We calculate the threshold value of Δ from Eq. 4.25 and plot in Fig. 4.7 (a). It is observed that 2PA increases the threshold of optical bistability. We also find the saddle-node positions $X_{\pm}$ of the bistable curve by plugging the Δ_{+} in Eq. 4.24.

$$\begin{aligned} X_{\pm} = & \pm\frac{4}{27}\left(\frac{1}{4+Q_2^2}\right)^2\left(\pm 4\Delta \mp 2Q_2 + \sqrt{4-3Q_2^2}\sqrt{\Theta}\right) \\ & \times \Bigg[12 + Q_2^2 + \Delta^2\left(4+3Q_2^2\right) \pm Q_2\sqrt{4-3Q_2^2}\sqrt{\Theta} \\ & + 2\Delta\left(4Q_2 \mp \sqrt{4-3Q_2^2}\sqrt{\Theta}\right)\Bigg] \end{aligned} \tag{4.26}$$

$$\Theta = \Delta^2 - \frac{16Q_2}{4-3Q_2^2}\Delta + \frac{Q_2^2-12}{4-3Q_2^2} \tag{4.27}$$

In the absence of 2PA, Eq. 4.26 reduces to the known expression:

$$X_{\pm} = \pm\left(\frac{2}{27}\right)\left(\pm 2\Delta + \sqrt{\Delta^2-3}\right)\left(3+\Delta^2 \mp \Delta\sqrt{\Delta^2-3}\right) \tag{4.28}$$

The intra-cavity steady-state power, $Y_{\pm}$ in the presence of 2PA can be given by,

$$Y_{\pm} = -\frac{1}{3}\frac{\left(Q_2-2\Delta\right)}{\left(1+\frac{Q_2^2}{4}\right)} \pm \frac{1}{6}\frac{\sqrt{4-3Q_2^2}}{\left(1+\frac{Q_2^2}{4}\right)}\sqrt{\Theta} \tag{4.29}$$

$$Y_{\pm} = \frac{1}{3}\left(2\Delta \pm \sqrt{\Delta^2-3}\right) \tag{4.30}$$

which reduces to the well-known Eq. 4.30 when $Q_2 = 0$. In Fig. 4.7 (b), $X_{\pm}$ and $X_{2\mathrm{PA}\pm}$ represent the values of normalized input pump power in the absence and presence of 2PA, respectively at which the BS starts (saddle nodes). In the absence of 2PA, both the curves (red curve) for X_{+} (X_{-}, blue curve) and the cyan curve for $X_{2\mathrm{PA}+}$ ($X_{2\mathrm{PA}-}$, magenta) initiate from the same point, as shown in Fig.

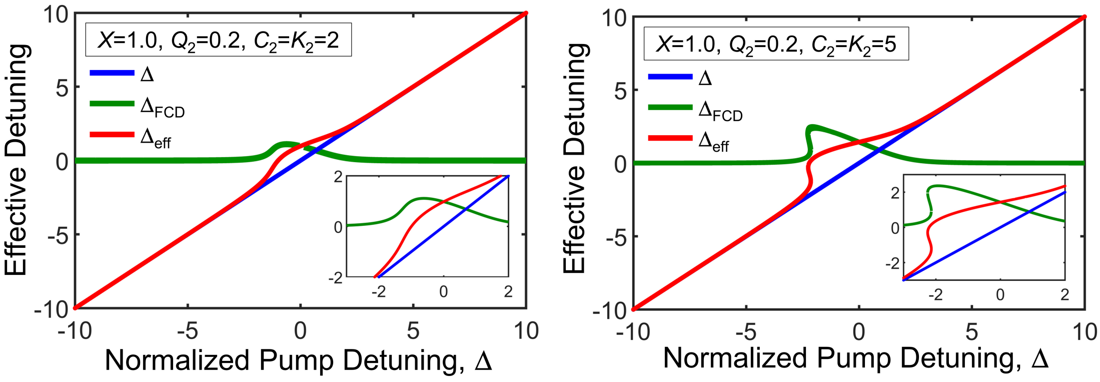

(a) (b)

Figure 4.11: Effective detuning Δ_{eff} (red curve) and FCD-induced detuning Δ_{FCD} (green curve), with the variation in pump detuning when (a) $C_2 = K_2 = 2$, and (b) $C_2 = K_2 = 5$ at input pump power, $X = 1$ in both the cases. Input pump detuning is also plotted (blue-curve) both in (a) and (b) to indicate the reference level in the absence of FCA-FCD. Δ_{FCD} can possess multiple values if FCA-FCD coefficients are high.

4.7 (b). For $Q_2 = 0.2$, when the detuning, Δ is 2.216, both the values of X_+ and X_- merge into 2.7762 and indicates that if the Q_2 is large, BS does not occur. As an example, we show that the 2PA increases the BS threshold as presented in Figs. 4.7 (c)–4.7 (f). If there is no 2PA, the BS occurs at $\Delta = \sqrt{3}$. However, if the 2PA coefficient Q_2 is 0.2 and 0.5, the minimum pump detuning that initiates the BS are 2.216 and 3.496, respectively. Also, it can easily be found that, for any of the two roots (Δ_+ or Δ_-) of Eq. 4.25 to be positive, the condition given by Eq. 4.31 has to be satisfied:

$$Q_2 \leq \frac{2}{\sqrt{3}} \text{ or } Q_2 \geq 2\sqrt{3} \tag{4.31}$$

Earlier, it has been predicted numerically that after a certain maximum value of 2PA coefficient, BS may cease to exist [95]. In contrast, our theoretical model predicts that it is possible to observe BS at $Q_2 \geq 2\sqrt{3}$ with a very small detuning (even less than $\sqrt{3}$) (as shown in Figs. 4.8(a)–4.8 (d)). For Figs. 4.8 (a)–4.8 (b), at first, we consider the case where Q_2 is less than $2/\sqrt{3}$ and show the values of intra-cavity and pump power for which the BS initiates. On the other hand, in Fig. 4.8 (c) we plot the intra-cavity and pump power for which the BS occurs when $Q_2 > 2\sqrt{3}$. To obtain BS in the latter case, the input pump power X and intra-cavity power Y both have to be negative, which is not possible in practice. Therefore, we restrict our analysis for 2PA coefficient within $2/\sqrt{3}(\approx 1.154)$ and discard the other possibilities. It should also be noted that although optical BS is a necessary condition for the formation of the optical cavity soliton, it is not a sufficient condition [95] to generate the cavity soliton.

B. Kerr-tilt with nonlinear losses

Resonance of a cavity is tilted as a consequence of Kerr nonlinearity. In these circumstances, the resonance peak occurs at the normalized pump detuning $\Delta = Y = X$ [94]. Therefore, the real roots of Eq. 4.32 which can be obtained by putting $\Delta = Y$ in Eq. 4.22, yield the maximum value of Y, i.e., $Y_{\max}$ for a particular normalized pump power, X in the presence of 2PA (n=2).

$$\frac{Q_{\mathrm{n}}^2}{n^2}Y^{2n-1} + \frac{2}{n}Q_{\mathrm{n}}Y^n + Y - X = 0 \tag{4.32}$$

The ratio of normalized intra-cavity power with respect to the normalized pump power (i.e. $Y_{\max}/X$) and the corresponding normalized detuning Δ at which the maxima occur are plotted in Figs. 4.9 (a) and 4.9 (b), respectively for different values of normalized TPA coefficients Q_2 (0-0.5). Figs. 4.9 (c) and 4.9 (d) show the Kerr-tilt for three distinct values of Q_2 (0, 0.2, and 0.5) at two different input pump powers ($X = 1$ and 1.5). It is apparent that higher the input pump power, greater is the slope of the Kerr-tilt, which means one requires larger external pump detuning to obtain maximum intra-cavity power. Besides, if the 2PA is present, with the increase in input pump power, intra-cavity power decreases as the nonlinear absorption is more prominent at comparatively high input power.

C. Bistability and Kerr-tilt in presence of FCA-FCD

In the previous section, we have provided a detailed quantitative analysis of the shift in Kerr-tilt as well as the reduction in the intra-cavity output power in the presence of 2PA. In this section, we discuss the optical BS and Kerr-tilt in the presence of FCA-FCD. To investigate the effect of FCA-FCD, we have assumed arbitrary values of FCA and FCD coefficients. The BS curves at a fixed pump detuning are plotted in Fig. 4.10 (a) for different values of FCA and FCD co-

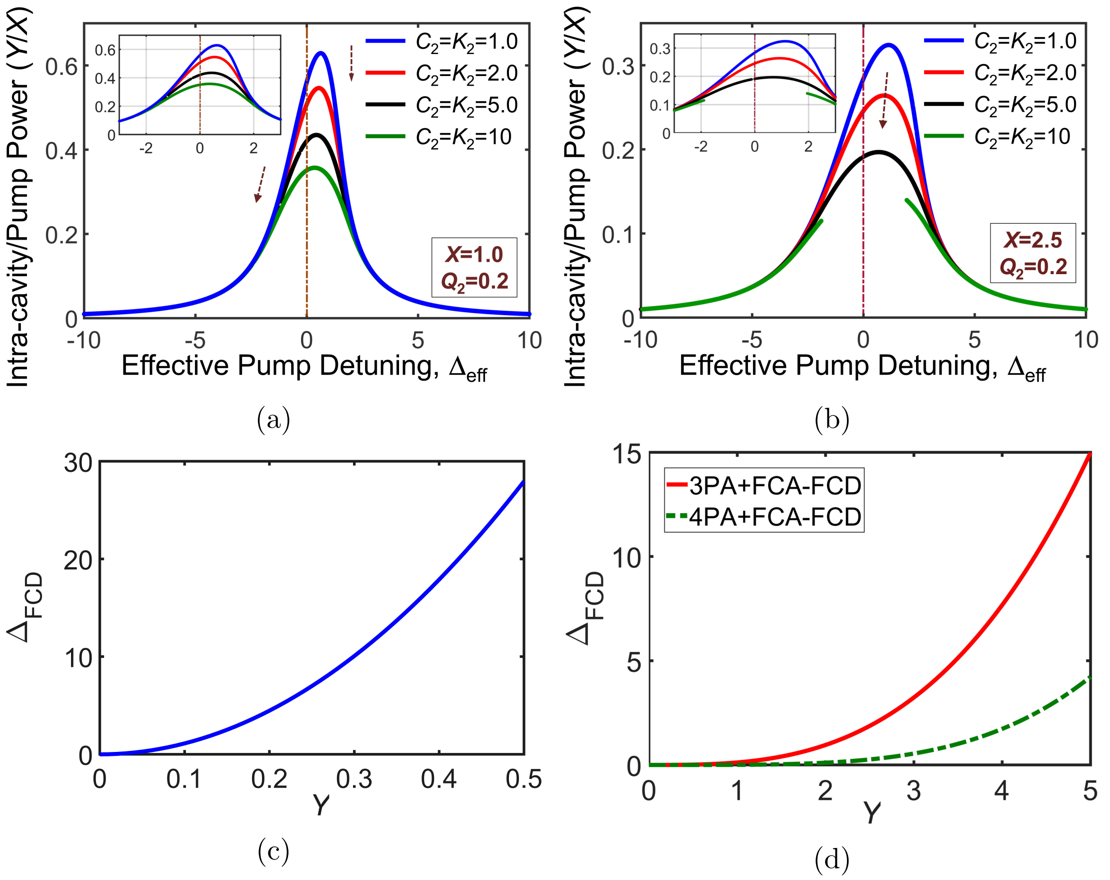

(a) (b)

(c) (d)

Figure 4.12: Kerr-tilt (Y/X) with the change in effective detuning (Δ_{eff}), instead of pump detuning (Δ) for two different pump powers: (a), $X = 1$, and (b) $X = 2.5$. FCD induced steady-state cavity detuning (Δ_{FCD}) with the intra-cavity power (Y) when the free-carriers are generated due to the (c) 2PA (solid blue curve), (d) 3PA (solid red curve), and 4PA (dotted green curve).

efficients. Figures 4.10 (b)-4.10 (c) exhibit the Kerr-tilt as a function of pump detuning. FCA induced loss has a similar effect on BS curve that of the multi-photon absorption. It is also evident that FCD introduces a cavity detuning that manifests itself through the reverse Kerr-tilt. In practice, reverse Kerr-tilt shown in Fig. 4.10 (b) indicates that with suitable FCD-induced cavity detuning, one can obtain maximum intra-cavity power even without any external pump detuning (solid pink curve). For a fixed value of FCA-FCD coefficient, the reverse tilt increases with the increase in the input pump power X, as depicted in Fig. 4.10 (c). It is seen that the intra-cavity power becomes multivalued with large detuning and pump power. Similar kind of reverse Kerr-tilt as shown in 4.10 (b)-4.10 (d) is also reported in a recently published manuscript that discusses the possibility of parametric oscillations in silicon micro-cavities in the presence of 2PA [96].

D. FCA-FCD induced cavity detuning

To explain the reverse Kerr-tilt analytically, we further modify the normalized LLE given in Eq. 4.16 as:

$$\begin{aligned}\frac{\partial u}{\partial \xi} &= -\left(1 + i\Delta_{\text{eff}}\right) u - \frac{1}{2}\phi_{\text{c}} u - i\frac{s}{2}\frac{\partial^2 u}{\partial \tau^2} \\ &+ \sum_{k\geq 3} \frac{d_{\text{k}}}{k!}\frac{\partial^k u}{\partial \tau^k} + i|u|^2 u - \frac{Q_{\text{n}}}{n}|u|^{2(n-1)} u + S \end{aligned} \tag{4.33}$$

$$\Delta_{\text{eff}} = \Delta + \Delta_{\text{FCD}} = \Delta + \frac{K\phi_{\text{c}}}{2} \tag{4.34}$$

where the effective cavity detuning Δ_{eff} is defined as the sum of the external pump detuning Δ and the FCD-induced detuning (Δ_{FCD}). It should be noted that the Δ_{eff} changes over round-trips. Effective detuning Δ_{eff} (solid red curve) and FCD-induced detuning Δ_{FCD} (solid green curve), for two sets of FCA-FCD coefficients, $C_2 = K_2 = 2$, and $C_2 = K_2 = 5$ at input pump power $X = 1$ are plotted in Figs. 4.11 (a) and 4.11 (b), respectively. In both the cases, input pump detuning has also been plotted (solid blue-curve) to indicate the reference level in the absence of FCA-FCD. Figs. 4.11 (a) and 4.11 (b) show how the overall cavity detuning is affected by the FCD induced detuning at different FCA-FCD coefficients. The intersection between the red and the green curves indicates the effective cavity detuning when the external pump detuning is zero. Generation of stable frequency comb even without external pump detuning with suitable initial pump power has been previously demonstrated [85].

Note that, in order to excite the temporal cavity soliton in the microresonator experimentally, one requires to modulate the phase of the microresonator driving field which can be done through electrical or thermal detuning. Recently, the effect of thermo-optical chaos on soliton generation is studied both numerically and experimentally [97]. Thermal detuning can easily be included in our numerical modeling following the approach adopted in [97]. However, we assume that the microresonator is in thermally equilibrium state and neglect such thermally induced detuning while studying the steady-state behavior and the MI in the presence of all nonlinear losses. We also plot the normalized intra-cavity power (Y/X) with the change in Δ_{eff} instead of Δ in Figs. 4.12 (a) and 4.12 (b) for two different values of X. As expected, this time, there is no tilt in the opposite direction. When the carrier accumulation reaches in the steady state, the effective detuning, Δ_{eff} can be written as

$$\Delta_{\text{eff}}^{(\text{Steady-state})} = \Delta + \frac{KC_{\text{n}}|u_0|^{2n}}{2} = \Delta + \frac{KC_{\text{n}}{Y_0}^{n}}{2} \tag{4.35}$$

where u_0 is the steady-state amplitude, and the Y_0 is the steady-state intra-cavity power. The steady-state FCD-induced cavity detuning for 2PA, as plotted in Fig. 4.12 (c), is much larger than the FCD-induced cavity detuning due to the 3PA and 4PA as shown in Fig. 4.12 (d). We have considered realistic values of FCA-FCD coefficients calculated from [76, 91] in order to obtain the steady-state maximum FCD induced cavity detuning for 2PA, 3PA, and 4PA as shown in Figs. 4.12 (c) and 4.12 (d).

4.3.4 Generalized Expression: Bistability & Self-Pulsation

The stability of Eq. 4.21 can be analyzed by perturbing the steady-state solutions u_0 and ϕ_0 with small variation in the amplitude, $\delta u(\xi)$ and the free-carriers, $\delta\phi_{\text{c}}(\xi)$ with respect to the slow-time, respectively. Thus if, $u(\xi) = u_0 + \delta u(\xi)$, and $\phi_{\text{c}}(\xi) = \phi_0 + \delta\phi_{\text{c}}(\xi)$, then the perturbation array, $\epsilon = (\delta u, \delta u^*, \delta\phi_{\text{c}})^T$ in the presence of nPA and corresponding FCA-FCD is found to satisfy the following linearized Eq.:

$$\frac{d\varepsilon}{d\xi} = {J_{\text{BS,SP}}}^{(\text{n})}\varepsilon \tag{4.36}$$

where ${J_{\mathrm{BS,SP}}}^{(\mathrm{n})}$ is the 3×3 Jacobian matrix of Eqs. 4.21-4.22, and is given by:

$$
{J_{\mathrm{BS,SP}}}^{(\mathrm{n})} = \begin{pmatrix} {R_{\mathrm{BS,SP}}}^{(\mathrm{n})} + i{I_{\mathrm{BS,SP}}}^{(\mathrm{n})} & -\left(\frac{n-1}{n}Y^{n-2}Q_{\mathrm{n}} - i\right)u_0^2 & -\frac{1}{2}\left(1+iK\right)u_0 \\ -\left(\frac{n-1}{n}Y^{n-2}Q_{\mathrm{n}} + i\right)u_0^{*2} & {R_{\mathrm{BS,SP}}}^{(\mathrm{n})} - i{I_{\mathrm{BS,SP}}}^{(\mathrm{n})} & -\frac{1}{2}\left(1-iK\right)u_0^* \\ nY^{n-1}u_0^*\theta_{\mathrm{c_n}} & nY^{n-1}u_0\theta_{\mathrm{c_n}} & -\frac{1}{\tau_c} \end{pmatrix} \tag{4.37}
$$

where ${R_{\mathrm{BS,SP}}}^{(\mathrm{n})}$ and ${I_{\mathrm{BS,SP}}}^{(\mathrm{n})}$ are:

$$
{R_{\mathrm{BS,SP}}}^{(\mathrm{n})} = -\left[1 + \frac{C_{\mathrm{n}}}{2}Y^n + Q_{\mathrm{n}}Y^{(n-1)}\right] \tag{4.38}
$$

$$
{I_{\mathrm{BS,SP}}}^{(\mathrm{n})} = -\left[\Delta + \frac{KC_{\mathrm{n}}}{2}Y^n - 2Y\right] \tag{4.39}
$$

The conditions for BS and SP (free-carrier oscillation) can be obtained from ${J_{\mathrm{BS,SP}}}^{(\mathrm{n})}$ in the presence of FCA-FCD which can be written in a general form as:

$$
\text{BS: } \det\left({J_{\mathrm{BS,SP}}}^{(\mathrm{n})}\right) > 0 \tag{4.40}
$$

$$
\text{SP: } \left\{\mathrm{tr}\left({J_{\mathrm{BS,SP}}}^{(\mathrm{n})}\right)^2 - \mathrm{tr}\left(\left({J_{\mathrm{BS,SP}}}^{(\mathrm{n})}\right)^2\right)\right\}\mathrm{tr}\left({J_{\mathrm{BS,SP}}}^{(\mathrm{n})}\right) - 2\det\left({J_{\mathrm{BS,SP}}}^{(\mathrm{n})}\right) > 0 \tag{4.41}
$$

where det and tr are the determinant and the trace, respectively. Equation 4.41 corresponds to the Hopf-bifurcation.

4.3.5 Linear Stability Analysis

In this section, we perform the linear stability analysis of the stationary CW solutions (u_0 and ϕ_0) of free-carrier driven LLE. The evolution of normalized carrier density and signal amplitude due to the spatiotemporal perturbations are given by Eqs. 4.42 and 4.43, respectively in the presence of nonlinear losses including FCA-FCD. In each case, we find the MI gain λ with the normalized side-band frequency Ω. We also show the dependence of MI gain and bandwidth on normal-

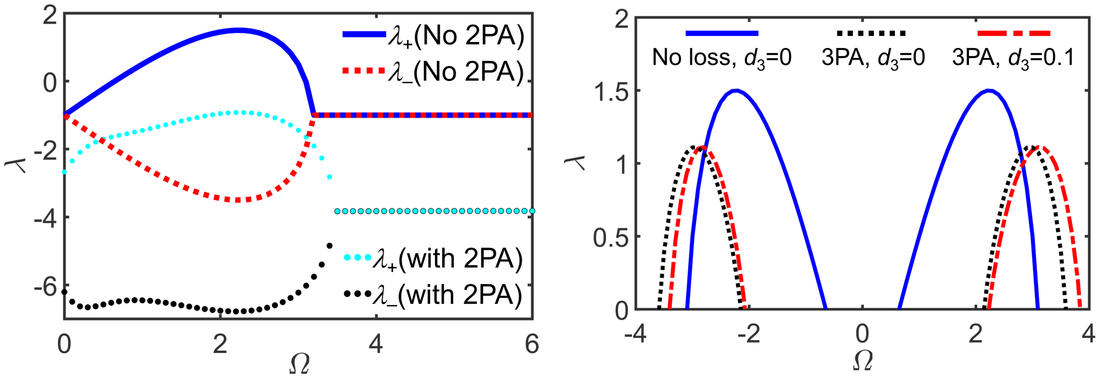

(a) (b)

Figure 4.13: (a) MI-gain lobes $\lambda_{\pm}$ in the absence and presence of 2PA for $\Omega > 0$, (b) λ_{+} in the presence and absence of 3PA. Simulation parameters are: $s = 1, Y = 2.5, \Delta = 7.5, Q_2 = 1, K_2 = 0.05, C_2 = 0.1, \theta_{\mathrm{c}2} = 0.05, \theta_{\mathrm{c}3} = 6.31 \times 10^{-7}, Q_3 = 8.73 \times 10^{-4}, C_3 = 0.049, K_3 = 4.9$. Effect of third-order dispersion ($d_3 = 0.1$) is also considered in Fig. 4.13 (b) (red-curve). Third order dispersion induces asymmetry in the gain lobe with respect to $\Omega = 0$.

ized detuning Δ, signal power Y, and higher-order dispersion. Finally, we provide a general expression of MI-gain for multi-photon absorptions. Throughout our manuscript, superscript (n) stands for nPA and unlike the powers, the super and subscripts are not italics.

$$\phi_{\mathrm{c}}\left(\xi\right) \approx \phi_0\left(\xi\right) + \delta\phi\left(\xi\right) \tag{4.42}$$

$$u\left(\xi,\tau\right) = u_0\left(\xi\right) + u_{+}\left(\xi\right)e^{i\Omega\tau} + u_{-}\left(\xi\right)e^{-i\Omega\tau} \tag{4.43}$$

The carriers cannot follow the quick oscillation of the optical field and therefore, unlike the optical field amplitude (u) the carrier density cannot change in fast-time τ. In the presence of nPA at the onset of the MI, the carrier density is equal to ϕ_0. Substituting the ϕ_{c} and u given by Eqs. 4.42 and 4.43 into Eqs. 4.14 and 4.15 respectively, the general expressions for homogeneous solutions for the normalized free-carrier and the intra-cavity field amplitude (ϕ_0, u_0, respectively) can be obtained as:

$$\phi_0 = \theta_{\mathrm{c_n}}\tau_{\mathrm{c}}|u_0|^{2n} = C_{\mathrm{n}}|u_0|^{2n} \tag{4.44}$$

$$\begin{aligned}\frac{\partial u_0}{\partial \xi} =& -\left(1+i\Delta\right)u_0 - \frac{1}{2}\left(1+iK\right)\theta_{\mathrm{c_n}}\tau_{\mathrm{c}}|u_0|^{2n}u_0 \\ &+ i|u_0|^2 u_0 - \frac{Q_{\mathrm{n}}}{n}|u_0|^{2(n-1)}u_0 + S \end{aligned} \tag{4.45}$$

Whereas, the perturbations signal amplitudes (u_+ and $u_-{}^*$) are written as:

$$\begin{aligned}
&\frac{\partial u_+}{\partial \xi} = -\left(1+i\Delta\right)u_+ - \frac{1}{2}\left(1+iK\right)\phi_0 u_+ + i\frac{s}{2}\Omega^2 u_+ \\
&- i\frac{d_3}{6}\Omega^3 u_+ + i\left(2|u_0|^2 u_+ + (u_0)^2 u_-^*\right) \\
&- \frac{Q_{\mathrm{n}}}{n}\left(n|u_0|^{2(n-1)}u_+ + \left(n-1\right)|u_0|^{2(n-2)}(u_0)^2 u_-^*\right) \\
&\text{and,} \\
&\frac{\partial u_-^*}{\partial \xi} = -\left(1-i\Delta\right)u_-^* - \frac{1}{2}\left(1-iK\right)\phi_0 u_-^* - i\frac{s}{2}\Omega^2 u_-^* \\
&+ i\frac{d_3}{6}\Omega^3 u_-^* - i\left(2|u_0|^2 u_-^* + (u_0^*)^2 u_+\right) \\
&- \frac{Q_{\mathrm{n}}}{n}\left(n|u_0|^{2(n-1)}u_-^* + \left(n-1\right)|u_0|^{2(n-2)}(u_0^*)^2 u_+\right)
\end{aligned} \tag{4.46}$$

Note that for the weak amplitudes and exponentially growing solutions, $u_-{}^* = u_+$. The Jacobian, JMI to find MI growth rate (gain) can be written as:

$$J^{\mathrm{MI}} = \begin{bmatrix} \frac{\partial}{\partial u_+}\left(\frac{\partial u_+}{\partial \xi}\right) & \frac{\partial}{\partial u_-^*}\left(\frac{\partial u_+}{\partial \xi}\right) \\ \frac{\partial}{\partial u_+}\left(\frac{\partial u_-^*}{\partial \xi}\right) & \frac{\partial}{\partial u_-^*}\left(\frac{\partial u_-^*}{\partial \xi}\right) \end{bmatrix} = \begin{bmatrix} J_{11}^{\mathrm{MI}} & J_{12}^{\mathrm{MI}}(u_0)^2 \\ J_{21}^{\mathrm{MI}}(u_0^*)^2 & J_{22}^{\mathrm{MI}} \end{bmatrix} \tag{4.47}$$

The eigenvalues of the matrix J^{MI} yields the modulation instability growth-rate, λ which is calculated by equating the $\det(J^{\mathrm{MI}} - \lambda\mathbb{I}) = 0$ where $\mathbb{I}$ is a 2×2 identity matrix. The growth of the side-band amplitude can be expressed as $u_+ = C \cdot \exp(\lambda\xi)$ where C is an arbitrary constant. One can write $J_{\mathrm{pq}}{}^{\mathrm{MI}}$ in the following form:

$$J_{\mathrm{pq}}^{\mathrm{MI}} = \begin{cases} R_{\mathrm{MI}}^{(\mathrm{n})} + (-1)^{(q-1)} i I_{\mathrm{MI}}^{(\mathrm{n})};\ \text{when, } p{=}q \\ \left(-\alpha_{\mathrm{MI}}^{(\mathrm{n})}\right) + (-1)^{(q)} i\left(-\beta_{\mathrm{MI}}^{(\mathrm{n})}\right);\ \text{when, } p \neq q \end{cases} \tag{4.48}$$

The MI-gain can be obtained by solving the quadratic Eq. 4.49 of λ only for the real values:

$$\left(\frac{\left\{{R_{\mathrm{MI}}}^{(\mathrm{n})}-\lambda\right\}^2+\left\{{I_{\mathrm{MI}}}^{(\mathrm{n})}\right\}^2}{\{{\alpha_{\mathrm{MI}}}^{(\mathrm{n})}\}^2+\left\{{\beta_{\mathrm{MI}}}^{(\mathrm{n})}\right\}^2}-Y^2\right)=0 \tag{4.49}$$

Here, the LLE is truncated up to the 3rd order dispersion. ${R_{\mathrm{MI}}}^{(\mathrm{n})}$,${I_{\mathrm{MI}}}^{(\mathrm{n})}$, $\alpha^{(\mathrm{n})}$, and $\beta^{(\mathrm{n})}$ are given as,

$${R_{\mathrm{MI}}}^{(\mathrm{n})}=-\left[1+\frac{C_{\mathrm{n}}}{2}Y^n+Q_nY^{(n-1)}\right] \tag{4.50}$$

$${I_{\mathrm{MI}}}^{(\mathrm{n})}=-\left[\Delta+\frac{KC_n}{2}Y^n-\frac{s}{2}\Omega^2+\frac{d_3}{6}\Omega^3-2Y\right] \tag{4.51}$$

$$\alpha_{\mathrm{MI}}^{(\mathrm{n})}=\left[\frac{n-1}{n}Q_nY^{(n-2)}\right] \tag{4.52}$$

$$\beta_{\mathrm{MI}}^{(\mathrm{n})}=-1 \tag{4.53}$$

Equation 4.49 can be simplified in a more convenient form given by Eq. 4.54,

$$\left[\lambda^2-2R_{\mathrm{MI}}^{(\mathrm{n})}\lambda+{R_{\mathrm{MI}}^{(\mathrm{n})}}^2+{I_{\mathrm{MI}}^{(\mathrm{n})}}^2-\left({\alpha_{\mathrm{MI}}^{(\mathrm{n})}}^2+{\beta_{\mathrm{MI}}^{(\mathrm{n})}}^2\right)Y^2\right]=0 \tag{4.54}$$

Note that, in absence of all nonlinear losses (multi-photon absorption, FCA, FCD) and the higher-order dispersion terms, ${R_{\mathrm{MI}}}^{(\mathrm{n})}$, ${I_{\mathrm{MI}}}^{(\mathrm{n})}$, ${\alpha_{\mathrm{MI}}}^{(\mathrm{n})}$, and ${\beta_{\mathrm{MI}}}^{(\mathrm{n})}$ becomes -1, $-(\Delta-s\Omega^2/2-2Y)$, 0 and -1, respectively such that the λ reduces to the well-known expression 4.55 for MI-gain [89, 90]:

$$\lambda_{\pm}(\Omega)=-1\pm\sqrt{4Y\left(\Delta-\frac{s\Omega^2}{2}\right)-\left(\Delta-\frac{s\Omega^2}{2}\right)^2-3Y^2} \tag{4.55}$$

A. MI in normal dispersion regime ($s=+1$)

It is known that unlike straight waveguide or optical fiber, MI can occur in

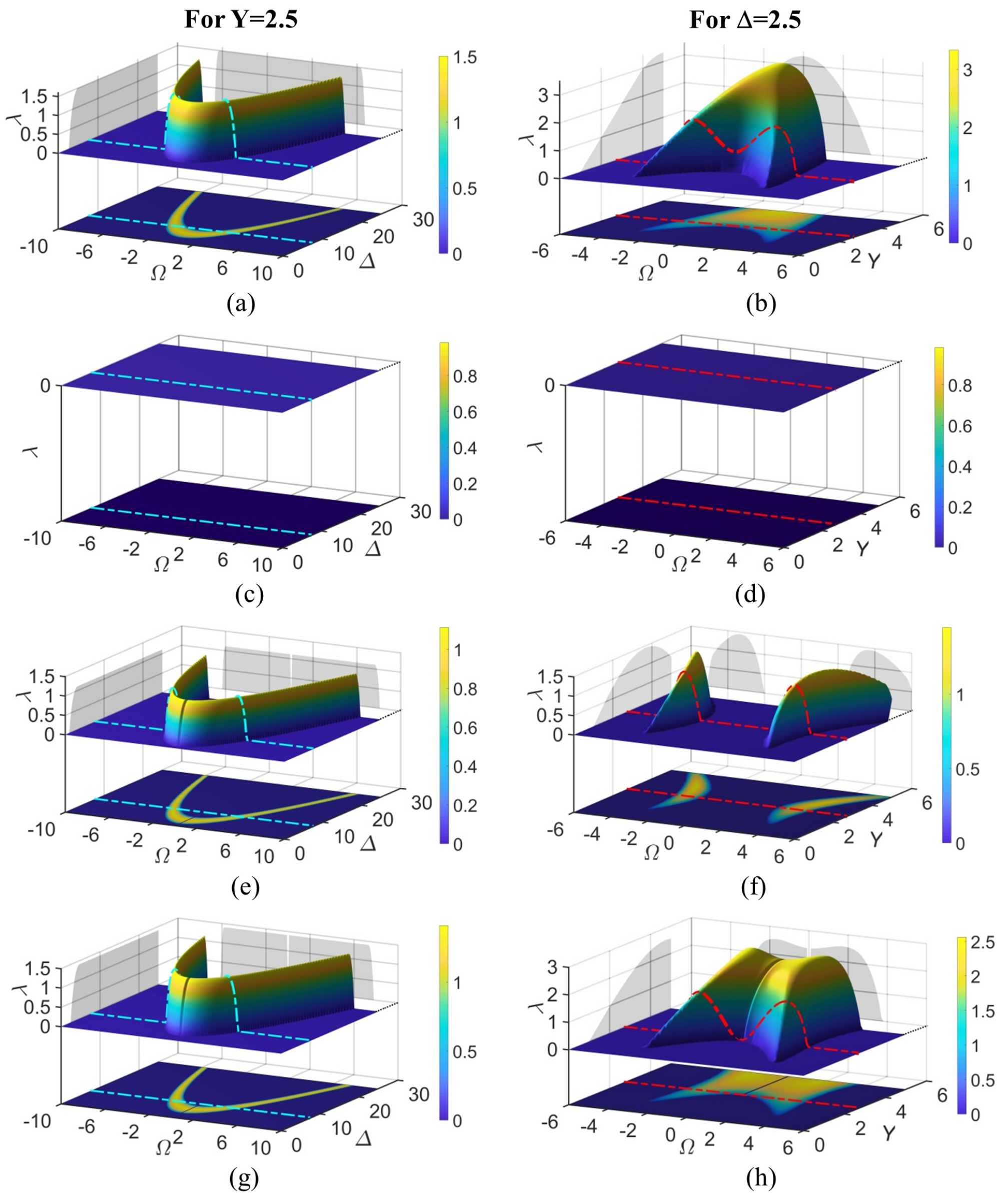

Figure 4.14: Real part of the MI gain λ vs. (a) Ω and Δ (at $Y = 2.5$), (b) Ω and Y (at $\Delta = 7.5$) in absence of all nonlinear losses. Variation of λ with (c) Ω and Δ (at $Y = 2.5$), (d) Ω and Y (at $\Delta = 7.5$) while 2PA, FCA-FCD are present. Change in λ with the change in (e) Ω and Δ (at $Y = 2.5$), and (f) Ω and Y (at $\Delta = 7.5$) when 3PA, FCA-FCD are present. λ with (g) Ω and Δ (at $Y = 2.5$), and (h) Ω and Y (at $\Delta = 7.5$) in presence of 4PA, FCA-FCD. For all the cases, 3$^{\text{rd}}$ order dispersion ($d_3 = 0.1$) is taken into consideration. Other simulation parameters are: $s = 1$, $\theta_{c2} = 0.0005$, $Q_2 = 0.93$, $C_2 = 29.81$, $K_2 = 7.5$ (at $\lambda_0 \sim 1.56\mu$m); $\theta_{c3} = 6.31 \times 10^{-7}$, $Q_3 = 8.73 \times 10^{-4}$, $C_3 = 0.049$, $K_3 = 4.9$ (at $\lambda_0 \sim 2.4\mu$m); $\theta_{c4} = 6.018 \times 10^{-8}$, $Q_4 = 6.16 \times 10^{-6}$, $C_4 = 4.66 \times 10^{-3}$, $K_4 = 2.9$ (at $\lambda_0 \sim 4.0\mu$m). The cyan and magenta lines overlaid on the 2D plots indicate the corresponding values of λ for $\Delta = 7.5$ and $Y = 2.5$, respectively.

synchronously driven optical cavities or ring lasers even if the system is pumped in normal dispersion regime [89]. As a result, a stable stationary train of pulses can be generated in the cavity irrespective of the sign of the dispersion.

In this section, we discuss the dependency of MI-gain λ on Ω and Δ (at $Y = 2.5$) as well as on Ω and Y (at $\Delta = 7.5$), respectively in the normal dispersion region. At first, we plot MI-gain, $\lambda_{\pm}$ with respect to normalized frequency $\Omega(> 0)$ in Fig. 4.13 (a). It is seen that 2PA in silicon can completely inhibit the parametric oscillations. Fig. 4.13 (b) shows the MI-gain in the presence of 3PA. Non-zero third-order dispersion ($d_3 = 0.1$) induces the asymmetry in MI-gain lobe with respect to $\Omega = 0$ and thereby enhances the MI-bandwidth [36]. The values of nPA, FCA-FCD coefficients are taken from [76]. Figs. 4.14 (a) and 4.14 (b) depict the dependency of MI gain λ on Ω and Δ(at $Y = 2.5$) as well as on Ω and Y (at $\Delta = 7.5$), respectively, in normal dispersion region while all the nonlinear losses are ignored.

To produce rest of curves (Fig 4.14 (c)-4.14 (h)) we use the realistic values of nPA, FCA-FCD coefficients for silicon (c-Si) waveguides from [76, 91]. In the presence of 2PA no parametric gain lobe has been observed (Fig. 4.14 (c) and 4.14 (d)). The MI gain in the presence of 3PA, 4PA, and the corresponding FCA-FCD is plotted in the Figs. 4.14 (e)–4.14 (h). The cyan and magenta lines are drawn on the 2-D plots to indicate the corresponding values of λ for $\Delta = 7.5$ and $Y = 2.5$, respectively [89]. Projection of the 2-D plot on each axis through the shadow-plot helps to anticipate the approximate values of the MI-gain with respect to different parameters.

B. MI in anomalous dispersion regime ($s = -1$) and the Effect of FCA-FCD on MI-growth rate

Similar curves can be plotted for the MI gain in case of anomalous dispersion regime of operation. We observe there is no parametric gain in presence of 2PA at telecom wavelengths. It is previously reported by Lau et al. [76] that in MIR while the dominant loss mechanism in 3PA, the effect of 3PA induced FCA-FCD is prominent and the parametric oscillations can only take place if the pump power is sufficiently low [76]. In their simulations, the waveguide is pumped at the anomalous region ($s = 1$). This claim can be supported analytically through the

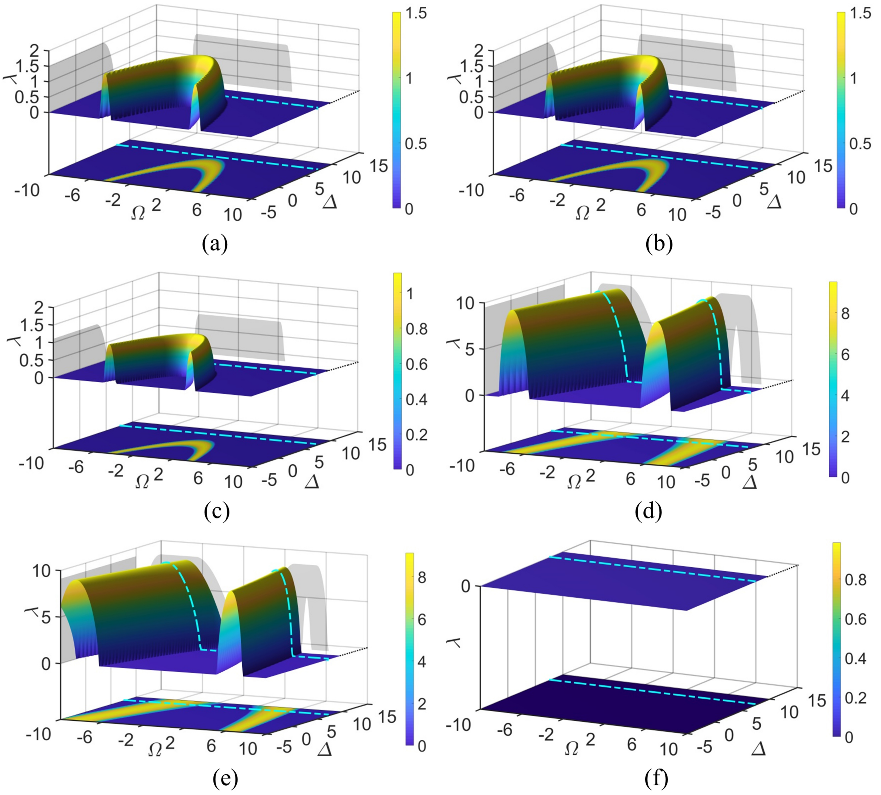

(a) (b) (c) (d) (e) (f)

Figure 4.15: MI-gain λ with respect to Ω and Δ when Y is fixed at 2.5 in (a) absence of all nonlinear losses, (b) presence of only 3PA and no FCA-FCD, (c) presence of 3PA, FCA-FCD. MI-gain λ with respect to Ω and Δ when $Y = 10.5$ in (d) absence of all nonlinear losses, (e) presence of only 3PA and no FCA-FCD, (f) presence of 3PA, FCA-FCD. It is observed that if input power X is high (high intra-cavity power Y) parametric oscillation ceases to occur in presence of FCA-FCD along with 3PA.

MI-analysis in presence of nonlinear losses as shown in Fig. 4.15. We plot the λ with Ω and Δ in Fig. 4.15 (a) in absence of any nonlinear losses, whereas Fig. 4.15 (b) dictates the MI-gain in the absence of FCA-FCD while 3PA is present. Fig. 4.15 (c) shows the MI-gain in presence of 3PA, FCA-FCD at $Y = 2.5$. Similarly, when the intra-cavity power is almost quadrupled ($Y = 10.5$) the corresponding MI-gain has been plotted in Figs. 4.15 (d)–4.15 (f) for three different cases as described earlier. It is conspicuous from Figs. 4.15 (c) and 4.15 (f) that there is no parametric oscillation if FCA-FCD is present while the intra-cavity power is high ($Y = 10.5$) however, MI gain lobes exist for relatively low intra-cavity power ($Y = 2.5$). Therefore, in the case of 3PA, the principle mechanisms to inhibit the comb formation are 3PA-induced FCA and FCD [76]. To obtain parametric oscillation in presence of 3PA, either the generated free-carriers have to be swept away by suitable external-bias or the input pump power X (consequently, Y) has to be sufficiently low.

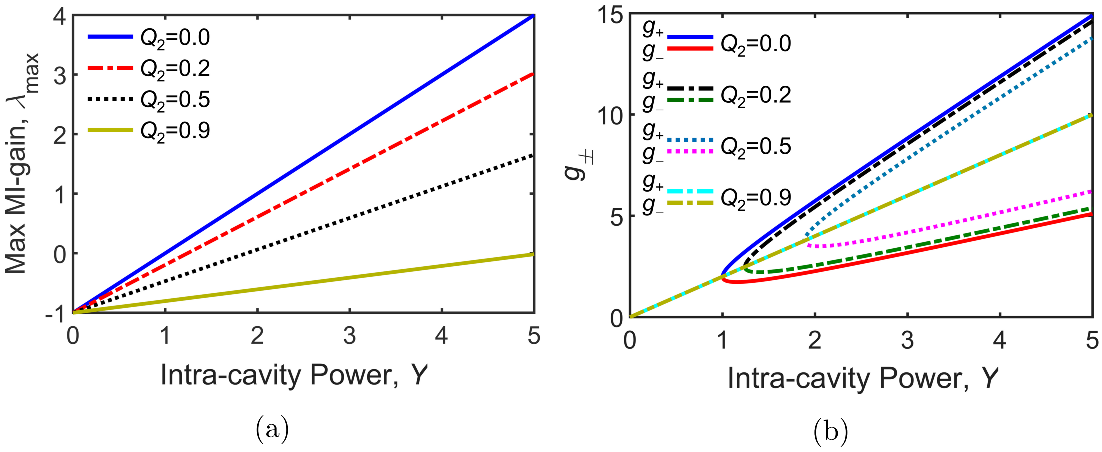

Figure 4.16: (a) Maximum MI-gain with the change in intra-cavity power Y with a set of four 2PA coefficients ($Q_2 = 0, 0.2, 0.5, 0.9$), (b) Range of Δ for which MI can initiate with different 2PA coefficients ($Q_2 = 0, 0.2, 0.5, 0.9$). As 2PA coefficient increases, the range of Δ for which MI can initiate, becomes narrower.

4.3.6 Condition for Maximum MI-Gain and Threshold Intensity

It is known [90] that the MI-gain in the absence of nonlinear losses can be given by Eq. 4.56 while the maximum gain ($\lambda = \lambda_{\max} = Y - 1$) can be achieved if $\Delta k = 0$,

$$\lambda_\pm(\Omega) = -1 \pm \sqrt{Y^2 - (\Delta k)^2} \tag{4.56}$$

where Δk is given by,

$$\Delta k = \left(\Delta - \frac{s}{2}\Omega^2 - 2Y\right) \tag{4.57}$$

Therefore, the steady state solution will always be stable if $Y < 1$. However, in presence of nonlinear losses, the solution of λ can be written as 4.58 instead of Eq.

4.56.

$$\lambda^{(\mathrm{n})} = R_{\mathrm{MI}}^{(\mathrm{n})} \pm \sqrt{\left\{\left(\alpha_{\mathrm{MI}}^{(\mathrm{n})}\right)^2 + \left(\beta_{\mathrm{MI}}^{(\mathrm{n})}\right)^2\right\} Y^2 - \left(I_{\mathrm{MI}}^{(\mathrm{n})}\right)^2} \tag{4.58}$$

In this case, the maximum gain can be obtained if ${I_{\mathrm{MI}}}^{(\mathrm{n})} = 0$. One can write the general expression of λ_{max} in terms of Y, ${\alpha_{\mathrm{MI}}}^{(\mathrm{n})}$, ${\beta_{\mathrm{MI}}}^{(\mathrm{n})}$, and ${R_{\mathrm{MI}}}^{(\mathrm{n})}$ as follows:

$$\lambda_{\mathrm{max}}^{(\mathrm{n})} = Y\sqrt{\left\{\left(\alpha_{\mathrm{MI}}^{(\mathrm{n})}\right)^2 + \left(\beta_{\mathrm{MI}}^{(\mathrm{n})}\right)^2\right\}} + R_{\mathrm{MI}}^{(\mathrm{n})} \tag{4.59}$$

If the FCA and FCD are neglected, the expression of maximum gain becomes:

$$\lambda_{\mathrm{max}}^{(\mathrm{n})} = Y\sqrt{\left(\frac{n-1}{n}\right)^2 Q_{\mathrm{n}}^2 Y^{2(n-2)} + 1} - \left(1 + Q_{\mathrm{n}} Y^{n-1}\right) \tag{4.60}$$

We further deduce the expression for the minimum intensity to initiate the MI. It can be shown after algebraic simplification that the steady-state solution will always be stable for,

$$Y \leq \frac{-R_{\mathrm{MI}}^{(\mathrm{n})}}{\sqrt{\left\{\left(\alpha_{\mathrm{MI}}^{(\mathrm{n})}\right)^2 + \left(\beta_{\mathrm{MI}}^{(\mathrm{n})}\right)^2\right\}}} \tag{4.61}$$

As an example, in the presence of only 2PA, the value of Y for which the steady-state solution of the LLE will always be stable in the presence of only 2PA is,

$$Y \leq \frac{1}{\left(\sqrt{\left(\frac{Q_2^2}{4} + 1\right)} - Q_2\right)} \tag{4.62}$$

Maximum MI gain λ_{max} is plotted in Fig. 4.16 (a) for four different values (0, 0.2, 0.5, and 0.9) of 2PA coefficients Q_2 in the absence of FCA-FCD. It should be noted that 2PA coefficient for silicon at telecom wavelength, Q_2 is ~ 0.9.

4.3.7 Range of Normalized Detuning to obtain MI

In this section, we find the range of possible normalized detuning to initiate the MI and compare the results for different cases such as, while all the nonlinear losses are absent, only nPA is present, both the nPA, FCA are present, and all the nonlinear losses are present. The condition for threshold can be found by equating λ given by Eq. 4.59 to 0. It is known [90] that in absence of nonlinear losses,

$$\frac{s}{2}\Omega^2 = (\Delta - g_{\pm}) \tag{4.63}$$

where $g_{\pm}$ can be expressed in terms of Y,

$$g_{\pm} = 2Y \pm \sqrt{Y^2 - 1} \tag{4.64}$$

Note that, in anomalous dispersion region, for Ω to possess real solution, Δ must be less than g_{+} whereas, for normal dispersion regime, the required detuning Δ should be more than g_{-} for MI to occur. When, the pump detuning lies in between $\in(g_{-},\, g_{+})$, i.e. $g_{-} < \Delta < g_{+}$, MI can be initiated for both the anomalous and normal dispersion regimes. Similarly, in presence of all the nonlinear losses, the general expression to obtain the threshold condition can be determined from Eq. 4.54,

$$\left\{I_{\mathrm{MI}}^{(\mathrm{n})}\right\}^2 = \left\{\left(\alpha_{\mathrm{MI}}^{(\mathrm{n})}\right)^2 + \left(\beta_{\mathrm{MI}}^{(\mathrm{n})}\right)^2\right\} Y^2 - \left\{R_{\mathrm{MI}}^{(\mathrm{n})}\right\}^2 \tag{4.65}$$

However, the relation of MI Gain, Ω with Δ and output power Y obtained from the Eqs. 4.63-(IR) can be given by a 3^{rd}-th order polynomial of Ω,

$$-\frac{d_3}{6}\Omega^3 + \frac{s}{2}\Omega^2 = \left(\Delta - g_{\pm}^{(\mathrm{n})'}\right) \tag{4.66}$$

where,

$$g_{1\pm}^{(\mathrm{n})} = 2Y \pm \sqrt{\left\{\left(\alpha_{\mathrm{MI}}^{(\mathrm{n})}\right)^2 + \left(\beta_{\mathrm{MI}}^{(\mathrm{n})}\right)^2\right\} Y^2 - \left(R_{\mathrm{MI}}^{(\mathrm{n})}\right)^2} \tag{4.67}$$

$$g_{\pm}^{(\mathrm{n})'} = g_{1\pm}^{(\mathrm{n})} - \frac{KC_n}{2}Y^n \tag{4.68}$$

If the carrier-lifetime can be reduced by sweeping the carriers applied the external bias voltage across the device cross-section, which often can be done by forming a p-i-n junction across the waveguide cross-section, then the square of τ_c term can be negligible. The situation is equivalent to the case when nPA is present while FCA and FCD are absent. In this case, neglecting the higher-order dispersion terms ($d_\mathrm{k}(k \geq 3) = 0$) the Eqs. 4.66-4.68 are reduced into,

$$\frac{s}{2}\Omega^2 = \left(\Delta - g_{1\pm}^{(\mathrm{n})}\right) \tag{4.69}$$

For 2PA without FCA-FCD,

$$\frac{s}{2}\Omega^2 = \left(\Delta - g_{1\pm}^{(2)}\right) \tag{4.70}$$

$$g_{1\pm}^{(2)} = 2Y \pm \sqrt{\left(\left(\frac{n-1}{n}\right)^2 Q_\mathrm{n}^2 Y^{2(n-2)} + 1\right) Y^2 - \left(1 + Q_\mathrm{n} Y^{n-1}\right)^2} \tag{4.71}$$

In Fig. 4.16 (b) we plot the range of Δ both in absence of all nonlinear losses and in presence of only 2PA, for which the steady-state solution can be unstable. It is discussed earlier that in absence of all nonlinear losses the steady-state solution will be unstable in the range: $g_- < \Delta < g_+$ where $g_\pm$ is given by Eq. 4.70. From Fig. 4.16 (b) it can be seen clearly that with the gradual increase in the 2PA coefficient, the range of Δ for which MI can initiate, gradually shrinks.

Recently, we have noticed an in-depth existing study on optical micro-cavity that discusses the generation of Turing pattern analytically for two distinct cases considering either intensity dependent nonlinear losses or intensity dependent nonlinear refractive index of the medium. However, the mathematical framework outlined in [98] did not include the effects of multi-photon absorptions, FCA and FCD. Another interesting work led by Chembo [46] presents the generation of Turing rolls as well as the generation of bright and dark temporal solitons in anomalous and normal dispersion regimes, respectively without considering nonlinear losses. We believe that our work can further be extended following the mathematical analysis given in [46, 98] including all the nonlinear losses and our formalism is amenable to the incorporation of other associated physical effects like thermal detuning [97].

4.4 Summary and Conclusion

To conclude the chapter, we have derived analytical expressions of steady-state homogeneous solutions of free-carrier driven Kerr FC. Higher-order (> 3) characteristic polynomial of intra-cavity power describing the steady-state homogeneous solution of the modified LLE are discussed in detail. The nonlinear phase detuning of the cavity has been observed through negative Kerr-tilt. We also find an analytical expression for the steady-state FCD induced cavity detuning. Expression of MI-gain in the presence of all nonlinear losses is found, and the threshold detuning along with the range of normalized pump detuning to initiate MI are discussed. The maximum allowed value of 2PA coefficient for which the optical bistability can occur and the analytical expression of the threshold pump detuning to initiate the MI are important parameters from the experimental point of view. Therefore, our theoretical study is a step towards predicting comb dynamics in the realistic cases where all the nonlinear losses and higher-order dispersion are present.

References

[1] S. T. Cundiff and J. Ye, "Colloquium: Femtosecond optical frequency combs," *Reviews of Modern Physics*, vol. 75, no. 1, pp. 325–342, 2003.

[2] T. W. Hänsch, "Nobel lecture: Passion for precision," *Reviews of Modern Physics*, vol. 78, no. 4, pp. 1297–1309, 2006.

[3] T. M. Fortier, M. S. Kirchner, F. Quinlan, J. Taylor, J. Bergquist, T. Rosenband, N. Lemke, A. Ludlow, Y. Jiang, C. Oates *et al.*, "Generation of ultrastable microwaves via optical frequency division," *Nature Photonics*, vol. 5, no. 7, pp. 425–429, 2011.

[4] J. Wu, X. Xu, T. G. Nguyen, S. T. Chu, B. E. Little, R. Morandotti, A. Mitchell, and D. J. Moss, "Harnessing optical micro-combs for microwave photonics," *IEEE Journal of Selected Topics in Quantum Electronics*, vol. 24, no. 4, pp. 1–20, 2018.

[5] Y. K. Chembo, "Kerr optical frequency combs: theory, applications and perspectives," *Nanophotonics*, vol. 5, no. 2, pp. 214–230, 2016.

[6] J. Pfeifle, V. Brasch, M. Lauermann, Y. Yu, D. Wegner, T. Herr, K. Hartinger, P. Schindler, J. Li, D. Hillerkuss *et al.*, "Coherent terabit communications with microresonator Kerr frequency combs," *Nature Photonics*, vol. 8, no. 5, pp. 375–380, 2014.

[7] S. A. Diddams, L. Hollberg, and V. Mbele, "Molecular fingerprinting with the resolved modes of a femtosecond laser frequency comb," *Nature*, vol. 445, no. 7128, pp. 627–630, 2007.

[8] N. Picqué and T. W. Hänsch, "Frequency comb spectroscopy," *Nature Photonics*, vol. 13, no. 3, pp. 146–157, 2019.

[9] T. Steinmetz, T. Wilken, C. Araujo-Hauck, R. Holzwarth, T. W. Hänsch, L. Pasquini, A. Manescau, S. D'odorico, M. T. Murphy, T. Kentischer *et al.*, "Laser frequency combs for astronomical observations," *Science*, vol. 321, no. 5894, pp. 1335–1337, 2008.

[10] M.-G. Suh, X. Yi, Y.-H. Lai, S. Leifer, I. S. Grudinin, G. Vasisht, E. C. Martin, M. P. Fitzgerald, G. Doppmann, J. Wang *et al.*, "Searching for exoplanets using a microresonator astrocomb," *Nature Photonics*, vol. 13, pp. 25–30, 2019.

[11] Y. K. Chembo, "Quantum dynamics of kerr optical frequency combs below and above threshold: Spontaneous four-wave mixing, entanglement, and squeezed states of light," *Physical Review A*, vol. 93, no. 3, p. 033820, 2016.

[12] C. Reimer, M. Kues, P. Roztocki, B. Wetzel, F. Grazioso, B. E. Little, S. T. Chu, T. Johnston, Y. Bromberg, L. Caspani *et al.*, "Generation of multiphoton entangled quantum states by means of integrated frequency combs," *Science*, vol. 351, no. 6278, pp. 1176–1180, 2016.

[13] T. Udem, J. Reichert, R. Holzwarth, and T. Hänsch, "Absolute optical frequency measurement of the cesium D_1 line with a mode-locked laser," *Physical Review Letters*, vol. 82, no. 18, pp. 3568–3571, 1999.

[14] A. Beyer, L. Maisenbacher, A. Matveev, R. Pohl, K. Khabarova, A. Grinin, T. Lamour, D. C. Yost, T. W. Hänsch, N. Kolachevsky *et al.*, "The Rydberg constant and proton size from atomic hydrogen," *Science*, vol. 358, no. 6359, pp. 79–85, 2017.

[15] T. W. Hänsch, "The impact of frequency combs," *Nature Photonics*, vol. 5, p. 193, 2011.

[16] S. A. Diddams, D. J. Jones, J. Ye, S. T. Cundiff, J. L. Hall, J. K. Ranka, R. S. Windeler, R. Holzwarth, T. Udem, and T. Hänsch, "Direct link between microwave and optical frequencies with a 300 THz femtosecond laser comb," *Physical Review Letters*, vol. 84, no. 22, pp. 5102–5105, 2000.

[17] D. J. Jones, S. A. Diddams, J. K. Ranka, A. Stentz, R. S. Windeler, J. L. Hall, and S. T. Cundiff, "Carrier-envelope phase control of femtosecond mode-locked lasers and direct optical frequency synthesis," *Science*, vol. 288, no. 5466, pp. 635–639, 2000.

[18] S. A. Diddams, "The evolving optical frequency comb," *JOSA B*, vol. 27, no. 11, pp. B51–B62, 2010.

[19] J. Ye and S. T. Cundiff, *Femtosecond optical frequency comb: principle, operation and applications.* Springer Science & Business Media, 2005.

[20] T. J. Kippenberg, R. Holzwarth, and S. A. Diddams, “Microresonator-based optical frequency combs,” *Science*, vol. 332, no. 6029, pp. 555–559, 2011.

[21] P. Del’Haye, A. Schliesser, O. Arcizet, T. Wilken, R. Holzwarth, and T. J. Kippenberg, “Optical frequency comb generation from a monolithic microresonator,” *Nature*, vol. 450, no. 7173, pp. 1214–1217, 2007.

[22] T. Herr, K. Hartinger, J. Riemensberger, C. Wang, E. Gavartin, R. Holzwarth, M. Gorodetsky, and T. Kippenberg, “Universal formation dynamics and noise of kerr-frequency combs in microresonators,” *Nature Photonics*, vol. 6, no. 7, pp. 480–487, 2012.

[23] T. Kippenberg, S. Spillane, and K. Vahala, “Kerr-nonlinearity optical parametric oscillation in an ultrahigh-Q toroid microcavity,” *Physical Review Letters*, vol. 93, no. 8, p. 083904, 2004.

[24] T. Herr, “Solitons and dynamics of frequency comb formation in optical microresonators,” EPFL, Tech. Rep., 2013.

[25] G. Lin, A. Coillet, and Y. K. Chembo, “Nonlinear photonics with high-Q whispering-gallery-mode resonators,” *Advances in Optics and Photonics*, vol. 9, no. 4, pp. 828–890, 2017.

[26] M. Karpov, M. H. Pfeiffer, J. Liu, A. Lukashchuk, and T. J. Kippenberg, “Photonic chip-based soliton frequency combs covering the biological imaging window,” *Nature Communications*, vol. 9, no. 1, p. 1146, 2018.

[27] F. Van Laere, G. Roelkens, M. Ayre, J. Schrauwen, D. Taillaert, D. Van Thourhout, T. F. Krauss, and R. Baets, “Compact and highly efficient grating couplers between optical fiber and nanophotonic waveguides,” *Journal of Lightwave Technology*, vol. 25, no. 1, pp. 151–156, 2007.

[28] N. Lindenmann, G. Balthasar, D. Hillerkuss, R. Schmogrow, M. Jordan, J. Leuthold, W. Freude, and C. Koos, “Photonic wire bonding: a novel concept for chip-scale interconnects,” *Optics Express*, vol. 20, no. 16, pp. 17 667–17 677, 2012.

[29] Y. Chen, R. Halir, Í. Molina-Fernández, P. Cheben, and J.-J. He, “High-efficiency apodized-imaging chip-fiber grating coupler for silicon nitride waveguides,” *Optics Letters*, vol. 41, no. 21, pp. 5059–5062, 2016.

[30] X. Xue and A. M. Weiner, “Microwave photonics connected with microresonator frequency combs,” *Frontiers of Optoelectronics*, vol. 9, no. 2, pp. 238–248, 2016.

[31] T. Carmon, L. Yang, and K. J. Vahala, “Dynamical thermal behavior and thermal self-stability of microcavities,” *Optics Express*, vol. 12, no. 20, pp. 4742–4750, 2004.

[32] C. Joshi, J. K. Jang, K. Luke, X. Ji, S. A. Miller, A. Klenner, Y. Okawachi, M. Lipson, and A. L. Gaeta, “Thermally controlled comb generation and soliton modelocking in microresonators,” *Optics Letters*, vol. 41, no. 11, pp. 2565–2568, 2016.

[33] A. S. Raja, A. S. Voloshin, H. Guo, S. E. Agafonova, J. Liu, A. S. Gorodnitskiy, M. Karpov, N. G. Pavlov, E. Lucas, R. R. Galiev *et al.*, “Electrically pumped photonic integrated soliton microcomb,” *Nature Communications*, vol. 10, no. 1, p. 680, 2019.

[34] F. Li, J. Yuan, Z. Kang, Q. Li, and P. Wai, “Modeling frequency comb sources,” *Nanophotonics*, vol. 5, no. 2, pp. 292–315, 2016.

[35] M. Yu, Y. Okawachi, A. G. Griffith, M. Lipson, and A. L. Gaeta, “Mode-locked mid-infrared frequency combs in a silicon microresonator,” *Optica*, vol. 3, no. 8, pp. 854–860, 2016.

[36] S. Coen, H. G. Randle, T. Sylvestre, and M. Erkintalo, “Modeling of octave-spanning Kerr frequency combs using a generalized mean-field Lugiato–Lefever model,” *Optics Letters*, vol. 38, no. 1, pp. 37–39, 2013.

[37] S. Coen and M. Erkintalo, “Universal scaling laws of Kerr frequency combs,” *Optics Letters*, vol. 38, no. 11, pp. 1790–1792, 2013.

[38] Y. K. Chembo, D. V. Strekalov, and N. Yu, “Spectrum and dynamics of optical frequency combs generated with monolithic whispering gallery mode resonators,” *Physical Review Letters*, vol. 104, no. 10, p. 103902, 2010.

[39] Y. K. Chembo and N. Yu, “Modal expansion approach to optical-frequency-comb generation with monolithic whispering-gallery-mode resonators,” *Physical Review A*, vol. 82, no. 3, p. 033801, 2010.

[40] T. J. Kippenberg, A. L. Gaeta, M. Lipson, and M. L. Gorodetsky, “Dissipative Kerr solitons in optical microresonators,” *Science*, vol. 361, no. 6402, p. eaan8083, 2018.

[41] X. Xue, X. Zheng, and B. Zhou, “Super-efficient temporal solitons in mutually coupled optical cavities,” *Nature Photonics*, vol. 13, no. 1, pp. 616–622, 2019.

[42] T. Hansson, D. Modotto, and S. Wabnitz, “On the numerical simulation of Kerr frequency combs using coupled mode equations,” *Optics Communications*, vol. 312, pp. 134–136, 2014.

[43] A. M. Weiner, “Frequency combs: Cavity solitons come of age,” *Nature Photonics*, vol. 11, no. 9, pp. 533–535, 2017.

[44] M. Haelterman, S. Trillo, and S. Wabnitz, “Dissipative modulation instability in a nonlinear dispersive ring cavity,” *Optics Communications*, vol. 91, no. 5-6, pp. 401–407, 1992.

[45] I. Barashenkov and Y. S. Smirnov, “Existence and stability chart for the ac-driven, damped nonlinear Schrödinger solitons,” *Physical Review E*, vol. 54, no. 5, pp. 5707–5725, 1996.

[46] C. Godey, I. V. Balakireva, A. Coillet, and Y. K. Chembo, “Stability analysis of the spatiotemporal Lugiato-Lefever model for Kerr optical frequency combs in the anomalous and normal dispersion regimes,” *Physical Review A*, vol. 89, no. 6, p. 063814, 2014.

[47] A. Griffith, J. Cardenas, C. B. Poitras, and M. Lipson, “High quality factor and high confinement silicon resonators using etchless process,” *Optics Express*, vol. 20, no. 19, pp. 21 341–21 345, 2012.

[48] A. A. Savchenkov, A. B. Matsko, V. S. Ilchenko, I. Solomatine, D. Seidel, and L. Maleki, “Tunable optical frequency comb with a crystalline whispering gallery mode resonator,” *Physical Review Letters*, vol. 101, no. 9, p. 093902, 2008.

[49] R. Henriet, G. Lin, A. Coillet, M. Jacquot, L. Furfaro, L. Larger, and Y. K. Chembo, “Kerr optical frequency comb generation in strontium fluoride whispering-gallery mode resonators with billion quality factor,” *Optics Letters*, vol. 40, no. 7, pp. 1567–1570, 2015.

[50] W. Liang, A. Savchenkov, A. Matsko, V. Ilchenko, D. Seidel, and L. Maleki, "Generation of near-infrared frequency combs from a MgF_2 whispering gallery mode resonator," *Optics Letters*, vol. 36, no. 12, pp. 2290–2292, 2011.

[51] G. Lin, S. Diallo, R. Henriet, M. Jacquot, and Y. K. Chembo, "Barium fluoride whispering-gallery-mode disk-resonator with one billion quality-factor," *Optics Letters*, vol. 39, no. 20, pp. 6009–6012, 2014.

[52] C. Y. Wang, T. Herr, P. Del'Haye, A. Schliesser, J. Hofer, R. Holzwarth, T. Hänsch, N. Picqué, and T. J. Kippenberg, "Mid-infrared optical frequency combs at 2.5 μm based on crystalline microresonators," *Nature Communications*, vol. 4, p. 1345, 2013.

[53] I. S. Grudinin, N. Yu, and L. Maleki, "Generation of optical frequency combs with a CaF_2 resonator," *Optics Letters*, vol. 34, no. 7, pp. 878–880, 2009.

[54] L. Razzari, D. Duchesne, M. Ferrera, R. Morandotti, S. Chu, B. Little, and D. Moss, "CMOS-compatible integrated optical hyper-parametric oscillator," *Nature Photonics*, vol. 4, no. 1, pp. 41–45, 2010.

[55] B. Hausmann, I. Bulu, V. Venkataraman, P. Deotare, and M. Lončar, "Diamond nonlinear photonics," *Nature Photonics*, vol. 8, no. 5, pp. 369–374, 2014.

[56] S. B. Papp and S. A. Diddams, "Spectral and temporal characterization of a fused-quartz-microresonator optical frequency comb," *Physical Review A*, vol. 84, no. 5, p. 053833, 2011.

[57] H. Jung, C. Xiong, K. Y. Fong, X. Zhang, and H. X. Tang, "Optical frequency comb generation from aluminum nitride microring resonator," *Optics Letters*, vol. 38, no. 15, pp. 2810–2813, 2013.

[58] H. Jung and H. X. Tang, "Aluminum nitride as nonlinear optical material for on-chip frequency comb generation and frequency conversion," *Nanophotonics*, vol. 5, no. 2, pp. 263–271, 2016.

[59] M. Zhang, C. Wang, R. Cheng, A. Shams-Ansari, and M. Lončar, "Monolithic ultra-high-Q lithium niobate microring resonator," *Optica*, vol. 4, no. 12, pp. 1536–1537, 2017.

[60] M. Pu, L. Ottaviano, E. Semenova, and K. Yvind, "Efficient frequency comb generation in AlGaAs-on-insulator," *Optica*, vol. 3, no. 8, pp. 823–826, 2016.

[61] K. Saha, Y. Okawachi, B. Shim, J. S. Levy, R. Salem, A. R. Johnson, M. A. Foster, M. R. Lamont, M. Lipson, and A. L. Gaeta, "Modelocking and femtosecond pulse generation in chip-based frequency combs," *Optics Express*, vol. 21, no. 1, pp. 1335–1343, 2013.

[62] K. Saleh and Y. K. Chembo, "Advances in microwave generation using kerr optical frequency combs," in *Laser Resonators, Microresonators, and Beam Control XIX*, vol. 10090. International Society for Optics and Photonics, 2017, p. 100900P.

[63] A. Dutt, "On-chip quantum and nonlinear optics: from squeezing to spectroscopy," Ph.D. dissertation, Cornell University, 2017.

[64] D. J. Lockwood and L. Pavesi, "Silicon fundamentals for photonics applications," in *Silicon Photonics.* Springer, 2004, pp. 1–50.

[65] Q. Xu, D. Fattal, and R. G. Beausoleil, “Silicon microring resonators with 1.5-μm radius,” *Optics Express*, vol. 16, no. 6, pp. 4309–4315, 2008.

[66] Q. Lin, O. J. Painter, and G. P. Agrawal, “Nonlinear optical phenomena in silicon waveguides: modeling and applications,” *Optics Express*, vol. 15, no. 25, pp. 16 604–16 644, 2007.

[67] J. Leuthold, C. Koos, and W. Freude, “Nonlinear silicon photonics,” *Nature photonics*, vol. 4, no. 8, pp. 535–544, 2010.

[68] L. Zhang, Y. Yue, R. G. Beausoleil, and A. E. Willner, “Analysis and engineering of chromatic dispersion in silicon waveguide bends and ring resonators,” *Optics Express*, vol. 19, no. 9, pp. 8102–8107, 2011.

[69] B. Jalali, “Silicon photonics: Nonlinear optics in the mid-infrared,” *Nature Photonics*, vol. 4, no. 8, pp. 506–508, 2010.

[70] L. Yin, Q. Lin, and G. P. Agrawal, “Soliton fission and supercontinuum generation in silicon waveguides,” *Optics Letters*, vol. 32, no. 4, pp. 391–393, 2007.

[71] Q. Xu and M. Lipson, “All-optical logic based on silicon micro-ring resonators,” *Optics Express*, vol. 15, no. 3, pp. 924–929, 2007.

[72] C. Koos, L. Jacome, C. Poulton, J. Leuthold, and W. Freude, “Nonlinear silicon-on-insulator waveguides for all-optical signal processing,” *Optics Express*, vol. 15, no. 10, pp. 5976–5990, 2007.

[73] K. Li and A. C. Foster, “Nonlinear optics in hydrogenated amorphous silicon,” *IEEE Journal of Selected Topics in Quantum Electronics*, vol. 24, no. 6, pp. 1–12, 2018.

[74] C. A. Husko, A. S. Clark, M. J. Collins, A. De Rossi, S. Combrié, G. Lehoucq, I. H. Rey, T. F. Krauss, C. Xiong, and B. J. Eggleton, “Multi-photon absorption limits to heralded single photon sources,” *Scientific Reports*, vol. 3, p. 3087, 2013.

[75] R. Sun, P. Dong, N.-n. Feng, C.-y. Hong, J. Michel, M. Lipson, and L. Kimerling, “Horizontal single and multiple slot waveguides: optical transmission at λ=1550 nm,” *Optics Express*, vol. 15, no. 26, pp. 17 967–17 972, 2007.

[76] R. K. Lau, M. R. Lamont, Y. Okawachi, and A. L. Gaeta, “Effects of multiphoton absorption on parametric comb generation in silicon microresonators,” *Optics Letters*, vol. 40, no. 12, pp. 2778–2781, 2015.

[77] A. Dutt, K. Luke, S. Manipatruni, A. L. Gaeta, P. Nussenzveig, and M. Lipson, “On-chip optical squeezing,” *Physical Review Applied*, vol. 3, no. 4, p. 044005, 2015.

[78] Y. Okawachi, K. Saha, J. S. Levy, Y. H. Wen, M. Lipson, and A. L. Gaeta, “Octave-spanning frequency comb generation in a silicon nitride chip,” *Optics Letters*, vol. 36, no. 17, pp. 3398–3400, 2011.

[79] A. G. Griffith, R. K. Lau, J. Cardenas, Y. Okawachi, A. Mohanty, R. Fain, Y. H. D. Lee, M. Yu, C. T. Phare, C. B. Poitras *et al.*, “Silicon-chip mid-infrared frequency comb generation,” *Nature Communications*, vol. 6, p. 6299, 2015.

[80] I. Demirtzioglou, C. Lacava, K. R. Bottrill, D. J. Thomson, G. T. Reed, D. J. Richardson, and P. Petropoulos, "Frequency comb generation in a silicon ring resonator modulator," *Optics Express*, vol. 26, no. 2, pp. 790–796, 2018.

[81] S. Miller, K. Luke, Y. Okawachi, J. Cardenas, A. L. Gaeta, and M. Lipson, "On-chip frequency comb generation at visible wavelengths via simultaneous second-and third-order optical nonlinearities," *Optics Express*, vol. 22, no. 22, pp. 26 517–26 525, 2014.

[82] C. Castellan, "Second order nonlinearities in silicon photonics," Ph.D. dissertation, University of Trento, 2019.

[83] X. Shen, R. C. Beltran, V. M. Diep, S. Soltani, and A. M. Armani, "Low-threshold parametric oscillation in organically modified microcavities," *Science Advances*, vol. 4, no. 1, p. eaao4507, 2018.

[84] B. Yao, S.-W. Huang, Y. Liu, A. K. Vinod, C. Choi, M. Hoff, Y. Li, M. Yu, Z. Feng, D.-L. Kwong *et al.*, "Gate-tunable frequency combs in graphene–nitride microresonators," *Nature*, vol. 558, no. 7710, pp. 410–414, 2018.

[85] T. Hansson, D. Modotto, and S. Wabnitz, "Mid-infrared soliton and raman frequency comb generation in silicon microrings," *Optics Letters*, vol. 39, no. 23, pp. 6747–6750, 2014.

[86] M. Yu, J. K. Jang, Y. Okawachi, A. G. Griffith, K. Luke, S. A. Miller, X. Ji, M. Lipson, and A. L. Gaeta, "Breather soliton dynamics in microresonators," *Nature Communications*, vol. 8, p. 14569, 2017.

[87] S. Malaguti, G. Bellanca, A. de Rossi, S. Combrié, and S. Trillo, "Self-pulsing driven by two-photon absorption in semiconductor nanocavities," *Physical Review A*, vol. 83, no. 5, p. 051802, 2011.

[88] R. Haldar, P. Mondal, V. Mishra, and S. K. Varshney, "Stability analysis and bandwidth estimation of free-carrier driven Kerr frequency-comb," in *2017 Conference on Lasers and Electro-Optics Pacific Rim (CLEO-PR)*. IEEE, 2017, pp. 1–2.

[89] M. Haelterman, S. Trillo, and S. Wabnitz, "Additive-modulation-instability ring laser in the normal dispersion regime of a fiber," *Optics Letters*, vol. 17, no. 10, pp. 745–747, 1992.

[90] T. Hansson, D. Modotto, and S. Wabnitz, "Dynamics of the modulational instability in microresonator frequency combs," *Physical Review A*, vol. 88, no. 2, p. 023819, 2013.

[91] R. Haldar, A. Roy, P. Mondal, V. Mishra, and S. K. Varshney, "Generalized mathematical formalism governing free-carrier driven Kerr frequency comb in optical micro-cavities," *arXiv preprint arXiv:1802.00391*, 2018.

[92] R. Haldar, A. Roy, P. Mondal, V. Mishra, and S. K. Varshney, "Free-carrier-driven Kerr frequency comb in optical microcavities: Steady state, bistability, self-pulsation, and modulation instability," *Physical Review A*, vol. 99, no. 3, p. 033848, 2019.

[93] Y. Okawachi, M. Yu, K. Luke, D. O. Carvalho, S. Ramelow, A. Farsi, M. Lipson, and A. L. Gaeta, "Dual-pumped degenerate Kerr oscillator in a silicon nitride microresonator," *Optics Letters*, vol. 40, no. 22, pp. 5267–5270, 2015.

[94] P. Grelu, *Nonlinear Optical Cavity Dynamics: From Microresonators to Fiber Lasers.* John Wiley & Sons, 2015.

[95] A. Sahoo and S. Roy, “Effect of two-photon absorption on cavity soliton: stability and perturbation analysis,” in *Frontiers in Optics.* Optical Society of America, 2017, pp. JW4A–118.

[96] R. Hamerly, D. Gray, C. Rogers, and K. Jamshidi, “Conditions for parametric and free-carrier oscillation in silicon ring cavities,” *Journal of Lightwave Technology*, vol. 36, no. 19, pp. 4671–4677, 2018.

[97] C. Bao, Y. Xuan, J. A. Jaramillo-Villegas, D. E. Leaird, M. Qi, and A. M. Weiner, “Direct soliton generation in microresonators,” *Optics Letters*, vol. 42, no. 13, pp. 2519–2522, 2017.

[98] G. Kozyreff, “Localized turing patterns in nonlinear optical cavities,” *Physica D: Nonlinear Phenomena*, vol. 241, no. 10, pp. 939–946, 2012.

CHAPTER 5

Dual-pump Kerr Microresonators

In this chapter, we explore the advantages of using dual-pump Kerr microresonator (MR) frequency comb (FC) over conventional single-pump Kerr FC. In the first part of the chapter, detailed analytical formulations of dual-pump Kerr FC supported by numerical results are presented. In the next part of this chapter, we uncover the synchronous nature and the robustness of dual-pump configuration against the writing jitters, third-order dispersion, self-steepening effects, and stimulated Raman scattering in optical buffer applications. Finally, we wind up the chapter presenting a brief discussion on the existence of super-cavity solitons in dual-pumped Kerr MRs. [1]

5.1 Fundamentals and Background

Frequency comb offers an exciting field of active research, due to its potential applications in frequency metrology, arbitrary waveform synthesis, precision-clocking and as highly coherent integrated optical sources or data carriers [1–6] for optical communications. Kerr microresonator based FC has paved the way for the generation of on-chip mode-locked cavity soliton (CS) [1]. CS belongs to a class of

---

[1] Publications related to this chapter are [26], [27], [64], [68], [76].

dissipative solitons which are stable, temporally confined optical pulses and corresponds to a broad FC, where the frequency lines are typically separated by one cavity free spectral range (FSR) apart [7, 8]. Microresonators are the dissipative systems that exploit the optical nonlinearity to generate CSs under the applications of an external driving field. A single continuous wave (CW) pump is mostly employed in such configuration to generate the CS from vacuum fluctuations in a high Q-factor cavity by transitioning through the modulation instability (MI) and chaotic regime [9, 10], which is realized by making adjustments to the pump detuning and the pump power [7–10]. Apart, from FC corresponding to CS, there are other variants including Turing pattern, and variable FSR frequency Comb, etc. [4].

Singly-pumped MR based FC has been recently employed for terabit communications [11, 12], high data-rate transmission via coherent wavelength division multiplexing (WDM), and orthogonal frequency domain multiplexing schemes. Micro-resonator based FC provides attractive solutions for RF photonics applications [13], spectroscopy [14] and optical frequency synthesizer [15]. Recently, MR based tunable repetition rate clock source has also been demonstrated [16]. Chip-scale transceivers can be realized based on microresonator FC operating at low powers. Such devices are capable of generating comb lines that span over enormous bandwidth often covering multiple telecommunication bands [17]. This clearly indicates that MR based FC is a potential candidate for optical communication systems which is capable to replace separate laser sources supporting individual channels in WDM systems and equally useful for wide bandwidth utilization. Therefore, it is highly desirable to produce several coherent comb lines spanning the spectrum of interest.

Although CW-driven Kerr FC has been widely used for the above-mentioned applications, researchers are now looking at different configurations and material platforms for more versatility, flexibility, and application-specific benefits. These endeavors include the dual-comb spectroscopy, coupled microresonator-based FC for improving the nonlinear conversion efficiency, FC generation in MRs possessing simultaneous second and third order nonlinearity for locking the carrier envelope offset frequency [5, 18], use of organic molecules, graphene or carbon nano-tube for low-threshold, and tunable FC generations, respectively [19–22] etc. Deploying

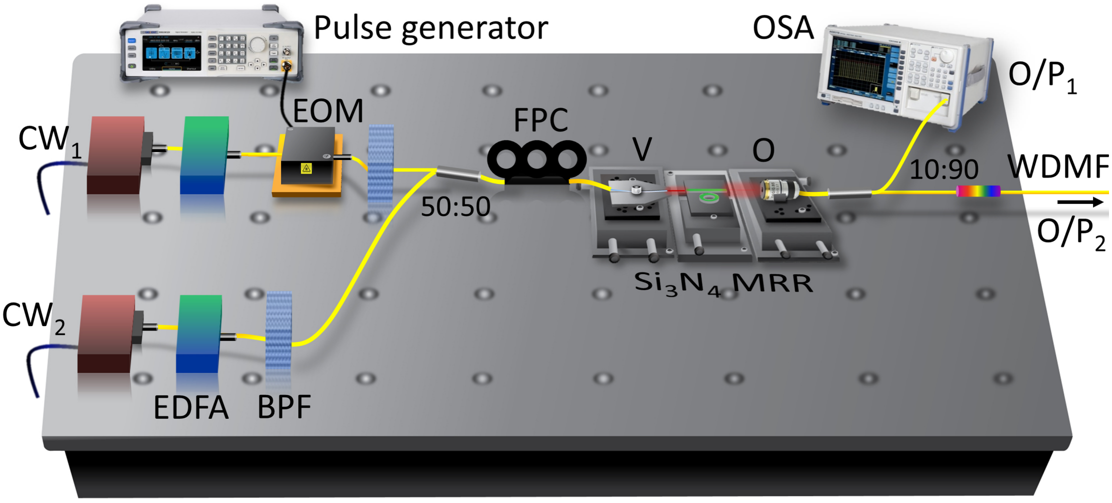

Figure 5.1: Dual-pump Kerr MR frequency comb. Two CW pumps (CW$_1$ and CW$_2$) of slightly different center frequencies are deployed. The first source can be modulated with an electro-optic modulator (EOM) or an acousto-optic modulator (AOM). Both the inputs are coupled to the device under test (DUT) (silicon-nitride microring resonator in this case) through a 50:50 combiner, a fiber polarization controller (FPC), by any of the fiber-to-waveguide (edge-to-edge/butt/grating) coupling methods. The output from the MRR is collected through an objective and divided into two parts by a splitter. The Smaller part of the output (O/P1) is observed by an optical spectrum analyzer (OSA) and the other part (O/P2) can be used for several applications. EDFA: erbium doped fiber amplifier, BPF: band-pass filter, V: V-groove, O: Objective, WDMF: wavelength division multiplexing filter.

two pumps instead of a single CW input is another interesting dimension to explore [23–25]. These schemes can either include two separate input laser sources, or one of the two laser sources can be modulated by an external modulator which is shown in Fig. 5.1. Consequently, we can access a whole new regime and tweaking parameters including equal/unequal detuning, equal/unequal pump power, and modulating frequency between the two pumps and so on.

We have studied this exciting, nevertheless less-explored operating regime of FC i.e. dual-pump configuration which is alternatively known as bi-chromatic pumping scheme. In the first part of our work, we develop an analytical model to predict the onset of MI in this configuration [26]. It is to be noted that the FC generation in dual-pump configuration proceeds via threshold-less non-degenerate four-wave mixing (FWM) and also through degenerate MI. Using our model, we can identify these distinct regimes of operations and used the analytical results to predict MR parameters (namely the second-order group velocity dispersion

(GVD), detuning, and input power) for flexible composite FC generation possessing tunable primary and secondary side-bands. Our model is also capable of determining the transition from structured FC to monotonic FC with a single spectral envelope.

In the next part of our work, we investigate the time-domain behavior of the dual-pump Kerr MR and its benefits to several applications. We propose synchronous all-optical buffer based on CS supported in bi-chromatically pumped micro-cavity [27]. The synchronous nature arises because of the harmonic potential-well originating from the oscillatory background. The extremums of the oscillatory lobes in case of operation below the symmetry breaking bi-furcation threshold represent robust trapping centers for CS which results in the optical buffer being immune to the writing jitters. In the case of CS-based all-optical buffer, writing of the optical bits is done using suitable addressing seed pulses. We have also numerically demonstrated the ability of these synchronous buffers to perform elementary logic operations like AND, OR, rendering these units simultaneous buffering and logical capability. We have noticed the suppression of third-order GVD induced temporal drift up to a critical value. We also show that these optical bits are Raman-resilient. Moreover, the limiting factors such as very high cavity detuning that can diminish or cause the wreckage of the robust optical trapping centers are numerically demonstrated in the final part of this chapter. Dual-pump CS parameters obtained from the variational formalism based on Euler-Lagrange equations of motions [28–32] match closely with those obtained from the numerical simulations performed using the split-step Fourier method (SSFM).

It is evident that the dual pump based design is promising. Besides robust operations, microresonator in dual-pump configuration provides additionally the advantage of tunability and composite FC generation [17, 23, 24, 32–35] although they suffer from thermal effect induced resonance shift under high pump intensity. Such arrangements are potential candidates to study several nonlinear phenomena if the issues related to thermal effect are addressed properly. We have listed some of the advantages and disadvantages of using the dual-pump MR configuration over the single-pump configuration in the next section. It is possible to extract versatile features from the dual pump based Kerr MR which would otherwise not have been possible in the single-pump configuration once one can address the issues associated with the dual-pump configuration.

5.1.1 Single Pumping versus Dual Pumping

There are several advantages of using dual-pump over a single-pump configuration as listed below:

5.1.1.1 Advantages

(i) Thresholdless comb generation
(ii) Variable FSR Comb
(iii) Synchronous all-optical buffer
(iv) Robust against writing jitters, third order dispersion
(v) Raman resilience

A. Thresholdless comb generation:
As discussed earlier, integrated optical parametric oscillators (OPOs) having numerous applications in photonics, spectroscopy, sensing, quantum information processing require the parametric gain to be equal to the microcavity loss for the frequency conversion [36–40]. In a cavity with third order/Kerr nonlinearity, two pump photons (ω_p) are converted into a signal (ω_s) and an idler (ω_I) photon by interacting with two vacuum states at the signal and pump frequencies, respectively. In order to occur such parametric (also known as hyperparametric oscillation [38]) oscillation, energy and momentum both must be conserved simultaneously [36]. As the signal and idler mode numbers l_s and l_I, respectively are symmetrically located with respect to the pump mode (l_p), i.e. $l_\mathrm{s,I}$=$l_\mathrm{p}$$\pm N$, momentum has to be conserved automatically. However, the cavity modes are not exactly equidistant to each other due to the waveguide and material dispersions. Therefore, energy conservation ($2\hbar\omega_\mathrm{p}$=$\hbar\omega_\mathrm{s}$+$\hbar\omega_\mathrm{I}$) gradually starts violating for the cavity modes away from the pump mode (Fig. 2) which results in the parametric gain as a function of the frequency detuning, $\Delta\omega = 2\omega_\mathrm{p} - \omega_\mathrm{s} - \omega_\mathrm{I}$. If for a particular cavity-mode the detuning $\Delta\omega$ exceeds the parametric gain bandwidth (Ω=$4c\gamma P/n_0$) then the parametric gain is no longer able to generate the frequency side-band at that particular mode and beyond, thereby restricting the span of the FC through OPO.

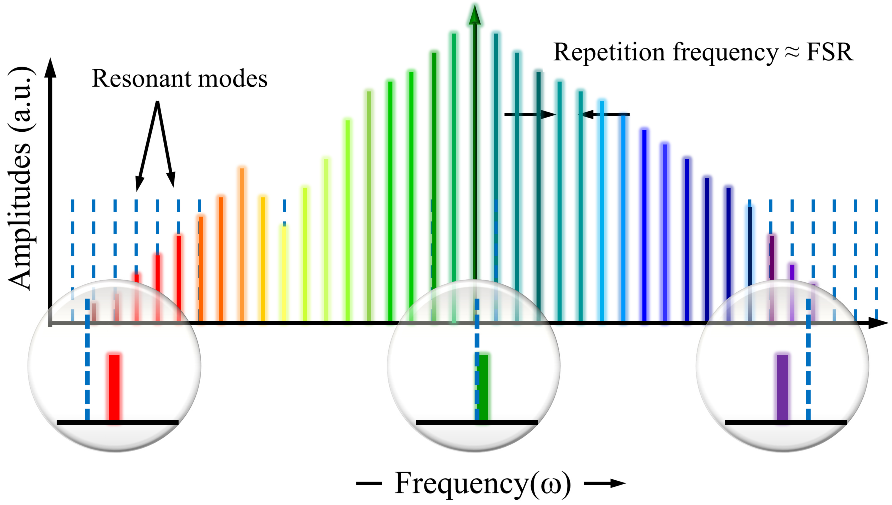

Figure 5.2: Finite FC-bandwidth as a result of non-equidistant cavity modes due to GVD.

Here, $\gamma\,(=\omega n_2/cA_{\text{eff}})$, P, n_0, n_2, ω, c, A_{eff} are the nonlinear coefficient, intra-cavity power, linear refractive index (RI), nonlinear RI, operating angular frequency, the speed of light in vacuum, and effective modal area, respectively. The threshold pump power for parametric oscillation can be given by [36],

$$P_{\text{Th}}^{\text{Kerr}}\,(\Delta\omega) = \frac{\omega_0^2 Q_0^{-2}(1+K)^2 + \left(\frac{\Delta\omega}{2}\right)^2}{\gamma\Delta\omega\frac{c}{n_{\text{eff}}}} \times \frac{C\,(\Gamma)\,\pi^2 R n_{\text{eff}}}{2\lambda_0} \times \frac{(K+1)^2}{Q_0 K} \tag{5.1}$$

where Q_0, K, n_{eff}, $C(\Gamma)$, λ_0 are the intrinsic quality factor of the cavity, mode coupling coefficient, effective refractive index, modal power correction factor, and pumping wavelength, respectively. For a cavity with extremely high Q-factor, the beat-note signal produced by the mixing of the optical pump and the generated side-bands does not depend upon the pump power, Q-factor of the mode, and the laser detuning from the pump mode [38]. In this case, the threshold pump power (P_{th}) for the oscillation can be found out by perturbing the steady-state solutions of the intra-cavity field A. One can use either the Langevin formalism [38], modal expansion approach, or the Lugiato-Lefever equation (LLE) to find out the threshold pump power [37, 39].

If a, b_+, b_- represent the pump mode and the sidebands at angular frequency ω_0, ω_+, and ω_-, respectively then the total Hamiltonian describing the three-mode interaction in presence of third-order nonlinearity can be given by, $H_{\text{tot}} = H_0 + H_{\text{int}}$ where H_0 is the system Hamiltonian without Kerr nonlinearity and the H_{int} is the interaction Hamiltonian due to Kerr nonlinearity and can be written as,

$$H_0 = \hbar\omega_0 a^\dagger a + \hbar\omega_+ b_+^\dagger b_+ + \hbar\omega_- b_-^\dagger b_- \tag{5.2}$$

$$\begin{aligned} V = & -\hbar\tfrac{g}{2} : (a + b_+ + b_- + h.c)^4 : \\ = & -\hbar\tfrac{g}{2}\left(a^\dagger a^\dagger aa + b_+^\dagger b_+^\dagger b_+ b_+ + b_-^\dagger b_-^\dagger b_- b_-\right) \\ & -2\hbar g\left(b_-^\dagger b_+^\dagger b_+ b_- + a^\dagger b_+^\dagger b_+ a + a^\dagger b_-^\dagger b_- a\right) \\ & -\hbar g\left(b_-^\dagger b_+^\dagger aa + a^\dagger a^\dagger b_+ b_-\right) \end{aligned} \tag{5.3}$$

": $\cdots$:" means the normal ordering assuming rotating wave approximation. g denotes the nonlinear coupling coefficient as given by Eq. 5.4,

$$g = \frac{\hbar\omega_0^2 c n_2}{n_0^2 V_{\text{eff}}} \tag{5.4}$$

$$V_{\text{eff}} = \frac{\int \varepsilon(\vec{r})\left|\vec{A}\,(\vec{r})\right|^2 dV}{\max\left[\varepsilon(\vec{r})\left|\vec{A}\,(\vec{r})\right|^2\right]} = A_{\text{eff}} L \tag{5.5}$$

where, A, L, and V_{eff} are the mode amplitude, cavity length, and the effective modal volume of the cavity, respectively. In Heisenberg's picture, the evolution of an operator with respect to time can be given by,

$$\frac{d\hat{Q}\,(t)}{dt} = \frac{i}{\hbar}\left[H, \hat{Q}\,(t)\right] \tag{5.6}$$

where H is the overall Hamiltonian of the system. However, in practice a microcavity is an open system having loss compensated by the external input power (P_{in}). Hence, the decay term, as well as the Langevin fluctuation force, have to be included to account the realistic scenario. Adding the cavity losses and Langevin forces one obtains,

$$\begin{aligned}\dot{a} = &-\left[i\omega_0 + ik_0\left(T\right) + \gamma_0 + \gamma_{c0}\right]a + ig\left[a^\dagger a + 2b_+^\dagger b_+ + 2b_-^\dagger b_-\right]a \\ &+2iga^\dagger b_+ b_- + f_0 + f_{c0}\end{aligned} \tag{5.7a}$$

$$\begin{aligned}\dot{b}_+ = &-\left[i\omega_+ + ik_+\left(T\right) + \gamma_+ + \gamma_{c+}\right]b_+ + ig\left[2a^\dagger a + b_+^\dagger b_+ + 2b_-^\dagger b_-\right]b_+ \\ &+igb_-^\dagger aa + f_+ + f_{c+}\end{aligned} \tag{5.7b}$$

$$\begin{aligned}\dot{b}_- = &-\left[i\omega_- + ik_-\left(T\right) + \gamma_- + \gamma_{c-}\right]b_- + ig\left[2a^\dagger a + 2b_+^\dagger b_+ + b_-^\dagger b_-\right]b_- \\ &+igb_+^\dagger aa + f_- + f_{c-}\end{aligned} \tag{5.7c}$$

γ_0, γ_+, γ_- are intrinsic decay rates, whereas, γ_{c0}, γ_{c+}, γ_{c-} are the decay rates due to external coupling. Coefficients $\kappa_0(T)$, $\kappa_+(T)$, and $\kappa_-(T)$ account the frequency shifts of the modes a, b_+, and b_- due to the temperature change, respectively. Where,

$$\begin{aligned}\left[f_0\left(t\right), f_0^\dagger\left(t'\right)\right] &= 2\gamma_0\delta\left(t-t'\right), & \left[f_{c0}\left(t\right), f_{c0}^\dagger\left(t'\right)\right] &= 2\gamma_{c0}\delta\left(t-t'\right) \\ \left[f_+\left(t\right), f_+^\dagger\left(t'\right)\right] &= 2\gamma_+\delta\left(t-t'\right), & \left[f_{c+}\left(t\right), f_{c+}^\dagger\left(t'\right)\right] &= 2\gamma_{c+}\delta\left(t-t'\right) \\ \left[f_-\left(t\right), f_-^\dagger\left(t'\right)\right] &= 2\gamma_-\delta\left(t-t'\right), & \left[f_{c-}\left(t\right), f_{c-}^\dagger\left(t'\right)\right] &= 2\gamma_{c-}\delta\left(t-t'\right)\end{aligned} \tag{5.8}$$

and, the expectation values of the Langevin forces are as follows:

$$\langle f_{c0}\rangle = \sqrt{\frac{2\gamma_{c0}P_0}{\hbar\omega_0}}e^{-i\omega t}, \ \ \langle f_0\rangle = \langle f_+\rangle = \langle f_-\rangle = \langle f_{c+}\rangle = \langle f_{c-}\rangle = 0 \tag{5.9}$$

We assume the slowly varying harmonic mode amplitudes given by,

$$\begin{aligned}a &= Ae^{-i\omega t} \\ b_+ &= B_+e^{-i\tilde{\omega}_+ t} \\ b_- &= B_-e^{-i\tilde{\omega}_- t}\end{aligned} \tag{5.10}$$

ω, $\tilde{\omega}_+$, and $\tilde{\omega}_-$ are the carrier frequencies of modes a, b_+, and b_-, respectively.

Finally, taking an average over a full-cycle, one can obtain the steady-state expectation values of the mode amplitudes given by,

$$\begin{aligned}\Gamma_0 \langle A\rangle = ig\left[|\langle A\rangle|^2 + 2|\langle B_+\rangle|^2 + 2|\langle B_-\rangle|^2\right]\langle A\rangle \\ +2ig\langle A^*\rangle\langle B_+\rangle\langle B_-\rangle + \langle F_{\mathrm{c}0}\rangle\end{aligned} \tag{5.11a}$$

$$\begin{aligned}\Gamma_+ \langle B_+\rangle = ig\left[2|\langle A\rangle|^2 + |\langle B_+\rangle|^2 + 2|\langle B_-\rangle|^2\right]\langle B_+\rangle \\ +ig\left\langle B_-^*\right\rangle\langle A\rangle^2\end{aligned} \tag{5.11b}$$

$$\begin{aligned}\Gamma_- \langle B_-\rangle = ig\left[2|\langle A\rangle|^2 + 2|\langle B_+\rangle|^2 + |\langle B_-\rangle|^2\right]\langle B_-\rangle \\ +ig\left\langle B_+^*\right\rangle\langle A\rangle^2\end{aligned} \tag{5.11c}$$

where,

$$\Gamma_0 = i\left(\omega_0 - \omega + \kappa_0\left(T\right)\right) + \gamma_0 + \gamma_{\mathrm{c}0} \tag{5.12a}$$

$$\Gamma_+ = i\left(\omega_+ - \tilde{\omega}_+ + \kappa_+\left(T\right)\right) + \gamma_+ + \gamma_{\mathrm{c}+} \tag{5.12b}$$

$$\Gamma_- = i\left(\omega_- - \tilde{\omega}_- + \kappa_-\left(T\right)\right) + \gamma_- + \gamma_{\mathrm{c}-} \tag{5.12c}$$

From the steady-state solution, the expression for the threshold power P_{th} that can initiate the optical parametric oscillation can be found as,

$$P_{\mathrm{th}} \approx 1.54\left(\frac{\pi}{2}\right)\frac{\gamma_0+\gamma_{\mathrm{c}0}}{2\gamma_{\mathrm{c}0}}\frac{n_0^2 V_{\mathrm{eff}}}{n_2\lambda {Q_{\mathrm{L}}}^2} = 1.54\left(\frac{\pi}{2}\right)\frac{Q_{\mathrm{c}}}{2Q_{\mathrm{L}}}\frac{n_0^2 V_{\mathrm{eff}}}{n_2\lambda {Q_{\mathrm{L}}}^2} \tag{5.13}$$

where the numerical factor 1.54 appears due to the self-phase modulation effects on the oscillation threshold. It is important to note that the threshold power (P_{th}) is directly proportional to the mode volume of the cavity V_{eff} and inversely proportional to the square of the overall or loaded Q-factor, Q_L=$(\omega/2)(\gamma_0+\gamma_{\mathrm{c}0})^{-1}$ of the cavity. Q_{c} denotes the Q-factor only for the coupling. For sub-milli-Watt threshold power, small V_{eff} and high Q-factor are always desirable, however, the value of the Q-factor is generally restricted by the V_{eff} as the bending loss increases with the decrease in device size [41] thereby eventually dominates the material and scattering losses. If the device is carefully designed, an ultra-high Q and very low mode-volume with a sub-microwatt parametric threshold-power can be obtained [42–44] For dual-pump configuration, there exists no such restriction of the input pump power to initiate the parametric oscillation [26, 40].

B. Variable FSR frequency comb:

The free spectral range (f_{FSR}) of the optical microresonator for a particular mode around an operating frequency f_0 can be given by,

$$f_{\text{FSR}}(f_0) = \frac{c}{2\pi R n_g} = \frac{1}{t_{\text{R}}} \tag{5.14}$$

where R, n_{g}, and t_{R} are the radius of the microresonator, the group index, and the round-trip time, respectively. It is seen that if the cavity perimeter is larger, then the FSR becomes smaller. Alternatively, the FSR can also be written as Eq. 5.15 in terms of the wavelength,

$$\lambda_{\text{FSR}}(\lambda_0) = \frac{\lambda_0^2}{2\pi R n_{\text{g}}} \tag{5.15}$$

It is well-known that the group index is related to the effective RI (n_{eff}) of a particular mode by,

$$n_{\text{g}}(\omega) = n_{\text{eff}}(\omega) + \omega \frac{\partial n_{\text{eff}}(\omega)}{\partial \omega} \tag{5.16}$$

Therefore, the conventional ways to change the FSR or to obtain a variable FSR frequency-comb are:

(i) Changing the cavity size (by using different ring radius/perimeter),

(ii) Altering the mode of operation (TE/TM),

(iii) Changing the effective RI by using different cladding materials,

Transmission spectra for microrings with two different radii (R_1=15 μm and R_2=30 μm) obtained from FDTD simulations are shown in Fig. 5.3. However, for a particular design, the length of the cavity is fixed. One can change the overall

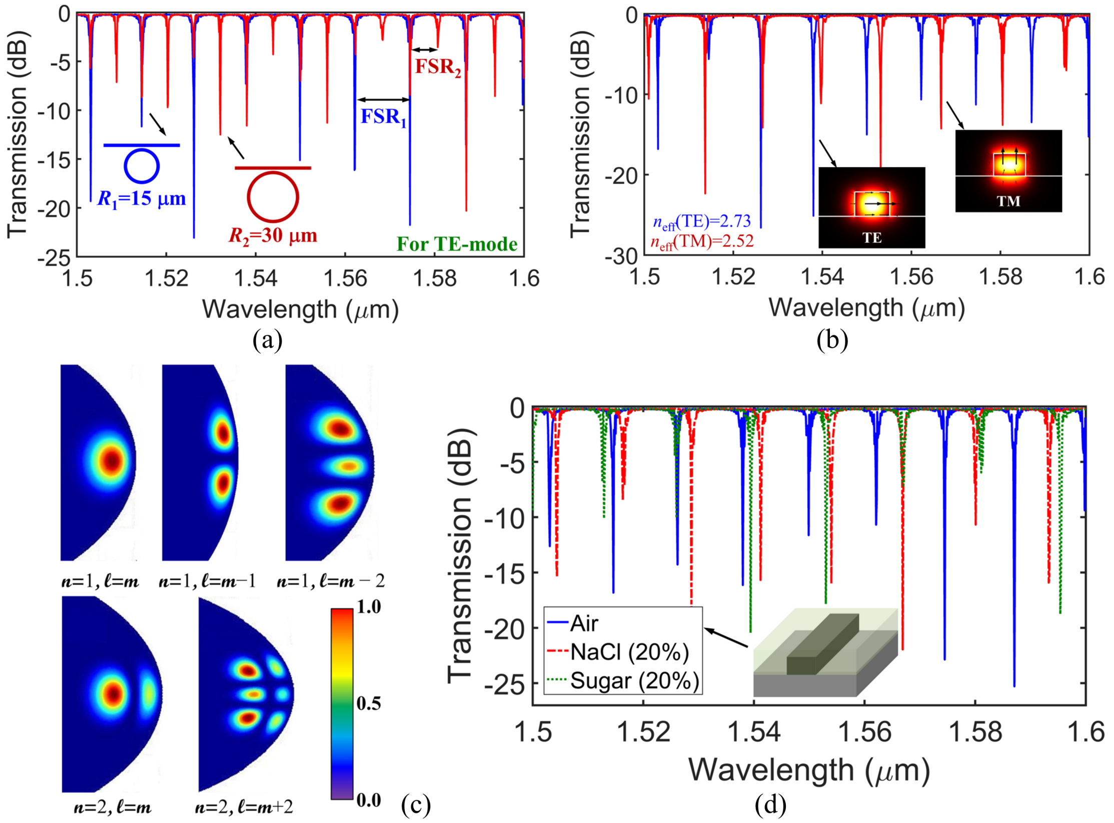

(a) (b)

(c) (d)

Figure 5.3: Transmission spectra of the microring resonator (MRR) for, (a) two different ring radii, R_1=15 μm, R_2=30 μm, (b) TE ($n_{\mathrm{eff}} = 2.73$) and TM ($n_{\mathrm{eff}} = 2.52$)-modes. (c) Spatial distributions of different modes in a spherical resonator, and MRR (d) when the cladding materials are air, saline water (20%), and glucose water (20%), respectively (for TE-mode).

n_g (or n_{eff}) either by altering the mode of operation or by using different cladding materials on top of the optical waveguides. This is also shown in Fig. 5.3 (b) and Fig. 5.3 (c). Further, one can use different cladding materials as shown in Fig. 5.3 (d). In that case, the FSR can slightly vary depending upon the RI and material dispersion of the cladding material. Nevertheless, none of these methods provide much freedom to change the FSR. On contrary, one of the most important features of dual-pump configuration is that using the bichromatic pump provides us the freedom to desirably tune the comb-FSR as an integral multiple of the FSR of the cavity modes just by changing the modulation frequency between the two pumps [23,24] (Fig. 5.1). Robustness of the synchronous all-optical buffers against the third-order dispersion, self-steepening, and the Raman effect is discussed in detail in the subsequent sections.

Despite having the aforementioned advantages, the dual-pump configuration has many drawbacks which prohibit us to use of the configuration, frequently. Only a few experimental demonstrations on bichromatic Kerr FC exist in the literature [17, 23, 25].

5.1.1.2 Disadvantages

(i) Complex circuitry and difficult to implement,
(ii) Power-inefficient,
(iii) Possibility of thermal instability,
(iv) Volatile in nature,

As listed above, most importantly, the configuration is power-inefficient and volatile in nature, which implies that the moment the external laser source driving the MR is switched off the configuration becomes unable to perform the logic operations, does not show the robustness against the detrimental parameters such as writing jitters, and can no longer be able to retain the optical bits intact and the rotating solitons quickly decay over time.

5.2 Analytical Model of Dual-pump Microresonators

It is well known that degenerate modulation instability (MI) is the driving mechanism for single pump configuration, whereas in case of dual-pump it is governed by both threshold-less non-degenerate four-wave mixing (FWM) and threshold intensity dependent MI [24,45]. Therefore, understanding these underlying mechanisms and differentiating their regimes of operations without investing huge computational time and resources are essential to acquire better control of the comb generation process. In this section, we have investigated both analytically and numerically, the importance of different primary physical mechanisms (non-degenerate FWM, MI) and their regimes of operations responsible for FC generations in the context of dual-pump. In addition, we study the implications of different physical mechanisms in generating variable free spectral range (FSR) and composite combs in desired spectral locations. The theoretical model assists in the quick prediction of regimes without performing intensive numerical simulations of Lugiato-Lefever equation (LLE). One can easily determine the necessary parameters (pump power, cavity detuning and so on) for application-specific FC generation. Our model finds a close agreement with the numerically simulated results for dual-pump MR configuration [26].

5.2.1 Theory

5.2.1.1 Governing equations and threshold-less comb

The driven and damped nonlinear system is modeled using normalized mean-field LLE incorporating the dual-pump as [24],

$$\frac{\partial A}{\partial t} + i\beta\frac{\partial^2 A}{\partial \tau^2} - i|A|^2 A = -(1 + i\Delta)A + f_0 \cos(\Omega\tau) \tag{5.17}$$

where A is the normalized electric-field envelope, t is the slow-time variable and τ denotes the normalized fast-time ranging from $-\pi$ to π. The remaining parameters are the normalized second-order dispersion coefficient β, normalized cavity detuning Δ, normalized pump amplitude f_0, and the modulation frequency Ω. Note that in deriving the normalized LLE as given in Eq. 5.17, equal pump amplitudes (f_0) have been assumed for both the pumps, also the difference in detuning between two pumps is assumed sufficiently small to be neglected compared to the average detuning [24]. By choosing suitable MR parameters and modulation frequency, we can excite a variety of homogeneous or patterned steady-state solutions both in the normal and anomalous dispersion regimes owing to the rich dynamics exhibited by the dual-pump configuration [24].

Single pump FC generation is attributed to the degenerate MI which takes place only above a particular threshold of the pump intensity [9] where the pump corresponds to a cavity mode. The suitably detuned pump can further excite symmetric side-bands through MI route and gradually leads to the formation of FC via degenerate and non-degenerate FWM. In the case of dual-pump configuration, it is known that FC can be generated without the requirement of pump threshold,

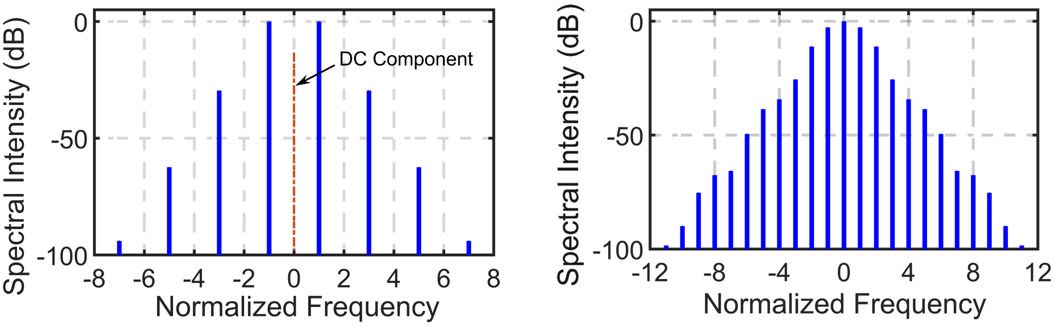

(a) (b)

Figure 5.4: Frequency comb in dual-pump MR configuration, (a) primary comb lines corresponding to β=1, Ω=1, Δ=5, f_0=3, produced through non-degenerate FWM, (b) both the secondary and primary comb lines when f_0 is increased to 4.5, displaying the existence of dc spectral component and even modes due to intensity-dependent MI besides the FWM process.

and is referred to as threshold-less FC generation [24, 40]. In the latter case, the FC generation is due to non-degenerate FWM where two cavity modes annihilate and give rise to symmetric side-bands following the phase and frequency matching conditions. However, if any such mode possesses enough intensity to meet the threshold requirement for MI then the comb generation would be governed by both non-degenerate FWM and MI processes [24].

We numerically simulate dual-pump MR configuration by solving the LLE through SSFM. The direct current (dc) component (zero normalized frequency) and the even modes do not appear in the spectrum if the FC generation takes place solely due to the threshold-less, non-degenerate FWM, as shown in Fig. 5.4 (a). On contrary, if both the non-degenerate FWM and MI act simultaneously on FC generation, then both the dc component and the even modes appear in the comb spectrum as depicted in Fig. 5.4 (b). Thus, MI leads to the formation of secondary comb in the latter case in addition to the primary comb which occurs only due to the non-degenerate FWM. Note that, additive white Gaussian noise noise is assumed as an initial seed along with two pumps with proper detuning in simulating the FCs.

5.2.1.2 Four-wave model and the stationary states

The complicated dynamics of a dual-pump system can reasonably be well approximated by the four-wave model which is sufficiently good to predict the stationary states. The four-wave model [24] sheds light on the stability and can also provide insight into the complete solution space that can be achieved via soft and/or hard excitations. In the four-wave model, it is assumed that most of the spectral power is confined in the pump modes and the first side-bands.

In the single pump case, there exists a homogeneous stationary solution (HSS) over which other temporal patterns rest. This HSS is supported by the external CW pumping and shows bistable behavior in the unperturbed steady state when $\Delta \geq \sqrt{3}$ [7]. However, in the dual-pump case, no such HSS can exist. If the pump frequencies correspond to Ω and $-\Omega$ (symmetric pumping in normalized frequency), it can be shown that the solution of the form: $C\left(\mathrm{e}^{\mathrm{i}\,\Omega\tau} + \mathrm{e}^{-\,\mathrm{i}\,\Omega\tau}\right)$ cannot be a steady-state solution of Eq. 5.17, where C is an arbitrary constant. It must at least excite other side-bands to satisfy the steady state of Eq. 5.18 which we consider as,

$$\frac{1}{2}\left(A_{\mathrm{p}}\left(\mathrm{e}^{\mathrm{i}\,\Omega\tau} + \mathrm{e}^{-\mathrm{i}\,\Omega\tau}\right) + A_{\mathrm{s}}\left(\mathrm{e}^{\mathrm{i}3\Omega\tau} + \mathrm{e}^{-\mathrm{i}3\Omega\tau}\right)\right) \tag{5.18}$$

where, A_{p} and A_{s} are the normalized pump and the first side-band amplitudes, respectively. We know from [24] that the stationary fixed points are obtained from the following coupled Eqs. 5.19–5.20,

$$\frac{|f_0|^2}{2I_0} = \left[\left(\Delta - \beta\Omega^2 - \frac{3I_0}{2}\right) - g_{+}\frac{1-\eta}{\eta}\right]^2 + \frac{1}{\eta^2} \tag{5.19}$$

$$9\beta\Omega^2 = \Delta - g_{-} - \frac{3I_0(1-\eta)}{2\eta} \tag{5.20}$$

where,

$$g_{\pm} = I_0[1 + \cos\varphi(2\cos\varphi + \frac{(2\pm 1)}{2}\sqrt{{}^{1-\eta}/_{\eta}})] \tag{5.21}$$

$$\cos\varphi = \frac{\Delta - 9\beta\Omega^2 - I_0 - \frac{3}{2}I_0\frac{1-\eta}{\eta}}{\sqrt{\left(\Delta - 9\beta\Omega^2 - I_0 - \frac{3I_0(1-\eta)}{2\eta}\right)^2 + 1}} \tag{5.22}$$

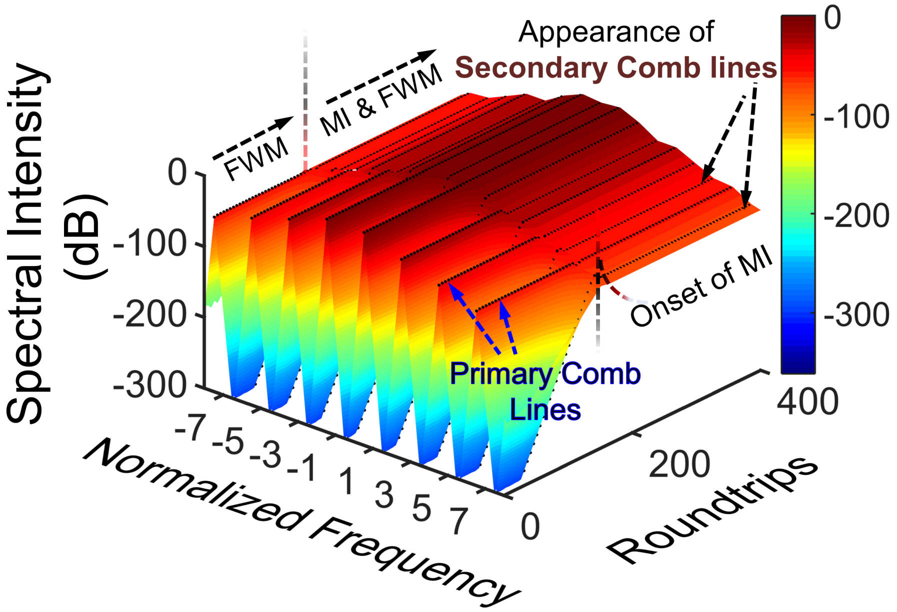

Figure 5.5: The gradual build-up of secondary comb lines over the threshold-less FWM induced background of primary comb lines due to the inception of intensity dependent MI. The color map indicates the spectral intensity in dB. Vertical dashed line dictates the boundary between two processes.

and,

$$\eta = \frac{|A_{\mathrm{p}}|^2}{P_0} \tag{5.23}$$

$$P_0 = |A_{\mathrm{p}}|^2 + |A_{\mathrm{s}}|^2 \tag{5.24}$$

$$I_0 = \frac{P_0 \eta}{2} \tag{5.25}$$

where ϕ=$(\phi_s - \phi_p)$ is the relative phase between the pump mode and the sidebands.

In our calculations, we consider the steady state predicted from the four-wave model as the equivalent HSS for the dual-pump configuration. This is because the MI grows over the non-degenerate FWM generated FC, as shown in Fig. 5.5 where the evolution of comb lines as a function of roundtrips is plotted. The colors represent the spectral intensity (in dB) of the comb lines. The figure clearly highlights the transition of the FC into the FWM and MI combined regime from the FWM regime through the initiation of secondary comb lines.

5.2.2 Analytical Modelling

We perform the MI analysis by linearizing Eq. 5.17 about the steady state solution predicted from the four-wave model. The MI analysis for a bi-chromatic pump in the non-resonant case can be found in [46]. We assume a perturbation of the form of Eq. 5.26 to perform linear stability analysis,

$$\frac{1}{2}\left(A_\mathrm{p}\left(\mathrm{e}^{\mathrm{i}\,\Omega\tau}+\mathrm{e}^{-\,\mathrm{i}\,\Omega\tau}\right)+A_\mathrm{s}\left(\mathrm{e}^{\mathrm{i}\,3\Omega\tau}+\mathrm{e}^{-\,\mathrm{i}\,3\Omega\tau}\right)\right)\times\left(1+\sum_{\mu=k\Omega}a_\mu\mathrm{e}^{\mathrm{i}\,\mu\tau}+\sum_{\mu=k\Omega}a_{-\mu}\mathrm{e}^{-\,\mathrm{i}\,\mu\tau}\right) \tag{5.26}$$

Where k takes integer values and a is the amplitude of the noise at the corresponding normalized frequency.

At the onset of modulation instability, the dc (zero-frequency) MI growth rate owes to the contribution of amplitude growth rates corresponding to zero normalized frequency. For the dc MI growth rate at onset, one should consider only dc terms in the expansion of $|A|^2A$. The perturbative terms arise due to $\mu=\Omega$, termed as first lobe contribution, are given as:

$$\begin{aligned}
&a_\Omega\left(3|A_p|^2+4|A_s|^2+2{A_p}^*A_s+{A_s}^*A_p+2A_s^2\tfrac{A_p^*}{A_p}\right)\tfrac{A_p}{4}\\
&+a_{-\Omega}\left(3|A_p|^2+4|A_s|^2+2{A_p}^*A_s+{A_s}^*A_p+2A_s^2\tfrac{A_p^*}{A_p}\right)\tfrac{A_p}{4}\\
&+{a^*}_\Omega\left(3|A_p|^2+4|A_s|^2+2{A_p}^*A_s+{A_s}^*A_p+2A_s^2\tfrac{A_p^*}{A_p}\right)\tfrac{A_p}{8}\\
&+{a^*}_{-\Omega}\left(3|A_p|^2+4|A_s|^2+2{A_p}^*A_s+{A_s}^*A_p+2A_s^2\tfrac{A_p^*}{A_p}\right)\tfrac{A_p}{8}
\end{aligned} \tag{5.27}$$

The first lobe refers to the MI gain curve responsible for the instability that corresponds to the dc component. This is contributed by the cavity modes located at the spectral location $\mu=\Omega$. Similarly, second and third lobes also indicate the MI gain curves contributed by the cavity modes situated at the spectral locations $\mu=2\Omega$, and $\mu=3\Omega$, respectively. Note that, no term arises due to $\mu=2\Omega$ (second lobe contribution). Terms arising due to third lobe contribution ($\mu=3\Omega$ are given as:

$$a_{3\Omega}\ \left(4|A_\mathrm{p}|^2+3|A_\mathrm{s}|^2+\tfrac{2{A_p}^2A_s^*}{A_s}+\tfrac{A_p|A_p|^2}{A_s}\right)\tfrac{A_\mathrm{s}}{4}$$

$$\begin{aligned}
&+a_{-3\Omega}\ \left(4|A_{\mathrm{p}}|^2+3|A_{\mathrm{s}}|^2+\tfrac{2{A_p}^2A_s^*}{A_s}+\tfrac{A_p|A_p|^2}{A_s}\right)\tfrac{A_{\mathrm{s}}}{4}\\
&+a_{3\Omega}^*\left(4|A_{\mathrm{p}}|^2+3|A_{\mathrm{s}}|^2+\tfrac{2{A_p}^2A_s^*}{A_s}+\tfrac{A_p|A_p|^2}{A_s}\right)\tfrac{A_{\mathrm{s}}}{8}\\
&+{a^*}_{-3\Omega}\left(4|A_{\mathrm{p}}|^2+3|A_{\mathrm{s}}|^2+\tfrac{2{A_p}^2A_s^*}{A_s}+\tfrac{A_p|A_p|^2}{A_s}\right)\tfrac{A_{\mathrm{s}}}{8}
\end{aligned} \tag{5.28}$$

No contribution comes from higher-order lobes at the onset of instability. While deriving the MI gain expression using the linear stability analysis, we have neglected the contributions of the dispersion of the HSS and only considered the dispersion of the noise signals in the perturbation expansion of $\beta\partial^2A/\partial\tau^2$. Due to symmetry in the frequency domain LLE (where we neglect higher-order dispersion, self-steepening effect, and other higher-order nonlinearities), we take the ansatz of the form as:

$$a_{\Omega}\ +a_{-\Omega}\ =k_1\mathrm{e}^{\lambda_1 t} \tag{5.29}$$

$$a_{3\Omega}\ +a_{-3\Omega}\ =k_3\mathrm{e}^{\lambda_3 t} \tag{5.30}$$

Where λ_1 and λ_3 are the dc MI growth rates due to the first and third lobe contributions, respectively, while k_1 and k_3 are constants. If the perturbation does not contain the term, the MI growth rate is governed by the first lobe contribution ($a_{3\Omega}\,\mathrm{e}^{\mathrm{i}\,3\Omega\tau}+a_{-3\Omega}\,\mathrm{e}^{-\,\mathrm{i}\,3\Omega\tau}$), as shown in Fig. 5.6 (a). Looking for the non-trivial solution of Eqs. 5.17, 5.27, and 5.29, we obtain the expression for the MI gain as:

$$\begin{gathered}
\lambda=\lambda_1=-1-2\,\mathrm{Im}(X)+\sqrt{\Lambda_1};\\
\Lambda_1=4\{\mathrm{Im}(X)\}^2-\left(|K_1|^2-|X|^2\right);\\
X=\tfrac{1}{4}\left(3|A_{\mathrm{p}}|^2+4|A_{\mathrm{s}}|^2+2A_p^*A_s+A_s^*A_p+2A_s^2\tfrac{A_p^*}{A_p}\right);\\
|K_1|^2=\left(\Delta-\beta\Omega^2-2X\right)\left(\Delta-\beta\Omega^2-2X^*\right)
\end{gathered} \tag{5.31}$$

Similarly, if we consider that the perturbation does not contain, $a_{\Omega}\,\mathrm{e}^{\mathrm{i}\,\Omega\tau}+a_{-\Omega}\,\mathrm{e}^{-\,\mathrm{i}\,\Omega\tau}$ then the MI growth rate will be determined by third lobe contribution ($\lambda=\lambda_3$), as shown in Fig. 5.6 (b). In that case, the expression for the MI-gain is obtained from Eqs. 5.17, 5.28, and 5.30 and can be given by Eq. 5.32.

$$\begin{gathered}
\lambda = \lambda_3 = -1 - 2\,\mathrm{Im}(Y) + \sqrt{\Lambda_3};\\
\Lambda_3 = 4\{\mathrm{Im}(Y)\}^2 - \left(|K_3|^2 - |Y|^2\right);\\
Y = \tfrac{1}{4}\left(4|A_\mathrm{p}|^2 + 3|A_\mathrm{s}|^2 + \tfrac{2{A_p}^2 A_s^*}{A_s} + \tfrac{A_p|A_p|^2}{A_s}\right);\\
|K_3|^2 = \left(\Delta - \beta(3\Omega)^2 - 2Y\right)\left(\Delta - \beta(3\Omega)^2 - 2Y^*\right)
\end{gathered} \tag{5.32}$$

Where A_p and A_s are obtained from the four-wave model relations given by Eq. 5.24; Λ_1 and Λ_3 are the discriminants of λ_1 and λ_3 which determine the threshold criterion.

Another interesting feature arises from the fact that X and Y can potentially be complex with the non-zero imaginary component. In such a scenario, the MI gain depends on $\mathrm{Im}(X)$ and $\mathrm{Im}(Y)$ as depicted in Fig. 5.6 (c).

In Fig. 5.7, we plot the pump amplitude, f_0 as a function of normalized detuning Δ. Critical values of the pump amplitude f_0, demarcating the FWM and MI regions for different detuning values, are obtained numerically and analytically. The solid blue curve with filled circles corresponds to the analytical solution, which is in close agreement with the numerically obtained solution (solid-red curve). We explore three different scenarios (A, B, C) for three different normalized pump amplitudes at a fixed detuning value. For pump amplitude much smaller than the critical value (case A), the FC will be generated through threshold-less non-degenerate FWM, resulting in narrow bandwidth, as shown in sub-figure A. When the pump amplitude is close to the critical value (case B), the comb generation is governed by threshold less non-degenerate FWM process with larger FC bandwidth than in case A, as depicted in sub-figure B. As the pump amplitude crosses the critical value (case C), the comb generation takes place via both non-degenerate FWM and intensity dependent MI routes, possessing secondary comb lines, as shown in sub-figure C. In order to create variable FSR comb, one should ensure that the pump amplitude must be smaller than the critical pump amplitude. However, if f_0 is greater than the MI threshold, no control over the FSR of the comb lines can be retained.

The slight discrepancy between numerical and analytical results arises due to

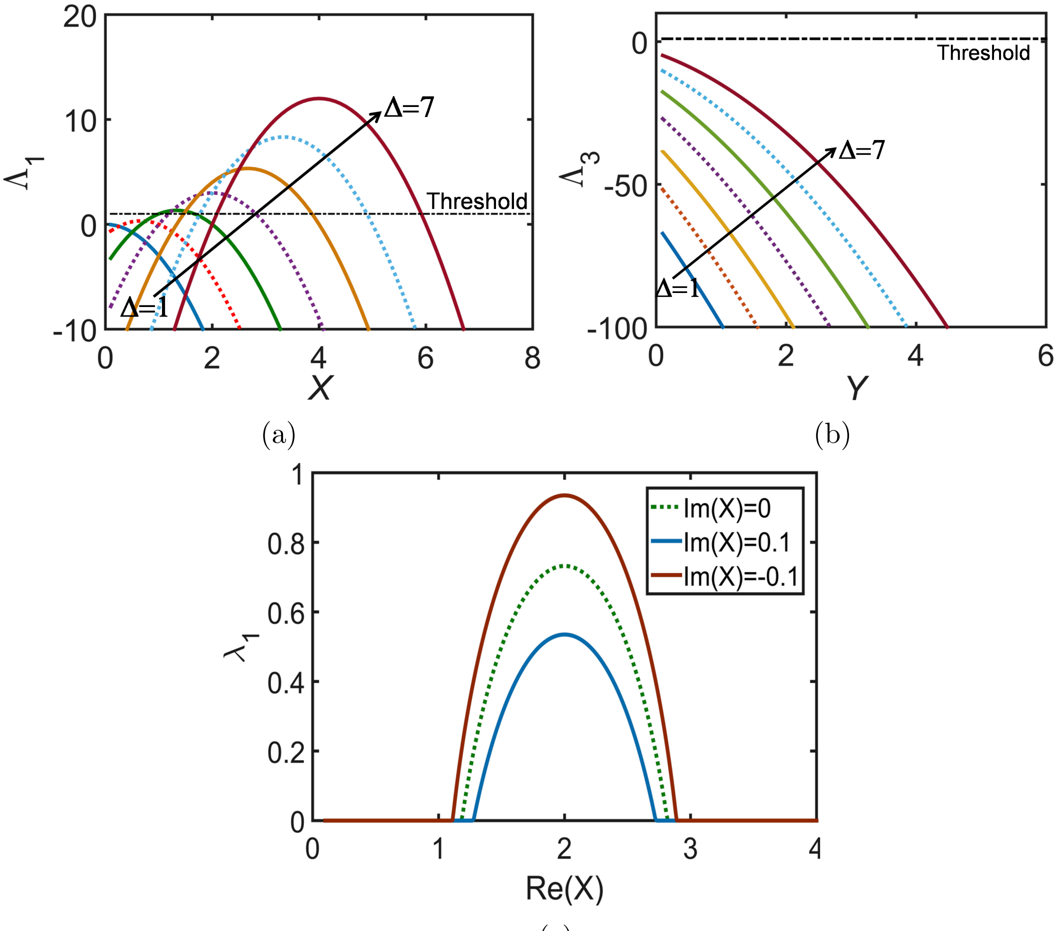

(a) (b)

(c)

Figure 5.6: Threshold dependence of MI gain due to (a) first-lobe contribution, $\mu = \Omega$, and (b) third-lobe contribution, $\mu = 3\Omega$ for various detuning values as a function of X and Y, respectively. X and Y are assumed to be real. The threshold is shown by the black dashed curve. (c) MI growth rate due to the first lobe contribution at a fixed detuning of $\Delta = 4$, when X assumes particular values of the imaginary part as mentioned in the legend.

the fact that four-wave model relies on the representation of the steady state as truncated four modes. However, some fraction of spectral energy must be present in other cavity modes which are not being considered in the four-wave model. Note that in Fig. 5.4 (b), the spectral amplitude of the dc component is greater than the pump modes whereas in the inset C of Fig. 5.7 it is smaller—i.e. a situation similar to the single-pump case. This is mainly due to contribution by MI lobe created by two pumps.

For $\beta = 1$ and $\Omega = 1$ the first lobe is the major contributor towards the non-

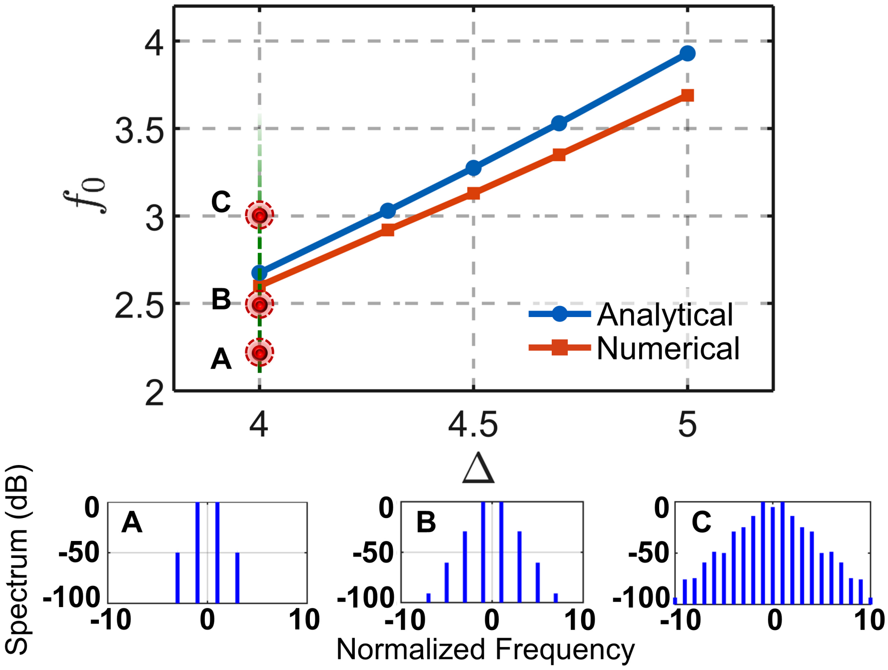

Figure 5.7: Critical values of pump amplitude obtained numerically (solid red curve) and analytically (solid blue curve) for a range of detuning parameters. Sub-figures A, B, and C represent three different cases where the pump amplitude is varied at a fixed detuning. A close agreement is observed between the two approaches.

degenerate MI process which makes the normalized dc component as the most MI susceptible spectral component. In general, we need to locate the principle MI gain lobe and identify the most susceptible spectral component and proceed in a similar fashion. In the following section, such scenarios arise and are explained in details.

5.2.3 Results and Discussions

5.2.3.1 Variable free spectral range frequency comb

Wang *et al.* have recently shown the advantage of dual-pump configuration in creating variable FSR frequency comb [23]. It is always desired in optical communication to produce FC whose FSR is several multiples of the intrinsic FSR of the MR to avoid the cross-talk between the adjacent channels. Therefore, variable FSR comb [23, 47] generation can be ensured if the MR is driven with two pumps possessing the modulation frequency equals to the desired FSR of the FC, provided we operate in the threshold-less non-degenerate FWM regime (i.e. in the parameter space below the solid red curve in Fig. 5.7). Once the threshold boundary is crossed as dictated in Fig. 5.7, the combined MI and non-degenerate FWM processes rule (sub-figure C). In this region, secondary comb generation takes place resulting in filling up of rest of the cavity modes in between the primary comb lines. Therefore, extra care must be taken to operate in the suitable parameter space which can be easily predicted from our proposed analytical model. Moreover, one does not have the luxury of operating at low pump powers to avoid the MI because it leads to narrow FC generation as is the case in sub-figure A. Pump power should be sufficiently high to yield broader FC with variable FSR like the one shown in the sub-figure B, however, it must be less than the MI threshold. The proposed analytical model is capable to estimate the required input pump power in optimizing the variable FSR frequency comb for optical communication applications.

5.2.3.2 Tunable Composite Frequency Comb for WDM

Most of the composite comb structures reported so far [48,49] make use of a single-pump and depend on parametric seeding, which needs a stringent requirement of injecting the seed once the primary comb generation is completed. The generated sub-comb lines disappear as soon as the seed is removed. However, the dual-pump configuration does not suffer from this limitation. With the help of the proposed analytical model, we present a multitude of tunable primary comb lines along with associated sub-comb lines suitable for multichannel communications by selecting suitable microresonator FC parameters in dual pump configuration. We gain further insight into the tunability aspect by leveraging our analytical model.

When the cavity is driven by two pumps, excited pump modes undergo threshold less FWM responsible for sub-comb line formation. If the power in the pump mode and adjacent sidebands are greater than the MI threshold, primary comb lines will be created at the spectral location where the resultant instability gain is the maximum. Thereafter, these comb lines again undergo threshold-less FWM combined with MI-induced gain, giving rise to additional sub-comb lines, as illus-

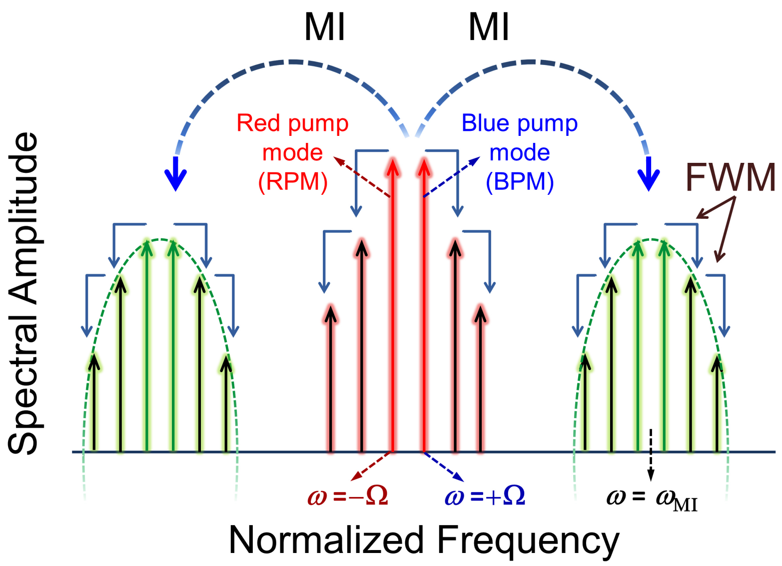

Figure 5.8: Cartoon depicting the formation of primary and secondary comb lines using dual-pump configuration. Red arrows denote two pump modes; green arrows correspond to primary comb lines whereas the black arrows indicate the secondary comb lines. The MI gain lobe is shown by the green dashed curves.

trated in Fig. 5.8.

Figure 5.8 shows the two pump modes designated as blue pump mode (BPM) at frequency Ω and red pump mode (RPM) at frequency $-\Omega$. It depicts the emergence of primary comb lines due to MI at a frequency ω_{MI} and secondary sub-comb lines due to cascaded FWM. The green-dashed parabolic envelopes dictate the MI gain region in both the sides of the pumps. Thus the primary comb lines get flanked by secondary ones and are capable of spanning a wide frequency range owing to this cascading nature of comb formation as visualized in Fig. 5.8. The resultant composite comb can be used conveniently as separate channels for WDM applications. In order to find out the spectral locations of the primary comb lines, we perform the MI analysis.

5.2.3.3 MI Gain

It is evident that the pump modes, BPM ($\omega = \Omega$) and RPM ($\omega = -\Omega$), dominantly contribute to the MI gain as most of the spectral power is concentrated in these modes. The MI induced spectral peaks are situated at $\omega_{\mathrm{MI}} - \Omega$ from the BPM and at $\omega_{\mathrm{MI}} + \Omega$ from the RPM, respectively with reference to ω_{MI} as depicted in Fig. 5.8. For the MI growth rate at onset, we need to consider only $\exp(i\omega_{\mathrm{MI}}t)$ terms in the expansion of $|A|^2A$. The perturbative terms arising due to $\mu = \omega_{\mathrm{MI}} - \Omega$ (contribution from the BPM) are:

$$a_{(\omega_{\mathrm{MI}}-\Omega)}\left(3|A_p|^2\right)\frac{A_p}{4} + a^*_{(\omega_{\mathrm{MI}}-\Omega)}\left(3|A_p|^2\right)\frac{A_p}{8} \tag{5.33}$$

And terms arising due to the RPM contribution $\mu = \omega_{\mathrm{MI}} + \Omega$ are:

$$a_{(\omega_{\mathrm{MI}}+\Omega)}\left(3|A_p|^2\right)\frac{A_p}{4} + a^*_{(\omega_{\mathrm{MI}}+\Omega)}\left(3|A_p|^2\right)\frac{A_p}{8} \tag{5.34}$$

Contributions due to side-bands of amplitude A_{s} are neglected as they are negligible in the regime of interest. Due to the symmetry in the frequency domain of LLE, under assumptions mentioned in the previous section, we can write noise amplitudes as:

$$a_{(\omega_{\mathrm{MI}}-\Omega)} = a^*_{-(\omega_{\mathrm{MI}}-\Omega)} = k_1\mathrm{e}^{\lambda_1 t} \tag{5.35}$$

$$a_{(\omega_{\mathrm{MI}}+\Omega)} = a^*_{-(\omega_{\mathrm{MI}}+\Omega)} = k_2\mathrm{e}^{\lambda_2 t} \tag{5.36}$$

where λ_1 and λ_2 are the MI growth rate at the onset of instability due to the BPM and RPM contributions, respectively while k_1 and k_2 are the constants. After performing linearization of the nonlinear LLE akin to conventional MI analysis, we get

$$\lambda_1 = -1 + \left(\left(\frac{3}{4}|A_p|^2\right)^2 - \left(\beta(\omega_{\mathrm{MI}} - \Omega)^2 + 2\left(\frac{3}{4}|A_p|^2\right) - \Delta\right)^2\right)^{\frac{1}{2}} \tag{5.37}$$

and,

$$\lambda_1 = -1 + \left(\left(\frac{3}{4}|A_p|^2\right)^2 - \left(\beta(\omega_{\mathrm{MI}} + \Omega)^2 + 2\left(\frac{3}{4}|A_p|^2\right) - \Delta\right)^2\right)^{\frac{1}{2}} \tag{5.38}$$

Modulation instability growth rate can be given approximately by ($\lambda = \lambda_1 + \lambda_2$). We can add two contributions since there is no phase difference between the pump modes (following the assumption that the detuning of two pumps is identical). Primary comb lines will appear at the spectral location where λ is the highest for all ω_{MI}. Two spectral locations appear due to inherent beating nature of the dual pump. From Eqs. 5.37 and 5.38, we can obtain the threshold intensity for MI to occur which is dependent on the requirement that the term inside the square root must be greater than one.

The tunability of Primary Comb and Sub-comb Lines Spectral Locations

The primary comb lines will appear at the location $(\omega_{\mathrm{PC}} + \Omega)$ and $(\omega_{\mathrm{PC}} - \Omega)$ where the MI gain is maximum. The subscript PC refers to primary comb. The cascaded generation will lead to primary comb location at $\omega = \pm m\omega_{\mathrm{PC}} \pm \Omega$, where m takes integer values and the normalized zero frequency lies between two pump modes. This can be tuned by a suitable selection of MR parameters. Figure 5.9 (a) shows the dependence of MI gain for two sets of MR parameters. The solid blue curve corresponds to set of parameters, $\Delta = -6$, $\Omega = 1$, $\beta = -0.0005$, $f_0 = 8.25$ (set-1) whereas the solid red curve corresponds to $\Delta = -4$, $\Omega = 1$, $\beta = -0.0001$, $f_0 = 6$ (set-2). Corresponding composite combs for parameter (set-1) and (set-2) are exhibited in Figs. 5.9 (b)-5.9 (c), respectively. We can select the suitable set of parameters as per the requirement of gain spectral location. Sub-comb lines are formed due to parametric non-degenerate FWM combined with MI-induced gain circumscribing the newly created primary comb lines. Their spectral locations are given by $\omega = \pm m\omega_{\mathrm{PC}} \pm n\Omega$ where n is an integer. Clearly, they can be manipulated by changing the modulation frequency of the dual pump as illustrated in Figs. 5.9 (d)-5.9 (e). The requirement on sub-comb line separation fixes the pump modulation frequency, Ω. The other free normalized parameters namely β, Δ and f_0 can suitably be chosen to cater the requirement on cascaded primary comb location. Thus, the four-wave model helps us to map these parameters for tunable composite FC generation. The primary comb lines that are formed are found to be highly coherent following the coherence calculation methodology in [50].

This fact is experimentally demonstrated in [17, 35]. The temporal evolution of the coherence clearly suggests the growth of primary comb lines via MI. The reason behind the slight mismatch between the analytical and numerical results

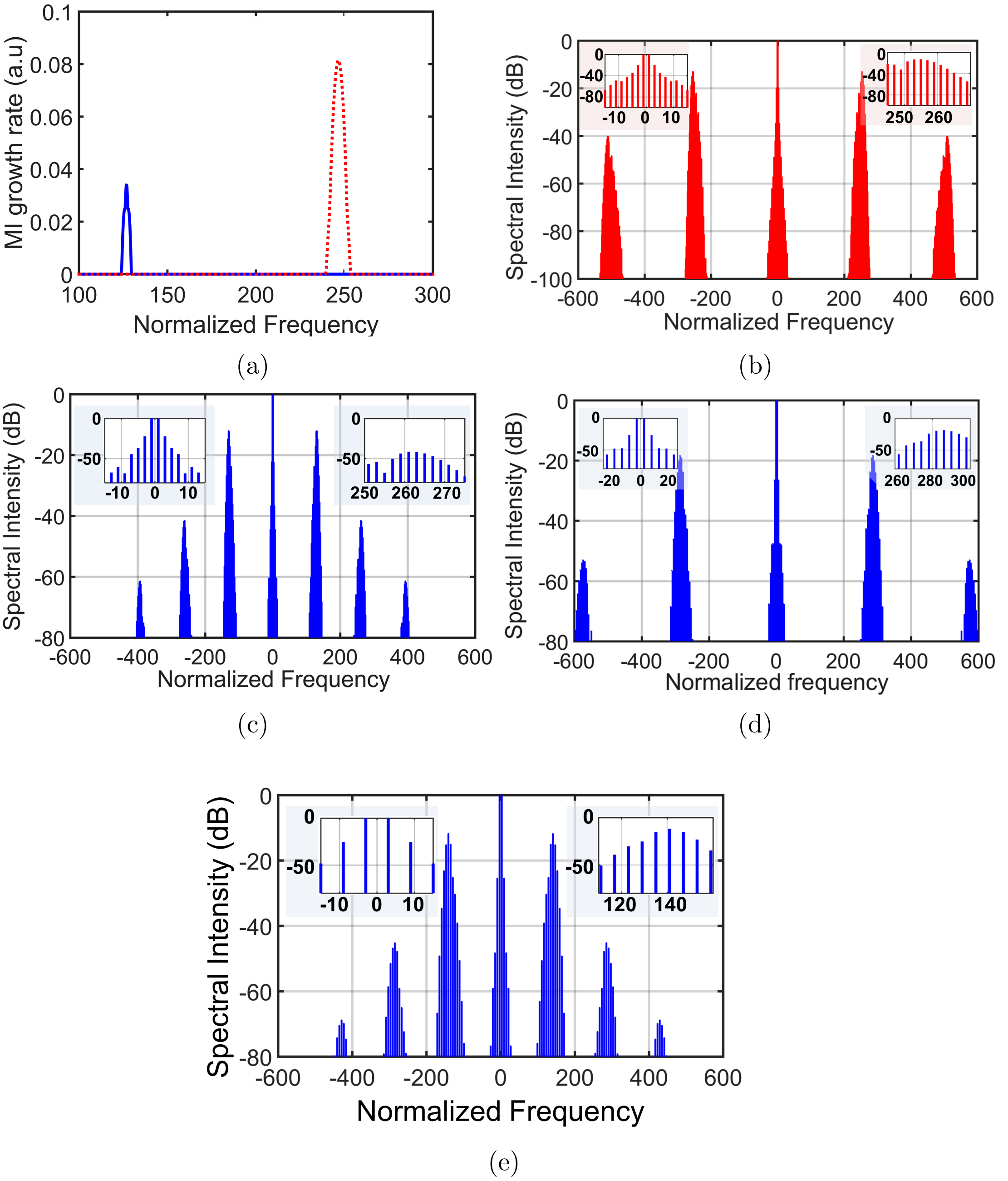

(a) (b) (c) (d) (e)

Figure 5.9: (a) MI gain curve, solid blue curve (set-1 parameters) and solid red curve (set-2 parameters). The composite comb for (b) set-2 and (c) set-1 parameters, (d) composite comb for $\Delta = -6$, $\Omega = 2$, $\beta = -0.0001$, $f_0 = 7.7$, dictating sub-comb lines separation by four FSR, (e) the composite comb for $\Delta = -7.5$, $\Omega = 3$, $\beta = -0.0005$, $f_0 = 10.5$, with sub-comb lines spacing of six FSR. Insets show the variable FSR separation of the sub-comb lines.

Table 5.1: Normalized spectral locations of primary combs obtained numerically and analytically for different cases along with respective sub-comb lines separation in units of intrinsic microresonator FSR.

Primary comb line locations			**Secondary-comb line separation**
Fig. number	**Numerical**	**Analytical**	
Fig. 5.9 (b)	$\pm m \cdot 254 \pm 1$	$\pm m \cdot 248 \pm 1$	2
Fig. 5.9 (c)	$\pm m \cdot 130 \pm 1$	$\pm m \cdot 128 \pm 1$	2
Fig. 5.9 (d)	$\pm m \cdot 284 \pm 2$	$\pm m \cdot 280 \pm 2$	4
Fig. 5.9 (e)	$\pm m \cdot 138 \pm 3$	$\pm m \cdot 140 \pm 3$	6

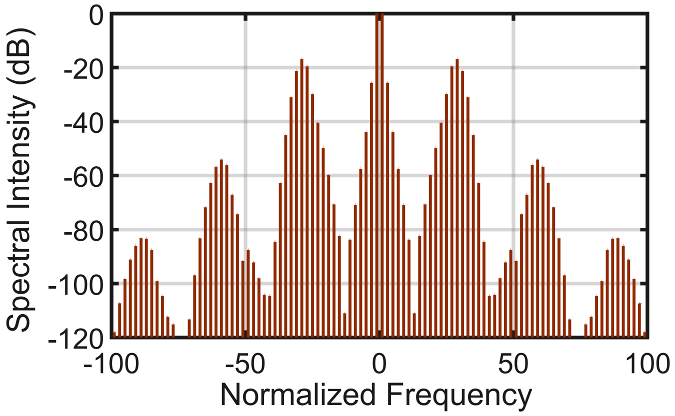

Figure 5.10: Merging of primary comb islands with the secondary comb lines for $\Delta = -6$, $\Omega = 1$, $\beta = -0.001$, $f_0 = 9$ parameters, as predicted through analytical model.

of Table 5.1 similar to the mismatch shown in Fig. 5.7 and is already discussed in the previous section.

Finally, we predict the merging of primary comb islands as depicted in Fig. 5.10 with the help of the analytical model. When the separation between primary comb lines (generated due to MI) decreases beyond a certain extent (called as limiting case), secondary comb lines produced due to FWM starts to overlap, resulting in the collapse of composite FC structure. This limiting case is illustrated in Fig. 5.10 where the secondary comb lines are just about to overlap with each other. Thereafter, it would yield a monotonic comb similar to a single-pump based frequency comb. The set of parameters, estimated quickly from the analytical model for this limiting case is, $\Delta = -6$, $\Omega = 1$, $\beta = -0.001$, $f_0 = 9$.

5.2.4 Concluding Remarks

We have used the four-wave model to distinguish the regimes of operation: thresholdless non-degenerate FWM and threshold intensity dependent MI for dual-pumped microresonators. The proposed analytical model provides an efficient and quick estimation of the design parameters to generate variable FSR frequency combs and composite combs with tunable sub-comb lines. The model holds good for both anomalous and normal dispersion regimes. Our analytical results closely match with computationally intensive numerical simulations. Our method also helps to provide more insight into the dynamics of operation of the dual-pump MR configuration. We explore the flexibility of the coherent composite frequency combs which we believe would be quite useful for WDM applications. In addition, the parametric seeding can be combined with dual-pump to attain extra flexibility for frequency comb, leading to tertiary comb generation apart from the primary and secondary ones supported by the dual-pump.

5.3 Robust Synchronous All-optical Buffer and Logic Operations

5.3.1 Introduction

Optical buffer (OB) is one of the crucial components for realizing optical delay lines in integrated photonic systems. The ability to store and manipulate data is highly desirable as far as a true all-optical network is concerned. OBs have been achieved using optical waveguides [51], coupled resonators [52], grating structure [53], photonic crystals [54], and frequency conversion-dispersion technique [55]. Recently, temporal CSs in microresonator has been deployed to realize all OB where the CSs play the role of optical bits [56, 57]. Temporal CSs are stable patterns which correspond to a FC [1, 4, 5] in the spectral domain and arise due to the mutual interplay between dispersion, nonlinearity, attenuation, and driving pump. Most of the works have focused on single-pump driven MRs to generate FC. Dual-pumping, also familiarly known as bichromatic pumping [23–26, 34], provides greater flexibility and control in the generation of FC and supports the rich dynamics of CSs [24]. For the bi-chromatic pumping, the normalized LLE is given by [24]:

$$\frac{\partial A}{\partial t} + \mathrm{i}\,\frac{\beta_2}{2}\frac{\partial^2 A}{\partial \tau^2} - \frac{\beta_3}{6}\frac{\partial^3 A}{\partial \tau^3} - \mathrm{i}\,|A|^2 A = -(1 + \mathrm{i}\,\Delta)A + f_0\cos(\Omega\tau) \tag{5.39}$$

where A, t and τ are the normalized electric-field envelope, slow-time and fast-time (ranging from $-\pi$ to π), respectively. β_2, β_3, Δ, and f_0 are the normalized second-order dispersion coefficient, third-order dispersion (TOD) coefficient, cavity detuning, and the pump amplitude, respectively, whereas the modulation frequency is given by Ω. We have neglected the effect of other higher-order dispersion terms. Note that, equal amplitudes of the pump are considered while deriving the normalized LLE as given in Eq. 5.39. Again, the difference in detuning between two pumps is assumed sufficiently small to be negligible compared to the average detuning [24]. Two pumps are separated in frequency by multiples of the FSR, referred to as the modulation frequency Ω. By choosing appropriate values of these parameters, we can excite a variety of homogeneous or patterned steady state solutions both in the normal and anomalous dispersion regimes owing to the rich dynamics exhibited by the dual-pump configuration [24]. Hansson *et al.* have recently proposed the use of CS in a dual-pump driven Kerr MR as bits in synchronous OB. However, they did not explore the advantages associated with such synchronous OB and the associated detailed analysis is also missing. Therefore, in this section, we investigate the versatility of these synchronous OB along with their robustness in performance via numerical simulations corroborated with analytical results.

5.3.2 Analytic Modelling of Synchronous OB

The rich solution space of a dual-pump LLE can be attained either by soft or hard excitations [24]. For certain values of normalized detuning and pump power, the MR with dual-pump configuration supports temporal CS that rests on a periodic background [24], which is a synchronous event as the CSs can exist only at the top of the oscillatory lobes (i.e. equilibrium position) given that we operate in the suitable parametric space. The regime of these set of parameters is demarcated by a bifurcation phenomenon, as mentioned in the latter part of this section, whereby the CSs cease to exist on top of the oscillatory lobes. For the rest of this chapter, we will assume that we operate in a suitable parametric space unless otherwise specified. The number of such lobes is twice the modulation frequency [24]. The inherent beating of two pumps provides a temporal synchronization analogous to the functionality of a master clock in digital electronic circuits. Thus, these CSs can be used to store optical bits thereby forming a synchronous buffer [24]. Mode-locked CS supported in a dual-pump MR configuration can reasonably be well approximated as given by Eq. 5.40, that accounts for the oscillatory background (the first term and second term) and the CS (the third term).

$$\Psi\left(\tau\right)=\tilde{C}_1\cos(\Omega\tau)+\tilde{C}_2\cos\left(3\Omega\tau\right)+\tilde{C}_3\,\mathrm{sech}\left(B\left(\tau-\tau_0\right)\right)\mathrm{e}^{\mathrm{i}\,\phi_p} \tag{5.40}$$

$\tilde{C}_1 = C_1\mathrm{e}^{\mathrm{i}\,\phi_{C_1}}$, and $\tilde{C}_2 = C_2\mathrm{e}^{\mathrm{i}\,\phi_{C_2}}$, where C_1 and C_2 are the amplitudes of the fundamental and the third harmonic components of the oscillatory background respectively, and ϕ_{C1} and ϕ_{C2} denote the corresponding phases. The amplitude C_1 and C_2 can be obtained with the help of four-wave model [24]. $\tilde{C}_3 = C_3\mathrm{e}^{\mathrm{i}\,\phi_{C_3}}$ where C_3 and ϕ_{C3} represent the amplitude and the phase of the hyperbolic secant pulse, respectively. B is related to the temporal width of the hyperbolic secant pulse. ϕ_{p} is the phase of the soliton envelope contributed by the addressing pulse and τ_0 is the temporal location of the center of the soliton on the fast-time. The mathematical expressions of C_3, ϕ_{C3}, and B for a single pump case can be found in [4,58]. On the other hand, for the dual-pump, these parameters can be obtained using semi-analytical variational method [28–32] as given in the *appendix* B, Eq. B.4. Dual-pumped based Kerr solitons frequency comb in the temporal domain exhibit an oscillatory background where the CS may rest on any of the oscillatory peaks [24].

The system that we consider in this work is similar to that given in [56] with a MR replacing the fiber-cavity along with another modification whereby we use a dual-pump instead of a single-pump. Figure 5.11 depicts multiple CS patterns generated for a MR with $\Delta = 1.8$, $f_0 = 1.4$, $\Omega = 12$, $\beta_2 = -0.002$ set of normalized parameters. Each CS representing a logical bit 1 rests on the oscillatory background, as seen clearly in Fig. 5.11 and each lobe without a CS in the os-

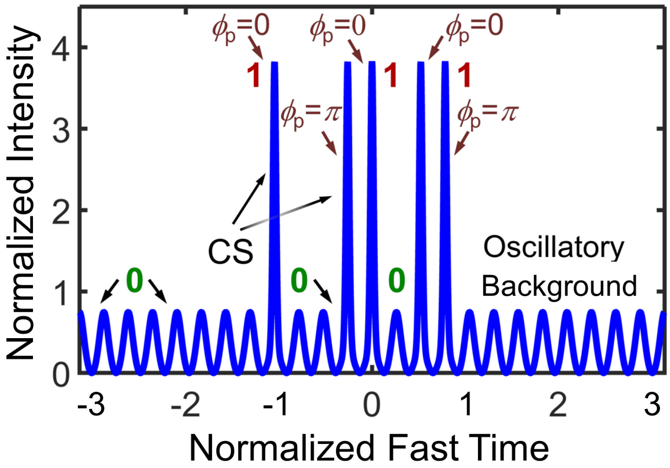

Figure 5.11: Temporal cavity solitons in dual-pump MR for $\Delta = 1.8$, $f_0 = 1.4$, $\Omega = 12$, $\beta_2 = -0.002$ set of parameters. Multiples CSs are generated through suitable seeds with the $\phi_\text{p} = 0$ or $\phi_\text{p} = \pi$ as marked in the figure. Each CS appearing on the oscillatory lobes is attributed as bit 1 for OB applications.

cillatory background is attributed as bit 0. CS can selectively be excited using suitable seed pulses with a change in phase of pumps. It is also possible to impart a suitable delay in the bit pattern that has been generated and distributed in the resonator by changing the phase of dual-pump.

5.3.3 Simulation Results and Discussions

5.3.3.1 Immune to the Writing Jitter

Figure 5.12 demonstrates that the CS excitation process is immune to the writing jitters. Seed pulses which are not exactly aligned initially with the steady state, the temporal position of CS automatically adjust to the top of the oscillatory lobes, as shown in the cartoon picture in Fig. 5.12 (a). This owes to the fact that the dual-pump creates a potential well in which CS gets trapped. The CS experiences a restoring force that eventually aligns itself to its equilibrium position. Based on the approach given in [58], we derive analytical relations of the restoring force that attracts the CSs on the top of the oscillatory lobes, which makes the CSs immune to the writing jitters. Such dual-pumped MR based optical buffers can be very robust in performance. The pulse momentum can be defined as [58],

$$P = \frac{1}{2}\int_{-\pi}^{\pi} \mathrm{d}\,\tau A^{*}\left(-\,\mathrm{i}\,\frac{\partial}{\partial\tau}\right)A + \mathrm{c}\,.c \tag{5.41}$$

where A is the intra-cavity field. If we differentiate Eq. 5.41 with respect to the slow time, we get restoring force, as given by Eq. 5.42,

$$\begin{aligned} \frac{\mathrm{d}}{\mathrm{d}\,t}P &= \frac{1}{2}\int_{-\pi}^{\pi}\mathrm{d}\,\tau\left[\frac{\partial A^{*}}{\partial t}\left(-\,\mathrm{i}\,\frac{\partial}{\partial\tau}\right)A + A^{*}\left(-\,\mathrm{i}\,\frac{\partial^{2}}{\partial\tau\partial t}\right)A\right] + \mathrm{c.\,c} \\ &= \int_{-\pi}^{\pi}\mathrm{d}\,\tau\left[\frac{\partial}{\partial t}A^{*}\left(-\,\mathrm{i}\,\frac{\partial}{\partial\tau}\right)A\right] + \mathrm{c}\,.c \end{aligned} \tag{5.42}$$

where periodic boundary condition of the LLE has been used. Making substitution of $\partial A/\partial t$ from Eq. 5.39 into 5.42, the restoring force can be recast as:

$$\frac{\mathrm{d}}{\mathrm{d}\,t}P = -2P + \int_{-\pi}^{\pi}\mathrm{d}\,\tau\left[A^{*}\left(-\,\mathrm{i}\,\frac{\partial}{\partial\tau}\right)f_0\cos\left(\Omega\tau\right)\right] + \mathrm{c}\,.c \tag{5.43}$$

After performing algebraic simplification, considering narrow solitonic pulse-width, we arrive a simple form of the restoring force which is given in Eq. 5.44.

$$\tfrac{\mathrm{d}}{\mathrm{d}\,t}P = -2P + 2\Omega f_0 C_3 S\sin(\Omega\tau_0)\sin(\phi_{C3}),\ \phi_p = 0 \tag{5.44a}$$

$$= -2P + 2\Omega f_0 C_3 S\cos(\Omega\tau_0)\cos(\phi_{C3}), \phi_p = \pi \tag{5.44b}$$

where $S = \int_{-\pi}^{\pi}\mathrm{d}\,\tau\,\mathrm{sech}\left[B\left(\tau-\tau_0\right)\right]$ is the area under the solitonic pulse. Equation 5.44 clearly states that the presence of an induced force due to dual pumping is responsible for the displacement of the misaligned CSs towards the equilibrium positions. The induced force resembles as restoring force of a simple harmonic oscillator. The stable equilibrium position from 5.44 (a) can be given by, $\Omega\tau_0 = 2m\pi$ when $\phi_{\mathrm{p}} = 0$ and in case of 5.44 (b), it is given by $\Omega\tau_0 = (2m+1)\pi$ when $\phi_{\mathrm{p}} = \pi$ here m is an integer. Both the cases are exhibited in Fig. 5.11. Note that in deriving Eq. 5.44, we assume that the oscillatory background varies

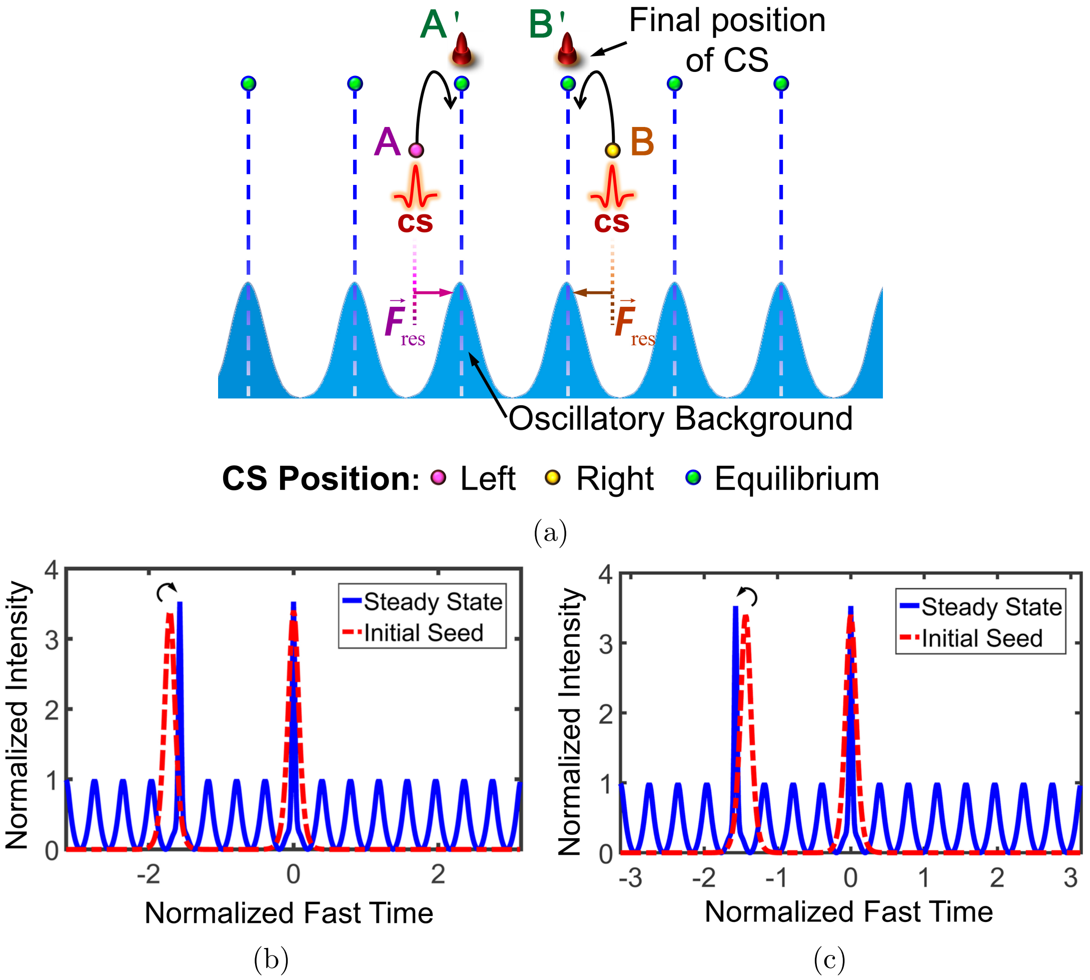

(a)

(b)

(c)

Figure 5.12: Robustness of the OB to the writing jitter. (a) Cartoon picture depicting the underlying mechanism for CS alignment, (b) and (c) exhibit the concept when the initial seed pulse is not exactly aligned. Normalized parameters used in the simulation are $\Delta = 1.7$, $f_0 = 1.3$, $\Omega = 8$, $\beta_2 = -0.002$.

slowly as compared to the width of the soliton. This assumption leads to a simple integration of Eq. 5.43 considering the quasi-static background. If the oscillatory background varies rapidly within the solitonic width, we cannot perform the said approximation and the equilibrium positions are then obtained by performing numerical integration in Eq. 5.43. It turns out that the equilibrium positions are offset to the extremas of the oscillatory background as shown in Fig. 5.13 when the oscillatory background varies rapidly. This phenomenon arises from a pitch-fork bifurcation and results in spontaneous symmetry breaking as reported in [59, 60].

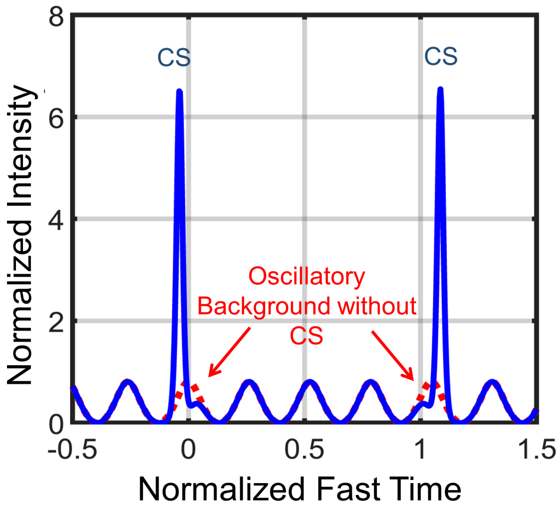

Figure 5.13: Spontaneous symmetry breaking phenomena when the oscillatory background changes rapidly within the solitonic temporal width. Normalized parameters used in simulations are: $\Delta = 2.7$, $f_0 = 2.1$, $\Omega = 12$, $\beta_2 = -0.002$.

In order to avoid such symmetry breaking and attaining robust synchronous buffer operation, we must operate in the set of parameter regimes of CS existence, where the amplitude of driving pumps is smaller than the critical bifurcation value at a corresponding detuning.

5.3.3.2 Resilience to the TOD Induced Temporal Drift

When we incorporate the third-order dispersion parameter in the LLE for a single pump case, it leads to the generation of the dispersive wave (DW) under a phase-matched condition [61]. The DW emission is accompanied with the CS attaining a drift velocity in the reference frame where the CS was stationary in the absence of TOD, owing to momentum conservation relation. CSs in single pump MR based OB suffer from this drifting phenomenon in the presence of the TOD and makes reading and writing of data bits difficult. This drifting problem can be overcome if we use two pumps up to a critical value of TOD. To derive the critical value of the TOD parameter $\beta_{3,\text{cr}}$, we have adopted the particle analogy of solitons [62, 63]. This analogy helps in estimating the $\beta_{3,\text{cr}}$ theoretically, where we restrict the kinetic energy (KE) acquired by the CS in the presence of TOD to be less than the maximum harmonic potential energy set up by the dual-pump. The

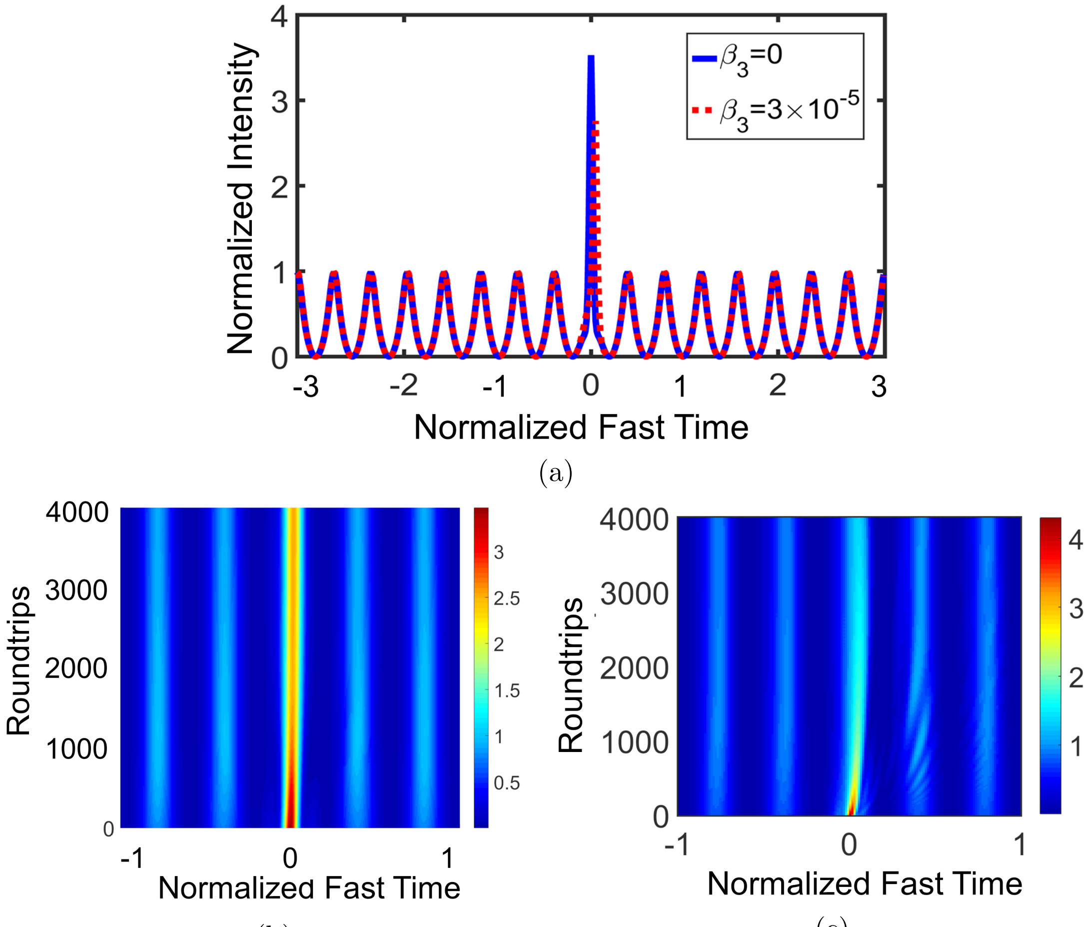

(a)

(b)

(c)

Figure 5.14: Resilience towards TOD induced drift for dual-pump MR. (a) Steady-state CS in presence of TOD and (b) its temporal evolution for simulation parameters: $\Delta = 1.7$, $f_0 = 1.3$, $\Omega = 8$, $\beta_2 = -0.002$, $\beta_3 = 3 \times 10^{-5}$ (c) A situation where the CS slowly vanishes when $\beta_3 > \beta_{3,\mathrm{cr}}$, MR parameters used in the simulation are: $\Delta = 1.7$, $f_0 = 1.3$, $\Omega = 8$, $\beta_2 = -0.002$, $\beta_3 = 1.8 \times 10^{-4}$. The round-trip evolution shows the disappearance of the CS and gradual decay of the CS energy into the oscillatory background. In (b) and (c) we have shown a truncated plot along the fast-time co-ordinate for better visualization.

maximum potential energy (PE) and the corresponding kinetic energy of the CS in the reference frame of fast time τ, taken from [62], is given by Eq. 5.45 (a) and 5.45 (b), respectively. The critical value of TOD is thus obtained by equating 5.45 (a) and 5.45 (b), which is shown in Eq. 5.45 (c). If the value of TOD is greater than the critical value, then the CS dissipates its energy into the dispersive wave

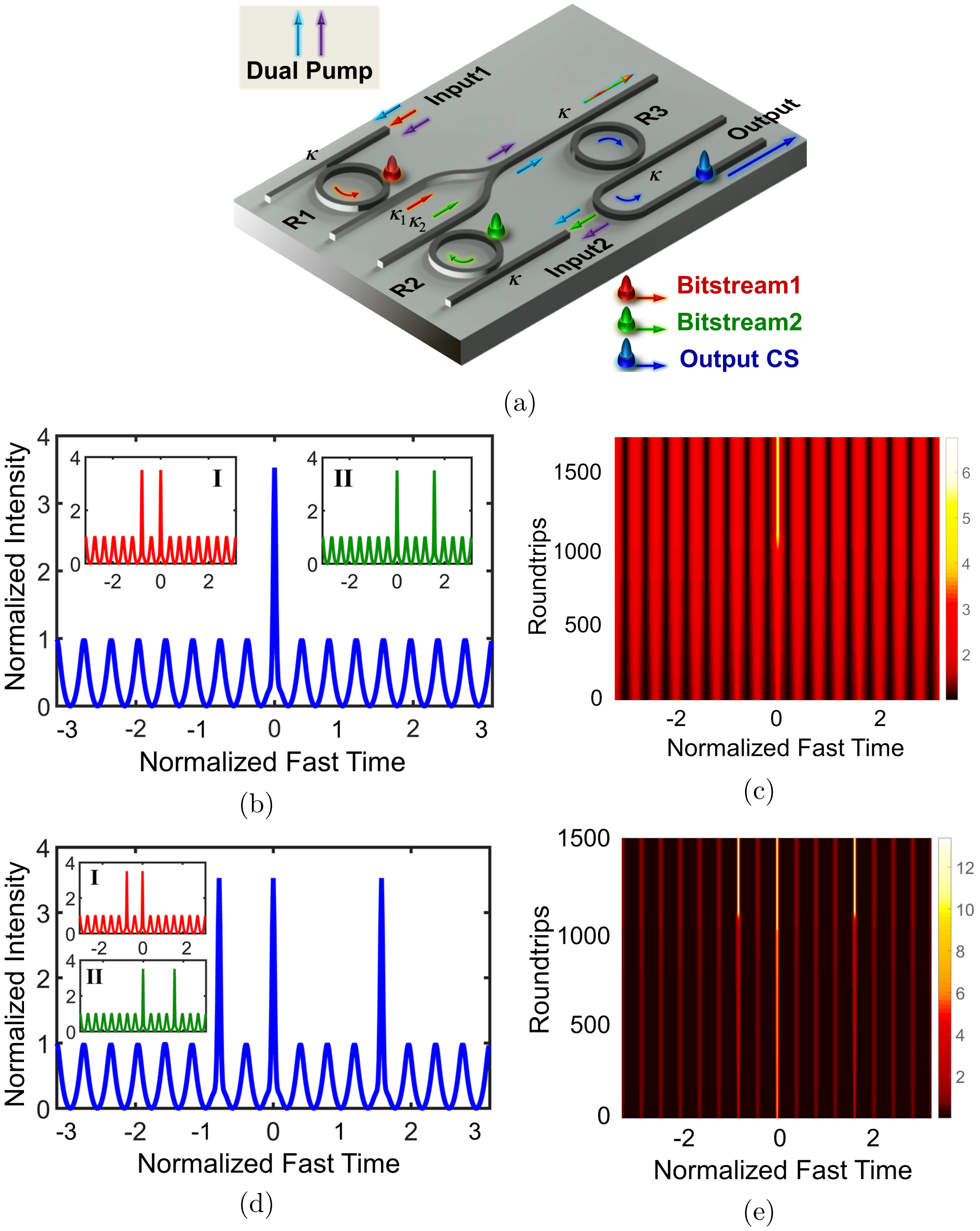

(a)

(b)

(c)

(d)

(e)

Figure 5.15: Basic logic operations in synchronous OB (a) Schematic describing the logical AND and OR operations in dual-pumped MRRs (b) logical AND, (c) corresponding round-trip slow-time evolution, (d) logical OR output, (e) corresponding round-trip slow-time evolution when the bit streams (input 1 and input 2) are fed through rings R1 and R2 while the output is taken from ring R3. All possible bit-stream combinations are considered. Insets I & II depict the input bit streams I and II, respectively. The color map represents the scaled intra-cavity intensity in arbitrary units for better clarity.

and merges with the oscillatory background.

$$\mathrm{PE} = \frac{1}{2}\left(2\Omega^2 f_0 C_3 S \sin\left(\phi_{C_3}\right)\right)\left(\frac{\pi}{\Omega}\right)^2 \tag{5.45a}$$

$$\mathrm{KE} = \frac{{C_3}^2}{6} + \frac{v^2}{2} \tag{5.45b}$$

$$\beta_{3,\mathrm{cr}} = \left(72 f_0 C_3 S \sin\left(\phi_{C_3}\right)\pi^2 - 12{C_3}^2\right)^{\frac{1}{2}} {\beta_2}^{\frac{3}{2}} \tag{5.45c}$$

Where ν in presence of the TOD is given by $\nu = \beta_3/(6{\beta_2}^{3/2})$ [61]. The variables in Eq. 5.45 (c) can be obtained from the variational principle, as given in the *Appendix* B. The critical value of TOD computed numerically is 1.2×10^{-4} which is in close agreement with the value (1.1×10^{-4}) obtained analytically using Eq. 5.45 (c) for the set of MR parameters ($\Delta = 1.7$, $f_0 = 1.3$, $\Omega = 8$, $\beta_2 = -0.002$).

For $\beta_3 < \beta_{3,\mathrm{cr}}$, CSs are trapped within the harmonic potential established by the dual-pump and do not undergo relative temporal drift. We may conclude that the synchronous behavior is retained in the presence of TOD as shown in Fig. 5.14 (a). The round-trip evolution is depicted in Fig. 5.14 (b) which clearly shows that CS in dual-pumped MR does not experience temporal drift. With $\beta_3 > \beta_{3,\mathrm{cr}}$, the dual-pump cannot support CS and it will gradually shed its energy into the background, resulting into the oscillatory intra-cavity field which is shown as round-trip slow time evolution in Fig. 5.14 (c).

5.3.3.3 Ability to Perform Logic Operations

It is always desirable to perform logical operations in the buffer itself. We have recently explored that the synchronous buffer can be used to execute logic operations efficiently [27, 64]. The schematic of the proposed architecture to perform logical operations (AND, OR) is shown in Fig. 5.15 (a). The proposed configuration consists of two microrings, viz. R1 and R2 which prepares the corresponding input CS patterns from the respective input bit patterns. These CS patterns are coupled to another micro-ring R3 which then produces the output bit pattern after a few round-trips of transients. All these rings are driven by the dual-pump. The

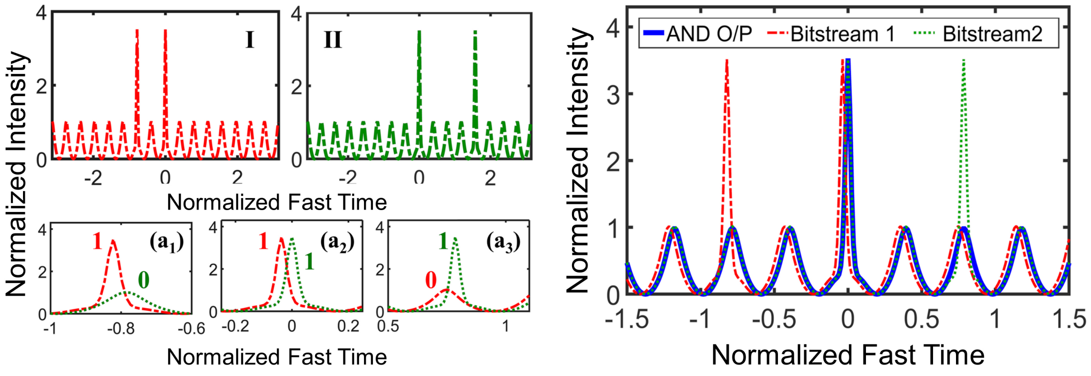

(a) (b)

Figure 5.16: Robustness in performing logical operations. (a) Input bitstream (I), and bitstream (II), the insets (a_1), (a_2), (a_3) show the misalignment between the temporal input bits, (b) logical AND output (shown by the solid blue curve). It is clearly observed that the output is not affected even if the two input bit-streams are not perfectly aligned.

steady-state output of Ring R1 and Ring R2 are amplitude scaled by the factor $\kappa \cdot \kappa_1$ and $\kappa \cdot \kappa_2$, respectively following which these two intra-cavity waveforms are added coherently. This in turn is used as an initial seed for the simulation governed by the LLE in Ring R3. The desired logic operations can be obtained by controlling the coupling factors of the resonators (κ, κ_1, and κ_2). Figures 5.15 (b, c) and 5.15 (d, e) dictate the use of the proposed OB to perform the logical AND, logical OR operations, respectively. The AND operation requires that for (1, 1) combination the intra-cavity power should be able to support a CS at that temporal position, while the OR operation requires the same for all sets of combinations except (0, 0). This will determine the required values of the coupling factors mentioned above. The input bit-streams that are stored in R1 and R2, respectively and coupled into R3 should be in phase though not necessarily exactly identical, an artifact arising due to the robust operation as discussed later. The OB operating as logic gates have a finite response time as evident from the round-trip evolution (Fig. 5.15 (c) and Fig. 5.15 (e)) while the steady state is attained. In the simulation of AND logic gate, we have considered the coupling factors as $\kappa \cdot \kappa_1 = \kappa \cdot \kappa_2 = 0.28$, whereas for the OR logic gate, the coupling factors are $\kappa \cdot \kappa_1 = \kappa \cdot \kappa_2 = 0.45$. It should be noted that the OB realized through CSs supported by a single pump MR configuration can also perform these logic operations, provided the bit streams are perfectly synchronized. However, unlike a single-pump MR based OB, the performance of the dual-pump MR based OB does not demand of perfect synchronization between bit-streams while $\beta_3 < \beta_{3,\mathrm{cr}}$. A slight mismatch in the temporal positions of the logical bits can be tolerated as the bit-streams adjust themselves on the top of the oscillatory background automatically after a few round-trips, thereby not affecting the logical operations in such dual-pump configuration. This is demonstrated in Fig. 5.16 for logical AND operation. Input bit streams (I and II), shown in Fig. 5.16 (a), are slightly dislocated temporally, which is conspicuous from Figs. 5.16 (a_1), 5.16 (a_2), and 5.16 (a_3). The dashed red and dotted green curves correspond to bitstream I and bitstream II, respectively. When there is bit 1 (CS) in the bitstream I and bit 0 (no CS) in the bitstream II, the output is bit 0 (shown by the solid blue curve). When there is logic 1 in both the bitstreams with the slight temporal deviation (see the magnified view in Fig. 5.16 (a_2)), the logical output remains high (bit 1), as shown by the solid blue curve in Fig. 5.16 (b), which means one would see a stable CS at the output of the third MR. This clearly establishes the fact that the performance of the dual-pumped MR based OB is not affected even if the input bit streams are not temporally aligned perfectly. This demonstrates the robust logical capability of these devices which is attributed to the presence of the same restoring force, as discussed earlier.

5.3.3.4 Effect of Non-idealities on Synchronous OB

Effect of Unequal Pump Amplitudes

Till now, we have assumed equal pump amplitudes for both the pumps. While this is highly desired, there might be small fluctuations in the power of the pumps, leading to a mismatch in their normalized amplitudes. To understand the effect of mismatch in pump amplitudes, we consider the normalized pump amplitude of each of the dual-pump as $f_1/2$ and $f_2/2$, such that $\Delta f = |f_1 - f_2|/2$. The LLE then takes the following form given in Eq. 5.46 where the parameters bear their usual meaning.

$$\frac{\partial A}{\partial t} + \frac{\mathrm{i}\,\beta_2}{2}\frac{\partial^2 A}{\partial \tau^2} - \mathrm{i}\,|A|^2 A = -\,(1 + \mathrm{i}\,\sigma)\,A + \frac{f_1}{2}\mathrm{e}^{-\,\mathrm{i}\,\Omega\tau} + \frac{f_2}{2}\mathrm{e}^{\mathrm{i}\,\Omega\tau} \tag{5.46}$$

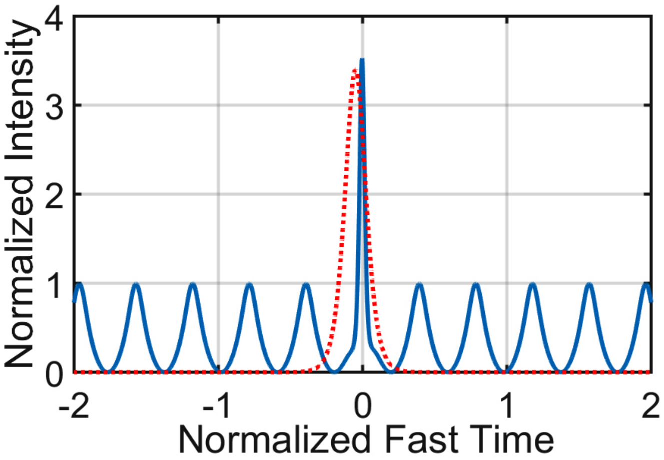

Figure 5.17: Robustness to writing jitter for unequal pump amplitude. The dashed red curve represents the seed pulse. The numerical simulation parameters are $\sigma = 1.7$, $\beta_2 = -0.002$, and $\Omega = 8$, with $f_1 = 1.31$ & $f_2 = 1.29$ ($\Delta f = 0.01$).

Here, 'σ' is used to denote the detuning factor instead of 'Δ' to avoid the confusion between detuning coefficient and the small parameter mismatch due to different non-ideal scenarios. The amplitude mismatch will result in a change in the equilibrium positions of the CSs. However, the synchronous nature of the OB still remains intact and the CSs continue to exist at well-defined positions that can be obtained when there is no restoring force on the system i.e. by equating Eq. 5.47 to zero. Note that, Eq. 5.47 is a general expression of Eq. 5.44.

$$\frac{\mathrm{d}\,P}{\mathrm{d}\,t} = -2P + \Omega C_3 S\left[\mp f_1 \cos\left(\phi_{C_3} + \Omega\tau\right) + f_2 \cos\left(\phi_{C_3} - \Omega\tau\right)\right] \;\; ; \; \phi_p = 0, \pi \qquad (5.47)$$

Fig. 5.17 shows the simulated result for the mismatch in pump amplitude. We observe that the robustness to writing jitter and the synchronous nature of the OB along with other features remain valid and preserved even in the situation where the pump amplitudes are not equal to each other.

Effect of Unequal Pump Detuning

In all the analysis done so far, equal pump detuning for both the pumps has been considered. However, it is required that the difference in detuning between two pumps should be sufficiently small, to be negligible compared to the average detuning. The difference in the detuning, if is too large, may introduce a time-dependent phase difference on the slow-time scale between two pumps, which may have a detrimental effect on the comb generation process [24]. If the dual-pump excitation scheme is similar to as mentioned in [17], the aforesaid condition can be easily met. Also, the same can be attained via fine-tuning and feedback mechanism if we use two separate laser sources. Nevertheless, it is interesting to examine the effect when the difference in detuning is not negligible.

To study this system under detuning mismatch, we derive the LLE based on nonlinear coupled mode equations. Our approach closely resembles to that of [58]. We write the amplitude evolution of each of the cavity modes in the non-normalized form, as given in Eq. 5.48.

$$\begin{aligned}\frac{\mathrm{d}\,A_j}{\mathrm{d}\,t} &= -\frac{\Delta\omega_j}{2}A_j - \mathrm{i}\,\gamma\sum_{l,m,n}\delta_{j-(l-m+n)}A_l A_m^* A_n \exp\left[\mathrm{i}\left(\omega_l-\omega_m+\omega_n-\omega_j\right)t\right]\\ &+ \sqrt{\Delta\omega_{e,j_1}}F_1\exp\left[\mathrm{i}\left(\Omega_1-\omega_{j_1}\right)t\right] + \sqrt{\Delta\omega_{e,j_2}}F_2\exp\left[\mathrm{i}\left(\Omega_2-\omega_{j_2}\right)t\right] \qquad (5.48)\end{aligned}$$

where A_j represents the complex amplitude of the j-th cavity mode, j_1 and j_2 are the cavity mode numbers closest to the two pumps. δ is the Kronecker delta function. F_1 and Ω_1 are the amplitude and the frequency, respectively of the first pump, while F_2 and Ω_2 represent the same quantities for the second pump. ω_j is the resonance frequency of the j-th cavity mode, and $\Delta\omega_\mathrm{j}$ is the Full Width at Half Maximum (FWHM) of the j-th mode which takes into consideration the losses in the cavity. $\Delta\omega_\mathrm{e,j}$ takes into account the losses incurred due to external coupling between the bus waveguide and the cavity and γ denotes the Kerr nonlinearity factor.

The resonance frequencies of the cavity are expressed in Taylor expansion as: $\omega_\mathrm{j} = \omega_\mathrm{j0}+D_1(j-j_0)+D_2(j-j_0)^2/2+\cdots$ where the expansion is done around j_0. D_1, D_2, etc. represent the various orders of the group velocity dispersion coefficients. The discrete Fourier transform of the intra-cavity field envelope yields Eq. 5.49.

$$A\left(t,\tau\right) = \sum_j A_j\left(t\right)\exp\left[\mathrm{i}\left(\omega_j-\omega_{j_0}\right)t - \mathrm{i}\left(j-j_0\right)\tau\right] \qquad (5.49)$$

Using Eqs. 5.49 in Eq. 5.48, and doing algebraic simplifications, we arrive at following mathematical expressions, 5.50 and 5.51.

$$\frac{\mathrm{d}}{\mathrm{d}\,t}A=\sum_j\left[\frac{\mathrm{d}}{\mathrm{d}\,t}A_j+\mathrm{i}\left(\omega_j-\omega_{j_0}\right)A_j\right]\exp\left[\mathrm{i}\left(\omega_j-\omega_{j_0}\right)t-\mathrm{i}\left(j-j_0\right)\tau\right]\qquad(5.50)$$

and,

$$\mathrm{i}^n\frac{\partial^n}{\partial\tau^n}A=\sum_j\left(j-j_0\right)^nA_j\exp\left[\mathrm{i}\left(\omega_j-\omega_{j_0}\right)t-\mathrm{i}\left(j-j_0\right)\tau\right]\qquad(5.51)$$

With the help of Eqs. 5.48-5.51, we can derive the time domain formulation of LLE with mismatched detuning given in Eq. 5.52.

$$\begin{aligned}\frac{\partial A}{\partial t}&=\left(-\frac{\Delta\omega}{2}-\mathrm{i}\,\gamma|A|^2+\sum_{n\geq2}\mathrm{i}^{n+1}\frac{D_n}{n!}\frac{\partial^n}{\partial\tau^n}\right)A\\&+\sqrt{\Delta\omega_{e,j_1}}F_1\exp\left\{\mathrm{i}\left[\sigma_1t+D_{res}\left(\eta=j_1-j_0\right)t+\left(j_1-j_0\right)\left(D_1t-\tau\right)\right]\right\}\\&+\sqrt{\Delta\omega_{e,j_2}}F_2\exp\left\{\mathrm{i}\left[\sigma_2t+D_{res}\left(\eta=j_2-j_0\right)t+\left(j_2-j_0\right)\left(D_1t-\tau\right)\right]\right\}\end{aligned}\qquad(5.52)$$

where, σ_k is the detuning of pump k from the nearest cavity resonance, i.e. $\sigma_\mathrm{k}=\Omega_\mathrm{k}-\omega_\mathrm{jk}$, where $k\in\{1,2\}$. $\eta=j-j_0$ is the relative mode number, and $D_\mathrm{res}(\eta)$ denotes the residual dispersion and is defined as $D_{res}\left(\eta\right)=\frac{1}{2!}D_2\eta^2+\frac{1}{3!}D_3\eta^3+\cdots$. Also, we have assumed that the FWHM of all the cavity modes is the same and equals to $\Delta\omega$. Applying the following transformations, $\tau-D_1t\to\tau$, and $t\to t$, we get the transformed version of Eq. 5.52.

$$\begin{aligned}\frac{\partial A}{\partial t}&=\left(-\frac{\Delta\omega}{2}-\mathrm{i}\,\gamma|A|^2+\sum_{n\geq2}\mathrm{i}^{n+1}\frac{D_n}{n!}\frac{\partial^n}{\partial\tau^n}\right)A\\&+\sqrt{\Delta\omega_{e,j_1}}F_1\exp\left\{\mathrm{i}\left[\sigma_1t+D_{res}\left(\eta=j_1-j_0\right)t-\left(j_1-j_0\right)\tau\right]\right\}\\&+\sqrt{\Delta\omega_{e,j_2}}F_2\exp\left\{\mathrm{i}\left[\sigma_2t+D_{res}\left(\eta=j_2-j_0\right)t-\left(j_2-j_0\right)\tau\right]\right\}\end{aligned}\qquad(5.53)$$

Special Case: Equal Detuning $\sigma_1=\sigma_2=\sigma$, equal pump amplitude: $F_1=F_2$, equidistant pump in the frequency domain: $j_1-j_0=-(j_2-j_0)=\Omega$, and $\Delta\omega_{\mathrm{e,j_1}}=$

$\Delta\omega_{\mathrm{e,j_2}}$. In this case, Eq. 5.53 reduces to the familiar form Eq. 5.54.

$$\frac{\partial A}{\partial t} = \left(-\alpha - \mathrm{i}\,\tilde{\sigma} - \mathrm{i}\,\gamma|A|^2 + \sum_{n\geq 2} \mathrm{i}^{n+1}\frac{D_n}{n!}\frac{\partial^n}{\partial \tau^n}\right) A + 2\sqrt{\Delta\omega_e}F\cos\left(\Omega\tau\right) \tag{5.54}$$

where we have replaced $\Delta\omega/2$ with α and made the transformation,
$A \rightarrow \exp\left(-i\sigma t - iD_{\mathrm{res}}(\Omega)t\right)$ such that $\widetilde{\sigma} = \sigma + D_{\mathrm{res}}(\Omega)$.

The case of Interest: Unequal Detuning: $\sigma_1 \neq \sigma_2$, equidistant pump in the frequency domain: $j_1 - j_0 = -(j_2 - j_0) = \Omega$. We neglect D_3 and all higher-order group velocity dispersion contributions for simplicity. In this case, we obtain :

$$\begin{aligned} \frac{\partial A}{\partial t} = & \left(-\alpha - \mathrm{i}\,\gamma|A|^2 + \sum_{n\geq 2} \mathrm{i}^{n+1}\frac{D_n}{n!}\frac{\partial^n}{\partial \tau^n}\right) A \\ & + \sqrt{\Delta\omega_{e,j_1}}F_1\exp\left\{\mathrm{i}\left[\sigma_1 t + D_{res}\left(\Omega\right)t - \Omega\tau\right]\right\} \\ & + \sqrt{\Delta\omega_{e,j_2}}F_2\exp\left\{\mathrm{i}\left[\sigma_2 t + D_{res}\left(-\Omega\right)t + \Omega\tau\right]\right\} \end{aligned} \tag{5.55}$$

If we make the following transformation $A \rightarrow A\exp\left(-i\sigma_1 t - iD_{\mathrm{res}}(\Omega)t\right)$, Eq. 5.55 can be re-expressed as,

$$\begin{aligned} \frac{\partial A}{\partial t} = & \left(-\alpha - \mathrm{i}\,\tilde{\sigma} - \mathrm{i}\,\gamma|A|^2 + \sum_{n\geq 2} \mathrm{i}^{n+1}\frac{D_n}{n!}\frac{\partial^n}{\partial \tau^n}\right) A \\ & + \sqrt{\Delta\omega_{e,j_1}}F_1\exp\left\{-\mathrm{i}\,\Omega\tau\right\} + \sqrt{\Delta\omega_{e,j_2}}F_2\exp\left\{\mathrm{i}\left[\Delta\sigma t + \Omega\tau\right]\right\} \end{aligned} \tag{5.56}$$

where $\Delta\sigma = \sigma_2 - \sigma_1$ and $\widetilde{\sigma} = \sigma_1 + D_{\mathrm{res}}(\Omega)$. The presence of detuning difference $(\Delta\sigma)$ in the exponent of the third-term in Eq. 5.56 clearly indicates the extra time-dependent phase difference between the pumps. We observe that a small difference in detuning, $\Delta\sigma < 10\%$ (Fig. 5.18 (a)) causes the drift in an entire bit-stream pattern along the fast-time coordinate. This is because the CS equilibrium positions creating the optical lattice now become slow-time dependent. If $\Delta\sigma \ll 1\%$, (Fig 5.18 (b)), which is the desired operating condition, then no observable significant effect appears by the virtue of detuning mismatch. However, if $\Delta\sigma > 10\%$, it will disrupt the CS bit-stream and wont support CS in the dual-pump configuration. This can also be understood from the restoring force i.e. pulse

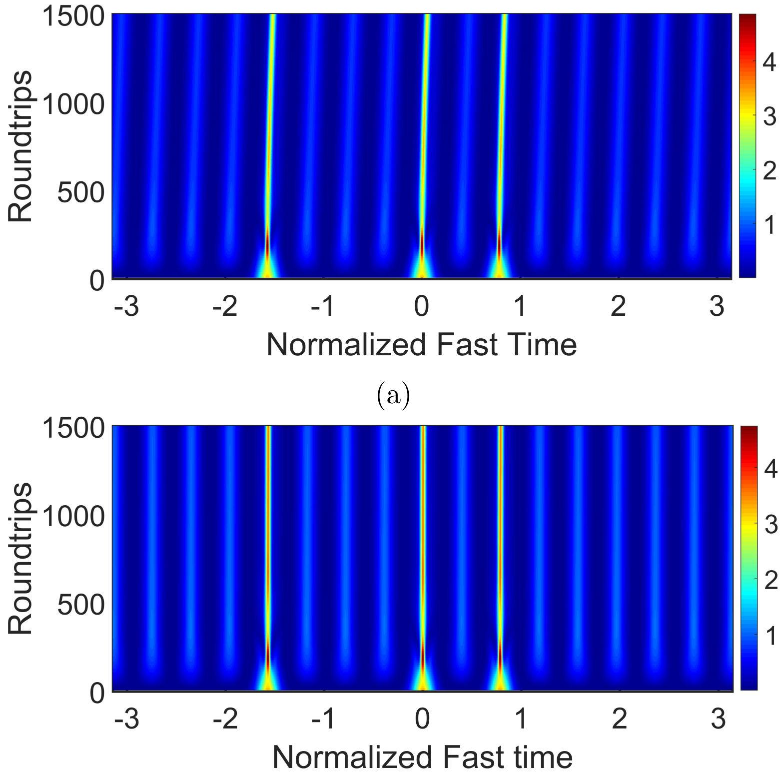

(a)

(b)

Figure 5.18: Effect of pump detuning mismatch. Round-trip evolution of the CS for the set of parameters: $f_0 = 1.3$, $\sigma = 1.7$, $\beta_2 = -0.002$, $\Omega = 8$, (a) $\Delta\sigma = 0.1$, and (b) $\Delta\sigma = 0.01$. Color scale represents the normalized intensity.

momentum as derived for unequal pump detuning, given in Eq. (59).

$$\begin{aligned}\frac{\mathrm{d}\,P}{\mathrm{d}\,t} = -2P + 2\Omega C_3 S\Bigg[&\mp \sqrt{\Delta\omega_{e,j_1}} F_1 \cos\left(\phi_{C_3} + \Omega\tau\right) \\ &+ \sqrt{\Delta\omega_{e,j_2}} F_2 \cos\left(\phi_{C_3} - \Omega\tau - \Delta\sigma t\right)\Bigg] \\ &;\text{ for, } \phi_p = 0, \pi \end{aligned} \tag{5.57}$$

5.3.3.5 Robustness against Raman and Self-steepening Effects

So far in our discussion, we have neglected the effects of self-steepening (SS) and the stimulated Raman scattering (SRS) as they are justifiably small to be neglected in those simulations. However, the effects of SS are prominent in case of ultra-short ($\lessapprox$ ps) pulses [29]. SS arises due to the intensity dependence of the group velocity and is responsible for introducing an asymmetry in the pulse spectrum. In temporal domain, the pulse gets tilted thereby developing an optical shock either at the trailing or the leading edge depending upon the dispersion of the medium. Similarly, SRS is an intrinsic nonlinear mechanism that affects the characteristics of Kerr micro-resonator based FC in a single pump case. SRS includes the self-frequency shift which is manifested as red-shift in the CS spectrum and a temporal drift along the fast-time [29]. In addition, due to SRS, Kerr CS operated at large detuning faces bandwidth limitation that truncates the CS regime of existence [65]. Therefore, in general, SRS acts detrimentally on FC formation [66, 67]. Nevertheless, one can get rid of the SRS if one operates at low pump detuning or in a particular spatial mode of operation [27]. In this section, we investigate the robustness of dual-pump MR based optical buffer in presence of self-steepening effect and stimulated Raman scattering [68].

Effect of Self-steepening: The effect of the SS is investigated by modified LLE (normalized) as given in Eq. 5.58 (a) (Eq. 5.58 (b)). T_{R}, t, and τ represent the round-trip time, slow-time and the fast-time, respectively; α, L, $\beta_2(\eta)$, γ, $\delta_0(\Delta)$, ω_0, θ, $E_{\mathrm{in}}(f_0)$, and ξ are the round-trip loss, cavity perimeter, 2nd order GVD coefficient (normalized dispersion), Kerr nonlinear coefficient, central frequency of the comb envelope, pump detuning (normalized detuning), coupling factor, driving pump amplitude (normalized pump), and normalized SS factor, respectively.

$$\begin{aligned} T_R\frac{\partial E}{\partial t} &= \sqrt{\theta}E_{in}\cos(\Omega\tau) + \left[-\alpha - \mathrm{i}\,\delta_0 - \mathrm{i}\,L\frac{\beta_2}{2}\frac{\partial^2}{\partial\tau^2}\right]E \\ &\quad + \left(1 + \frac{\mathrm{i}}{\omega_0}\frac{\partial}{\partial\tau}\right)\left(\mathrm{i}\,\gamma L|E|^2\right)E \end{aligned} \tag{5.58a}$$

$$\frac{\partial E}{\partial t} = f_0\cos(\Omega\tau) + \left[-1 + \mathrm{i}\left(|E|^2 - \Delta\right) - \mathrm{i}\,\eta\frac{\partial^2}{\partial\tau^2}\right]E$$

$$-\xi\frac{\partial}{\partial\tau}\left(|E|^2E\right);\ \text{where, } \xi=\frac{1}{\omega_0}\sqrt{\frac{2\alpha}{|\beta_2L|}} \tag{5.58b}$$

We plot the CS in the absence (red dashed curve) and presence (blue solid curve) of SS in Fig. 5.19 (a) while Fig. 5.19 (b) shows the temporal evolution of the CS in presence of SS. From Fig. 5.19 (a) and Fig. 5.19 (b) it is conspicuous that SS has a negligible impact on the operation of synchronous OB, and in particular on the behaviour of dual-pump based CS.

Effects of SRS

The SRS effect has been modelled through the normalized LLE as given by Eq. 5.59 (a) and Eq. 5.59 (b). Here f_{R}, and $h_{\mathrm{R}}(\tau)$ denote the fractional Raman contribution and the time domain Raman response function, respectively. The convolution ($\otimes$) term is evaluated through the linear approximation of the Raman response function (Γ and T_{RM}) given by: $\Gamma(\tau,\tau_{\mathrm{s}})\otimes|\mathrm{E}|^2\approx|\mathrm{E}|^2-T_{\mathrm{RM}}(f_{\mathrm{R}}\tau_{\mathrm{s}})^{-1}\partial\,|\mathrm{E}|^2\,/\partial\tau$.

$$\begin{aligned}T_R\frac{\partial E}{\partial t}&=\sqrt{\theta}E_{in}\cos\left(\Omega\tau\right)+\left[-\alpha-\mathrm{i}\,\delta_0-\mathrm{i}\,L\frac{\beta_2}{2}\frac{\partial^2}{\partial\tau^2}\right]E\\&+\mathrm{i}\,\gamma L\left[\left(1-f_R\right)|E|^2+f_Rh_R(\tau)\otimes|E|^2\right]E\end{aligned} \tag{5.59a}$$

$$\begin{aligned}\frac{\partial E}{\partial t}&=f_0\cos\left(\Omega\tau\right)+\left[-1-\mathrm{i}\,\Delta-\mathrm{i}\,\eta\frac{\partial^2}{\partial\tau^2}\right]E\\&+\mathrm{i}\left[\left(1-f_R\right)|E|^2+f_R\left(\Gamma\left(\tau,\tau_s\right)\otimes|E|^2\right)\right]E;\end{aligned} \tag{5.59b}$$

where, $\Gamma(\tau,\tau_{\mathrm{s}})=\tau_{\mathrm{s}}h_{\mathrm{R}}(\tau,\tau_{\mathrm{s}})$ and $\tau_{\mathrm{s}}=\sqrt{\frac{|\beta_2|L}{2\alpha}}$. In Fig. 5.19 (c) and Fig. 5.19 (d) we plot the round-trip temporal evolution of the CS in the single-pumped and dual-pumped MR. It is clear that in case of a single pump, the CS experiences a temporal drift in fast-time scale which corresponds to a red shift in the frequency domain whereas, in the case of dual-pump, the temporal drift is prevented. The spectral profile of CS helps us to explain this phenomenon. The redshift associated with the Raman gain is also accompanied by four-wave mixing (FWM) which causes partial power transfer to the blue side of the spectrum. The FWM is facil-

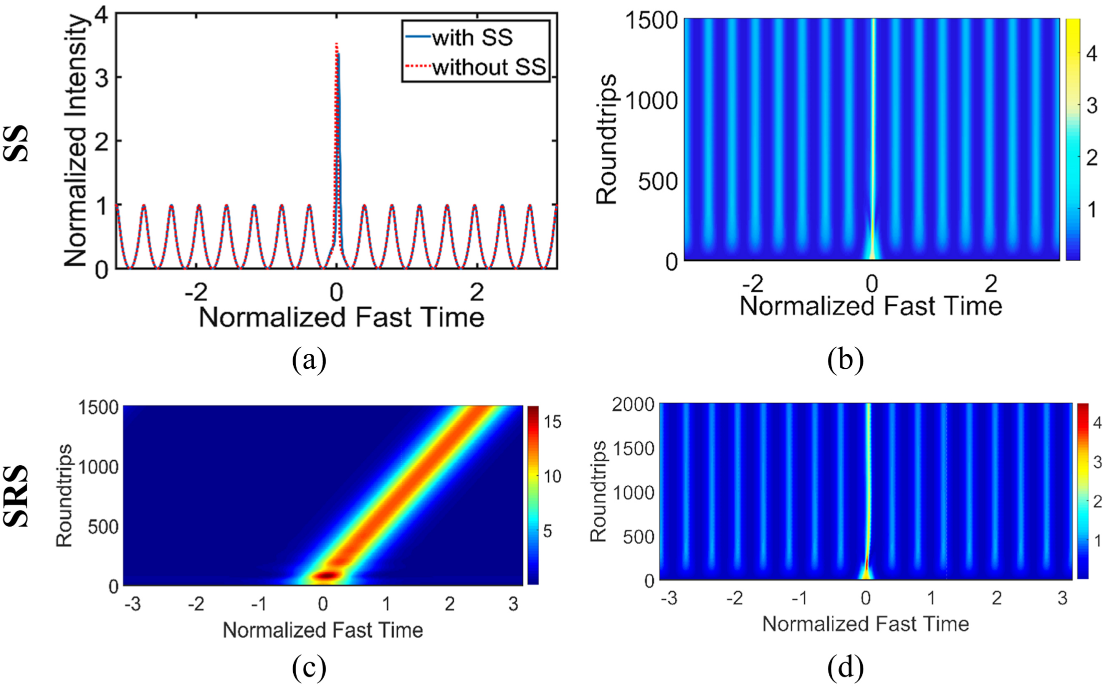

(a) (b)

(c) (d)

Figure 5.19: (a) CS in the absence (red dashed curve) and in the presence (blue solid curve) of SS. (b) The round-trip temporal evolution of the CS in presence of SS. Simulation parameters: $f_0 = 1.3$, $\Delta = 1.7$, $\eta = -0.002$, $\Omega = 8$, $\xi = 0.002$. Round-trip temporal evolution of CS in presence of SRS: (c) single-pump case, (d) dual-pump case. Rest of the simulation parameters: $\eta = -0.002$, $f_R = 0.18$, $T_{RM} = 3$ fs, $\tau_s = 2$ ps.

itated by the dual-pump. Thus, the effect of red-shift due to SRS is compensated by FWM in case of dual-pump based CS. In other words, the intra-cavity field potential induced by the oscillatory background thwarts the temporal drift in the presence of SRS. This effect can be observed from the spectra of the dual-pumped Kerr comb as shown in Fig. 5.20. All the normalized simulation parameters are calculated from the realistic non-normalized parameters which can easily be achieved through the current optical fabrication technologies [5, 26, 27]. Therefore, numerical results prove the resilience of the dual-pumped OB against the non-Kerr nonlinearities. Note that, the generation of CS in our model is assumed to be based on transiently triggered seed pulse that makes our model thermally stable [69]. The mode-locking of CSs can be preserved if the modulation frequency of the pumps is adiabatically changed in presence of a programmable microheater capable to balance the effect of modulation, thermally [70]. This will assist in

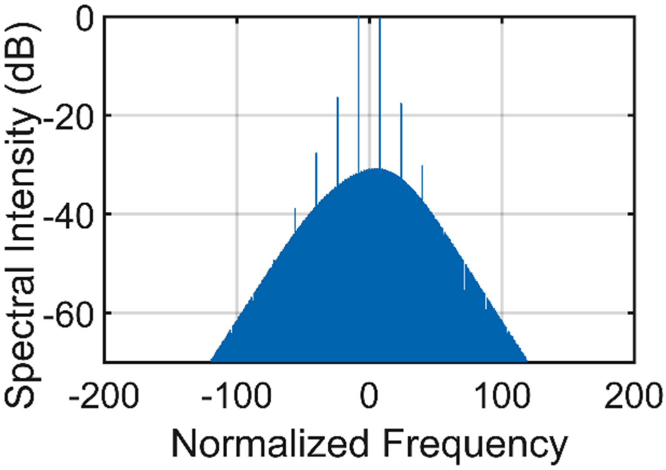

Figure 5.20: Dual-pumped Kerr frequency comb spectra under the influence of stimulated Raman scattering.

flexible dual-pump based comb generation. However, a detailed investigation on the same needs to be carried out and is beyond the scope of this work. Therefore, to summarize, in this section, we have presented an elegant methodology based on dual-pumped Kerr microresonator to compensate the self-steepening and Raman effects which might be advantageous in several photonic applications including all-optical buffer. As a future prospect, such devices can also be useful in on-chip entangled photon pair generation.

5.3.4 Conclusions

As a summary of section 5.3, we have presented the flexibility of the synchronous optical buffer based on dual-pumped MR configuration. The numerical results are well supported by the analytical model which was derived to understand the trapping of CS in the dual-pump scheme that leads to its robustness to writing jitter. The inherent logical capability combined with the clocked behavior is very appealing. In our study, we have not identified the MR parameter space for CS existence under dual pumping as well as the range where we can avoid spontaneous symmetry breaking. Future studies focusing on these aspects can help in figuring out the optimal operating MR parameters for synchronous OB. The impact of non-idealistic situations on the performance of OB has been evaluated. If the challenges concerning bi-chromatic pumping can be overcome then these devices can provide robust performance apart from being scalable.

5.4 Breakdown of Optical Lattice formation

5.4.1 Introduction

In this section, we inspect the super cavity soliton (SCS) states in MR under bi-chromatic pumping scheme and the conditions for the breakdown of optical lattice formation in dual-pumped SCSs. The SCS states are known to exist under the application of high pump power when the Kerr induced phase shift exceeds 2π [71–75]. This leads to the observation of multi-stability and supports several exciting nonlinear states which we observe in dual-pump configuration-akin to a single-pump driven MR system under similar scenarios [76]. We have performed numerical simulations of such systems based on the Ikeda formalism [71]. We explore the possibility of optical lattice formation in dual-pump MR configuration for the SCS states. It is shown that the optical lattice formation takes place conditionally for the case of SCSs. The analytical relation to describe the steady-state of the optical lattice in the context of dual-pump driven MR is derived [76]. In the previous sections, we observe that the CS resting on a CW background allows the formation of an optical lattice. Even if the CS originates from chaotic MI region randomly, it gets slowly attracted to the nearest equilibrium position. However, we notice a breakdown of this optical lattice formation in case of CS existing on MI induced temporal background. Apart from indicating the caveats in the process of lattice formation with regards to the SCS states, our work will help to gain an insight into the process of the formation of cavity solitons from MI and the resulting phase of the generated solitons in the context of bi-chromatic pumping.

5.4.2 Theoretical Analysis

The cavity resonances tilt in the presence of the Kerr effect, due to the occurrence of intensity dependent phase-shift. These tilted resonances may become multivalued and exhibits bi-stability. However, under strong pumping conditions, when the nonlinear phase shift attributed to the Kerr effect exceeds 2π, even adjacent resonances can overlap and lead to tri-stability and/or higher order stabilities [71, 72]. As discussed earlier, the behavior of Kerr MR under strong pumping is modeled by the Ikeda map. The description is given by coupled equations 5.60 and 5.61, one representing the boundary condition of coherent driving while the other involves the evolution of the electric field envelope along with the round trip [72].

$$E_{\mathrm{m+1}}\left(z=0,\tau\right)=\sqrt{\theta}E_{\mathrm{in}}+\sqrt{\rho}E_{\mathrm{m}}\left(z=L,\tau\right)\mathrm{e}^{-i\delta_0} \tag{5.60}$$

$$\frac{\partial E_{\mathrm{m}}\left(z,\tau\right)}{\partial z}=\frac{-\,\mathrm{i}\,\beta_2}{2}\frac{\partial^2 E_{\mathrm{m}}}{\partial\tau^2}+\mathrm{i}\,\gamma|E_{\mathrm{m}}|^2E_{\mathrm{m}} \tag{5.61}$$

where E_{m}, $E_{\mathrm{m+1}}\cdots$ are the field envelopes after the m-th and $(m+1)$-th $\cdots$ round-trips, respectively. L represents the cavity round-trip length, θ is related to the coupling coefficient of the resonator and ρ depends on the cavity Finesse ($\Im$) as $\rho\simeq 1-\frac{2\pi}{\Im}$. E_{in} is the amplitude of the driving field, z stands for the coordinate along the cavity round-trip and τ denotes the time variable in a reference frame moving with the group velocity of light in the medium. β_2 stands for the second-order GVD coefficient and γ is the Kerr non-linearity co-efficient. The pump detuning is given by δ_0. The CW steady state solution relates the intra-cavity power as [72]:

$$P=\frac{\theta P_{in}}{\left(1-\sqrt{\rho}\right)^2\left[1+\Im\sin^2\left(\frac{\delta_0-\gamma LP}{2}\right)\right]} \tag{5.62}$$

where δ_0 is the linear detuning induced phase difference, and γLP is the intensity dependent phase term, P and P_{in} are given by, $P=|E|^2$ and $P_{\mathrm{in}}=|E_{\mathrm{in}}|^2$. The Kerr-tilt of the resonances is shown in Fig. 5.21. Anderson *et al.* [72] has demonstrated multiple nonlinear states in these systems including, (I) homogeneous steady state, (II) modulation instability induced periodic Turing pattern, (III) CS resting on a continuous wave background, (IV) CS resting on a periodic MI pattern and (V) co-

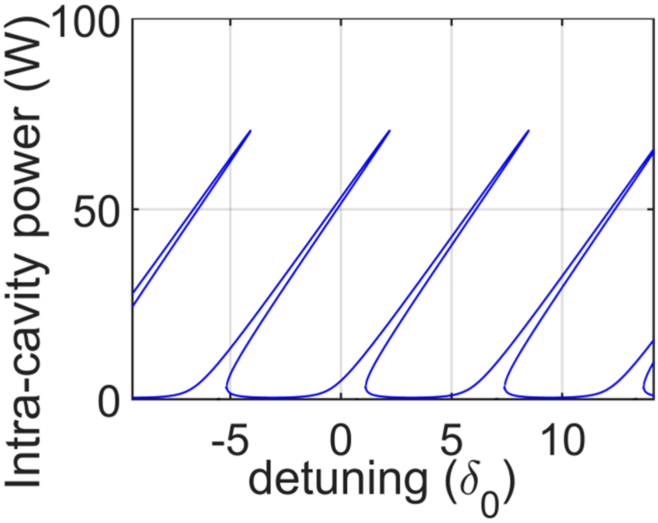

Figure 5.21: Kerr-tilt of the resonances obtained from the Ikeda map depicts the steady state intra-cavity field with respect to the detuning. Clearly, the overlapping of adjacent resonances and the tilt of resonances in excess of 2π is observed.

existence of two different CS states. Cases (I), (II) and (III) arise in conventional Kerr MR, however, under strong pumping SCS states belonging to cases (IV) and (V) may also exist. Case (IV) arises when the CS regime of one resonance coincides with the MI regime of the other resonance. The case (V) appears when the CS regime of adjacent resonances overlaps. In our work, we deal with the case (III) and the case (IV).

Kerr MR in bi-chromatic configuration is driven by two pumps which are spectrally separated by modulation frequency Ω . If we assume that the detuning of the two pumps are equal and they are having the same power then we can modify Eq. 5.60 to incorporate the effect of the dual pump as,

$$E_{\mathrm{m}+1}\left(z=0,\tau\right)=\sqrt{\theta}E_{\mathrm{in}}\cos\left(\Omega\tau\right)+\sqrt{\rho}E_{\mathrm{m}}\left(z=L,\tau\right)\mathrm{e}^{-i\delta_0} \tag{5.63}$$

We depict the cases (III) and (IV) in Figs. 5.22 (a) and Fig. 5.22 (b), respectively. We observe that the background gets modulated depending on the modulation frequency Ω where the number of oscillatory lobes is double the dimensionless Ω, which is a typical signature of dual pump configuration [24].

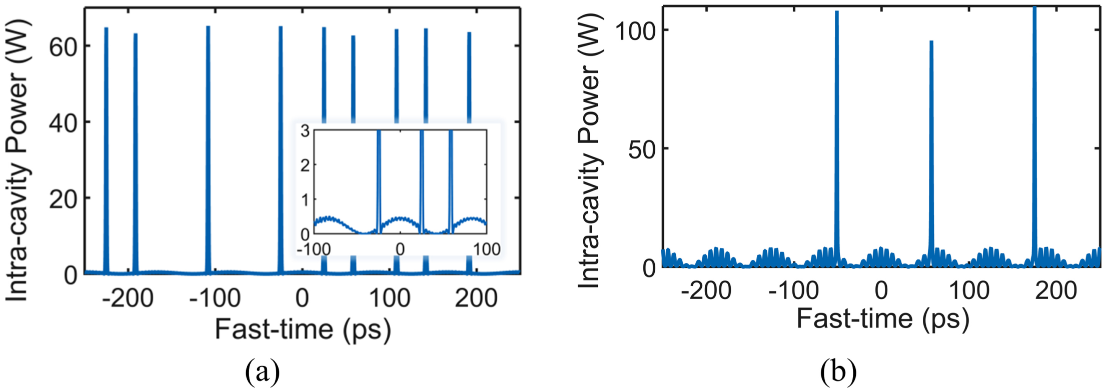

Figure 5.22: (a) The existence of CS on an oscillatory background owing to the dual pump configuration. Steady state simulation parameters are: $\delta_0 = 3$, $\Omega = 3$, $P_{\mathrm{in}} = 15$ W. This belongs to the category of Case III. (b) The existence of SCS on an oscillatory background modulated by MI induced temporal background. Steady-state simulation parameters for case (IV) are: $\delta_0 = 5.8$, $\Omega = 4$, $P_{\mathrm{in}} = 15$ W. Other simulation parameters that are used and remain unchanged throughout this work are: $\theta = 0.1$, $\rho = 0.73$, $\beta_2 = -22$ ps^2/km, $\gamma = 1.2$ W^{-1}km^{-1}, $L = 0.1$ km.

5.4.3 Results and Discussions

5.4.3.1 Optical Lattice Formation driven by dual-pump

Taheri *et al.* showed that an optical lattice trap is formed when the Kerr MR is driven by two CW optical pumps. This results in solitons existing at specific equilibrium locations along the fast time co-ordinate which can be determined analytically with the help of the approach mentioned in ref. [58]. When the Kerr induced phase shift is less than 2π the description given by Ikeda map is well approximated by the mean-field Lugiato-Lefever equation that can be rewritten for dual-pump as [72]:

$$T_{\mathrm{R}}\frac{\partial E}{\partial t} + \mathrm{i}\,\frac{\beta_2 L}{2}\frac{\partial^2 E}{\partial \tau^2} - \mathrm{i}\,\gamma L |E|^2 E = -(\alpha + \mathrm{i}\,\delta_0)E + \sqrt{\theta}E_{\mathrm{in}}\cos(\Omega\tau) \tag{5.64}$$

Where E is the electric field envelope, T_{R} is the round-trip time and $\alpha \simeq \frac{(1-\rho)}{2}$. Other parameters are already mentioned earlier, t and τ represent the slow time and fast time, respectively. A single CS supported in the dual pump configuration can be expressed by:

$$E(\tau) = \tilde{C}_1\cos(\Omega\tau) + \tilde{C}_2\,\mathrm{sech}\left(B(\tau - \tau_0)\right)\mathrm{e}^{\mathrm{i}\,\phi_p} \tag{5.65}$$

Where $\tilde{C}_1 = C_1 e^{i\phi_{C1}}$ represents the amplitude and phase of the oscillatory background and can be obtained from the four-wave model described in [24]. $\tilde{C}_2 = C_2 e^{i\,\phi_{C_2}}$, C_2 is the amplitude and B is the temporal width of the hyperbolic secant pulse representing the soliton, ϕ_p is the phase of the soliton envelope. τ_0 is the location of the center of soliton pulse on the fast time co-ordinate. $\tilde{C}_1, \tilde{C}_2, B$ for the single pump case are mentioned in [5]. In that case, the pulse momentum is defined by the Eq. 5.41. As already derived, the restoring force exerted on the CS due to the potential set up by the dual-pump is given by,

$$\frac{\mathrm{d}}{\mathrm{d}\,t}P = -2\frac{\alpha}{T_R}P + 2\frac{\sqrt{\theta}E_{in}}{T_R}\Omega C_2 S \sin(\Omega\tau_0)\sin(\phi_{C_2}) \tag{5.66}$$

This force is responsible for the formation of an optical lattice. The steady-state CS location (i.e the lattice points) will be given by $\Omega\tau = m\pi$, where m is an integer. However, we find that the lattice points are displaced from the position as obtained analytically. This is shown in Figs. 5.23 (a)–(c). This is because the base on which the CS is resting gets locally modified. As a result, the potential gets perturbed, thereby altering the equilibrium CS location. Also, it is attributed to the cause that the LLE cannot accurately describe the dynamics of SCS states. These lattice points form a regular array and act as CS trapping site which is located symmetrically about by $\Omega\tau = m\pi$. CS gets attracted towards these positions as is evident from the bent trajectory in the round-trip evolution. Thus, if we know the temporal position of one CS we can deterministically locate other CSs. It is to be noted that in the numerical simulation we have varied the detuning δ_0 gradually from an initial value of -0.65 rad to the required final detuning value over 350 round-trips. Thereafter, the roundtrip evolution is captured until the steady state is attained. This leads to the excitation of CS spontaneously without the need of suitable seed pulse [8].

5.4.3.2 Break-down of Optical Lattice Formation

Case (IV) of SCS states arise when the CS rests on the oscillatory background is modified by the MI of the adjacent resonance MI regime. The equilibrium positions now deviate from the normal lattice points and become randomly oriented as

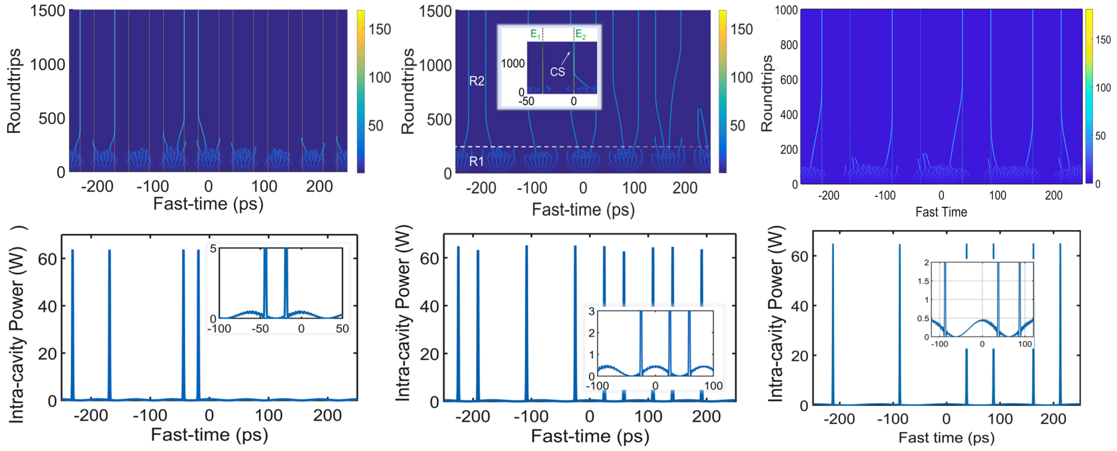

(a) (b) (c)

Figure 5.23: The top row of each of sub-figures a, b, c represents the evolution of the intra-cavity field as the circulating light traverses several round trips. Formation of the optical lattice is evident from the fact that the steady state location of the CS is aligned with the optical lattice equilibrium positions which are depicted as vertical lines. The bottom row of each of the subfigures (a), (b), (c) show the temporal field profile along the fast time when the steady state is attained. Parameters used in each of these simulations are: (a) $\delta_0 = 3$, $\Omega = 4$, $P_{\text{in}} = 15$ W, (b) $\delta_0 = 3$, $\Omega = 3$, $P_{\text{in}} = 15$ W, and (c) $\delta_0 = 3$, $\Omega = 2$, $P_{\text{in}} = 15$ W.

depicted in Fig 5.24. The modulation instability induced periodic background can locally trap the SCS and hence the regular array of lattice points no more exists. This marks the breakdown of the optical lattice.

5.4.4 Conclusions

In section 5.4, we have derived the lattice points corresponding to CS equilibrium positions. We also presented that the dual pump configuration can support SCS states. Observations made regarding the breakdown of optical lattice formation demonstrate the conditional lattice existence. Our study will have severe implications in studies involving the utilization of SCS states as bits of an all-optical buffer.

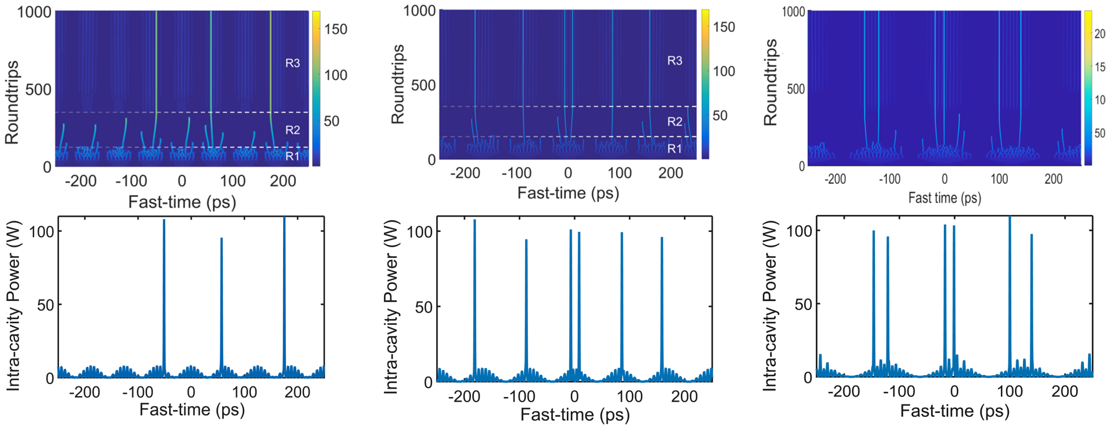

(a) (b) (c)

Figure 5.24: The top row of each of sub-figures a, b, c represents the evolution of the intra-cavity field as the circulating light traverses several round trips. Different regimes in the roundtrip evolution are demarcated as R1, R2, and R3. Clearly, the MI-induced background is visible in the R3 regime which is responsible for the breakdown of the optical lattice. The bottom row of each of the subfigures (a), (b), (c) shows the temporal field profile along the fast time when the steady state is attained. Parameters used in each of these simulations are: (a) $\delta_0 = 5.8$, $\Omega = 4$, $P_{\text{in}} = 15$ W, (b) $\delta_0 = 3$, $\Omega = 3$, $P_{\text{in}} = 15$ W, and (c) $\delta_0 = 3$, $\Omega = 2$, $P_{\text{in}} = 15$ W.

5.5 Summary

Therefore, to summarize the chapter,

- In the first section, the background-study of dual-comb Kerr frequency comb has been briefly covered. We have also highlighted the advantages and disadvantages of using dual-pump configuration over single-pump.

- In section 5.2, four-wave model has been used to distinguish the regimes of operation, viz. (i) threshold-less non-degenerate FWM, and (ii) threshold intensity dependent MI for dual-pumped microresonators. The proposed analytical model provides an efficient and quick estimation of the design parameters to generate variable FSR frequency combs and composite combs with tunable sub-comb lines.

- Section 5.3 have discussed the flexibility of the dual-pump synchronous all-optical buffers and their robustness against the writing jitters, third order dispersion, self-steepening, and stimulated Raman scattering. These buffers are also capable to perform logic operations.

- In section 5.4 we have presented a detailed numerical study on the existence of super-cavity solitons in the dual-pump configuration. We have also demonstrated the breakdown of optical lattice formation demonstrate under certain conditions. We believe, this study has severe implications in determining the utilization of super-cavity soliton states as bits of an all-optical buffer.

References

[1] T. J. Kippenberg, R. Holzwarth, and S. A. Diddams, "Microresonator-based optical frequency combs," *Science*, vol. 332, no. 6029, pp. 555–559, 2011.

[2] Y. Okawachi, K. Saha, J. S. Levy, Y. H. Wen, M. Lipson, and A. L. Gaeta, "Octave-spanning frequency comb generation in a silicon nitride chip," *Optics Letters*, vol. 36, no. 17, pp. 3398–3400, 2011.

[3] H. Jung, C. Xiong, K. Y. Fong, X. Zhang, and H. X. Tang, "Optical frequency comb generation from aluminum nitride microring resonator," *Optics Letters*, vol. 38, no. 15, pp. 2810–2813, 2013.

[4] S. B. Papp, K. Beha, P. DelHaye, F. Quinlan, H. Lee, K. J. Vahala, and S. A. Diddams, "Microresonator frequency comb optical clock," *Optica*, vol. 1, no. 1, pp. 10–14, 2014.

[5] T. Herr, V. Brasch, J. D. Jost, C. Y. Wang, N. M. Kondratiev, M. L. Gorodetsky, and T. J. Kippenberg, "Temporal solitons in optical microresonators," *Nature Photonics*, vol. 8, no. 2, pp. 145–152, 2014.

[6] S. T. Cundiff and A. M. Weiner, "Optical arbitrary waveform generation," *Nature Photonics*, vol. 4, no. 11, pp. 760–766, 2010.

[7] S. Coen and M. Erkintalo, "Universal scaling laws of Kerr frequency combs," *Optics Letters*, vol. 38, no. 11, pp. 1790–1792, 2013.

[8] M. R. Lamont, Y. Okawachi, and A. L. Gaeta, "Route to stabilized ultrabroadband microresonator-based frequency combs," *Optics Letters*, vol. 38, no. 18, pp. 3478–3481, 2013.

[9] C. Godey, I. V. Balakireva, A. Coillet, and Y. K. Chembo, "Stability analysis of the spatiotemporal lugiato-lefever model for kerr optical frequency combs in the anomalous and normal dispersion regimes," *Physical Review A*, vol. 89, no. 6, p. 063814, 2014.

[10] I. Barashenkov and Y. S. Smirnov, "Existence and stability chart for the ac-driven, damped nonlinear Schrödinger solitons," *Physical Review E*, vol. 54, no. 5, pp. 5707–5725, 1996.

[11] J. Pfeifle, V. Brasch, M. Lauermann, Y. Yu, D. Wegner, T. Herr, K. Hartinger, P. Schindler, J. Li, D. Hillerkuss *et al.*, "Coherent terabit communications with microresonator Kerr frequency combs," *Nature Photonics*, vol. 8, no. 5, pp. 375–380, 2014.

[12] P. Marin-Palomo, J. N. Kemal, M. Karpov, A. Kordts, J. Pfeifle, M. H. Pfeiffer, P. Trocha, S. Wolf, V. Brasch, M. H. Anderson *et al.*, “Microresonator-based solitons for massively parallel coherent optical communications,” *Nature*, vol. 546, no. 7657, pp. 274–279, 2017.

[13] J. Wu, X. Xu, T. G. Nguyen, S. T. Chu, B. E. Little, R. Morandotti, A. Mitchell, and D. J. Moss, “Rf photonics: An optical microcombs’ perspective,” *IEEE Journal of Selected Topics in Quantum Electronics*, vol. 24, no. 4, pp. 1–20, 2018.

[14] M.-G. Suh, Q.-F. Yang, K. Y. Yang, X. Yi, and K. J. Vahala, “Microresonator soliton dual-comb spectroscopy,” *Science*, vol. 354, no. 6312, pp. 600–603, 2016.

[15] D. T. Spencer, S. H. Lee, D. Y. Oh, M.-G. Suh, K. Y. Yang, and K. Vahala, “An optical-frequency synthesizer using integrated photonics,” *Nature*, vol. 557, no. 7703, pp. 81–85, 2018.

[16] W. Wang, W. Zhang, S. T. Chu, B. E. Little, Q. Yang, L. Wang, X. Hu, L. Wang, G. Wang, Y. Wang *et al.*, “Repetition rate multiplication pulsed laser source based on a microring resonator,” *ACS Photonics*, vol. 4, no. 7, pp. 1677–1683, 2017.

[17] C. Bao, P. Liao, A. Kordts, L. Zhang, M. Karpov, M. H. Pfeiffer, Y. Cao, Y. Yan, A. Almaiman, G. Xie *et al.*, “Dual-pump generation of high-coherence primary Kerr combs with multiple sub-lines,” *Optics Letters*, vol. 42, no. 3, pp. 595–598, 2017.

[18] S. Miller, K. Luke, Y. Okawachi, J. Cardenas, A. L. Gaeta, and M. Lipson, “On-chip frequency comb generation at visible wavelengths via simultaneous second-and third-order optical nonlinearities,” *Optics Express*, vol. 22, no. 22, pp. 26 517–26 525, 2014.

[19] X. Shen, R. C. Beltran, V. M. Diep, S. Soltani, and A. M. Armani, “Low-threshold parametric oscillation in organically modified microcavities,” *Science Advances*, vol. 4, no. 1, p. eaao4507, 2018.

[20] M. Barturen, N. Abadía, J. Milano, P. A. C. Caso, and D. V. Plant, “Manipulation of extinction features in frequency combs through the usage of graphene,” *Optics Express*, vol. 26, no. 12, pp. 15 490–15 502, 2018.

[21] B. Yao, S.-W. Huang, Y. Liu, A. K. Vinod, C. Choi, M. Hoff, Y. Li, M. Yu, Z. Feng, D.-L. Kwong *et al.*, “Gate-tunable frequency combs in graphene–nitride microresonators,” *Nature*, vol. 558, no. 7710, pp. 410–414, 2018.

[22] S. Yamashita, “Nonlinear optics in carbon nanotube, graphene, and related 2D materials,” *APL Photonics*, vol. 4, no. 3, p. 034301, 2019.

[23] W. Wang, S. T. Chu, B. E. Little, A. Pasquazi, Y. Wang, L. Wang, W. Zhang, L. Wang, X. Hu, G. Wang *et al.*, “Dual-pump Kerr micro-cavity optical frequency comb with varying FSR spacing,” *Scientific Reports*, vol. 6, p. 28501, 2016.

[24] T. Hansson and S. Wabnitz, “Bichromatically pumped microresonator frequency combs,” *Physical Review A*, vol. 90, no. 1, p. 013811, 2014.

[25] Y. Okawachi, M. Yu, K. Luke, D. O. Carvalho, S. Ramelow, A. Farsi, M. Lipson, and A. L. Gaeta, “Dual-pumped degenerate Kerr oscillator in a silicon nitride microresonator,” *Optics Letters*, vol. 40, no. 22, pp. 5267–5270, 2015.

[26] A. Roy, R. Haldar, and S. K. Varshney, "Analytical model of dual-pumped Kerr micro-resonators for variable free spectral range and composite frequency comb generation," *Journal of Lightwave Technology*, vol. 36, no. 12, pp. 2422–2429, 2018.

[27] A. Roy, R. Haldar, and S. K. Varshney, "Robust, synchronous optical buffer, and logic operation in dual-pump Kerr micro-resonator," *Journal of Lightwave Technology*, vol. 36, no. 24, pp. 5807–5814, 2018.

[28] D. Anderson, "Variational approach to nonlinear pulse propagation in optical fibers," *Physical Review A*, vol. 27, no. 6, p. 3135, 1983.

[29] G. P. Agrawal, *Nonlinear Fiber Optics.* Academic press, 2013.

[30] S. C. Cerda, S. Cavalcanti, and J. Hickmann, "A variational approach of nonlinear dissipative pulse propagation," *The European Physical Journal D-Atomic, Molecular, Optical and Plasma Physics*, vol. 1, no. 3, pp. 313–316, 1998.

[31] S. Roy and S. K. Bhadra, "Solving soliton perturbation problems by introducing Rayleigh's dissipation function," *Journal of Lightwave Technology*, vol. 26, no. 14, pp. 2301–2322, 2008.

[32] X. Yi, Q.-F. Yang, K. Y. Yang, and K. Vahala, "Theory and measurement of the soliton self-frequency shift and efficiency in optical microcavities," *Optics Letters*, vol. 41, no. 15, pp. 3419–3422, 2016.

[33] A. Antikainen and G. P. Agrawal, "Dual-pump frequency comb generation in normally dispersive optical fibers," *JOSA B*, vol. 32, no. 8, pp. 1705–1711, 2015.

[34] X. Hu, W. Wang, L. Wang, W. Zhang, Y. Wang, and W. Zhao, "Numerical simulation and temporal characterization of dual-pumped microring-resonator-based optical frequency combs," *Photonics Research*, vol. 5, no. 3, pp. 207–211, 2017.

[35] C. Bao, P. Liao, A. Kordts, M. Karpov, M. H. Pfeiffer, L. Zhang, Y. Cao, G. Xie, C. Liu, Y. Yan *et al.*, "Tunable insertion of multiple lines into a Kerr frequency comb using electro-optical modulators," *Optics Letters*, vol. 42, no. 19, pp. 3765–3768, 2017.

[36] T. Kippenberg, S. Spillane, and K. Vahala, "Kerr-nonlinearity optical parametric oscillation in an ultrahigh-Q toroid microcavity," *Physical Review Letters*, vol. 93, no. 8, p. 083904, 2004.

[37] T. Herr, K. Hartinger, J. Riemensberger, C. Wang, E. Gavartin, R. Holzwarth, M. Gorodetsky, and T. Kippenberg, "Universal formation dynamics and noise of Kerr-frequency combs in microresonators," *Nature Photonics*, vol. 6, no. 7, pp. 480–487, 2012.

[38] A. B. Matsko, A. A. Savchenkov, D. Strekalov, V. S. Ilchenko, and L. Maleki, "Optical hyperparametric oscillations in a whispering-gallery-mode resonator: Threshold and phase diffusion," *Physical Review A*, vol. 71, no. 3, p. 033804, 2005.

[39] Y. K. Chembo and N. Yu, "Modal expansion approach to optical-frequency-comb generation with monolithic whispering-gallery-mode resonators," *Physical Review A*, vol. 82, no. 3, p. 033801, 2010.

[40] D. V. Strekalov and N. Yu, "Generation of optical combs in a whispering gallery mode resonator from a bichromatic pump," *Physical Review A*, vol. 79, no. 4, p. 041805, 2009.

[41] S. Spillane, T. Kippenberg, K. Vahala, K. Goh, E. Wilcut, and H. Kimble, "Ultrahigh-Q toroidal microresonators for cavity quantum electrodynamics," *Physical Review A*, vol. 71, no. 1, p. 013817, 2005.

[42] J. Fürst, D. Strekalov, D. Elser, A. Aiello, U. L. Andersen, C. Marquardt, and G. Leuchs, "Low-threshold optical parametric oscillations in a whispering gallery mode resonator," *Physical Review Letters*, vol. 105, no. 26, p. 263904, 2010.

[43] X. Ji, F. A. Barbosa, S. P. Roberts, A. Dutt, J. Cardenas, Y. Okawachi, A. Bryant, A. L. Gaeta, and M. Lipson, "Ultra-low-loss on-chip resonators with sub-milliwatt parametric oscillation threshold," *Optica*, vol. 4, no. 6, pp. 619–624, 2017.

[44] M. Savanier, R. Kumar, and S. Mookherjea, "Photon pair generation from compact silicon microring resonators using microwatt-level pump powers," *Optics Express*, vol. 24, no. 4, pp. 3313–3328, 2016.

[45] G. Agrawal, *Applications of Nonlinear Fiber Optics.* Elsevier, 2001.

[46] A. Armaroli and S. Trillo, "Collective modulation instability of multiple four-wave mixing," *Optics Letters*, vol. 36, no. 11, pp. 1999–2001, 2011.

[47] X. Xue, M. Qi, and A. M. Weiner, "Normal-dispersion microresonator Kerr frequency combs," *Nanophotonics*, vol. 5, no. 2, pp. 244–262, 2016.

[48] G. Lin, R. Martinenghi, S. Diallo, K. Saleh, A. Coillet, and Y. K. Chembo, "Spectro-temporal dynamics of Kerr combs with parametric seeding," *Applied Optics*, vol. 54, no. 9, pp. 2407–2412, 2015.

[49] S. B. Papp, P. DelHaye, and S. A. Diddams, "Parametric seeding of a microresonator optical frequency comb," *Optics Express*, vol. 21, no. 15, pp. 17 615–17 624, 2013.

[50] M. Erkintalo and S. Coen, "Coherence properties of Kerr frequency combs," *Optics Letters*, vol. 39, no. 2, pp. 283–286, 2014.

[51] F. Xia, L. Sekaric, and Y. Vlasov, "Ultracompact optical buffers on a silicon chip," *Nature Photonics*, vol. 1, no. 1, pp. 65–71, 2007.

[52] J. Cardenas, M. A. Foster, N. Sherwood-Droz, C. B. Poitras, H. L. Lira, B. Zhang, A. L. Gaeta, J. B. Khurgin, P. Morton, and M. Lipson, "Wide-bandwidth continuously tunable optical delay line using silicon microring resonators," *Optics Express*, vol. 18, no. 25, pp. 26 525–26 534, 2010.

[53] J. Wang, R. Ashrafi, R. Adams, I. Glesk, I. Gasulla, J. Capmany, and L. R. Chen, "Sub-wavelength grating enabled on-chip ultra-compact optical true time delay line," *Scientific Reports*, vol. 6, p. 30235, 2016.

[54] Y. A. Vlasov, M. O'boyle, H. F. Hamann, and S. J. McNab, "Active control of slow light on a chip with photonic crystal waveguides," *Nature*, vol. 438, no. 7064, pp. 65–69, 2005.

[55] T. Sakamoto, K. Noguchi, R. Sato, A. Okada, Y. Sakai, and M. Matsuoka, "Variable optical delay circuit using wavelength converters," *Electronics Letters*, vol. 37, no. 7, pp. 454–455, 2001.

[56] F. Leo, S. Coen, P. Kockaert, S.-P. Gorza, P. Emplit, and M. Haelterman, "Temporal cavity solitons in one-dimensional Kerr media as bits in an all-optical buffer," *Nature Photonics*, vol. 4, no. 7, pp. 471–476, 2010.

[57] J. K. Jang, M. Erkintalo, J. Schröder, B. J. Eggleton, S. G. Murdoch, and S. Coen, "All-optical buffer based on temporal cavity solitons operating at 10 Gb/s," *Optics Letters*, vol. 41, no. 19, pp. 4526–4529, 2016.

[58] H. Taheri, A. B. Matsko, and L. Maleki, "Optical lattice trap for Kerr solitons," *The European Physical Journal D*, vol. 71, no. 6, p. 153, 2017.

[59] I. Hendry, W. Chen, Y. Wang, B. Garbin, J. Javaloyes, G.-L. Oppo, S. Coen, S. G. Murdoch, and M. Erkintalo, "Spontaneous symmetry breaking and trapping of temporal Kerr cavity solitons by pulsed or amplitude-modulated driving fields," *Physical Review A*, vol. 97, no. 5, p. 053834, 2018.

[60] E. Obrzud, S. Lecomte, and T. Herr, "Temporal solitons in microresonators driven by optical pulses," *Nature Photonics*, vol. 11, no. 9, pp. 600–607, 2017.

[61] N. Akhmediev and M. Karlsson, "Cherenkov radiation emitted by solitons in optical fibers," *Physical Review A*, vol. 51, no. 3, p. 2602, 1995.

[62] T. L. Belyaeva, C. Hernandez-Tenorio, L. M. Kovachev, R. Perez-Torres, and V. N. Serkin, "Nonlinear soliton tunneling effects: Applications to temporal and spatial optical solitons and matter wave solitons in Bose-Einstein condensate," *Int. Electron. J. Nanoc. Moletron.*, vol. 10, no. 2, p. 1915, 2012.

[63] A. M. Kosevich, "Particle and wave properties of solitons: Resonant and non-resonant soliton scattering by impurities," *Physica D: Nonlinear Phenomena*, vol. 41, no. 2, pp. 253–261, 1990.

[64] A. Roy, R. Haldar, and S. K. Varshney, "Synchronous all-optical buffer-cum-logic gates in dual-pump Kerr microring resonators," in *Frontiers in Optics*. Optical Society of America, 2017, pp. JTu3A–22.

[65] Y. Wang, M. Anderson, S. Coen, S. G. Murdoch, and M. Erkintalo, "Stimulated Raman scattering imposes fundamental limits to the duration and bandwidth of temporal cavity solitons," *Physical Review Letters*, vol. 120, no. 5, p. 053902, 2018.

[66] Y. Okawachi, M. Yu, V. Venkataraman, P. M. Latawiec, A. G. Griffith, M. Lipson, M. Lončar, and A. L. Gaeta, "Competition between Raman and Kerr effects in microresonator comb generation," *Optics Letters*, vol. 42, no. 14, pp. 2786–2789, 2017.

[67] M. Karpov, H. Guo, A. Kordts, V. Brasch, M. H. Pfeiffer, M. Zervas, M. Geiselmann, and T. J. Kippenberg, "Raman self-frequency shift of dissipative Kerr solitons in an optical microresonator," *Physical Review Letters*, vol. 116, no. 10, p. 103902, 2016.

[68] A. Roy, R. Haldar, and S. K. Varshney, "Dual-pumped Kerr cavity soliton based synchronous all-optical buffer: Raman resilience," in *Integrated Photonics Research, Silicon and Nanophotonics*. Optical Society of America, 2019, pp. IT1A–3.

[69] Z. Kang, F. Li, J. Yuan, K. Nakkeeran, J. N. Kutz, Q. Wu, C. Yu, and P. Wai, "Deterministic generation of single soliton Kerr frequency comb in microresonators by a single shot pulsed trigger," *Optics Express*, vol. 26, no. 14, pp. 18 563–18 577, 2018.

[70] X. Xue, Y. Xuan, C. Wang, P.-H. Wang, Y. Liu, B. Niu, D. E. Leaird, M. Qi, and A. M. Weiner, "Thermal tuning of Kerr frequency combs in silicon nitride microring resonators," *Optics Express*, vol. 24, no. 1, pp. 687–698, 2016.

[71] T. Hansson and S. Wabnitz, "Frequency comb generation beyond the Lugiato–Lefever equation: multi-stability and super cavity solitons," *JOSA B*, vol. 32, no. 7, pp. 1259–1266, 2015.

[72] M. Anderson, Y. Wang, F. Leo, S. Coen, M. Erkintalo, and S. G. Murdoch, "Coexistence of multiple nonlinear states in a tristable passive Kerr resonator," *Physical Review X*, vol. 7, no. 3, p. 031031, 2017.

[73] W. Chen, B. Garbin, A. U. Nielsen, S. Coen, S. G. Murdoch, and M. Erkintalo, "Experimental observations of breathing Kerr temporal cavity solitons at large detunings," *Optics Letters*, vol. 43, no. 15, pp. 3674–3677, 2018.

[74] M. Conforti and F. Biancalana, "Multi-resonant Lugiato–Lefever model," *Optics Letters*, vol. 42, no. 18, pp. 3666–3669, 2017.

[75] M. Anderson, Y. Wang, F. Leo, S. Coen, M. Erkintalo, and S. Murdoch, "Experimental observation of super cavity solitons," in *European Quantum Electronics Conference*. Optical Society of America, 2017, p. EF_1_5.

[76] A. Roy, R. Haldar, and S. K. Varshney, "Breakdown of optical lattice formation in dual-pumped supercavity soliton states," in *Nonlinear Optics and its Applications 2018*, vol. 10684. International Society for Optics and Photonics, 2018, p. 106841R.

CHAPTER 6

Spatially Entangled Continuous Variable States in Periodically Poled $LiNbO_3$ Waveguide Array

In this chapter, we theoretically and numerically investigate the parallel generation of spatially entangled continuous-variable (CV) states between different waveguide pairs of a 5×5 periodically poled lithium niobate ($LiNbO_3$) waveguide array for different pumping arrangements with a perspective of multipartite entanglement. The bipartite entanglement is determined by following the Peres-Horodecky criteria.[1]

6.1 Introduction

Quantum properties of light can be exploited in a myriad of applications such as quantum computing (QC), quantum teleportation, quantum information processing (QIP), quantum key distribution (QKD), and cryptography (QCr), quantum simulations, spectroscopy, metrology and even in sensing [1–4]. Photonic systems follow most of the DiVincenzo's Criteria for QC approaches [5]. Integrated on-chip

---

[1] This work is partially conducted under Raman-Charpak Fellowship 2017-2018 at CNRS.

waveguide based platform makes the technology scalable and compact for which the scientists were striving for a decade now. Being bosonic in nature, photons show less interaction with other particles and within themselves, thereby are less susceptible to the quantum noise or decoherence. Therefore, QIP using photons as qubits is a very robust approach over other existing approaches [1–4, 6]. Generation and manipulation of photons in an integrated on-chip waveguide-based platform are preferred over crystal-based bulk-optical components mainly due to their compactness, scalability, connectivity, reproducibility and very low power consumption [6, 7]. Recent developments in nano-fabrication technologies make the integrated quantum photonic circuit a promising and versatile candidate for future QIP technologies [6] as well as for quantum cryptography.

QIP and QKD through photonic technologies, both come in two possible forms based on discrete variable (DV) and continuous variable (CV) systems, each of them having its own pros and cons [8, 9]. Similar to the digital electronic systems, DV systems deal with the single photon's discrete degrees of freedom (number/polarization/phase) as qubits, whereas, CV systems encode position (x) and momentum (p) or amplitude (A) and phase (ϕ) of the electromagnetic fields as the quadratures residing in the infinite-dimensional Hilbert space. In QIP, DV has been a popular choice as it is notably more robust to noise. The advent of Knill, Laflamme and Milburn (KLM) protocol in 2001 that facilitates high-fidelity DV quantum computing only with the linear optical components, single-photon sources and detectors in a relatively deterministic way through quantum teleportation, is considered to be the cornerstone of quantum photonic technologies [10]. As opposed to DV, CV systems utilize coherent laser sources and homo/heterodyne receivers those are extensively used in present-day mature telecommunication systems. Therefore, photonic CV devices indeed would benefit from widely available laser sources operate deterministically and therefore, has been recently recognized as an extremely powerful alternative of DV for QIP [9]. CV detectors show quantum efficiency close to unity without demanding expensive laboratory equipment. Thus in the last decade, CV-versions of quantum protocols to logic gates, teleportation, search algorithms, Fourier transform, Deutsch algorithm etc. have been developed rapidly [1, 11, 12]. Nevertheless, recent developments in this direction shows that Gaussian CV operations in their present forms are not useful for more advanced quantum protocols such as entanglement distillation [13] and we should combine both the CV and DV approaches together to form a hybrid CV and DV quantum network [14].

Both for the CV and DV systems, generation of quantum entanglement is indispensable to realize different protocols for QIP and QKD [3]. Some of the QKD protocols (BB84, Decoy, BB92, SSP, SARG04, KMB09, S13 etc.) also known as 'prepare-and-measure' protocols are based on uncertainty principle, and no-cloning theorem whereas, entanglement is a crucial part of several quantum cryptographic protocols like E91, DPS, COW etc [8]. Multi-partite entanglement further enhances the performances of a quantum computer thanks to the elegance of algorithms leveraging the higher dimensionality [15, 16]. Security in quantum cryptography relies on the fact that the bipartite entanglement distributed between two parties cannot be shared with another/third party if the two parties are maximally entangled. Therefore, multi-partite entanglement is an essential candidate for a quantum communication link [17, 18]. Popular applications of multi-partite entanglement in quantum communication are the super-dense coding [19] and Byzantine agreement protocol [20]. Moreover, from this, highly entangled cluster states can be a very powerful tool to realize large scale linear optical quantum computing [21].

6.1.1 Choice of Materials

Quantum logic gates (Pauli-X bit-flip, Pauli-Y, Pauli-Z, Hadamard, SWAP, Phase-shift gate, arbitrary rotational gate, Controlled-Not CNOT, Toffoli gates), small-scale factoring algorithms, quantum simulations and entanglement generation and manipulation are already demonstrated in integrated platforms [1, 4, 22, 23]. Unfortunately, efficient generation, manipulation and detection on the same chip composed of same material have not yet been achieved [24]. Among $LiNbO_3$, Si, other III-V (GaAs etc.) semiconductors [24–26], which material will finally survive that continues to stay as an open question and still the development of integrated quantum photonic circuit is in its very early stage [26, 27].

Recent progresses in this direction show [28] that both Si and $LiNbO_3$ are becoming competitive materials to each other. In 2014, fully integrated quantum circuits has been demonstrated in silicon-on-insulator (SOI) platform where photon pairs are generated through spontaneous four-wave mixing (SFWM) exploiting Kerr/$\chi^{(3)}$ nonlinearity of Si within a very compact size. In general, silicon has a much higher refractive index contrast with silica and air in comparison with LiNbO$_3$. Therefore, silicon based devices are much more compact in size. However, in addition to the negligible propagation loss, the efficiency of the nonlinear conversion through quasi-phase matching is much higher in lithium niobate than that of silicon. Also, mature CMOS compatible fabrication techniques are available for these devices [28–31]. However, the two-photon absorption loss (2PA) at telecommunication wavelength ($\lambda < 2.2\,\mu$m), free-carrier absorption and dispersion, absence of Pockels/Electro-optic effect, very low Franz-Keldysh effect, high temperature sensitivity etc. limit the performance of SOI-based devices [32–34]. On the other hand, LiNbO$_3$ is preferred over Si mainly for the manipulation of photons [24, 26, 35, 36] due to its high $\chi^{(2)}$ nonlinearity, high acousto-optic and large electro-optic coefficient. Although the device size are relatively larger in comparison with Si-based devices, periodically poled lithium niobate (PPLN) waveguides recently have drawn significant attention for the generation of photon pairs exploiting spontaneous parametric down conversion (SPDC) through (type-I or type-II) quasi phase matching (QPM). LiNbO$_3$ is not CMOS compatible; nevertheless, standard fabrication techniques (proton exchange or Ti-indiffusion) are available to design such PPLN waveguides [26]. The most significant advancement in LiNbO$_3$ based integrated quantum technology comes forward in 2017 with the advent of highly entangled cluster states [37]. Complexity of the photonic circuitry exponentially increases with the increase in the number of qubits in cluster states. However, exploiting the spatial degrees of freedom of PPNL waveguide arrays, a cluster state of four qubits are realized with relative ease. The effect of nonlinear losses on the generation of quantum states in PPLN array waveguide is also studied [38]. Possibility of hybrid silicon and lithium niobate integrated platform harvesting the advantages of both the materials is also discussed in details in the literature [39, 40].

The primary objective of this work is to determine the best pumping scheme and the most suitable waveguide parameters to maximize the squeezing of light through spontaneous parametric down conversion (SPDC: $\chi^{(2)}$ method) by QPM in a PPLN waveguide coupler as well as the to maximize the entanglement between the non-classical optical modes propagating in the adjacent waveguides [41–43]. We investigate the generation of bipartite CV-entanglement between different guided-modes pairs of a PPLN waveguide array (WGA) made up of 5 waveguides in presence of symmetric and asymmetric optical pumping. Bipartite entanglement is assessed by the Peres-Horodecki criterion through the logarithmic negativity E_{N}, where $E_{\mathrm{N}} > 0$ is indicative of entanglement [15, 44–46]. WGA is a promising candidate for the generation of multipartite entanglement and Gaussian-steering [47–52]. We have chosen a 5×5 coupler as the architecture provides more degrees of freedom and output ports than the directional coupler. We implement different pumping scheme to gain insight about entanglement with large number of parties in more general optical lattices. This device is a new source of multiple bipartite entangled states to be sent through a quantum network. The results help us to get an idea of the suitable waveguide structure as well as the efficient waveguide architecture in terms of spatial CV entanglement. Finally, we attempt to find the best possible pumping scheme along with the optimized waveguide coupler architecture to achieve the maximum multipartite entanglement (both fully and genuinely) between the waveguides.

Recently on-chip optical squeezing of $\sim 1.7\,\mathrm{dB}$ and $\sim 1.83\,\mathrm{dB}$ have been demonstrated in integrated $\mathrm{Si_3N_4}$ [53], and periodically poled Lithium Niobate (PPLN) [54] platforms using spontaneous four-wave mixing and spontaneous parametric down conversion (SPDC) through quasi-phase matching (QPM), respectively. The possibility of achieving bipartite and multipartite multicolor CV-entanglement with realistic parameters with a PPLN-based waveguide directional coupler have been theoretically explored in [46, 55]. However, to the best of our knowledge, efficient generation of both bi-partite and multi-partite quantum entanglement and optical squeezing through spontaneous parametric down conversion have yet not been demonstrated simultaneously in an integrated platform. Our current work based on coupled PPLN array waveguides may facilitate the possibility of obtaining this goal. Once, we achieve the multipartite entanglement, we plan to use this in a known quantum protocol to verify the usefulness of our proposed scheme as well as the proposed device.

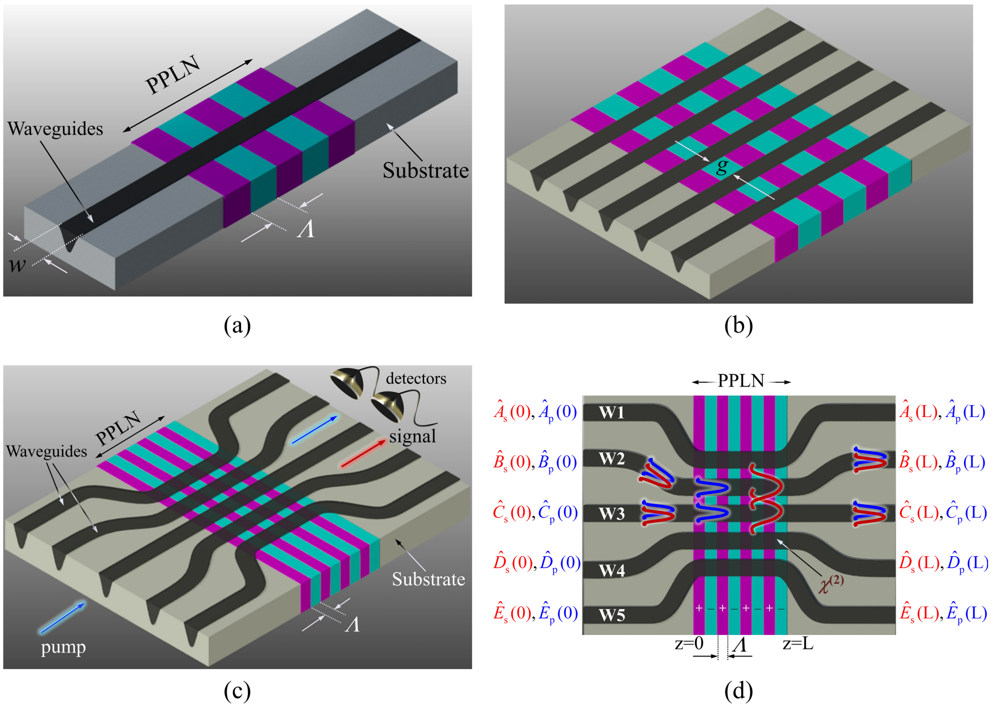

Figure 6.1: (a) Single PPLN waveguide, (b) PPLN waveguide array, (c) the perspective view, and (d) the top-view of the proposed 5×5 PPLN coupled waveguide array for CV-entanglement generation.

6.2 Theory and Numerical Results

6.2.1 Waveguide Structure

In our simulation to find the best pumping scheme, we consider the realistic waveguide parameters. The group performs experiments on PPLN chips consisting of buried waveguides as shown in Fig. 6.1 (a). The PPLN waveguides fabricated in lasi, RAMTECH, Romania and INPHYNI, Nice, France through soft photon exchange usually have diffusion induced Gaussian refractive index (RI) profiles with base width, $w \sim 6\,\mu$m and RI contrast, $\Delta n = 2.4 \times 10^{-2}$. The pitch of the PPLN, Λ is $\sim$16 μm. We show a typical PPLN AWG in Fig. 6.1 (b). The separation, g between any pair of waveguides in the array, shown in Fig. 6.1 (b), is typically 12–18 μm to achieve the desired coupling coefficient.

6.2.2 Theory

As mentioned earlier, in this work, we numerically investigate the generation of bipartite CV-entanglement between different waveguide pairs of five coupled PPLN waveguides in presence of symmetric and asymmetric optical pumping. The primary objective is to determine the best possible pumping scheme and the most suitable waveguide parameters to maximize the two-mode squeezing of light through SPDC and the entanglement between the desired waveguide pairs. Peres-Horodecki criterion is used to determine the bipartite entanglement between the desired quantum states by calculating the logarithmic negativity, E_{N} that is indicative of entanglement when $E_{\mathrm{N}} > 0$. A brief discussion related to the Peres Horodecki criteria/positive partial trace (PPT) method to distinguish the entangled and separable states along with the procedure that quantifies the entanglement mathematically is mentioned in the next section. A brief introduction on squeezed state is also discussed.

6.2.2.1 Peres Horodecki Criteria

Schmidt decomposition is extensively used to find if a composite pure state is entangled or separable. Schmidt decomposition does not apply for the mixed states [12]. Peres Horodecki criteria or positive partial transpose (PPT) comes to rescue in this regard. The PPT is a necessary condition for the joint density matrix (ρ_{AB}) of two quantum systems A and B, to be separable. Suppose the partial trace (PT) of the composite matrix ρ_{AB} with respect to A is defined as, $\rho^{\mathrm{B}}_{\mathrm{PT}} = tr_A(\rho_{\mathrm{AB}})$. PPT criterion states that if the density matrix of a composite state ρ_{AB} is still a positive semi-definite (i.e. none of the eigenvalues of the matrix is negative) matrix after the PT (with respect to A or B) of ρ_{AB}, then the state is separable. Even if a single eigenvalue after the PT becomes negative then the state must have entanglement. The number of negative eigenvalues is an indirect measurement of the entanglement. The PPT criteria is also a sufficient criteria for 2×2 and 2×3 cases.

6.2.2.2 PPT for Gaussian CV States

The Peres Horodecki criteria can be generalized for the Gaussian CV systems [12]. If a bipartite CV composite-state represented by the density matrix (ρ_{AB}) an be expressed in terms of a summation of the tensor products between two subsystems density matrices ρ_{A} and ρ_{B}, respectively as given by the Eq. 6.1 then the composite state is separable,

$$\rho_{AB} = \sum_{j} p_{\mathrm{j}} \rho_{A}^{j} \otimes \rho_{B}^{j} \tag{6.1}$$

Suppose, a composite system has a Wigner function (WF), $W(x_1, p_1, x_2, p_2)$ that depends upon the quadratures (position and momentum) of the two systems given in equation Eq. 6.2:

$$\begin{aligned} W(x_1, p_1, x_2, p_2) &= \left(\frac{1}{\pi}\right)^2 \iint dy_1 dy_2 \left(e^{2i(p_1 y_1 + p_2 y_2)}\right) \\ &\times \sum_{j} p_{\mathrm{j}} \langle x_1 - y_1 | \rho_1^{j} | x_1 + y_1 \rangle \otimes \langle x_2 - y_2 | \rho_2^{j} | x_2 + y_2 \rangle \end{aligned} \tag{6.2}$$

Partial transpose of the WF of the Gaussian CV states is reflected as the reflection of one of the momentum components, i.e. $p_2 \to -p_2$. Thus it can be written as:

$$W^{\mathrm{PT}}(x_1, p_1, x_2, p_2) = W(x_1, p_1, x_2, -p_2) \tag{6.3}$$

Therefore, for Gaussian CV states, PT≡reflection of the momentum direction. According to the Weyl correspondence, the Wigner distribution relates quantum operators to their corresponding phase space variables, in which for this situation, the operators and the variables are the quadratures. For convenience the quadratures are put together into a column vector. Thereby, the quadrature operators and the variables are expressed as follows:

$$\hat{\xi} = \begin{pmatrix} \hat{x}_1 \\ \hat{p}_1 \\ \hat{x}_2 \\ \hat{p}_2 \end{pmatrix}; \text{ and } \xi = \begin{pmatrix} x_1 \\ p_1 \\ x_2 \\ p_2 \end{pmatrix} \tag{6.4}$$

For our convenience we can also define the two matrices:

$$\Omega = \begin{pmatrix} J & 0 \\ 0 & J \end{pmatrix},\ J = \begin{pmatrix} 0 & 1 \\ -1 & 0 \end{pmatrix} \tag{6.5}$$

Where, $\left[\hat{\xi}_\alpha, \hat{\xi}_\beta\right] = i\Omega_{\alpha\beta}$ and α, β can run from 1 to 4. The result of performing a PT on the WF can be seen to be equivalent to perform an operator Λ on ξ, where Λ =diag(1, 1, 1, -1).

6.2.2.3 Uncertainty Principle as Separable Criteria

According to the quantum mechanics, every physical state requires to fulfil the uncertainty principle and the converse is also true [12]. To define the uncertainty principle for quadrature operators, a covariance matrix (V) is defined as follows,

$$\begin{aligned}
&V = \left\langle \left\{ \Delta\hat{\xi}_\alpha, \Delta\hat{\xi}_\beta \right\} \right\rangle = \left\langle \frac{1}{2}\left(\Delta\hat{\xi}_\alpha \Delta\hat{\xi}_\beta + \Delta\hat{\xi}_\beta \Delta\hat{\xi}_\alpha \right) \right\rangle \\
&\text{where,} \\
&\Delta\hat{\xi}_\alpha = \hat{\xi}_\alpha - \langle \xi \rangle \\
&\Delta\hat{\xi}_\beta = \hat{\xi}_\beta - \langle \xi \rangle \\
&\left\langle \hat{\xi} \right\rangle = \mathrm{Tr}\left(\hat{\rho}\hat{\xi} \right)
\end{aligned} \tag{6.6}$$

Therefore, the uncertainty principle can be written as:

$$V + \frac{i}{2}\Omega \geq 0 \tag{6.7}$$

After the PT the new covariance matrix would also follow the uncertainty principle in case it represent a realizable physical state. Hence, one can write:

$$\Lambda V \Lambda + \frac{i}{2}\Omega \geq 0 \tag{6.8}$$

If the condition does not follow, the state must not be separable.

6.2.2.4 Effect of Nonlinear Interactions

Now suppose for any waveguide-system at the input ($z = 0$) the covariance matrix be $V(z = 0) = V(0)$. The optical wave propagates along z direction and the effects of the nonlinear interactions can be accounted by the unitary operation $S(z)$. The evolution of the covariance matrix within the waveguide at distance z from the input-port can be given by,

$$V(z) = S\left(z\right)V(0)S(z)^T \tag{6.9}$$

$V(z)$ also should follow the uncertainty principle as given by Eq. 6.7. According to the PPT if entanglement exists then $\Lambda V(z)\Lambda$ must not satisfy the uncertainty principle. In that case, the entanglement can be measured by following the rule given in [46] from the density matrix of the composite state. The entanglement can also be calculated from the covariance matrix. If $V(z)^{\mathrm{PT}}$ denotes the partial transpose of $V(z)$, the logarithmic negativity is obtained from the symplectic spectrum $\{v_{\mathrm{k}}\}_{\mathrm{k}=1}^{4}$ calculated from the matrix $|i\Omega V(z)^{\mathrm{PT}}|$ must contain one or more negative eigenvalues. So, the entanglement, E_{N} can be given by,

$$E_{\mathrm{N}} = \sum_{k=1}^{4} F\left(v_k\right), \text{ with } F(v) = \begin{cases} 0, \text{ for } v \geq 1/2 \\ -\log_2\left(2v\right), \text{ for } v < 1/2\,; \end{cases} \tag{6.10}$$

Any value $E_{\mathrm{N}} > 0$ indicates the presence of entanglement.

6.2.3 Optical Squeezing and Covariance Matrix

In the previous section, we have described how to evaluate the CV-entanglement, numerically. This section briefly discusses the fundamental concepts of the squeezed light. In principle, the tangible measurement of the CV-entanglement is not straight-forward. The amount (dB) of the optical squeezing of two-mode squeezed coherent states at the outputs of the PPLN waveguide array can be measured, experimentally. From squeezing, the co-variance matrix (V) can be directly calculated. Once the co-variance matrix is obtained, as explained earlier, PPT criteria helps to identify the existence of the CV-entanglement. Further, the logarithmic negativity quantifies the spatial CV-entanglement.

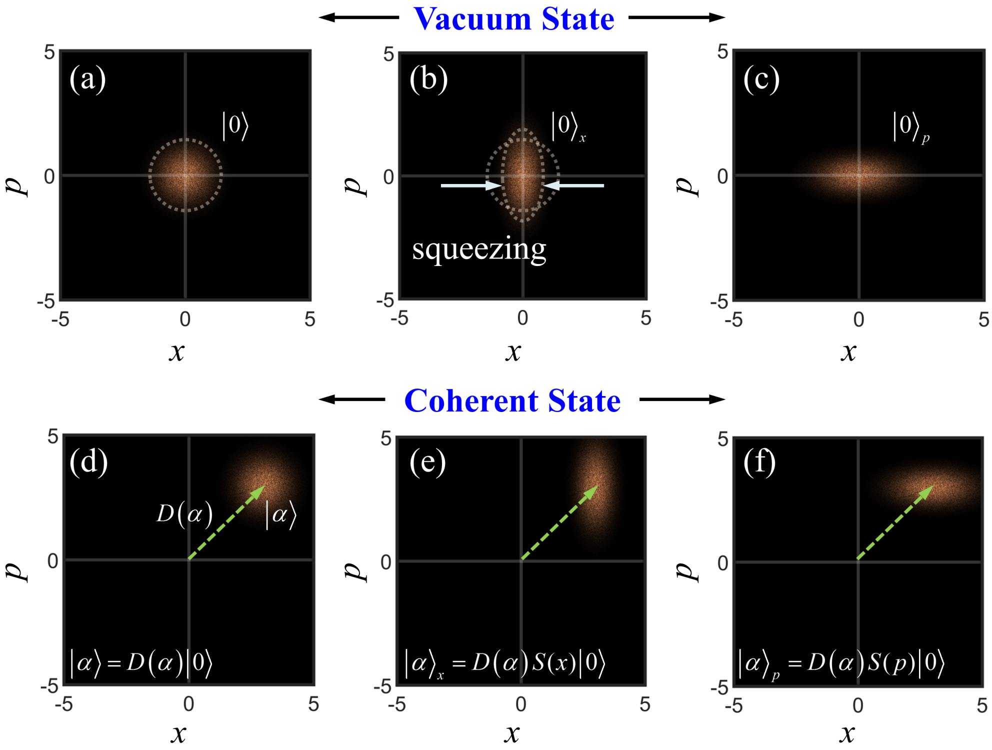

Figure 6.2: (a) Vacuum state, (b) squeezed (x-quadrature) vacuum, (c) squeezed (p-quadrature) vacuum, (d) coherent state, (e) squeezed (x-quadrature) coherent state, (f) coherent state squeezed in p-quadrature.

6.2.3.1 Squeezed State of Light

According to the Heisenberg's principle, all light fields inherently fluctuate and their amplitudes and phases are subject to a stochastic indeterminacy. The measured electric field amplitude (E) and the phase (ϕ) are the eigenvalues of the normalized position (x) and momentum (p) quadrature operators. If the fluctuations in these quadratures are denoted by Δx and Δp, respectively, then the product of the fluctuations must follow the Heisenberg's principle (normalized) given by,

$$\Delta x \Delta p \geq \frac{1}{2} \tag{6.11}$$

where, $[x, p] = i$. In Fig. 6.2 (a), (b), and (c), we illustrate the vacuum state ($|0\rangle$), squeezed vacuum with less amplitude noise ($|0\rangle_x$), and less noise in phase ($|0\rangle_p$),

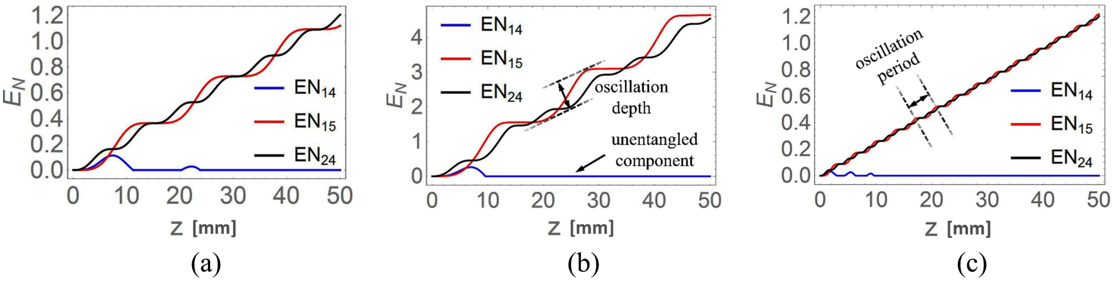

Figure 6.3: (a) EN_{14}, EN_{15}, EN_{24}; EN_{14}, EN_{15}, EN_{24} when the (b) pump power is doubled, (c) coupling coefficient become doubled.

respectively. Normal vacuum state possesses a circular Gaussian WF, whereas, the phase-space distribution of the squeezed state resembles to an ellipse. Again, the coherent state ($|\alpha\rangle$) having a Gaussian WF (Fig. 6.2 (d)) is a minimal uncertainty state where the $\Delta x \Delta p = 1/2$ and the fluctuation (shot-noise) in both the quadratures are the same (i.e. $\Delta x = 1/\sqrt{2}$, $\Delta p = 1/\sqrt{2}$). The WF of such coherent state is circularly symmetric with respect to its centre shifted by a displacement vector ($D(\alpha)$) from the vacuum state given by $|0\rangle$. In quantum physics, light is in squeezed state if the quantum uncertainty of one of the two quadratures x or p (amplitude (E) or phase (ϕ), respectively) is less than the coherent state. Therefore, for squeezed state, either, $\Delta x < 1/\sqrt{2}$ (Fig. 6.2 (e)) or $\Delta p < 1/\sqrt{2}$ (Fig. 6.2 (f)). Squeezed light has a myriad of applications in different domains [53, 56, 57]. We can measure the squeezed state just by using a homodyne detector [58], that can yield the co-variance matrix.

6.2.3.2 Theoretical Framework of Our Work

We have chosen a 5×5 coupler as the architecture provides more degrees of freedom in implementing the different pumping schemes. Besides, as a future scope, we believe this coupled array waveguide structure is a promising candidate for the generation of multipartite entanglement and Gaussian-steering.

The perspective view of the proposed nonlinear waveguide array (WGA) is shown in Fig. 6.1 (c). Optical modes are guided through the diffusion induced waveguides. Five identical $\chi^{(2)}$ waveguides are placed side by side as shown in Fig. 6.1. Note that, the waveguide separation is designed in such a way that the modes at $1.55\,\mu$m are evanescently coupled at the coupling region whereas, the pump-modes at 780 nm remained guided. The phase-matching condition is only fulfilled in the coupling region. Second harmonic generation, SPDC, and optical parametric amplification can happen in the 2nd order nonlinear waveguides depending upon the initial conditions. The effective interaction momentum operator ($\hat{M}$), for all of these processes, is the same, and for such a 5×5 waveguide-coupler can be written as:

$$\hat{M} = \hbar\Bigg(g_{\mathrm{A}} {A_{\mathrm{s}}^{\dagger}}^2 + g_{\mathrm{B}} {B_{\mathrm{s}}^{\dagger}}^2 + g_{\mathrm{C}} {C_{\mathrm{s}}^{\dagger}}^2 + g_{\mathrm{D}} {D_{\mathrm{s}}^{\dagger}}^2 + g_{\mathrm{E}} {E_{\mathrm{s}}^{\dagger}}^2 \\ + C_{\mathrm{AB}} A_{\mathrm{s}} {B_{\mathrm{s}}}^{\dagger} + C_{\mathrm{BC}} B_{\mathrm{s}} {C_{\mathrm{s}}}^{\dagger} + C_{\mathrm{CD}} C_{\mathrm{s}} {D_{\mathrm{s}}}^{\dagger} + C_{\mathrm{DE}} D_{\mathrm{s}} {E_{\mathrm{s}}}^{\dagger} + h.c. \Bigg) \tag{6.12}$$

Where A_{s} (${A_{\mathrm{s}}}^{\dagger}$), B_{s} (${B_{\mathrm{s}}}^{\dagger}$), C_{s} (${C_{\mathrm{s}}}^{\dagger}$), D_{s} (${D_{\mathrm{s}}}^{\dagger}$), and E_{s} (${E_{\mathrm{s}}}^{\dagger}$) are the annihilation (creation) operators of the harmonic optical modes propagating, respectively in waveguides labeled as A, B, C, D, and E in Fig. 6.1 (d). g_{i} is the efficiency of the 2nd order process in the i-th waveguide and C_{ij} represents the linear coupling coefficient between the adjacent i-th and j-th waveguides. $\hbar$ is the reduced Planck's constant. It is to be noted that the coupler is designed in such a way that pump modes cannot couple to each other. Coupling between the adjacent waveguides is only considered. Pump depletion is negligible and thus pump-modes A_{p}, B_{p} etc. do not appear in equation 6.12. In the Heisenberg's interaction picture, the mode-operators evolve along the propagation length z of the waveguides. Corresponding normalized quadrature operators of mode i are denoted by $\hat{x}_{\mathrm{i}}$ (position) and $\hat{p}_{\mathrm{i}}$ (momentum) where $[\hat{x}_{\mathrm{i}}, \hat{p}_{\mathrm{i}}] = i$. In our work, we have used the definition of the quadrature operators, $\hat{x}_{\mathrm{A}} = (A_{\mathrm{s}}^{\dagger} + A_{\mathrm{s}})/\sqrt{2}$, and $\hat{p}_{\mathrm{A}} = i(A_{\mathrm{s}}^{\dagger} - A_{\mathrm{s}})/\sqrt{2}$ and so on. The Heisenberg-Langevin equation for the system neglecting the loss can be given as: $d\hat{\xi}/dz = M_{10}\xi$, where, $\hat{\xi} = (\hat{x}_{\mathrm{A}}, \hat{p}_{\mathrm{A}}, \hat{x}_{\mathrm{B}}, \hat{p}_{\mathrm{B}}, \hat{x}_{\mathrm{C}}, \hat{p}_{\mathrm{C}}, \hat{x}_{\mathrm{D}}, \hat{p}_{\mathrm{D}}, \hat{x}_{\mathrm{E}}, \hat{p}_{\mathrm{E}})^{\mathrm{T}}$ and M_{10} is a 10×10 matrix given in Eq. 6.13. Thus the evolution of the co-variance matrix along the propagation length of the waveguide coupler follows Eq. 6.9, where $S(z) = \exp(M_{10}z)$ and $V_0 = I_{10}/2$ represents the vacuum fluctuation at the input port of the WGA. From the matrix V, CV bi-partite entanglement is determined by calculating the logarithmic negativity, E_{N} (> 0) following the procedure given in [41,42,46]. At first, we pump the 3rd waveguide (C) and plot the entanglement,

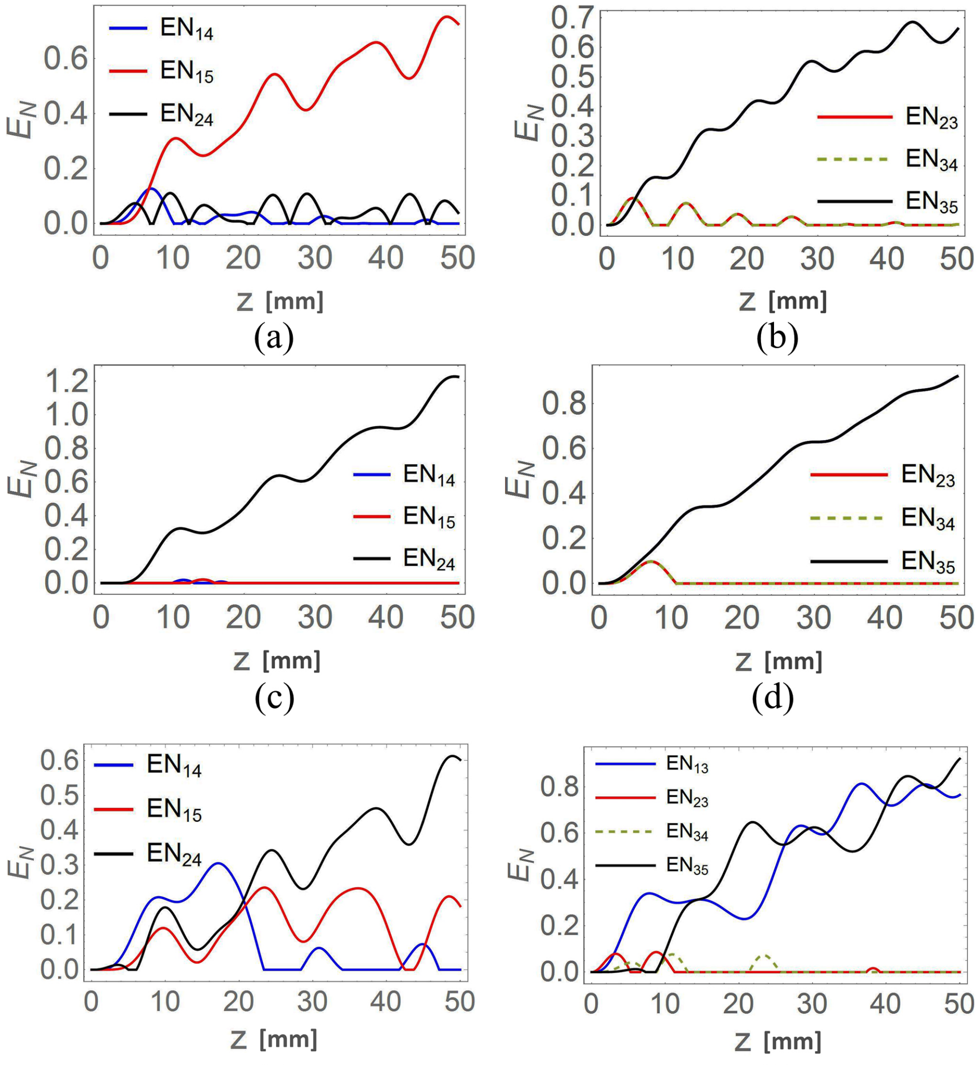

(a) (b) (c) (d) (e) (f)

Figure 6.4: (a) EN_{14}, EN_{15}, EN_{24}, and (b) EN_{23}, EN_{34}, EN_{35} while 2nd and 4th waveguides are pumped; (c) EN_{14}, EN_{15}, EN_{24}, and (d) EN_{23}, EN_{34}, EN_{35} while 1st, 3rd and 5th waveguides are pumped. (e) EN_{14}, EN_{15}, EN_{24}, (f) EN_{13}, EN_{23}, EN_{34}, EN_{35} while the 1st and 2nd waveguides are pumped (asymmetric case).

E_{N} with respect to the propagation length, z in Fig. 6.3 (a). Fig. 6.3 (a) shows that there is no CV-entanglement generated in asymmetric waveguide pairs such as 1 and 4 when the WGA is pumped symmetrically while entanglement between 2nd and 4th waveguides and 1st and 5th waveguides gradually builds-up. Realistic simulation parameters are identical to the ones used in Barral *et al.* [46]: We take all non-vanishing couplings to be equal to $C = C_{\mathrm{ij}} = 0.24\,\mathrm{mm}^{-1}$ and all nonlinear efficiency to $g = g_{\mathrm{i}} = 0.025\,\mathrm{mm}^{-1}$.

$$M_{10} = \begin{pmatrix} -S_{\mathrm{A}} & C_{\mathrm{A}} & S_{\mathrm{L}} & -C_{\mathrm{L}} & 0 & 0 & 0 & 0 & 0 & 0 \\ C_{\mathrm{A}} & S_{\mathrm{A}} & C_{\mathrm{L}} & S_{\mathrm{L}} & 0 & 0 & 0 & 0 & 0 & 0 \\ -S_{\mathrm{L}} & -C_{\mathrm{L}} & -S_{\mathrm{B}} & C_{\mathrm{B}} & S_{\mathrm{L}} & -C_{\mathrm{L}} & 0 & 0 & 0 & 0 \\ C_{\mathrm{L}} & -S_{\mathrm{L}} & C_{\mathrm{B}} & S_{\mathrm{B}} & C_{\mathrm{L}} & S_{\mathrm{L}} & 0 & 0 & 0 & 0 \\ 0 & 0 & -S_{\mathrm{L}} & -C_{\mathrm{L}} & -S_{\mathrm{C}} & C_{\mathrm{C}} & S_{\mathrm{L}} & -C_{\mathrm{L}} & 0 & 0 \\ 0 & 0 & C_{\mathrm{L}} & -S_{\mathrm{L}} & C_{\mathrm{C}} & S_{\mathrm{C}} & C_{\mathrm{L}} & S_{\mathrm{L}} & 0 & 0 \\ 0 & 0 & 0 & 0 & -S_{\mathrm{L}} & -C_{\mathrm{L}} & -S_{\mathrm{D}} & C_{\mathrm{D}} & S_{\mathrm{L}} & -C_{\mathrm{L}} \\ 0 & 0 & 0 & 0 & C_{\mathrm{L}} & -S_{\mathrm{L}} & C_{\mathrm{D}} & S_{\mathrm{D}} & C_{\mathrm{L}} & S_{\mathrm{L}} \\ 0 & 0 & 0 & 0 & 0 & 0 & -S_{\mathrm{L}} & -C_{\mathrm{L}} & -S_{\mathrm{E}} & C_{\mathrm{E}} \\ 0 & 0 & 0 & 0 & 0 & 0 & C_{\mathrm{L}} & -S_{\mathrm{L}} & C_{\mathrm{E}} & S_{\mathrm{E}} \end{pmatrix} \tag{6.13}$$

where,

$$\begin{aligned} S_{\mathrm{i}} &= 2\,|g_{\mathrm{i}}|\sin(\phi_{\mathrm{i}}) \\ C_{\mathrm{i}} &= 2\,|g_{\mathrm{i}}|\cos(\phi_{\mathrm{i}}) \\ S_{\mathrm{L}} &= |C_{\mathrm{ij}}|\sin(\phi_{\mathrm{ij}}) \\ C_{\mathrm{L}} &= |C_{\mathrm{ij}}|\cos(\phi_{\mathrm{ij}}) \end{aligned} \tag{6.14}$$

As demonstrated in Fig. 6.3, pump-power and coupling coefficient act as scaling factors on the CV-entanglement E_{N}. If the input power is increased, the oscillation depth enhances, entanglement is built faster and the unentangled component decays quickly. If the coupling coefficient increased by 4-times, the oscillation period of E_{N} decreases proportionately. Therefore, the entanglement configuration obtained in Fig 6.3 (a)–(c) is especially interesting to generate bipartite entangled states in ‘parallel’ (modes 1–5 and 2–4) in a compact stable device and distribute entangled telecom pairs in an optical network. This arises from a simple single waveguide pumping. Scaling up the number of generated entangled pairs or getting multipartite entangled states involves optimization of the pumping arrangement. Change of pumping scheme for entanglement optimization is readily implemented by changing the g coefficient values as exemplified in figure 6.3. Fig. 6.4 (a) and 6.4 (b) show the E_{N} while the 2nd and 4th waveguides are pumped and the entanglement between different waveguide pairs are shown in Fig. 6.4 (c) and 6.4 (d) while 1st, 3rd, and 5th waveguides are pumped. We also study the generation of CV-entanglement between the previously chosen pair of waveguides while the array is asymmetrically pumped. If only 1st and 2nd waveguides are pumped then entanglement between the 2nd and 4th waveguide (EN_{24}), entanglement between the 1st and 3rd waveguide (EN_{13}), and entanglement between the 3rd and 5th waveguide (EN_{35}) are gradually increased with the propagation length of the coupled region. The achieved entanglements are comparable with the entanglements that can be obtained in cavities [59].

6.3 Summary and Conclusion

To summarize, a theoretical study on the generation of CV-entanglement in PPLN waveguide arrays has been presented. This framework enables the determination of suitable device parameters (length, inter-waveguide distance) and pumping scheme (amplitude and phase) to conduct experiments. We exemplify this on the numerical evolution of bipartite entanglement in a 5×5 coupler for symmetric and asymmetric pumping configurations. We demonstrate the efficient parallel generation of two entangled pairs for injection in an optical network in a device without a bulk-optic analogue.

Multi-partite entanglement has well-known application in super-dense coding and can further enhance the performances of a quantum computer thanks to the elegance of algorithms leveraging the higher dimensionality. We believe the chosen waveguide array is a promising system for multipartite entanglement. Perspectives, of course, involve the determination of the best system and input parameters for maximal multipartite entanglement using Van Loock-Furusawa criteria.

References

[1] M. A. Nielsen and I. Chuang, “Quantum computation and quantum information,” 2002.

[2] J. L. O’brien, “Optical quantum computing,” *Science*, vol. 318, no. 5856, pp. 1567–1570, 2007.

[3] J. L. O’brien, A. Furusawa, and J. Vučković, “Photonic quantum technologies,” *Nature Photonics*, vol. 3, no. 12, pp. 687–695, 2009.

[4] A. Politi, J. C. Matthews, and J. L. O'brien, "Shors quantum factoring algorithm on a photonic chip," *Science*, vol. 325, no. 5945, pp. 1221–1221, 2009.

[5] A. Acín, I. Bloch, H. Buhrman, T. Calarco, C. Eichler, J. Eisert, D. Esteve, N. Gisin, S. J. Glaser, F. Jelezko *et al.*, "The quantum technologies roadmap: a European community view," *New Journal of Physics*, vol. 20, no. 8, p. 080201, 2018.

[6] A. Politi, M. J. Cryan, J. G. Rarity, S. Yu, and J. L. O'brien, "Silica-on-silicon waveguide quantum circuits," *Science*, vol. 320, no. 5876, pp. 646–649, 2008.

[7] M. G. Thompson, A. Politi, J. C. Matthews, and J. L. O'Brien, "Integrated waveguide circuits for optical quantum computing," *IET Circuits, Devices & Systems*, vol. 5, no. 2, pp. 94–102, 2011.

[8] E. Diamanti, H.-K. Lo, B. Qi, and Z. Yuan, "Practical challenges in quantum key distribution," *npj Quantum Information*, vol. 2, p. 16025, 2016.

[9] S. L. Braunstein and P. Van Loock, "Quantum information with continuous variables," *Reviews of Modern Physics*, vol. 77, no. 2, pp. 513–577, 2005.

[10] E. Knill, R. Laflamme, and G. J. Milburn, "A scheme for efficient quantum computation with linear optics," *Nature*, vol. 409, no. 6816, pp. 46–52, 2001.

[11] C. Weedbrook, S. Pirandola, R. García-Patrón, N. J. Cerf, T. C. Ralph, J. H. Shapiro, and S. Lloyd, "Gaussian quantum information," *Reviews of Modern Physics*, vol. 84, no. 2, p. 621, 2012.

[12] T. Deesuwan, "Entanglement criteria for continuous-variable states," Ph.D. dissertation, Master of Science of Imperial College London, 2010.

[13] J. Eisert, S. Scheel, and M. B. Plenio, "Distilling Gaussian states with Gaussian operations is impossible," *Physical review Letters*, vol. 89, no. 13, p. 137903, 2002.

[14] U. L. Andersen, J. S. Neergaard-Nielsen, P. Van Loock, and A. Furusawa, "Hybrid discrete- and continuous-variable quantum information," *Nature Physics*, vol. 11, no. 9, p. 713, 2015.

[15] P. van Loock and A. Furusawa, "Detecting genuine multipartite continuous-variable entanglement," *Physical Review A*, vol. 67, no. 5, p. 052315, 2003.

[16] W. McCutcheon, A. Pappa, B. Bell, A. McMillan, A. Chailloux, T. Lawson, M. Mafu, D. Markham, E. Diamanti, I. Kerenidis *et al.*, "Experimental verification of multipartite entanglement in quantum networks," *Nature Communications*, vol. 7, p. 13251, 2016.

[17] M. Epping, H. Kampermann, D. Bruß *et al.*, "Multi-partite entanglement can speed up quantum key distribution in networks," *New Journal of Physics*, vol. 19, no. 9, p. 093012, 2017.

[18] X. Su, X. Jia, C. Xie, and K. Peng, "Preparation of multipartite entangled states used for quantum information networks," *Science China Physics, Mechanics & Astronomy*, vol. 57, no. 7, pp. 1210–1217, 2014.

[19] J. T. Barreiro, T.-C. Wei, and P. G. Kwiat, "Beating the channel capacity limit for linear photonic superdense coding," *Nature Physics*, vol. 4, no. 4, pp. 282–286, 2008.

[20] M. Fitzi, N. Gisin, and U. Maurer, “Quantum solution to the Byzantine agreement problem,” *Physical Review Letters*, vol. 87, no. 21, p. 217901, 2001.

[21] N. C. Menicucci, P. Van Loock, M. Gu, C. Weedbrook, T. C. Ralph, and M. A. Nielsen, “Universal quantum computation with continuous-variable cluster states,” *Physical Review Letters*, vol. 97, no. 11, p. 110501, 2006.

[22] A. Peruzzo, M. Lobino, J. C. Matthews, N. Matsuda, A. Politi, K. Poulios, X.-Q. Zhou, Y. Lahini, N. Ismail, K. Wörhoff *et al.*, “Quantum walks of correlated photons,” *Science*, vol. 329, no. 5998, pp. 1500–1503, 2010.

[23] P. J. Shadbolt, M. R. Verde, A. Peruzzo, A. Politi, A. Laing, M. Lobino, J. C. Matthews, M. G. Thompson, and J. L. O’Brien, “Generating, manipulating and measuring entanglement and mixture with a reconfigurable photonic circuit,” *Nature Photonics*, vol. 6, no. 1, pp. 45–49, 2012.

[24] H. Jin, F. Liu, P. Xu, J. Xia, M. Zhong, Y. Yuan, J. Zhou, Y. Gong, W. Wang, and S. Zhu, “On-chip generation and manipulation of entangled photons based on reconfigurable lithium-niobate waveguide circuits,” *Physical Review Letters*, vol. 113, no. 10, p. 103601, 2014.

[25] R. Horn, P. Abolghasem, B. J. Bijlani, D. Kang, A. Helmy, and G. Weihs, “Monolithic source of photon pairs,” *Physical Review Letters*, vol. 108, no. 15, p. 153605, 2012.

[26] P. Sharapova, K. Luo, H. Herrmann, M. Reichelt, T. Meier, and C. Silberhorn, “Generation and active manipulation of qubits in $LiNbO_3$-based integrated circuits,” *arXiv preprint arXiv:1704.03769*, 2017.

[27] S. Takeuchi, “Recent progress in single-photon and entangled-photon generation and applications,” *Japanese Journal of Applied Physics*, vol. 53, no. 3, p. 030101, 2014.

[28] J. W. Silverstone, D. Bonneau, K. Ohira, N. Suzuki, H. Yoshida, N. Iizuka, M. Ezaki, C. M. Natarajan, M. G. Tanner, R. H. Hadfield *et al.*, “On-chip quantum interference between silicon photon-pair sources,” *Nature Photonics*, vol. 8, no. 2, pp. 104–108, 2014.

[29] C. Ma and S. Mookherjea, “Simultaneous dual-band entangled photon pair generation using a silicon photonic microring resonator,” *Quantum Science and Technology*, vol. 3, no. 3, p. 034001, 2018.

[30] F. Mazeas, M. Traetta, M. Bentivegna, F. Kaiser, D. Aktas, W. Zhang, C. A. Ramos, L. Ngah, T. Lunghi, E. Picholle *et al.*, “High-quality photonic entanglement for wavelength-multiplexed quantum communication based on a silicon chip,” *Optics Express*, vol. 24, no. 25, pp. 28 731–28 738, 2016.

[31] M. Savanier, R. Kumar, and S. Mookherjea, “Photon pair generation from compact silicon microring resonators using microwatt-level pump powers,” *Optics Express*, vol. 24, no. 4, pp. 3313–3328, 2016.

[32] J. Leuthold, C. Koos, and W. Freude, “Nonlinear silicon photonics,” *Nature Photonics*, vol. 4, no. 8, pp. 535–544, 2010.

[33] Y. Guo, W. Zhang, N. Lv, Q. Zhou, Y. Huang, and J. Peng, "The impact of nonlinear losses in the silicon micro-ring cavities on cw pumping correlated photon pair generation," *Optics Express*, vol. 22, no. 3, pp. 2620–2631, 2014.

[34] E. Engin, D. Bonneau, C. M. Natarajan, A. S. Clark, M. G. Tanner, R. H. Hadfield, S. N. Dorenbos, V. Zwiller, K. Ohira, N. Suzuki *et al.*, "Photon pair generation in a silicon micro-ring resonator with reverse bias enhancement," *Optics Express*, vol. 21, no. 23, pp. 27 826–27 834, 2013.

[35] P. Vergyris, T. Meany, T. Lunghi, G. Sauder, J. Downes, M. Steel, M. J. Withford, O. Alibart, and S. Tanzilli, "On-chip generation of heralded photon-number states," *Scientific Reports*, vol. 6, p. 35975, 2016.

[36] J. G. Titchener, A. S. Solntsev, and A. A. Sukhorukov, "Generation of photons with all-optically-reconfigurable entanglement in integrated nonlinear waveguides," *Physical Review A*, vol. 92, no. 3, p. 033819, 2015.

[37] J. G. Titchener, A. S. Solntsev, and A. A. Sukhorukov, "Reconfigurable cluster state generation in specially poled nonlinear waveguide arrays," *arXiv preprint arXiv:1704.03598*, 2017.

[38] D. A. Antonosyan, A. S. Solntsev, and A. A. Sukhorukov, "Effect of loss on photon-pair generation in nonlinear waveguide arrays," *Physical Review A*, vol. 90, no. 4, p. 043845, 2014.

[39] L. Chen, "Hybrid silicon and lithium niobate integrated photonics," Ph.D. dissertation, The Ohio State University, 2015.

[40] K.-H. Luo, S. Brauner, C. Eigner, P. R. Sharapova, R. Ricken, T. Meier, H. Herrmann, and C. Silberhorn, "Nonlinear integrated quantum electro-optic circuits," *Science Advances*, vol. 5, no. 1, p. eaat1451, 2019.

[41] J. Herec, J. Fiurášek, and L. Mišta Jr, "Entanglement generation in continuously coupled parametric generators," *Journal of Optics B: Quantum and Semiclassical Optics*, vol. 5, no. 5, p. 419, 2003.

[42] A. Rai, S. Das, and G. Agarwal, "Quantum entanglement in coupled lossy waveguides," *Optics Express*, vol. 18, no. 6, pp. 6241–6254, 2010.

[43] M. Kim, W. Son, V. Bužek, and P. Knight, "Entanglement by a beam splitter: Nonclassicality as a prerequisite for entanglement," *Physical Review A*, vol. 65, no. 3, p. 032323, 2002.

[44] L.-M. Duan, G. Giedke, J. I. Cirac, and P. Zoller, "Inseparability criterion for continuous variable systems," *Physical Review Letters*, vol. 84, no. 12, p. 2722, 2000.

[45] R. Simon, "Peres-horodecki separability criterion for continuous variable systems," *Physical Review Letters*, vol. 84, no. 12, pp. 2726–2729, 2000.

[46] D. Barral, N. Belabas, L. M. Procopio, V. d'Auria, S. Tanzilli, K. Bencheikh, and J. A. Levenson, "Continuous-variable entanglement of two bright coherent states that never interacted," *Physical Review A*, vol. 96, no. 5, p. 053822, 2017.

[47] I. Kogias, A. R. Lee, S. Ragy, and G. Adesso, "Quantification of Gaussian quantum steering," *Physical Review Letters*, vol. 114, no. 6, p. 060403, 2015.

[48] I. Kogias and G. Adesso, "Einstein–Podolsky–Rosen steering measure for two-mode continuous variable states," *JOSA B*, vol. 32, no. 4, pp. A27–A33, 2015.

[49] H. Leng, X. Yu, Y. Gong, P. Xu, Z. Xie, H. Jin, C. Zhang, and S. Zhu, "On-chip steering of entangled photons in nonlinear photonic crystals," *Nature Communications*, vol. 2, p. 429, 2011.

[50] X. Deng, Y. Xiang, C. Tian, G. Adesso, Q. He, Q. Gong, X. Su, C. Xie, and K. Peng, "Demonstration of monogamy relations for Einstein-Podolsky-Rosen steering in Gaussian cluster states," *Physical Review Letters*, vol. 118, no. 23, p. 230501, 2017.

[51] Y. Ming, A.-H. Tan, Z.-J. Wu, Z.-X. Chen, F. Xu, and Y.-Q. Lu, "Tailoring entanglement through domain engineering in a lithium niobate waveguide," *Scientific Reports*, vol. 4, p. 4812, 2014.

[52] D. Cavalcanti, P. Skrzypczyk, G. Aguilar, R. Nery, P. S. Ribeiro, and S. Walborn, "Detection of entanglement in asymmetric quantum networks and multipartite quantum steering," *Nature Communications*, vol. 6, p. 7941, 2015.

[53] A. Dutt, K. Luke, S. Manipatruni, A. L. Gaeta, P. Nussenzveig, and M. Lipson, "On-chip optical squeezing," *Physical Review Applied*, vol. 3, no. 4, p. 044005, 2015.

[54] F. Kaiser, B. Fedrici, A. Zavatta, V. DAuria, and S. Tanzilli, "A fully guided-wave squeezing experiment for fiber quantum networks," *Optica*, vol. 3, no. 4, pp. 362–365, 2016.

[55] D. Barral, K. Bencheikh, V. D'Auria, S. Tanzilli, N. Belabas, and J. A. Levenson, "Minimum resources for versatile continuous-variable entanglement in integrated nonlinear waveguides," *Physical Review A*, vol. 98, no. 2, p. 023857, 2018.

[56] R. Loudon and P. L. Knight, "Squeezed light," *Journal of Modern Optics*, vol. 34, no. 6-7, pp. 709–759, 1987.

[57] U. L. Andersen, T. Gehring, C. Marquardt, and G. Leuchs, "30 years of squeezed light generation," *Physica Scripta*, vol. 91, no. 5, p. 053001, 2016.

[58] X. Jin, J. Su, Y. Zheng, C. Chen, W. Wang, and K. Peng, "Balanced homodyne detection with high common mode rejection ratio based on parameter compensation of two arbitrary photodiodes," *Optics Express*, vol. 23, no. 18, pp. 23 859–23 866, 2015.

[59] S. Midgley, A. Bradley, O. Pfister, and M. Olsen, "Quadripartite continuous-variable entanglement via quadruply concurrent down-conversion," *Physical Review A*, vol. 81, no. 6, p. 063834, 2010.

CHAPTER 7

Conclusion and Future Scopes

7.1 Conclusion

This dissertation summarizes an attempt towards advancing some of the state-of-the-art integrated photonic technologies for their applications in linear (optical directional coupler (DC)), polarization beam-splitter (PBS), filters), nonlinear (frequency comb (FC)), and quantum (continuous-variable (CV) entanglement) optics. Current chapter discusses the possible scopes of improvement and future-direction of this thesis-work.

Chapter 2 presents a novel scheme to miniaturize the DC and PBS using off-centered and hybrid slot waveguides. Optimally placed off-centered slots can enhance the coupling coefficients between two adjacent waveguides by $> 88\%$. Employing this scheme, we have achieved a DC and a PBS of coupling length $\sim 0.9\,\mu$m, and $\sim 1.1\,\mu$m, respectively. In chapter 3, non-concentric nested microring resonators (NN-MRR) are proposed for ultra-compact broadband ($>$10 nm) filter design and for athermal electro-optic modulation. Such NN-MRRs are fabrication tolerant and can circumvent the stringent requirement of the critical-coupling to obtain the optimal performance. Next chapter onward we enter in the domain of nonlinear optics; we develop a theory of Kerr FC in the presence of all nonlinear losses and free-carrier effects based on modified Lugiato-Lefever Equation. Chapter 5 demonstrates the advantages of bi-chromatic pumping over the single-pump configuration to generate FC. Chapter 6 is dedicated to the quantum optics. We culminate our thesis-work by disserting the best possible pumping scheme for the parallel generation of spatially entangled (bipartite) CV-states in multiple waveguide pairs of a 5×5 periodically-poled lithium niobate (PPLN) waveguide array.

7.2 Future Scopes

Future scopes of the thesis are listed below:

- The strategy proposed in chapter 2 to shrink the optical devices is new, albeit, the slots are optimized by trial and error method. Sophisticated optimization techniques such as variational principle [1], evolutionary algorithms (genetic algorithm, particle swarm optimization etc.), machine learning can be used instead [2–4]. Also the fabrication of hybrid (horizontal and vertical together) slots is still a big challenge. Dearth of high-end fabrication facility precluded us to demonstrate the hybrid-slot PBS.
- The complete soliton dynamics in presence of nonlinear losses and free-carrier effects is yet to be explored and there remains a huge-scope to extend the theory presented in chapter 4. For instance, photo-refractive index induced reverse Kerr-tilt provides an alternative mechanism to soliton generation against the predominantly followed laser-detuning approach. The full potential of this approach deserves further exploration. The emergence of second-order nonlinear material based FC platforms, with lithium niobate being the dominant material of interest is also governed by strong photo-refractive effects. Thus identifying the role of the photo-refractive and photo-thermal effects in $\chi^{(2)}$ based FC is an important problem to consider. Some of the highly nonlinear materials (e.g. AlGaAs) simultaneously exhibit both $\chi^{(2)}$ and $\chi^{(3)}$ nonlinearity. The presented study requires to be modified to include the $\chi^{(2)}$ effects. Furthermore, recently, the advantages of coupled microresonators for FC generation is being studied extensively [5]. The proposed non-concentric microrings (Chapter 3) can be utilized to fetch all those ad-

vantages, however, within a compact geometry. Such NN-MRRs or internally cascaded MRRs when coupled with III-V semiconductor quantum dots can be a very efficient narrowband single-photon sources (SPSs) [6]. Spectrally engineered Kerr NN-MRRs can also be implemented as quasi-determinant SPSs [7].

- Complete spatio-temporal dynamics of the dual-pump microresonator (chapter 5) is yet to be discovered. It is already established that stimulated Raman scattering degrades the performance of the FC [8]. Currently, we are investigating the Raman-resilience and the possibility to obtain the breather soliton in the presence of dual-pump [9]. Whether dual-pump can amend the entanglement between the generated photon-pairs from a Kerr microresonator in the presence of Raman-effect would be a very interesting aspect to study [10]. In addition, $\mathcal{PT}$-Symmetric Non-Hermitian optical resonators have bright prospect because of their use as topological insulators or for nonlinear mixing [11].
- Chapter 6 of my thesis deals with the numerical study of the parallel generation of the CV entangled (bipartite) states in PPLN waveguide array. Our study shows further promise of generating higher dimensional entangled CV cluster states and unveils new avenues in the realization of photonic quantum computing [12]. We are currently examining the possibility of generating multipartite and cluster states in PPLN waveguide arrays. An immediate approach forward is to investigate the generation of higher dimensional Schrödinger cat states using such waveguide arrays.
- Apart from these, the generation of higher-dimensional discrete-variable entangled (time-energy) quantum states are already demonstrated on an integrated FC platform [13]. Quantum computing with CV-entangled states generated through the quantum optical FC can be another interesting domain to be explored. [14].

References

[1] K. Gehlot and A. Sharma, "Optimization of Si slot waveguide using approximate semi-analytical method," *Optics Express*, vol. 24, no. 5, pp. 4722–4729, 2016.

[2] A. N. Tait, T. F. De Lima, E. Zhou, A. X. Wu, M. A. Nahmias, B. J. Shastri, and P. R. Prucnal, “Neuromorphic photonic networks using silicon photonic weight banks,” *Scientific Reports*, vol. 7, no. 1, p. 7430, 2017.

[3] M. H. Tahersima, K. Kojima, T. Koike-Akino, D. Jha, B. Wang, C. Lin, and K. Parsons, “Deep neural network inverse design of integrated photonic power splitters,” *Scientific Reports*, vol. 9, no. 1, p. 1368, 2019.

[4] K. Yao, R. Unni, and Y. Zheng, “Intelligent nanophotonics: merging photonics and artificial intelligence at the nanoscale,” *Nanophotonics*, vol. 8, no. 3, pp. 339–366, 2019.

[5] X. Xue, X. Zheng, and B. Zhou, “Super-efficient temporal solitons in mutually coupled optical cavities,” *Nature Photonics*, vol. 13, no. 1, pp. 616–622, 2019.

[6] M. Davanco, J. Liu, L. Sapienza, C.-Z. Zhang, J. V. D. M. Cardoso, V. Verma, R. Mirin, S. W. Nam, L. Liu, and K. Srinivasan, “Heterogeneous integration for on-chip quantum photonic circuits with single quantum dot devices,” *Nature communications*, vol. 8, no. 1, p. 889, 2017.

[7] M. Heuck, J. G. Koefoed, J. B. Christensen, Y. Ding, L. H. Frandsen, K. Rottwitt, and L. K. Oxenløwe, “Unidirectional frequency conversion in microring resonators for on-chip frequency-multiplexed single-photon sources,” *New Journal of Physics*, vol. 21, no. 3, p. 033037, 2019.

[8] Y. Wang, M. Anderson, S. Coen, S. G. Murdoch, and M. Erkintalo, “Stimulated Raman scattering imposes fundamental limits to the duration and bandwidth of temporal cavity solitons,” *Physical Review Letters*, vol. 120, no. 5, p. 053902, 2018.

[9] A. Roy, R. Haldar, and S. K. Varshney, “Dual-pumped kerr cavity soliton based synchronous all-optical buffer: Raman resilience,” in *OSA Advanced Photonics Congress (AP) 2019 (IPR, Networks, NOMA, SPPCom, PVLED).* paper IT1A.3, OSA, 2019, pp. 1–2.

[10] A. S. Clark, M. J. Collins, A. C. Judge, E. C. Mägi, C. Xiong, and B. J. Eggleton, “Raman scattering effects on correlated photon-pair generation in chalcogenide,” *Optics Express*, vol. 20, no. 15, pp. 16 807–16 814, 2012.

[11] M.-A. Miri and A. Alù, “Exceptional points in optics and photonics,” *Science*, vol. 363, no. 6422, p. eaar7709, 2019.

[12] M. Gu, C. Weedbrook, N. C. Menicucci, T. C. Ralph, and P. van Loock, “Quantum computing with continuous-variable clusters,” *Physical Review A*, vol. 79, no. 6, p. 062318, 2009.

[13] M. Kues, C. Reimer, P. Roztocki, L. R. Cortés, S. Sciara, B. Wetzel, Y. Zhang, A. Cino, S. T. Chu, B. E. Little *et al.*, “On-chip generation of high-dimensional entangled quantum states and their coherent control,” *Nature*, vol. 546, no. 7660, pp. 622–626, 2017.

[14] O. Pfister, “Continuous-variable quantum computing in the quantum optical frequency comb,” *arXiv preprint arXiv:1907.09832*, 2019.

APPENDIX **A**

Kerr Frequency Comb with Nonlinear Losses

A.1 Nonlinear properties of different materials

Table A.1: Optical properties such as transparency (Tx), refractive indices (RIs), nonlinear (NL) RIs, thermo-optic coefficients (TOCs), band-gap (BG) energies of CFs, and the Q-factor of the CF based optical resonators achieved till date. Atomic numbers of the materials which are combined with fluorine to yield the CFs are mentioned in blue texts.

Material Platform	**Tx** (μm)	**RI** (n_0) (1.55 μm)	**NL-RI** (n_2) $\times 10^{-20}$ m^2/W	**TOC** $\times 10^{-6}$/K	**BG** (eV)	Q $\times 10^9$
$_{4}$**BeF$_2$**	soluble in water					
$_{12}$**MgF$_2$**	0.12–7	1.37 (o) 1.38 (e)	∼0.99	2.3 (o) 1.7 (e)	6.824	∼10
$_{20}$**CaF$_2$**	1.399–5	1.426	$1 - 3.2$	-10.6	∼12	300
$_{38}$**SrF$_2$**	0.13–11	1.43	∼1.51	-12.6	∼11.25	∼1.1
$_{56}$**BaF$_2$**	0.15–12	1.466	∼1.97	-15.2	∼11	∼1.3
$_{88}$**RaF$_2$**	radio-active, unsafe to use					

Important performance measures for the generation of the FC are: Q-factor of the micro-cavity, threshold power (P_{th}), FOM ($= \lambda^{-1} n_2/\beta_{2\text{PA}}$), etc. Note that,

Table A.2: Comparison of different nonlinear optical parameters such as BG, RI, N-RI, 2PA-coefficient (β_{2PA}), FCA-coefficient (σ_{FCA}) etc. for c-Si, a-Si, a-Si:H at operating wavelength 1.55μm. NA: Not available/found.

Material Platform	**BG** (eV)	**RI** (n_0)	**NL-RI** (n_2) $\times 10^{-18}$ m^2/W	β_{2PA} (cm/GW)	$\sigma_{\text{FCA}} \times 10^{-17}$ (cm^2)	τ (ns)
c-Si	1.14	3.477	(4.5±1.5)	$0.5 - 1.5$	1.47	0.45
a-Si	1.4-1.7	3.48	~ 42	~ 4.1	NA	0.4
a-Si:H	1.6-1.9	$3.4 - 3.48$	~ 42 $(3 - 70)$	4.1 $(0.14 - 7)$	19	0.4

crystals with energy bandgap (BG) $< 1.6\mu$m do not exhibit 2PA in telecom wavelength. In table A.1 the optical properties of the crystalline fluorides are provided. Table A.2 tabulates the optical properties of different the allotropes of widely used silicon. Finally, table A.3 discusses necessary properties (at 1.55 μm except Ge) of the extensively used $\chi^{(3)}$ materials.

Table A.3: Comparison of different optical parameters of various third-order nonlinear materials. NA: Not available

Material	**Tx** (μm)	n_0	$n_2 \times 10^{-20}$ (m^2/W)	**BG** (eV)	β_{2PA} (cm/GW)	P_{th} (mW)
Si	$1.2 - 9$	3.477	250	1.1	0.5	3
SiO_2	$0.18 - 3$	1.445	2.2	8.9	×	0.3
Si_3N_4	upto 7	1.98	25	5.0	×	0.3
SiC	$0.37 - 5.6$	2.6	80	$2.36 - 3.23$	×	NA
Diamond	$0.3- > 10$	2.4	8.2	5.5	×	20
Hydex	$0.18 - 3.5$	1.7	12	9.0	×	54
Ge	$1.8- > 15$	4	500	0.67	25.6	NA
$Al_xGa_{1-x}As$	$0.9 - 17$	3.3	2600	$1.42 - 2.16$	0.5	3
GaAs	$1 - 16$	3.37	2000	1.43	2.5	NA
GaP	$0.5- > 12$	3.128	600	2.26	×	NA
GaN	$0.36 - 7$	2.32	340	3.4	×	NA
AlN	$0.2 - 13.6$	2.1	23	6.0	×	200
TiO_2	> 0.5	2.4	16	3.2	×	NA
As_2S_3	$1 - 12$	2.44	$300 - 600$	$2.26 - 2.4$	×	NA
$Ga_xIn_{1-x}P$	NA	3.1	600	$1.8 - 1.9$	×	NA

A.2 Normalization of the modified LLE

Table A.4: Values of different parameters/symbols in the presence and absence of different nonlinear losses (NLL) and higher-order dispersion (HOD). NLL includes nPA, and free-carrier effects (FCE) i.e. FCA and FCD

Symbol	**No NLL No HOD**	**no NLL HOD**	**Only nPA**	**nPA & FCA**	**nPA, FCE, no HOD**	**nPA, FCE & HOD**
θ_{cn}	$=0$	$=0$	$\neq 0$	$\neq 0$	$\neq 0$	$\neq 0$
τ_{c}	$=0$	$=0$	$\to 0$	$\neq 0$	$\neq 0$	$\neq 0$
$C_{\mathrm{n}}(\theta_{\mathrm{cn}}\tau_{\mathrm{c}})$	$=0$	$=0$	$\to 0$	$\neq 0$	$\neq 0$	$\neq 0$
ϕ_{c}	$=0$	$=0$	$\to 0$	$\neq 0$	$\neq 0$	$\neq 0$
$\frac{\partial\phi_{\mathrm{c}}}{\partial\tau}$	$-\infty$	$-\infty$	$-\infty$	finite	finite	finite
Q_{n}	$=0$	$=0$	$\neq 0$	$\neq 0$	$\neq 0$	$\neq 0$
K	$=0$	$=0$	$=0$	$=0$	$\neq 0$	$\neq 0$
$d_k(k\geq 3)$	$=0$	$\neq 0$	$=0$	$=0$	$=0$	$\neq 0$

A.3 SSFM: Algorithm in a nutshell

LLE does not possess an exact analytic solution. Therefore, We adopt SSFM to solve the normalized LLE given by Eq. 4.10. The equation is divided into two different parts, viz. (a) Linear ($\mathcal{L}$), and (b) Nonlinear ($\mathcal{NL}$) with the pump term (S) given by,

$$\frac{\partial u}{\partial \xi} = \mathcal{L}u = -i\frac{s}{2}\frac{\partial^2 u}{\partial \tau^2} + \sum_{k\geq 3}\frac{d_k}{k!}\frac{\partial^k u}{\partial \tau^k} \tag{A.1}$$

$$\frac{\partial u}{\partial \xi} = -\left(\mathcal{NL}\right)u + S = -\left[1 + i\left(\Delta - |u|^2\right)\right]u + S \tag{A.2}$$

Eq. A.1 has analytical solution in Fourier-domain, whereas, the solution of Eq. A.2 can be approximated by the help of integrating factor in time-domain, given that the step-size $\Delta\xi$ is sufficiently small to converge the solution. During the thesis work, we perform the integral as given in Eq. A.2 by the well-known 'RK4-method'. The SSFM in elucidated in Fig. A.1 where one can initiate the algorithm following any of the two paths, 'Path 1' and 'Path 2', before entering the FFT-iFFT loop. Obeying the same algorithm we study the generation of FC in absence of any nonlinear losses, in presence of only 2PA, and in presence of only 3PA, in Si microresonators as illustrated in Fig. A.2. As discussed earlier, it is observed that the 2PA in silicon MR can completely inhibit the FC formation.

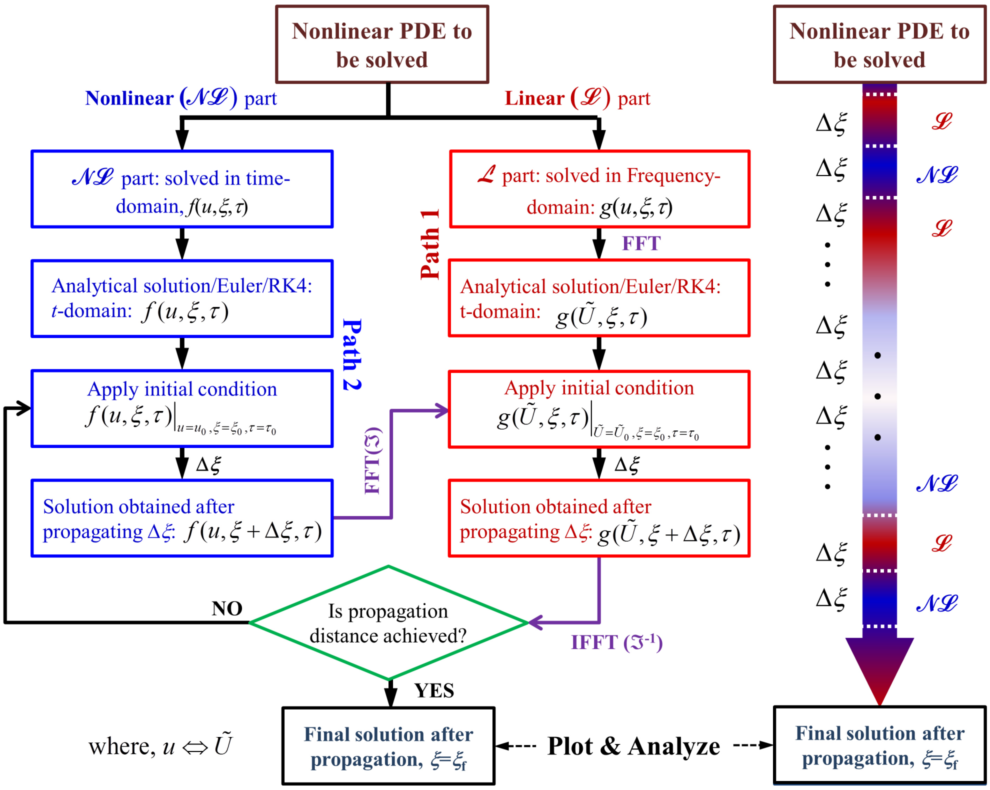

Figure A.1: Algorithm for SSFM in a nut-shell

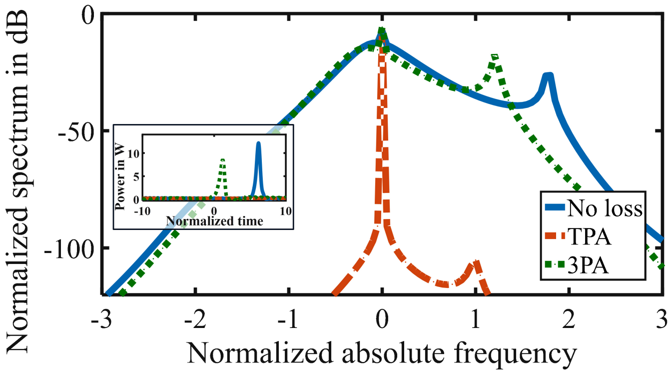

Figure A.2: Normalized spectrum of frequency-comb without any nonlinear losses (solid blue curve), with only 2PA (dashed red curve) and with 3PA (dotted green curve). The inset shows the final pulses in the time domain.

APPENDIX B

Dual-pump Kerr Microresonators

B.1 Variational Treatment for Dual-pump Frequency Comb

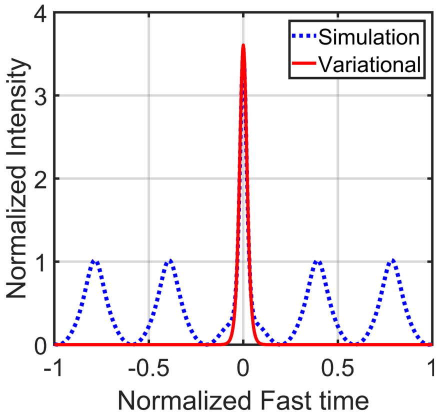

Figure B.1: Agreement between the temporal waveform obtained through simulation (blue dotted curve) with the one obtained using the variational method (red solid curve). Both the peak intensity and temporal width match closely. The MR parameters considered are: $\Delta = 1.7$, $\phi_0 = 1.3$, $\beta_2 = -0.002$, and $\Omega = 8$.

We adopt the semi-analytical variational approach to justify the ansatz of the CS supported by the dual pumped MR as given in Eq. 5.40. The normalized LLE can be expressed as,

$$\mathrm{i}\,\frac{\partial A}{\partial t} - \frac{\beta_2}{2}\frac{\partial^2 A}{\partial \tau^2} + |A|^2 A - \Delta A = \mathrm{i}\,\varepsilon\,(A) \tag{B.1}$$

We have neglected The higher-order dispersion terms. $\varepsilon(A)$ represents the perturbation arising due to the pump-term and linear absorption, which is given by:

$$\varepsilon\left(A\right) = f_o \cos\left(\Omega\tau\right) - A. \tag{B.2}$$

This analysis considers only the solitonic part, thereby excluding the oscillatory background from our ansatz. To completely match the numerical results with that of the results obtained from the variational method, one has to include the oscillatory background as well, which eventually leads to cumbersome calculations and hence not considered in this derivation. The ansatz can be written as:

$$A\left(t,\tau\right) = \left(\frac{E\left(t\right)\eta\left(t\right)}{2}\right)^{\frac{1}{2}} \left[\operatorname{sech}\left(\eta\left(t\right)\tau\right)\right] \exp\left(\mathrm{i}\,\phi\left(t\right)\right) \tag{B.3}$$

$$C_3 = \left(\frac{E\left(t_\infty\right)\eta\left(t_\infty\right)}{2}\right)^{\frac{1}{2}}, \;\; \text{B=}\eta\left(t_\infty\right) \;\text{ and }\; \phi_{C_3} = \phi\left(t_\infty\right) \tag{B.4}$$

where t_∞ represents the steady-state values. we obtain the following reduced Lagrangian equation:

$$L = \frac{\partial\phi}{\partial t} - \frac{\beta_2}{6}E\eta^2 - E^2\frac{\eta}{6} + \Delta E + \mathrm{i}\int_{-\pi}^{\pi} \left(\varepsilon A^* - \varepsilon^* A\right) \mathrm{d}\,\tau \tag{B.5}$$

which results in the following Euler-Lagrangian equations that describe the slow-time evolution of the variational parameters.

$$\frac{\partial\phi}{\partial t} = \frac{\eta}{3}\left(E + \frac{\beta_2}{2}\eta\right) - \Delta - f_0\left(\frac{1}{2E\eta}\right)^{\frac{1}{2}} \pi \sin\left(\phi\right) \operatorname{sech}\left(\frac{\Omega\pi}{2\eta}\right) \tag{B.6}$$

$$\frac{\partial E}{\partial t} = -2E + 2f_0\left(\frac{E}{2\eta}\right)^{\frac{1}{2}} \pi \cos\left(\phi\right) \operatorname{sech}\left(\frac{\Omega\pi}{2\eta}\right) \tag{B.7}$$

$$\eta = \frac{-2}{\beta_2}\left[\frac{E}{4} - \frac{3f_0}{2\eta}\left(\frac{1}{2E\eta}\right)^{\frac{1}{2}} \pi \sin\left(\phi\right) \operatorname{sech}\left(\frac{\Omega\pi}{2\eta}\right) + \frac{3f_0}{\eta}\left(\frac{1}{2E\eta}\right)^{\frac{1}{2}} \sin\left(\phi\right) I\right] \tag{B.8}$$

where,

$$I = \int_{-\pi}^{\pi} \Psi \operatorname{sech}\left(\Psi\right) \tanh\left(\Psi\right) \cos\left(\Omega\frac{\Psi}{\eta}\right) \mathrm{d}\,\Psi \tag{B.9}$$

Figure B.1 displays an excellent agreement between semi-analytical variational method and the numerical simulation based on SSFM. To conclude, our analytical expressions and numerical results obtained from the SSFM are validated through the semi-analytical variational principle.

Publications related to the Thesis

Journals

1. **R. Haldar**, D. Barral, K. Bencheik, A. Levenson, N. Belabas, "Parallel Generation of Spatially Entangled Continuous Variable States in a 5×5 Periodically Poled $LiNbO_3$ Waveguide Array," *under preparation.*
2. **R. Haldar**, A. Roy, P. Mondal, V. Mishra, and S. K. Varshney, "Free-carrier driven Kerr frequency comb in optical micro-cavities: Steady-state, bistability, self-pulsation, and modulation instability," *Phys. Rev. A*. vol. 99, no. 3, p. 033848, 2019.
3. A. Roy, **R. Haldar**, S. K. Varshney, "Robust, Synchronous Optical Buffer and Logic Operation in Dual-pump Kerr Micro-Resonator," *IEEE Journal of Lightwave Technology*, vol. 36, no. 24, pp. 5807–5814, 2018.
4. **R. Haldar**, V. Mishra, C. Koos, W. Freude, S. K. Varshney, "Fabrication-tolerant, Temperature Insensitive High-Q Single-bus Nested Off-axis Microring Resonators for Sensing and Nonlinear Applications," *under preparation.*
5. A. Roy, **R. Haldar**, and S. K. Varshney, "Analytical Model of Dual-Pumped Kerr Micro Resonators for Variable Free Spectral Range and Composite Frequency Comb Generation," *IEEE Journal of Lightwave Technology*, vol. 36, no. 12, pp. 2422–2429, 2018.
6. **R. Haldar**, V. Mishra, A. Dutt, S. K. Varshney, "On-chip Broadband Ultra-Compact Directional Couplers and Polarization Splitters based on Off-centred and Non-Symmetric Slotted Si Wire Waveguides," *Journal of Optics, IOP Science*, vol. 18, no. 10, p. 105801, 2016.
7. **R. Haldar**, Abhik D. Banik, and S. K. Varshney, "Design of CMOS compatible and compact, thermally-compensated electro-optic modulator based on off-axis microring resonator for dense wavelength division multiplexing applications," *Optics Express*, vol. 22, no. 19, pp. 22411–22420, 2014.
8. **R. Haldar**, S. Das and S. K. Varshney, "Theory and Design of Off-axis Microring resonators for on-chip photonics applications," *IEEE Journal of Lightwave Technology*, vol. 31, no. 24, pp. 3976–3986, 2013.

Conferences

1. A. Roy, **R. Haldar**, S. K. Varshney, "Dual-pump Kerr Microresonators: Raman resilience, Integrated Photonic Research (IPR), Silicon and Nanophotonics, Advanced Photonics Congress, California, USA, 2019. Paper ID: IT1A.3
2. **R. Haldar**, A. Roy, S. K. Varshney, "Bistability and Self-pulsation in Free-carrier Driven Optical Microcavities with all Nonlinear Losses, ICEE, Bangalore, India (2018).
3. A. Roy, **R. Haldar**, and S. K. Varshney, "Breakdown of optical lattice formation in dual-pumped supercavity soliton states," SPIE, Europe, Strasbourg, France, 2018 (Paper ID: 10684-65).
4. A. Roy, **R. Haldar**, and S. K. Varshney, "Synchronous All-Optical Buffer-cum-Logic Gates in Dual-Pump Kerr Microring Resonators, Frontiers in Optics and Laser Science (FiO/LS), Washington DC, USA 2017. (Paper ID: JTu3A.22)
5. **R. Haldar**, A. Roy, P. Mondal, V. Mishra, S. K. Varshney, "Analysis of Modulation Instability in Free-carrier Driven Microring Resonator Based Kerr Frequency Comb, FiO/LS, Washington DC, 2017 (Paper ID: JTu3A.13).
6. A. Roy, **R. Haldar**, and S. K. Varshney, "Implications of Self-Steepening in Temporal Tweezing of light for Optical Buffer Applications," FiO/LS, Washington DC, USA, 2017 (Paper ID: JTu3A.24)
7. **R. Haldar**, P. Mondal, V. Mishra and S. K. Varshney, "Steady-state Solutions of Free-carrier Driven Normalized Mean-field Lugiato-Lefever Equation: Observation of Negative Kerr-tilts," ICO'24, Tokyo, Japan, 2017. (Paper ID: C000577)
8. **R. Haldar**, P. Mondal, V. Mishra and S. K. Varshney, "Stability Analysis and Bandwidth Estimation of Free-carrier Driven Kerr Frequency-combs, CLEO-PR, Singapore, 2017. (Paper ID: s2572).
9. **R. Haldar**, P. Mondal, V. Mishra, S. K. Varshney, "Temperature-Insensitive Extremely Flat Dispersion in Highly-Nonlinear Si-Organic Hybrid Slot Waveguides, in The International Conference on Fiber Optics and Photonics, IIT Kanpur, Kanpur, India, 2016. (Paper ID: Th3A. 13)
10. **R. Haldar**, V. Mishra, C. Koos, W. Freude, S. K. Varshney, "Fabrication tolerant, Temperature Insensitive High-Q Single-bus Nested Off-axis Microring Resonators," IPR, Vancouver, Canada, 2016. (Paper ID: ITu1B.4).
11. **R. Haldar**, V. Mishra, Shailendra K. Varshney, "Ultra Compact Optical Switches and Polarization Splitter based on Non-Symmetric Slotted Si Wire Waveguides, IPR, Boston, Massachusetts, USA, 2015. (Paper ID: JM3A.24).
12. **R. Haldar**, Abhik D. Banik, Sanathanan M. S., S. K. Varshney, "Compact Athermal Electro-optic modulator design based on SOI Off-axis Microring Resonator, CLEO-USA, San Jose, CA, USA, 2014. (Paper ID: JW2A. 37).
13. **R. Haldar**, Sanathanan M. S., Abhik D. Banik, S. K. Varshney, "Compact design of Athermal Electro-optic modulator based on SOI Off-axis Microring Resonator, in International Workshop on Recent Advances in Photonics (WRAP), organized by IIT Delhi, 2013.
14. **R. Haldar**, S. Das and S. K.Varshney, "Theory and Design of Off-axis Microring Resonators based Compact Bandpass filter for On-chip Applications, FiO/LS, Orlando, Florida, 2013.

Author's Biography

Raktim Haldar was born in Kolkata (Calcutta), West Bengal, India (1989). His father is a retired Govt. employee, and his mother is a house-wife. He is currently enrolled as a research scholar (senior research fellow (SRF)) towards his Ph.D. degree since 2014 under the supervision of Prof. Shailendra K. Varshney, Electronics and Electrical Communication Engineering (E&ECE) Department, Indian Institute of Technology Kharagpur (IIT Kharagpur). Before that, Raktim has received M. Tech. degree from the same department in RF & Microwave Engineering in 2013. His research interests include nanophotonic devices, silicon photonics, plasmonics, electromagnetic theory, fiber-optic communication systems, integrated nonlinear and quantum optics, quantum computation, quantum cryptography, and optimization techniques using different evolutionary algorithms, etc. During his M. Tech and Ph.D. tenure, he has served as teaching assistant for microwave engineering, satellite communication, optical communication, basic electronics, physics of photonic devices, and nonlinear optics. Raktim has authored and co-authored several peer-reviewed journals and international conferences. Among his journals, JOPT, *IOP* Science **18** (10), 105801 (2016) (authored), and *IEEE* JLT **36** (13), 2528 (2018) (co-authored) have been selected to be the 'Highlights', respectively. Raktim is a receiver of several travel grants—ICO'24, DST-ITS (Indian Govt.), OSA foundation student travel grant, OSA student leadership travel grant, Raman-Charpak Fellowship travel grant, etc. to attend conferences worldwide. He is also a regular reviewer of the prestigious *SPIE*-journal–'Optical Engineering (OE)', *OSA*-journal–'Photonics Research', 'Applied Optics', 'Optics Express', 'JOSA A', *Elsevier* journal viz. 'Optics Communications', and '*IEEE* Photonics Journal', etc. Being a student member of Optical Society of America (OSA) from 2015, he is actively involved in various activities of the OSA student chapter, IIT Kharagpur. He is also member of *SPIE* and *IEEE* (student chapter IIT Kharagpur). In 2017, Raktim received Raman-Charpak Fellowship to continue his research as a visiting scholar on experimental quantum photonics in CNRS/C2N, Marcoussis Campus, under Université Paris Saclay, France. In future, he is looking for an exposure to the integrated nanophotonic devices for nonlinear and quantum applications with a suitable balance between both theory and experiments.

Apart from being an academician, he is a painter. He has immense interest in learning and exploring different art genres, starting from the medieval, neo-classical to the modern era. In addition to his interest in drawing portraits and caricatures, he is currently dedicating most of his time to learn impressionism and cubism. He is also doing research on the different art-epochs of West Bengal (article coming soon). Raktim is an avid reader. Besides reading story books, his another hobby is photography. Some of his paintings and photographs can be found in his website/Indian newspapers. Story books and movies continue to inspire him are also enlisted in the resources tab of the website. He is fond of playing/watching cricket, chess, cycling, gyming, and listening to the music. Raktim is also a science-enthusiast and write articles both in Bengali and English to disseminate the interesting scientific facts and knowledge among children.

Contact Information

Email: `raktim.halder@gmail.com`, `raktim@ece.iitkgp.ernet.in`
Website link: https://sites.google.com/view/raktim-haldar/home

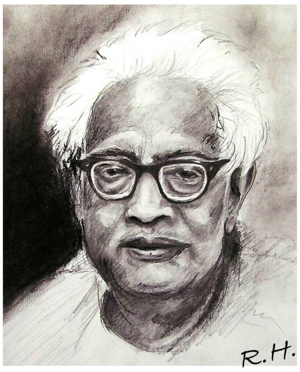

S. N. Bose (1894-1974)
Discovery of Bosons

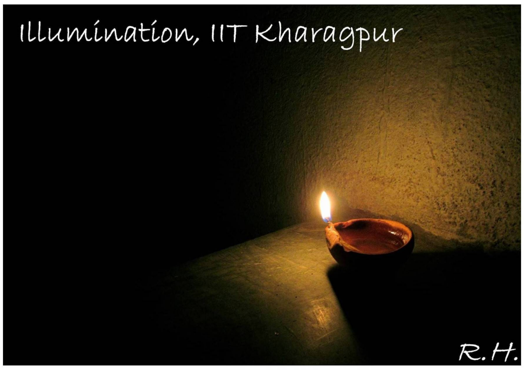

“तमसो मा ज्योतिर्गमय”
“From darkness to light”